

REPORT DOCUMENTATION PAGE

AFRL-SR-AR-TR-04-

0224

Public reporting burden for this collection of information is estimated to average 1 hour per response, including the time for reviewing instru-
data needed, and completing and reviewing this collection of information. Send comments regarding this burden estimate or any other asp-
this burden to Department of Defense, Washington Headquarters Services, Directorate for Information Operations and Reports (0704-0188
4302. Respondents should be aware that notwithstanding any other provision of law, no person shall be subject to any penalty for failing to
valid OMB control number. PLEASE DO NOT RETURN YOUR FORM TO THE ABOVE ADDRESS.

1. REPORT DATE (DD-MM-YYYY)
02/04/2003

2. REPORT TYPE
Final Technical

3. DATES COVERED (From - To)
01/01/2000 - 09/30/2002

4. TITLE AND SUBTITLE

Aeroacoustic Optimization and Control

5a. CONTRACT NUMBER

5b. GRANT NUMBER
F49620-00-1-0105

5c. PROGRAM ELEMENT NUMBER
61102F

5d. PROJECT NUMBER
2307

5e. TASK NUMBER
AX

5f. WORK UNIT NUMBER

6. AUTHOR(S)

Mingjun Wei, Jonathan B. Freund, John Kim

7. PERFORMING ORGANIZATION NAME(S) AND ADDRESS(ES)

Regents of the University of California, Los Angeles
University of California, Los Angeles
10920 Wilshire Boulevard, Suite 1200
Los Angeles, CA 90024-1406

8. PERFORMING ORGANIZATION REPORT NUMBER

9. SPONSORING / MONITORING AGENCY NAME(S) AND ADDRESS(ES)

USDAF Office of Scientific Research
4015 Wilson Boulevard, Room
Arlington, VA 22203-1954

10. SPONSOR/MONITOR'S ACRONYM(S)

11. SPONSOR/MONITOR'S REPORT NUMBER(S)

12. DISTRIBUTION / AVAILABILITY STATEMENT

Distribution is unlimited.

13. SUPPLEMENTARY NOTES

20040426 066

14. ABSTRACT

Much attention has been given to the jet noise problem since the jet engine became a power plant for aircraft after the Second World War, but there has been little modeling progress for realistic geometries. Scaling laws such as Lighthill's famous $P \propto U^8$, sound-power scaling with jet exit velocity that are derived from these theories have been enormously successful in motivating higher by-pass engines to reduce noise, but they have offered little further guidance for improvements through nozzle geometries or active flow control. The aircraft noise problem has recently become more pressing as both military and civilian use of air space increase. At present, the noise of some military aircraft is so intense that it can actually fatigue aircraft components. Airbase noise is becoming an important issue with several (some successful) lawsuits involved. Personnel are also affected - early predictions/results suggest that the JSF landing in vertical mode will be too loud for ground personnel to tolerate. The civilian aerospace sector faces their own serious aircraft noise problems. Technology transfer from the present work supports intense noise control efforts at domestic aerospace companies as well.

15. SUBJECT TERMS

acoustics, control, optimization, sound generation

16. SECURITY CLASSIFICATION OF:

unclassified

17. LIMITATION OF ABSTRACT

unlimited

18. NUMBER OF PAGES

151

19a. NAME OF RESPONSIBLE PERSON

John Kim

a. REPORT
unclassified

b. ABSTRACT
unclassified

c. THIS PAGE
unclassified

19b. TELEPHONE NUMBER (include area code)
310-825-4393

FINAL REPORT: AFOSR #F49620-00-1-0105

Aeroacoustic Optimization And Control

Mingjun Wei and Jonathan B. Freund

Theoretical and Applied Mechanics
University of Illinois at Urbana-Champaign
jbfreund@uiuc.edu

John Kim

Mechanical and Aerospace Engineering
University of California, Los Angeles

1 Introduction

1.1 Technological Background

Much attention has been given to the jet noise problem since the jet engine became a power plant for aircraft after the Second World War,¹ but there has been little modeling progress for realistic geometries. Scaling laws such as Lighthill's² famous $P \propto U_j^8$ sound-power scaling with jet exit velocity that are derived from these theories have been enormously successful in motivating higher by-pass engines to reduce noise, but they have offered little further guidance for improvements through nozzle geometries or active flow control. The aircraft noise problem has recently become more pressing as both military and civilian use of air space increase. At present, the noise of some military aircraft is so intense that it can actually fatigue aircraft components. Airbase noise is becoming an important issue with several (some successful) lawsuits involved. Personnel are also affected—early predictions/results suggest that the JSF landing in vertical mode will be too loud for ground personnel to tolerate. The civilian aerospace sector faces their own serious aircraft noise problems. Technology transfer from the present work supports intense noise control efforts at domestic aerospace companies as well.

Jet noise, like many complex fluid systems, has eluded control efforts for years simply because models lack the necessary fidelity. There is neither a sufficient understanding of the mechanics nor a practical simulation procedure to use in place of expensive trial-and-error experimentation. Aeroacoustic flows are particularly challenging examples of this. Although theoretical noise sources were first formulated 50 years ago,² their direct use in modeling and control has been limited since they require as input full flow field information. Even with this information, provided recently for the first time by direct numerical simulation (DNS),³ effective controls are not obvious due to the complexity of the flow. Noise control is particularly challenging since the acoustic energy is a tiny fraction of the flow energy (10^{-3} to 10^{-5} in even tremendously loud flows), making it easily "overlooked" by turbulence models. In addition, noise is an inherently unsteady phenomena, which makes noise modeling more challenging than standard turbulence modeling.

Both active and passive controls have been used to control jets for mixing enhancement and noise suppression. Passive controls invariably involves modification of the nozzle geometry. Addition of tabs to the nozzle^{4,5} and other modifications of its shape⁶⁻¹⁰ have been shown to increase mixing. The mechanism for this is typically thought to be the generation of streamwise vorticity.¹¹ It has been known for a long time that certain nozzle geometry modifications also reduce noise.

found to reduce noise a couple decibels (effective perceived noise) with minimal incurred loss.¹² However, there is no systematic procedure for designing them and no complete description of how they work. Trial-and-error iterations play a role in their design. There is no way of knowing how effective they can be.

Active control, which uses moving parts or other unsteady actuation such as small side jets,¹³ synthetic jets,¹⁴ or plasma discharge actuators,^{15,16} can in principle offer greater control authority. Very significant mixing enhancements have been reported¹³ using a technology that has been demonstrated effective on full-scale engines.¹⁷ The mechanism is typically understood in terms of interactions of turbulent flow structures. Our own simulations have been used to probe the details of this type of actuation and provide data difficult or impossible to measure in experiment.¹⁸ We and others have also used evolution algorithms to identify effective active controls for jet mixing enhancement.^{19,20}

However, there has been little or no success in using this actuator technology to control jet noise. By their nature they should offer greater effectiveness than passive controls, but it is simply not known how to use available actuators or how to optimize actuator designs to reduce noise. Our understanding of jet noise is too limited (or jet noise is too complex) to provide effective models, even at a phenomenological level, that can be used in an optimization procedure.

1.2 Approach

Faced with this poor understanding of jet noise, we developed and implemented an automatic means of reducing noise despite flow complexity. The control optimization is based on adjoint formulation, which circumvents the problem's complexity and facilitates the simultaneous optimization of literally thousands of control parameters. Recently, with the availability of high-speed computation, adjoint optimization procedures have been used in shape optimization of airfoils,^{21–25} minimization of dispersion of microchannel bends,²⁶ error estimation for discontinuous Galerkin approximations of hyperbolic systems,²⁷ studies of drag reduction in a turbulent channel flow,²⁸ analysis of mean flow refraction effects on sound radiated by localized sources in jets,²⁹ receptivity prediction in nonparallel flows,³⁰ and some attempts to control unsteady compressible flow properties.^{31–33} This project has pioneered its application to aeroacoustic control, which is in a sense more challenging because the underlying mechanism is less well understood than these other applications. There are reasonable reliable efficient tools (CFD) for predicting with (usually) acceptable accuracy the flow over an airfoil, the dispersion in a microchannel, or the drag force on an object, but tools with comparable fidelity do not exist for most aeroacoustic flows. Thus, it was even more important to develop techniques that circumvent the lack models and reduce noise anyhow. Our flows quieted by these methods also provided a unique opportunity to probe the flow physics and establish a deeper understanding of its working.

In the work reported here, we found for the first time active controls that substantially quiet the flow. The techniques for doing this are discussed in section 2, and a simple numerical test to check the method and code is presented in section 3. Having simultaneously similar flows that are loud and quieted offered a unique opportunity to study the mechanism. This is discussed in section 4. An iteration-based immersed boundary was developed as well in preparation for the inclusion of complex geometries in to our calculations. This is discussed in section 5.

2 Adjoint-based optimization

Our approach is an automatic control optimization that employs the adjoint of the perturbed compressible flow equations, as documented in our published papers.^{34,35} (For the remainder of

this report, they are simply called the “adjoint equations”, omitting “perturbed”.) The approach is shown schematically in figure 1. Given a numerical solution of the compressible flow equations for a jet, the adjoint equations are solved numerically backward in time to give the sensitivity of the noise, as defined quantitatively by an appropriate metric, to changes in the control at the nozzle. This sensitivity is used to update controls for the specific noise reduction objective that we have selected. It automatically tells us how to improve our controls, and it is insensitive to the complexity of the flow which has hampered progress in the past.

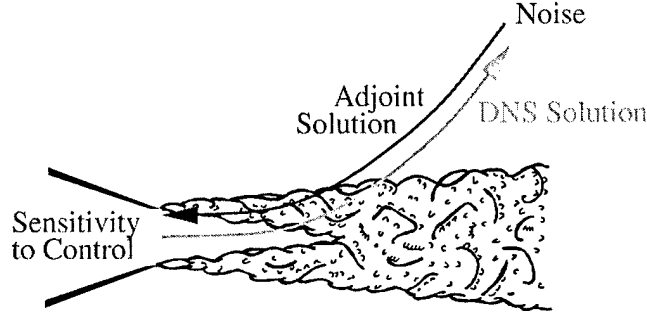


Figure 1: Schematic of the adjoint-based procedure for determining control sensitivity.

2.1 Adjoint equations

Extending Bewley’s work²⁸ on incompressible flow, we derived the continuous form of the adjoint equations of the compressible viscous flow. The compressible viscous flow equations are written compactly as

$$\mathcal{N}(\mathbf{q}) = \mathbf{F}(\mathbf{x}, t). \quad (1)$$

Accordingly, its linearized perturbation field is

$$\mathcal{N}'(\mathbf{q}') = \mathbf{F}'(\mathbf{x}, t), \quad (2)$$

where the quantities $()'$ are defined by the Frèchet differential as

$$\mathbf{q}' \equiv \lim_{\varepsilon \rightarrow 0} \frac{\mathbf{q}(\phi + \varepsilon \phi') - \mathbf{q}(\phi)}{\varepsilon}, \quad (3)$$

where ϕ is arbitrary perturbation. With an inner product defined as

$$\langle \mathbf{c}, \mathbf{d} \rangle = \int_0^T \int_S c(\mathbf{x}, t) d(\mathbf{x}, t) dA dt, \quad (4)$$

where S is problem specific space domain, we derive the adjoint equations by integration by parts,

$$\langle \mathcal{N}'(\mathbf{q}'), \mathbf{q}^* \rangle = -\langle \mathbf{q}', \mathcal{N}^*(\mathbf{q}^*) \rangle + \mathbf{b}, \quad (5)$$

where \mathbf{b} is the boundary terms and

$$\mathbf{q}^* = \begin{bmatrix} \rho^* \\ u^* \\ v^* \\ p^* \end{bmatrix} \quad (6)$$

is introduced as adjoint variables. Finally, we get the adjoint equations with the form

$$\mathcal{N}^*(\mathbf{q}^*) = \mathbf{C}^* \frac{\partial \mathbf{q}^*}{\partial t} + \mathbf{A}^* \frac{\partial \mathbf{q}^*}{\partial x} + \mathbf{B}^* \frac{\partial \mathbf{q}^*}{\partial y} + \mathbf{D}^* \mathbf{q}^* = \mathbf{F}^*, \quad (7)$$

where

$$\begin{aligned} \mathbf{A}^* &= \begin{bmatrix} u & u^2 & uv & \frac{1}{2}u(u^2 + v^2) \\ \rho & 2\rho u & \rho v & \frac{\gamma p}{\gamma-1} + \frac{1}{2}\rho(3u^2 + v^2) + \frac{5}{3\text{Re}}v_y \\ 0 & 0 & \rho u & \rho uv - \frac{5}{3\text{Re}}u_y \\ 0 & \gamma-1 & 0 & \gamma u \end{bmatrix}, \\ \mathbf{B}^* &= \begin{bmatrix} v & uv & v^2 & \frac{1}{2}v(u^2 + v^2) \\ 0 & \rho v & 0 & \rho uv - \frac{5}{3\text{Re}}v_x \\ \rho & \rho u & 2\rho v & \frac{\gamma p}{\gamma-1} + \frac{1}{2}\rho(u^2 + 3v^2) + \frac{5}{3\text{Re}}u_x \\ 0 & 0 & \gamma-1 & \gamma v \end{bmatrix}, \\ \mathbf{C}^* &= \begin{bmatrix} 1 & u & v & \frac{1}{2}(u^2 + v^2) \\ 0 & \rho & 0 & \rho u \\ 0 & 0 & \rho & \rho v \\ 0 & 0 & 0 & 1 \end{bmatrix}, \\ \mathbf{D}^* &= \frac{1}{\text{Re}} \begin{bmatrix} 0 & 0 & 0 & -\frac{\gamma p}{\text{Pr}(\gamma-1)}\rho^2(\frac{\partial^2}{\partial x^2} + \frac{\partial^2}{\partial y^2}) \\ 0 & \frac{4}{3}\frac{\partial^2}{\partial x^2} + \frac{\partial^2}{\partial y^2} & \frac{1}{3}\frac{\partial^2}{\partial x \partial y} & \frac{4u}{3}\frac{\partial^2}{\partial x^2} + u\frac{\partial^2}{\partial y^2} + \frac{v}{3}\frac{\partial^2}{\partial x \partial y} \\ 0 & \frac{1}{3}\frac{\partial^2}{\partial x \partial y} & \frac{4}{3}\frac{\partial^2}{\partial y^2} + \frac{\partial^2}{\partial x^2} & \frac{4v}{3}\frac{\partial^2}{\partial y^2} + v\frac{\partial^2}{\partial x^2} + \frac{u}{3}\frac{\partial^2}{\partial x \partial y} \\ 0 & 0 & 0 & \frac{\gamma}{\text{Pr}\rho}(\frac{\partial^2}{\partial x^2} + \frac{\partial^2}{\partial y^2}) \end{bmatrix}, \\ \mathbf{F}^* &= \begin{bmatrix} 0 \\ 0 \\ 0 \\ -2(p - p_\infty) \delta(\mathbf{x} \text{ on } \Omega) \end{bmatrix}. \end{aligned} \quad (8)$$

Coefficients matrices \mathbf{A}^* , \mathbf{B}^* , and \mathbf{C}^* depend solely on the flow variables, ρ , u , v , and p , thus the adjoint solution depends on the forward flow solution. The matrix-like operator \mathbf{D}^* , which also depends on the forward flow solution, essentially represents the viscous effects from the flow field upon the adjoint field. \mathbf{F}^* is an adjoint forcing vector set by our choice of cost function $\mathcal{J}(\phi)$, which will be discussed later (section 2.2).

2.2 Control optimization

We now need to define a control function ϕ , which represents the actuation that changes the flow, and cost function $\mathcal{J}(\phi)$, which in is a measure of the noise. ϕ has a dimension equal to the number of control parameters. We treat each space-time point as a distinct parameter. To reduce the cost $\mathcal{J}(\phi)$, the control ϕ is changed by

$$\phi^{\text{new}} = \phi^{\text{old}} + \alpha \mathbf{g}, \quad (9)$$

where the gradient is related to the derivative of the cost function by

$$\mathbf{g} = \frac{\mathcal{D}\mathcal{J}(\phi)}{\mathcal{D}\phi}, \quad (10)$$

so that \mathcal{J} decreases along this gradient direction. The differential here is defined in

$$\begin{aligned} \frac{\mathcal{D}\mathcal{J}(\phi)}{\mathcal{D}\phi} \cdot \phi' &\equiv \lim_{\varepsilon \rightarrow 0} \frac{\mathcal{J}(\phi + \varepsilon\phi') - \mathcal{J}(\phi)}{\varepsilon} \\ &= \int_0^T \int_{\Omega} 2(p - p_{\infty})p' d\Omega dt, \end{aligned} \quad (11)$$

where the last line results from our particular cost function

$$\mathcal{J}(\phi) = \int_0^T \int_{\Omega} (p - p_{\infty})^2 d\Omega dt, \quad (12)$$

which represents the total noise in area Ω from time $t = 0$ to $t = T$, where Ω is a subset of space S . In practice, Ω is where we want to reduce noise.

As an example to clarify the procedure, consider a generic term in energy equation used to control the flow. Thus the flow equations are

$$\mathcal{N}(\mathbf{q}) = \mathbf{F} \quad (13)$$

with

$$\mathbf{F} = \begin{bmatrix} 0 \\ 0 \\ 0 \\ \phi(\mathbf{x}, t) \end{bmatrix}. \quad (14)$$

In this example, the control function ϕ is constituted by the list of $\phi(\mathbf{x}, t)$ at discrete space-time points at which an energy “forcing” will be applied. The derivative of flow field is then

$$\mathcal{N}'(\mathbf{q}') = \mathbf{F}' \quad (15)$$

with

$$\mathbf{F}' = \begin{bmatrix} 0 \\ 0 \\ 0 \\ \phi'(\mathbf{x}, t) \end{bmatrix}. \quad (16)$$

We substitute (15) and (7) into (5) to get

$$\langle \mathbf{F}', \mathbf{q}^* \rangle = -\langle \mathbf{q}', \mathbf{F}^* \rangle + \mathbf{b}. \quad (17)$$

The boundary conditions and initial conditions of adjoint problem are not pre-defined and therefore can be chosen to eliminate \mathbf{b} . Thus the problem can be simplified in our case. A “radiation” condition appropriate for our free-space configuration eliminates space boundary terms. The initial condition $\mathbf{q}'|_{t=0} = 0$ eliminates terms at $t = 0$. The components of \mathbf{b} at $t = T$ are eliminated by selecting $\mathbf{q}^*|_{t=T} = 0$. Then it becomes a natural choice to calculate the adjoint field backward in time with well-defined zero “initial condition” at $t = T$.

Finally, using the corresponding forcing matrices (8) and (16) yields

$$\int_0^T \int_S p^*(\mathbf{x}, t) \phi'(\mathbf{x}, t) dA dt = \int_0^T \int_{\Omega} 2(p - p_{\infty})p' d\Omega dt, \quad (18)$$

which provides the gradient vector \mathbf{g} as a list of

$$g(\mathbf{x}, t) = p^*(\mathbf{x}, t) \quad (19)$$

at the same discrete space-time points as in the list ϕ with the same order. Therefore, the control ϕ can be updated by (9) accordingly.

2.3 Adjoint field boundary conditions

Specially designed non-reflecting boundary conditions can reduce spurious, nonphysical reflections at inflow and outflow boundaries, so that the calculated flow field is independent of the location of the far-field boundaries.³⁶ Reflections are also a concern for the adjoint, so we developed the non-reflecting boundary conditions for them as well.

On the far field boundary, viscous effect is negligible when $Re \gg 1$ ($\mathbf{D}^* = 0$), and there is no forcing ($\mathbf{F}^* = 0$). With some rearrangement, the governing equations become

$$\frac{\partial \mathbf{q}^*}{\partial t} + \mathbf{A}^{**} \frac{\partial \mathbf{q}^*}{\partial x} + \mathbf{B}^{**} \frac{\partial \mathbf{q}^*}{\partial y} = 0, \quad (20)$$

where

$$\begin{aligned} \mathbf{A}^{**} &= (\mathbf{C}^*)^{-1} \mathbf{A}^* \\ &= \begin{bmatrix} 0 & -u^2 + \frac{\gamma-1}{2}(u^2 + v^2) & -uv & \frac{\gamma-2}{2}u(u^2 + v^2) - \frac{\gamma u p}{(\gamma-1)\rho} + \frac{5}{3Re} \frac{vu_y - uv_y}{\rho} \\ 1 & (3-\gamma)u & v & -\gamma u^2 + \frac{1}{2}(3u^2 + v^2) + \frac{\gamma p}{(\gamma-1)\rho} + \frac{5}{3Re} \frac{v_y}{\rho} \\ 0 & (1-\gamma)v & u & (1-\gamma)uv - \frac{5}{3Re} \frac{u_y}{\rho} \\ 0 & \gamma-1 & 0 & \gamma u \end{bmatrix}, \\ \mathbf{B}^{**} &= (\mathbf{C}^*)^{-1} \mathbf{B}^* \\ &= \begin{bmatrix} 0 & -uv & -v^2 + \frac{\gamma-1}{2}(u^2 + v^2) & \frac{\gamma-2}{2}v(u^2 + v^2) - \frac{\gamma v p}{(\gamma-1)\rho} + \frac{5}{3Re} \frac{uv_x - vu_x}{\rho} \\ 0 & v & (1-\gamma)u & (1-\gamma)uv - \frac{5}{3Re} \frac{v_x}{\rho} \\ 1 & u & (3-\gamma)v & -\gamma v^2 + \frac{1}{2}(u^2 + 3v^2) + \frac{\gamma p}{(\gamma-1)\rho} + \frac{5}{3Re} \frac{u_x}{\rho} \\ 0 & 0 & \gamma-1 & \gamma v \end{bmatrix}. \end{aligned} \quad (21)$$

The remaining viscous terms in \square are now also dropped. Following steps are the same as those in regular characteristic analysis. We decompose the matrix \mathbf{A}^{**} as

$$\mathbf{A}^{**} = (\mathbf{S}^*)^{-1} \Lambda_A^* \mathbf{S}^*, \quad (22)$$

where

$$\mathbf{S}^* = \frac{1-\gamma}{a^2} \begin{bmatrix} 1 & u & v & \frac{u^2+v^2}{2} \\ -u & -uv & -v^2 - \frac{a^2}{\gamma-1} & -\frac{v}{2}(u^2 + v^2) - \frac{va^2}{\gamma-1} \\ -\frac{1}{2} & -\frac{u+a}{2} & -\frac{v}{2} & -\frac{u^2+v^2}{4} - \frac{ua}{2} - \frac{a^2}{2(\gamma-1)} \\ -\frac{1}{2} & -\frac{u-a}{2} & -\frac{v}{2} & -\frac{u^2+v^2}{4} + \frac{ua}{2} - \frac{a^2}{2(\gamma-1)} \end{bmatrix}, \quad (23)$$

$$(\mathbf{S}^*)^{-1} = \begin{bmatrix} \frac{u^2-v^2}{2} - \frac{a^2}{\gamma-1} & -v & \frac{u^2+v^2}{2} - \frac{ua}{\gamma-1} & \frac{u^2+v^2}{2} + \frac{ua}{\gamma-1} \\ -u & 0 & -u + \frac{a}{\gamma-1} & -u - \frac{a}{\gamma-1} \\ 0 & 1 & -v & -v \\ 1 & 0 & 1 & 1 \end{bmatrix}, \quad (24)$$

$$\Lambda_A^* = \begin{bmatrix} u & 0 & 0 & 0 \\ 0 & u & 0 & 0 \\ 0 & 0 & u+a & 0 \\ 0 & 0 & 0 & u-a \end{bmatrix}. \quad (25)$$

We noticed that the matrix \mathbf{A}^{**} has characteristic speeds u , u , $u+a$, and $u-a$ respectively, corresponding to entropy, vorticity and two acoustic waves of adjoint field. Recall that the variables without $*$ are from the flow field solution, which indicates that the adjoint field is not only a mathematical manipulation, but also a physical “mirror image” of flow field. Thus, we are able to understand and interpret informations in adjoint field in terms of physical phenomena. Similarly, \mathbf{B}^{**} is decomposed as

$$\mathbf{B}^{**} = (\mathbf{L}^*)^{-1} \Lambda_B^* \mathbf{L}^*, \quad (26)$$

where

$$\mathbf{L}^* = \frac{1-\gamma}{a^2} \begin{bmatrix} 1 & u & v & \frac{u^2+v^2}{2} \\ -u & -u^2 - \frac{a^2}{\gamma-1} & -uv & -\frac{u}{2}(u^2+v^2) - \frac{ua^2}{\gamma-1} \\ -\frac{1}{2} & -\frac{u}{2} & -\frac{v+a}{2} & -\frac{u^2+v^2}{4} - \frac{va}{2} - \frac{a^2}{2(\gamma-1)} \\ -\frac{1}{2} & -\frac{u}{2} & -\frac{v-a}{2} & -\frac{u^2+v^2}{4} + \frac{va}{2} - \frac{a^2}{2(\gamma-1)} \end{bmatrix}, \quad (27)$$

$$(\mathbf{L}^*)^{-1} = \begin{bmatrix} -\frac{u^2+v^2}{2} - \frac{a^2}{\gamma-1} & -u & \frac{u^2+v^2}{2} - \frac{va}{\gamma-1} & \frac{u^2+v^2}{2} + \frac{va}{\gamma-1} \\ 0 & 1 & -u & -u \\ -v & 0 & -v + \frac{a}{\gamma-1} & -v - \frac{a}{\gamma-1} \\ 1 & 0 & 1 & 1 \end{bmatrix}, \quad (28)$$

$$\Lambda_B^* = \begin{bmatrix} v & 0 & 0 & 0 \\ 0 & v & 0 & 0 \\ 0 & 0 & v+a & 0 \\ 0 & 0 & 0 & v-a \end{bmatrix}. \quad (29)$$

According to above decompositions, the propagating directions of the characteristic waves on right and left boundaries can be determined by Λ_A and those on top and bottom boundaries can be determined by Λ_B . Because the adjoint field is solved backward in time, we keep the “incoming” waves and suppress the “outgoing” waves to make the boundary of the adjoint field “non-reflecting”.

2.4 Other numerical details

The radiated acoustic energy of a jet, even one so loud that it might fatigue aircraft components, is a tiny fraction of the flow’s energy. Specialized numerical methods are therefore required to capture the sound.³⁷ The flow and sound fields, which are governed by the compressible Navier-Stokes equations, are solved numerically in two space dimensions without modeling assumptions using a fourth-order Runge-Kutta algorithm for time advancement. For spatial differencing, a sixth-order Padé scheme³⁸ is used in the x (streamwise) direction, and the Dispersion-Relation-Preserving (DRP) scheme³⁹ is used in the y (cross-stream) direction. The explicit DRP scheme facilitates decomposition across different processor on a parallel machine. The same schemes are used to solve the adjoint equations, also without modeling approximations.

In flow field calculation, a specialized buffer zone similar to that of Freund⁴⁰ and non-reflecting boundary conditions³⁶ are used in combination to absorb disturbances as they leave the finite com-

putational domain. As the non-reflecting boundary is derived in section 2.3, the same boundary treatments are applied in adjoint field calculation with a minor change to buffer zone coefficients*.

For the control update, the Polak-Ribiere variant of the conjugate gradient algorithm is used with Brent's line-minimization method.⁴¹ The conjugate gradient algorithm provides the optimal direction to change the control, while the line-minimization method determines the depth of each change. Each line-minimization includes about 10 evaluations of the cost function \mathcal{J} or the derivative of \mathcal{J} . One entire line-minimization procedure, which accomplishes the step along one conjugate gradient, is counted as one iteration.

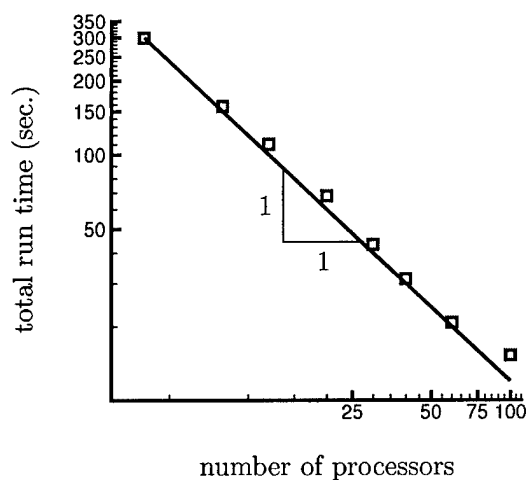


Figure 2: Run time scaling of parallel code running on the IBM SP.

The code has been parallelized using MPI. In the direction that is distributed onto separate processors, the explicit Dispersion-Relation-Preserving (DRP) scheme³⁹ was used. Run time scaling of the parallel code on an IBM SP is shown in figure 2. The run time decreases linearly as more processors are used. This good scalability guarantees the efficiency of our code in dealing with computationally large-size problems.

*Damping term in a time forward procedure appears typically as

$$\frac{dy}{dt} = -\sigma y,$$

where $\sigma > 0$, to provide solution

$$y = \exp[-\sigma t]$$

decreasing as time going forward. But for a time backward procedure, we need the damping term to be

$$\frac{dy}{dt} = +\sigma y.$$

so that the solution

$$y = \exp[\sigma t]$$

will decrease as time going backward.

3 Anti-sound cancellation

Anti-sound cancellation is a sound reduction method by using other sound sources to reduce the sound in a certain area by linear interference. As with any interference phenomena, while sound in some area is reduced, sound in some other area will be increased. Anti-sound controllability decreases rapidly as the control area becomes larger than the wave length of sound. We demonstrated and tested the control system on anti-sound, but it is not an appropriate solution to the jet noise problem.

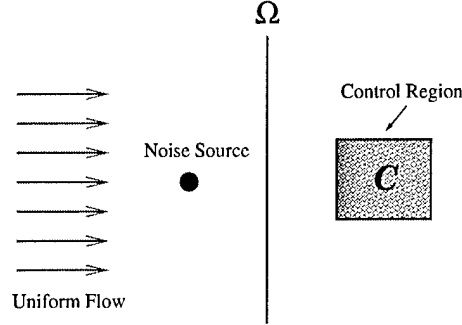


Figure 3: Anti-sound demonstration schematic.

The test configuration is illustrated in figure 3. A noise source represented by a mass source term

$$f(x, t) = 0.1 \exp[-\{(x/L + 3)^2 + (y/L)^2\}] \cos(\pi t a_\infty / L) \quad (30)$$

sits in a mean flow with Mach number 0.5 and Reynolds number 100, where a_∞ is the sound speed at infinity and L is the characteristic length defined by the scale of the mass source distribution. Our objective is to minimize the noise defined by the cost function \mathcal{J} in (12) on the vertical target line Ω at $x = 0$ and $-8 < y/L < 8$. The control is a mass source with support in \mathcal{C} with dimension $1 < x/L < 5$ and $-2 < y/L < 2$. Though it is a simple acoustic problem, full compressible viscous flow and its adjoint are solved in this test.

After 3 iterations, the sound on Ω is greatly reduced. The sound fields with and without control are compared in figure 4. Obvious sound reduction can be observed along the target line at $x = 0$.

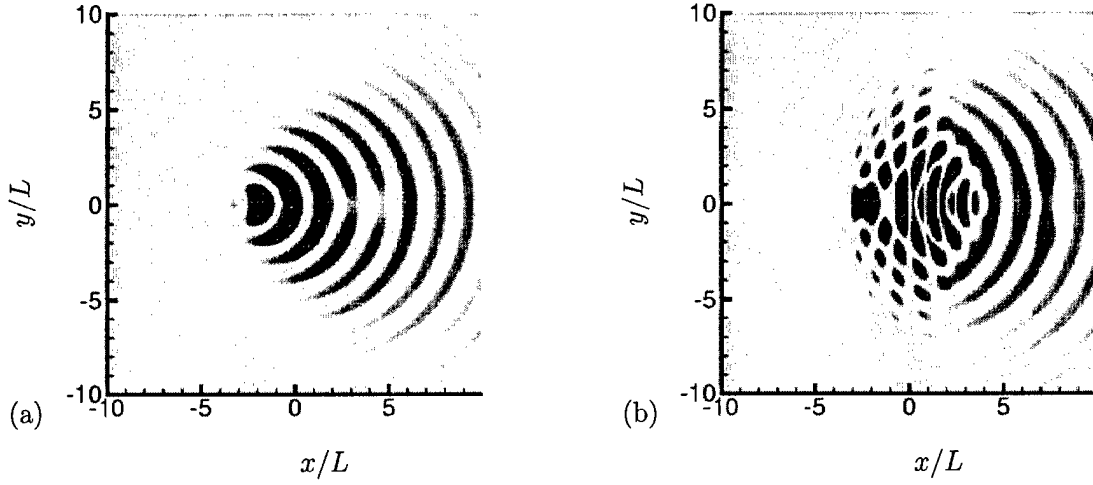


Figure 4: Comparison of sound fields (a) without control (b) with control. Blue and red shades indicate noisy area, while green shade indicates quiet area.

A quantitative result in figure 5 shows 95% sound reduction in terms of the cost \mathcal{J} .

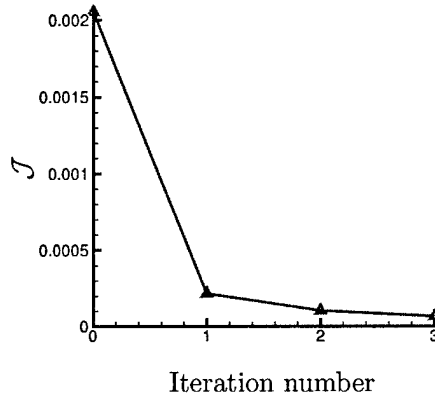


Figure 5: The reduction of sound in anti-sound problem.

4 Suppression of noise from a model jet

4.1 Formulation

A two-dimensional mixing layer is studied as a model of the near-nozzle region of jet. The mixing layer simulated is shown schematically in figure 6. The Reynolds number is $Re_\omega = 500$, based on vorticity thickness,

$$\delta_\omega = \left(\frac{\Delta U}{|du/dy|_{\max}} \right)_{x=0} \quad (31)$$

The Mach numbers of the top and bottom streams are $M_1 = 0.8$ and $M_2 = 0$, respectively. The inflow temperature is uniform.

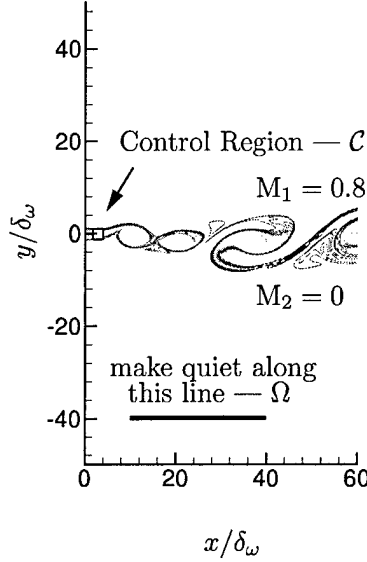


Figure 6: Mixing layer control schematic.

The black line Ω in figure 6 at $y = -40\delta_\omega$ and extending between $x = 10\delta_\omega$ and $x = 40\delta_\omega$ is our target line, where the noise will be reduced. Our initial objective is to establish the optimum that can be achieved in terms of noise reduction. For this reason, we have optimized a completely generic forcing. Sources are added to the flow equations as described in section 2.2 (14) in a small region demarked by a box \mathcal{C} , $x/\delta_\omega \in (1, 5)$ and $y/\delta_\omega \in (-2, 2)$, also shown in the figure. Each space-time point of a discrete representation of the forcing is optimized independently. Since the control is turned on for time period $200\delta_\omega/a_\infty$ in this region, we optimized in total about 3 million space-time points.

4.2 Flow simulation and its control

Instability theory predicts that the most unstable mode of the incompressible mixing layer has Strouhal number $St = \frac{f\delta_m}{U_c} = 0.032$,^{42,43} where f is the excitation frequency, δ_m is the momentum thickness, and U_c is the convection speed. This unstable mode provides an estimation of the fundamental frequency of our compressible mixing layer, since this frequency is not very sensitive to the present compressibility level.^{44,45} Therefor the fundamental frequency to excite our flow is $f_0 = \frac{St U_c}{\delta_m}$. Numerical experimentation confirms that the mixing layer does respond strongly to forcing at or near this frequency. To provide a richer flow for our scheme to control, we excite the flow at a total of eight frequencies, $f_0/4$, $f_0/2$, $3f_0/4$, f_0 , $5f_0/4$, $3f_0/2$, $7f_0/4$, and $2f_0$. These were selected in an *ad hoc* fashion for now. A more thorough investigation of the effects of this excitation on the noise and its controllability is underway.

To minimize the direct effect of the excitation on the sound field, we define a function ψ with the 8 frequencies f_i listed above as

$$\psi = \psi_0 e^{-\sigma_x(x-x_0)^2} e^{-\sigma_y(y-y_0)^2} \sum_{i=1}^8 \sin[2\pi f_i(x - x_0 - M_c t) + \beta_x^i] \sin[2\pi f_i(y - y_0) + \beta_y^i], \quad (32)$$

where ψ_0 is the amplitude, (x_0, y_0) is $(-5\delta_\omega, 0)$, both σ_x and σ_y are 0.2, $\beta_{x,y}$ are initial random

phases, and $M_c = \frac{1}{2}(M_1 + M_2)$. The excitation, which appears as body force, is then defined as

$$F_{ex} = \frac{\partial \psi}{\partial y}, \quad F_{ey} = -\frac{\partial \psi}{\partial x}, \quad (33)$$

so that it is solenoidal and therefore relatively quiet. We observed no sound directly from this excitation. The amplitude of each mode was $\psi_0 = 0.004\rho_\infty a_\infty^2/\delta_\omega$. Our selection of x_0 and y_0 puts the excitation upstream of the physically realistic portion of the computation. Our controller, of course, has no direct knowledge of this excitation.

The flow was simulated for time $400\delta_\omega/a_\infty$ to allow initial transients to decay and wash out. Then the controller was applied during the following $200\delta_\omega/a_\infty$.

4.3 Results and analyses

4.3.1 Noise Reduction

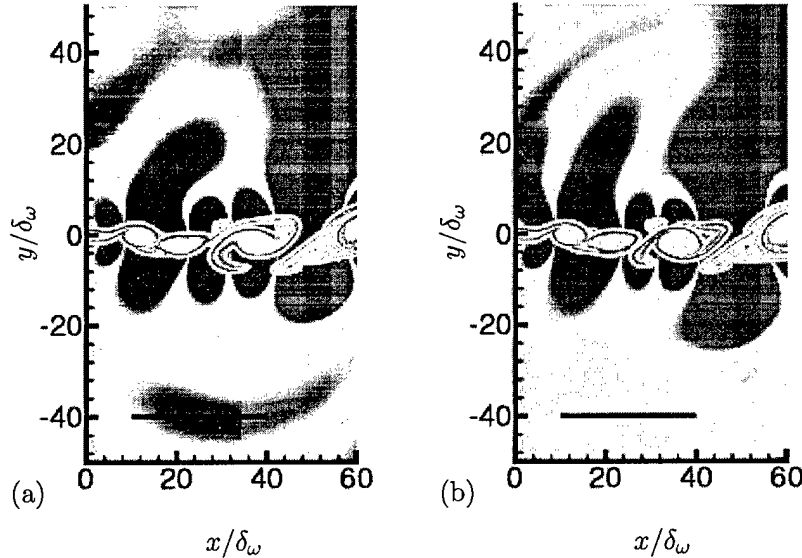


Figure 7: Comparison of the flow and sound field (a) without control (b) with control. Blue and red shades indicate noisy area with $|p'/p_\infty|$ up to 0.003 (blue is negative and red is positive), while green shade indicates quiet area. Contours show vorticity magnitude with peak $0.7a_\infty/\delta_\omega$.

Figure 7 (a) shows the instantaneous flow field before control with contours of vorticity and sound field with color indicating pressure level. The corresponding controlled case after 7 iterations is shown in figure 7 (b) at the same time instance. The noise is clearly reduced along the target line.

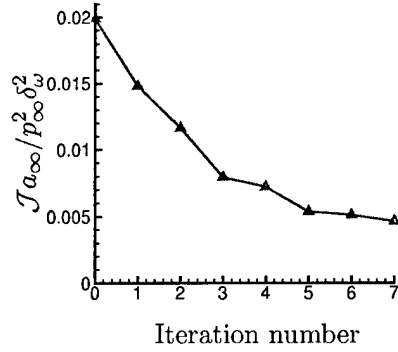


Figure 8: The reduction of the cost.

More quantitatively, figure 8 shows a 77% reduction (6.3dB) of cost function

$$\mathcal{J}(\phi) = \int_{t_0}^T \int_{\Omega} (p - p_\infty)^2 d\Omega dt. \quad (34)$$

The starting point t_0 in the cost function is chosen to be the time for sound to travel from control region \mathcal{C} to the closest point on Ω , assuming it propagates at the sound speed. Before this time, noise on the target line is not controllable. Even after t_0 , the sound on Ω is not fully controllable for two reasons: (1) the control reaches the closest point but not the farther points and (2) the rate at which the effect of the control travels is slower than sound speed. In the mixing layer it is the structure convective Mach number, $M_c \approx 0.4$. An overlapping-time control method²⁸ will remedy this. This will make the cost \mathcal{J} , as we compute it, decrease more, though we have already achieved the piecewise (in time) maximum reduction at later times.

It is important to verify that by reducing the sound in a particular direction we have not made it unacceptably louder in other directions. To see if the radiation increases elsewhere, we compare the cost with and without control on other lines besides the target line. As shown in figure 9, other costs have not changed much and some other directions are also quieter.

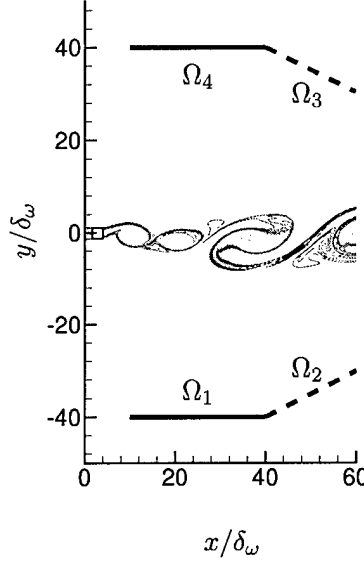


Figure 9: Cost value $\mathcal{J}a_\infty/p_\infty^2\delta_\omega^2$ without and with control on different lines: Ω_1 (target line Ω): 0.0199 (without control) \Rightarrow 0.00465 (with control); Ω_2 : 0.0746 \Rightarrow 0.0574; Ω_3 : 0.1065 \Rightarrow 0.0781; Ω_4 : 0.0394 \Rightarrow 0.0415.

4.3.2 Adjoint Field

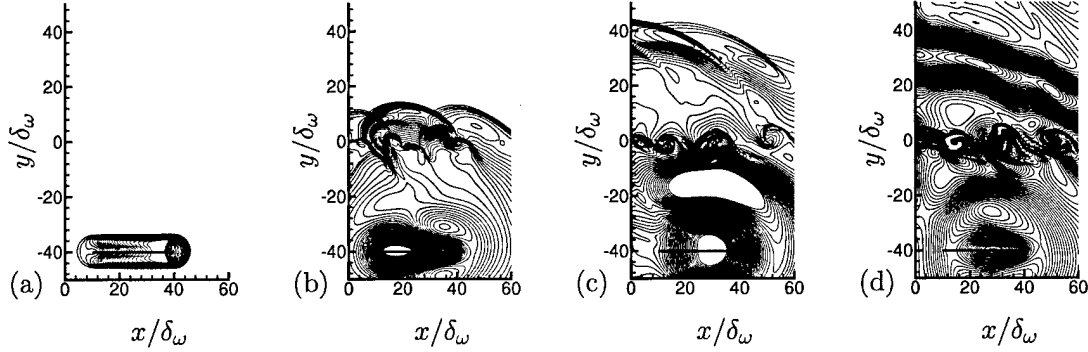


Figure 10: Adjoint pressure: (a) $t = 195\delta_\omega/a_\infty$, (b) $t = 150\delta_\omega/a_\infty$, (c) $t = 120\delta_\omega/a_\infty$, (d) $t = 75\delta_\omega/a_\infty$. The time goes backward in the adjoint solution.

To better understand the control process, the evolution of the adjoint pressure p^* is shown in figure 10. It is this quantity that provides the gradient information \mathbf{g} to update control equation (9). Since the flow equations are self-adjoint in the acoustic limit, the adjoint pressure is initially an adjoint sound wave, excited along the target line by the cost. As this wave encounters the mixing layer, it excites instability waves, which move upstream in the mixing layer to the control region. Finally, the gradient information is recorded inside this region. It is the instability waves in the adjoint that dominates the gradient, which suggests that the control mechanism is via the instabilities in the mixing layer.

Given this qualitative behavior of the adjoint, the mechanism of noise control can be expressed as follows. The control interacts with the flow. This excitation alters (slightly, we shall see) the instabilities in the flow. The modified flow field is quieter. This interpretation will be strengthened in the following sections.

4.3.3 Is It Anti-sound?

In section 3, we declared that anti-sound mechanism will not be used in jet noise control. For the same reason, anti-sound should not be the control mechanism in the mixing layer sound reduction either. That adjoint instability waves dominate the gradient information in \mathcal{C} suggests that the control mechanism is linked to the hydrodynamics. This assertion is discussed and supported more quantitatively in this section.

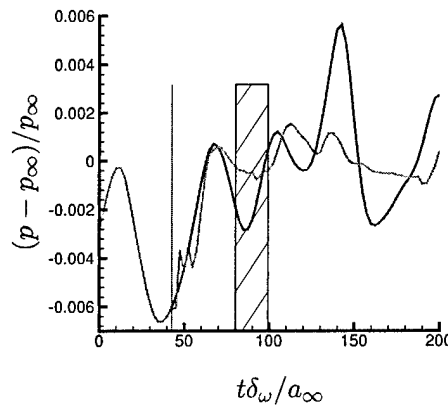


Figure 11: Pressure fluctuation changes at $x = 25\delta_\omega$, $y = -40\delta_\omega$: — without control; - - - with control.

Shown in figure 11, we record the pressure fluctuation history on a choosing point, $x = 25\delta_\omega$ and $y = -40\delta_\omega$ on Ω . The vertical blue line indicates the moment when the first sound wave from the control box would (and does) arrive. In these initial simulations the control is started impulsively causing the jagged burst we see. If the mechanism were anti-sound, the noise reduction should appear just after this point. However, the apparent control of the noise happens after a time delay due to the slower instability wave speed. The vertical black shaded bar shows the approximate time for a flow structure to convect to $x = 25\delta_\omega$ at $M_c \approx 0.4$, which is observed for this mixing layer (see figure 18), and then for sound to radiate from $y = 0$ to the Ω at $y = -40\delta_\omega$. This is when the control does indeed appear to take effect.

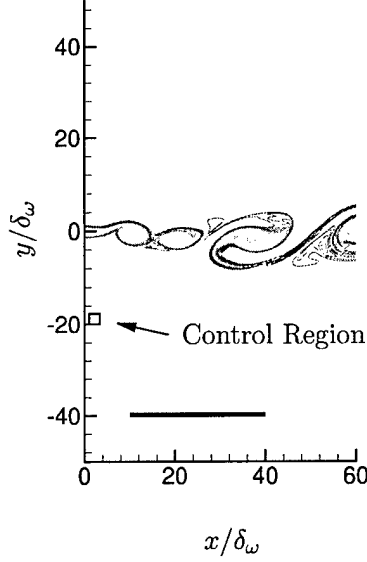


Figure 12: Anti-sound control test schematic.

To further demonstrate that our control is not by anti-sound, we designed the numerical experiment shown in figure 12. The control is moved to the region $x/\delta_\omega \in (1, 5)$ and $y/\delta_\omega \in (-20, -16)$, away from the shear layer. The adjoint instability wave never reaches this control region, only acoustic waves do, so control is principally by acoustic cancellation—anti-sound. After 7 iterations, a 45% reduction is observed (figure 13), which is not surprising because anti-sound is known to be effective locally.

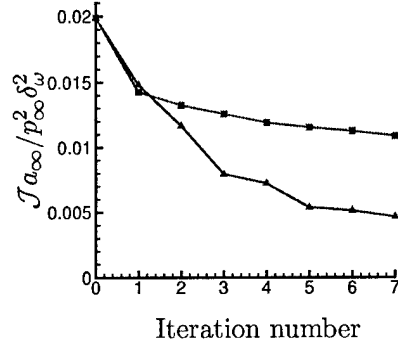


Figure 13: The cost reduction comparison: ▲ “near-nozzle” control; ■ anti-sound control.

However, anti-sound is also known to reinforce the sound elsewhere. So we again check other directions. Unlike the previous case, some of the costs increase substantially. The cost value $\mathcal{J} a_\infty / p_\infty^2 \delta_\omega^2$ changes on different lines (refer to figure 9) as: Ω_1 : $0.0199 \Rightarrow 0.0109$ (down 45%); Ω_2 : $0.0746 \Rightarrow 0.0899$ (up 21%); Ω_3 : $0.1065 \Rightarrow 0.1010$ (down 5%); Ω_4 : $0.0394 \Rightarrow 0.0539$ (up 37%).

4.3.4 Control Forcing

For the effective flow control (not anti-sound) case, it is interesting to see what the forcing does to the flow. Snapshots of the optimal control forcing in figure 14 give us a picture of the evolution of the control at different times. In the control box, the forcing is distributed in a non-intuitive manner. The individual “structures” in the control $\phi(x, y)$ moves at a speed between $0.7U_c$ and $1.7U_c$, where U_c is the anticipated structure convection velocity, which is close to the expected convective speed U_c , but little else can be understood via visualizations. Our ongoing effort will study the control and identify its essential components that reduce the noise.

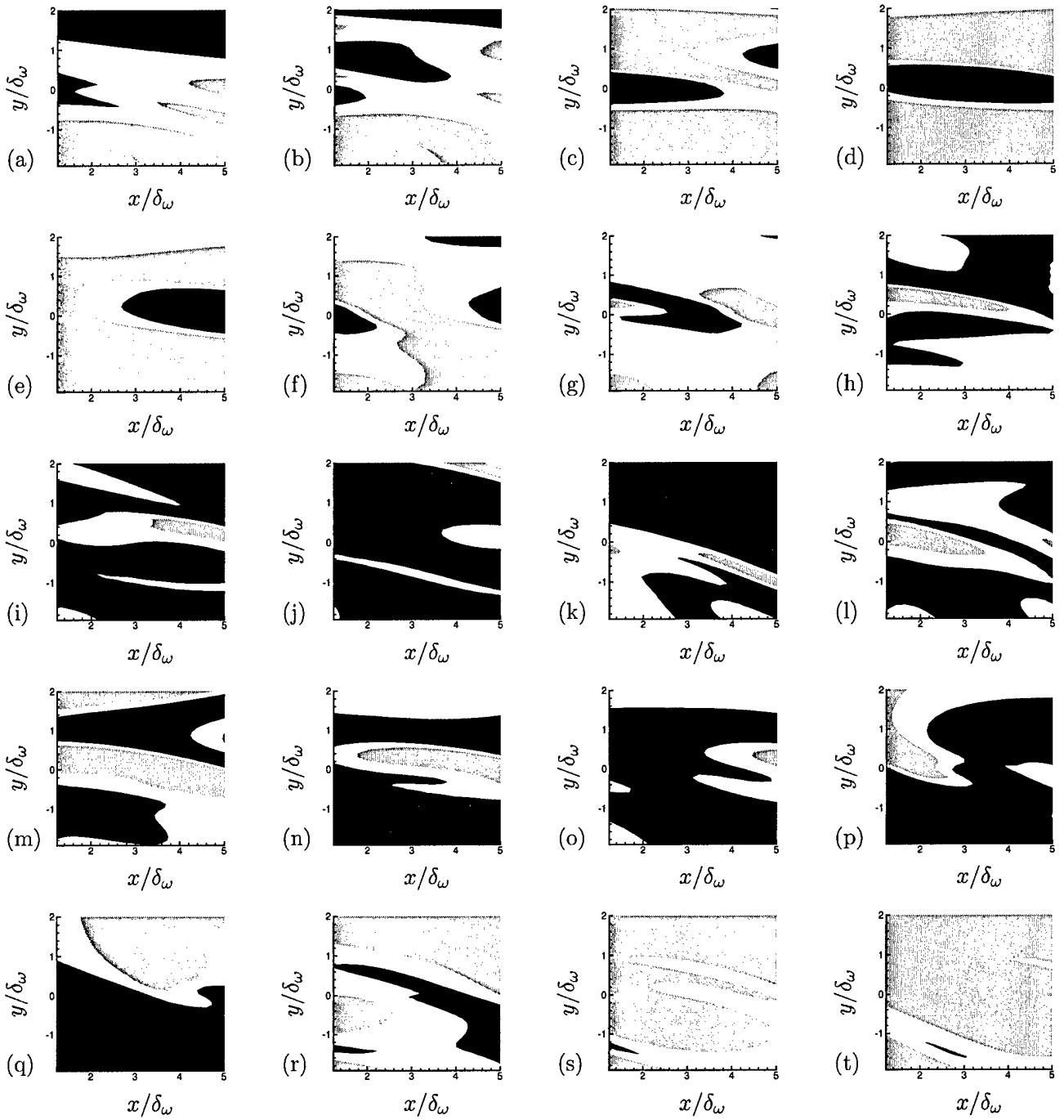


Figure 14: Control forcing: (a) $t = 0$, (b) $t = 5\delta_\omega/a_\infty$, (c) $t = 10\delta_\omega/a_\infty$, (d) $t = 15\delta_\omega/a_\infty$, (e) $t = 20\delta_\omega/a_\infty$, (f) $t = 25\delta_\omega/a_\infty$, (g) $t = 30\delta_\omega/a_\infty$, (h) $t = 35\delta_\omega/a_\infty$, (i) $t = 40\delta_\omega/a_\infty$, (j) $t = 45\delta_\omega/a_\infty$, (k) $t = 50\delta_\omega/a_\infty$, (l) $t = 55\delta_\omega/a_\infty$, (m) $t = 60\delta_\omega/a_\infty$, (n) $t = 65\delta_\omega/a_\infty$, (o) $t = 70\delta_\omega/a_\infty$, (p) $t = 75\delta_\omega/a_\infty$, (q) $t = 80\delta_\omega/a_\infty$, (r) $t = 85\delta_\omega/a_\infty$, (s) $t = 90\delta_\omega/a_\infty$, (t) $t = 95\delta_\omega/a_\infty$. Black indicates the positive forcing ($> 0.01\rho_\infty a_\infty^3/\delta_\omega$), and gray indicates the negative forcing ($< 0.01\rho_\infty a_\infty^3/\delta_\omega$).

In an attempt to develop a quantitative description of the action of the forcing, we define integrals over the control region to study the net influence on the flow:

$$Q(t) = \int_C q(\mathbf{x}, t) dC. \quad (35)$$

Figure 15 shows the history of the net energy, velocity and control forcing in the control region. We see no correlation between the forcing and integrated flow variables in the control region. We anticipate that there must be some correlation, but more data is needed to study its statistics if it is at all possible. The flat part ($160 < ta_\infty/\delta_\omega < 200$) at the end of the forcing history is caused by the time delay between the control and the target. Control in that flat piece would not alter \mathcal{J} on the target line in $t_0 < t < T$.

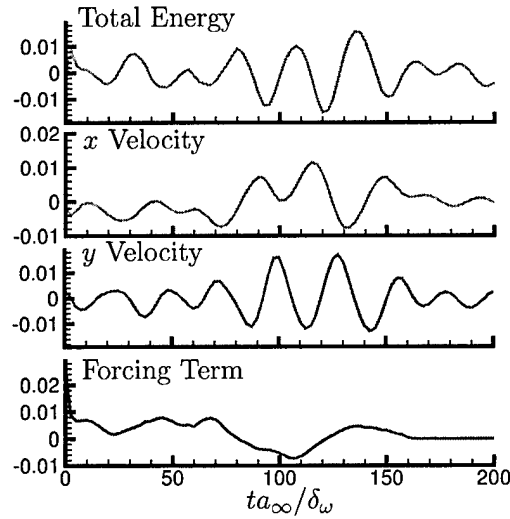


Figure 15: History of integrals inside the control region.

4.3.5 Effect of control on the flow field

Despite the large decrease in the radiated sound, the mixing layer flow is changed surprising little by the control. Figure 16 shows the spreading of its momentum thickness,

$$\delta_m = \int_{-\infty}^{+\infty} \frac{\rho(u - U_1)(U_2 - u)}{\rho_\infty \Delta U^2} dy. \quad (36)$$

We see that the control changes its downstream evolution only slightly. The waviness of the profiles is believed to be due to the limited statistical sample in the simulation time T , but might also be due to the nature of the paring which is known to cause jumps in thickness.

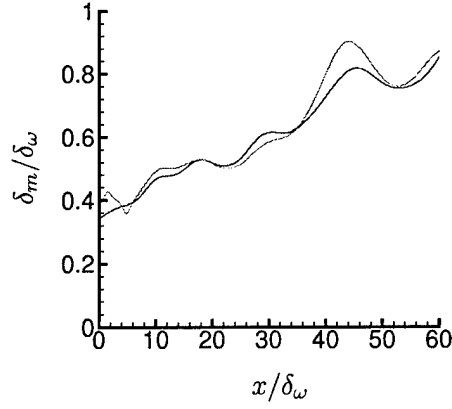


Figure 16: Change of the momentum thickness of the mean flow: — without control; ---- with control.

The turbulence kinetic energy, defined as

$$k = \frac{1}{2} \rho [(u')^2 + (v')^2], \quad (37)$$

where u' and v' are velocity fluctuations, is also nearly unchanged. Figure 17 shows

$$K_x(x) = \int_{-50\delta_\omega}^{50\delta_\omega} k \, dy \quad (38)$$

and

$$K_y(y) = \int_0^{60\delta_\omega} k \, dx \quad (39)$$

with and without control. The noise reduction is clearly not due to turbulence suppression.

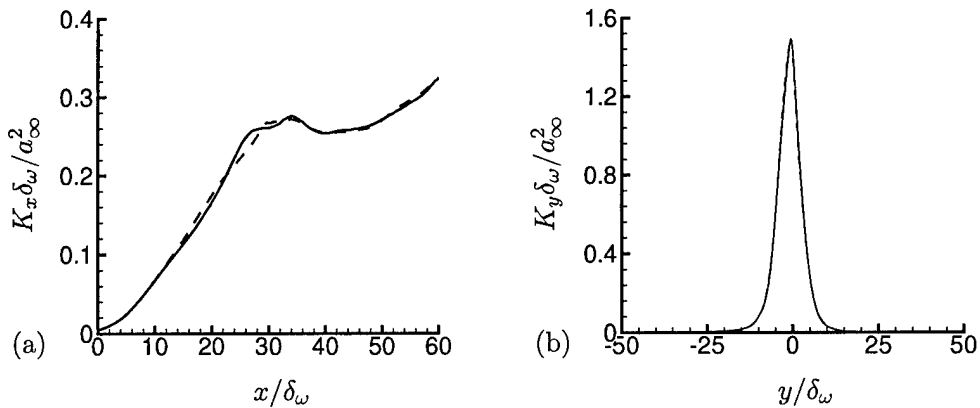


Figure 17: Comparison of integrated turbulence kinetic energy as defined in (a) equation (38) and (b) equation (39): case without control — ; case with control ---- .

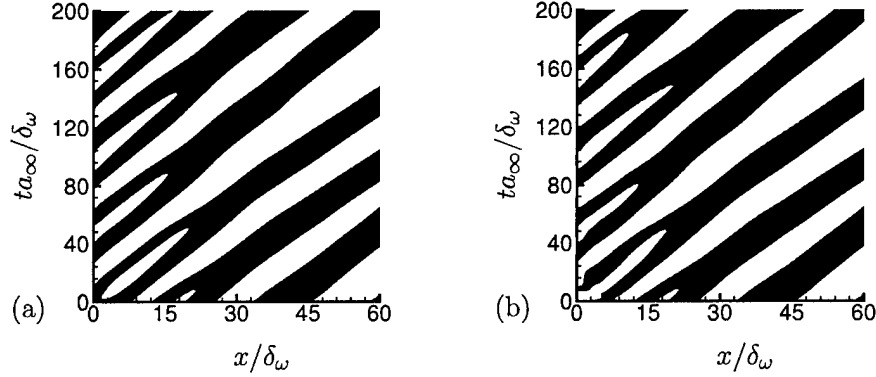


Figure 18: Pressure at $y = 0$ shows little change in large-scale structural evolution without (a) and with (b) control. Black is $(p - p_\infty) < 0$; white is $(p - p_\infty) > 0$.

The way in which the energetic structures are arranged has also changed little. Figure 18 shows the time evolution of the large structures, as demarked by pressure, at $y = 0$ with and without control. Small changes in the structural evolution are apparent, but the gross features are indistinguishable. For example, the pairing structures, which we see as the joining of the dark regions, are nearly indistinguishable before and after the control is applied.

4.4 Body force control

The control shown above to quiet the noise appears as an energy term (14). However, real active controls, such as synthetic jets, apply the effects on flows primarily by momentum changes. To make our work more practical, we assume a y -direction body force applying in the same control box \mathcal{C} . Also shown in figure 19, the target line extends to between $x = 0$ and $x = 60\delta_\omega$. The control time extends from $200\delta_\omega$ to $400\delta_\omega$, the Mach numbers are changed to $M_1 = 0.9$ and $M_2 = 0.2$, and other parameters and geometries are the same.

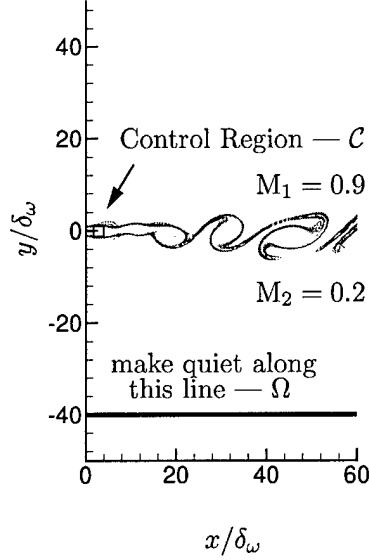


Figure 19: Mixing layer control schematic.

The mathematics associated with body force control are a little more complex than for the energy force control. The terms are added in both y -momentum equation and total energy equation

$$\mathbf{F} = \begin{bmatrix} 0 \\ 0 \\ \phi(\mathbf{x}, t) \\ v\phi(\mathbf{x}, t) \end{bmatrix}. \quad (40)$$

Therefore, the derivative becomes

$$\mathbf{F}' = \begin{bmatrix} 0 \\ 0 \\ \phi'(\mathbf{x}, t) \\ v\phi'(\mathbf{x}, t) + v'\phi(\mathbf{x}, t) \end{bmatrix}. \quad (41)$$

By integration by part, one extra term appears in adjoint equations (7) as

$$\mathcal{N}^*(\mathbf{q}^*) + \mathbf{E}^* = \mathbf{F}^*, \quad (42)$$

where

$$\mathbf{E}^* = \begin{bmatrix} 0 \\ 0 \\ p^*\phi(\mathbf{x}, t) \\ 0 \end{bmatrix}. \quad (43)$$

Solving this modified adjoint equations, we get the gradient vector \mathbf{g} for body force control as a list of

$$g(\mathbf{x}, t) = v^*(\mathbf{x}, t) + v(\mathbf{x}, t)p^*(\mathbf{x}, t) \quad (44)$$

at the same discrete space-time points with the same order.

The visual comparison of flow and sound field with and without control is in figure 20, which shows clearly sound reduction on the target line.

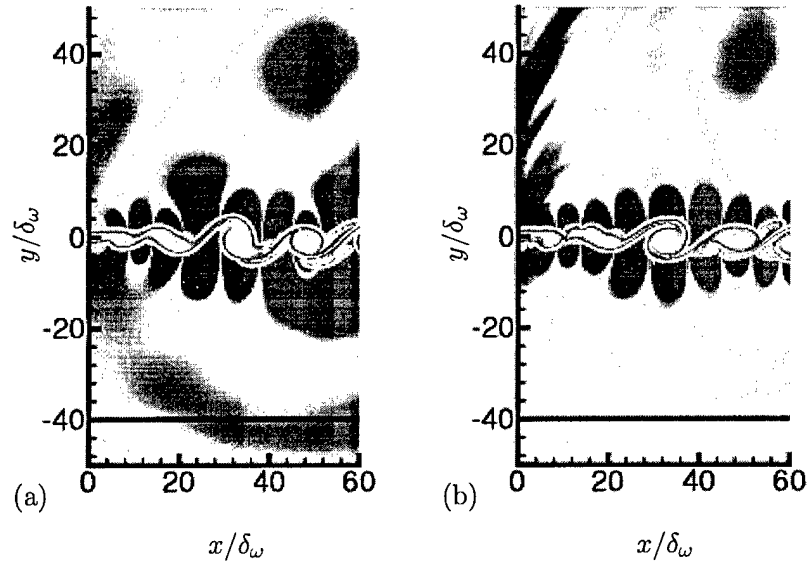


Figure 20: Comparison of the flow and sound field (a) without control (b) with control. Blue and red shades indicate noisy area with $|p'/p_\infty|$ up to 0.003 (blue is negative and red is positive), while green shade indicates quiet area. Contours show vorticity magnitude with peak $0.7a_\infty/\delta_\omega$.

Figure 21 shows the quantitative result that 73% reduction (5.7dB) of cost function is obtained after 7 iterations.

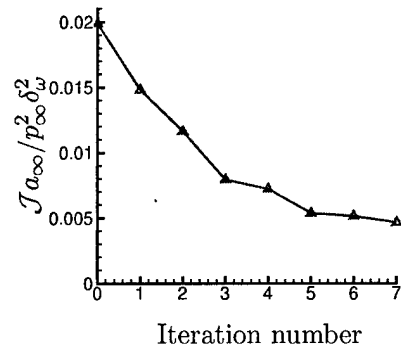


Figure 21: The reduction of the cost.

4.5 Summary

An adjoint-based approach has been developed to control the noise radiated from a two-dimensional mixing layer. The noise along a specified line in the far-field was reduced substantially by both energy and body force controls.

The changes of the flow field due to the control forcing are relatively minor, which is possible

because only a small fraction of the flow's energy, that with a supersonic phase velocity, radiates. Our simulations indicate that, at least in a two-dimensional mixing layer, this part can be altered to dramatically reduce the noise.

The control forcing itself is non-intuitive and the correlations between it and other flow properties are not yet clear. Work continues identifying practical control laws and understanding the details of how the present control works.

5 Iteration-based immersed boundary

It has been observed in trial-and-error experiments¹² that jet noise can be reduced a little by modifying the shape of engine nozzle with minor thrust loss. Finding an optimal nozzle shape under certain constraints is a long-term objective of our simulations. During the optimization process, the boundary defined by the nozzle is being changed and with irregular shape. In anticipation of this, we developed an *iteration-based immersed boundary* to treat complex geometries with little added computational complexity.

The immersed boundary method is an ideal choice to this type of boundaries.^{46–48} Because the physical boundary is not always on grid points, interpolation, extrapolation, and distribution functions are used to define the physical boundary which is not necessarily on the mesh. Some other methods, such as adaptive mesh refinement,⁴⁹ has made good progress in increasing the accuracy, but at the cost of simplicity. The complexity can also carry a significant computational expense. In acoustics problem, the above computational difficulties are enhanced, because the acoustic energy is only a small fraction of the whole flow energy.

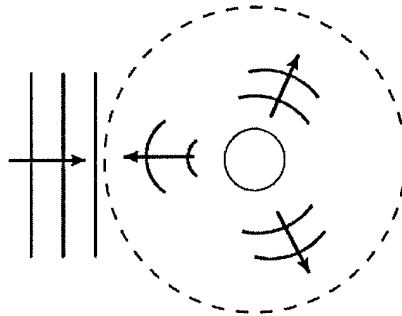


Figure 22: Acoustic reflection problem schematic.

A model problem is used to demonstrate this new method. Figure 22 shows plane acoustic waves traveling from the left to the right and scattering from a circular cylinder. The governing equations are linearized Euler equations,

$$\frac{\partial p}{\partial t} + \frac{\partial u_x}{\partial x} + \frac{\partial u_y}{\partial y} = 0 \quad (45)$$

$$\frac{\partial u_x}{\partial t} + \frac{\partial p}{\partial x} = f_x \quad (46)$$

$$\frac{\partial u_y}{\partial t} + \frac{\partial p}{\partial y} = f_y \quad (47)$$

$$(48)$$

where f_x and f_y on the right-hand-side are the body force terms to represent the immersed

boundary. The general form of those body forces is given by

$$f_n \equiv \vec{f} \cdot \vec{n} = \frac{u_{\text{target}} - u_n}{\Delta t} + \frac{\partial p}{\partial n}, \quad u_{\text{target}} = 0, \quad (49)$$

where u_{target} is chosen to be 0 to satisfy the physical non-penetrated boundary condition.

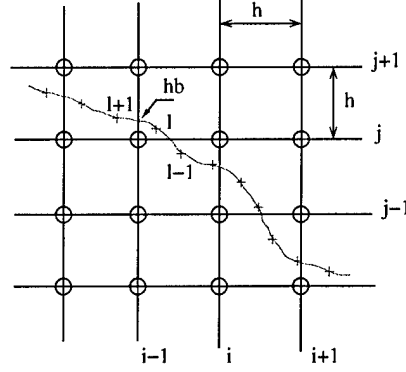


Figure 23: Schematic of immersed boundary (blue line) and grid system: red crosses mark boundary points.

Because the values of flow variables are computed on the mesh points and the immersed boundary is generally off mesh (figure 23), interpolation is need to transfer data between two grid systems. Our method combines a simple iteration method with the immersed boundary method developed by Mohd-Yusof.⁴⁸ The procedure is:

1. Distribute flow variables \vec{G} to boundary points with distribution function P_{for}

$$\vec{G}_l = \sum_{i,j=1}^N \vec{G}_{i,j} P_{\text{for}}(\mathbf{x}_{i,j} - \mathbf{x}_l) h^2, \quad l = 1, \dots, N_b. \quad (50)$$

2. Calculate body force on boundary points: $f_l = f(\vec{G}_l)$.
3. Distribute body force back to grid points with distribution function P_{back}

$$\mathbf{f}_{i,j} = \sum_{l=1}^{N_b} f_l P_{\text{back}}(\mathbf{x}_{i,j} - \mathbf{x}_l) h_b. \quad (51)$$

4. Estimate \vec{G}^e at next time step.
5. Distribute \vec{G}^e to boundary points.
6. Correct force

$$f_n^c = \frac{u_{\text{target}} - u_n^e}{\Delta t}, \quad u_{\text{target}} = 0. \quad (52)$$

7. Get a new force term

$$f_n^{\text{new}} = f_n + \gamma f_n^c. \quad (53)$$

8. Repeat until convergence.

This new iteration-based immersed boundary shows much better resolutions as shown in figure 24.

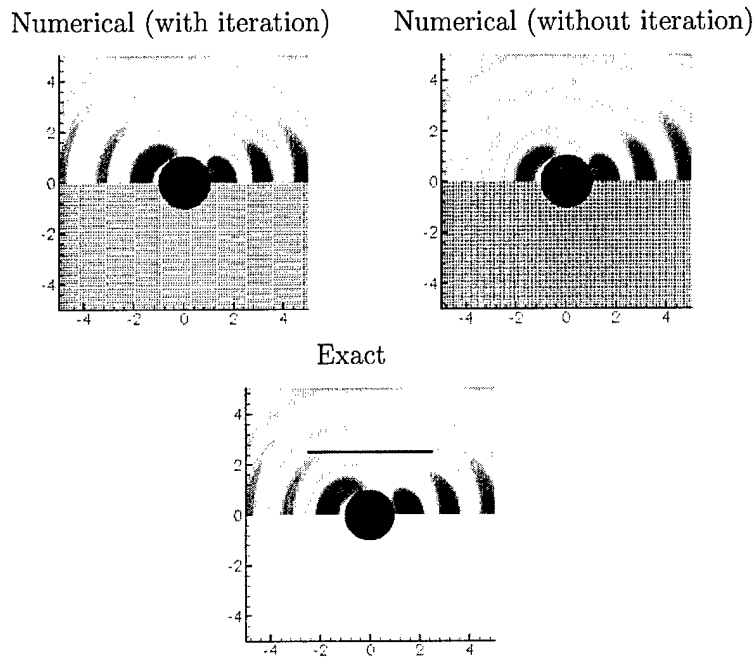


Figure 24: Comparison of the results by immersed boundary methods(with and w/o iteration) with exact solution. Contour shows the reflection waves.

This improvement is shown quantitatively in figure 25 by checking the contour value on a line marked in figure 24 (exact solution picture).

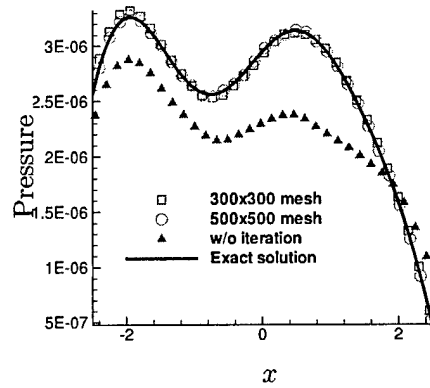


Figure 25: Contour values on marked line.

The accuracy of this method was confirmed to be 2nd order (figure 26).

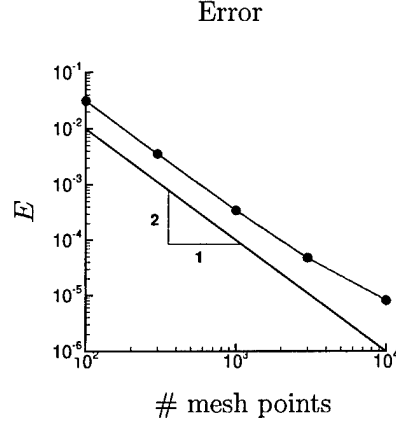


Figure 26: Algorithm accuracy.

As we mentioned before, the computational cost of this iteration-based immersed boundary process is negligible compared to the flow field calculations.

6 Discussion

A adjoint-based noise control method has been developed. The successful use of this method on a model jet is a novel means of exploring noise control mechanism and eventually provide a practical control in the real jet flow. Some ongoing work is:

- Simulations in a larger space domain and longer time. To generalize our results to “far-field”, we need to show the results are insensitive to the domain size. We also need a longer simulation time, the entire controlling process, to reach statistics.
- Three-dimensional simulations. It is a natural extent of present work. Of course, it will be more expensive to do iterations in three dimensional simulations.
- Nozzle optimization. All our works were focused on active control till now. We have known from trial-and-error experiments that nozzle modification can passively reduce the jet noise, although there is no conclusion how efficient it can eventually be. The combination of present adjoint-based optimization and immersed boundary technique will make the automatic nozzle optimization possible.

References

- [1] G. M. Lilley, “Jet noise: Classical theory and experiments,” In *Aeroacoustics of Flight Vehicles* edited by H. Hubbard. NASA RP 1258 (1991).
- [2] M. J. Lighthill, “On sound generated aerodynamically: I. General theory,” *Proc. Royal Soc. Lond. A* **211**, 564 (1952).
- [3] J. B. Freund, “Noise sources in a low-Reynolds-number turbulent jet at Mach 0.9,” *J. Fluid Mech.* **438**, 277 (2001).
- [4] K. B. M. Q. Zaman, M. F. Reeder and M. Samimy, “Control of an axisymmetric jet using vortex generators,” *Phys. Fluids* **6**, 778 (1994).

- [5] M. F. Reeder and M. Samimy, "The evolution of a jet with vortex generating tabs: real-time visualization and quantitative measurements," *J. Fluid Mech.* **311**, 73 (1996).
- [6] K. M. B. Q. Zaman, "Spreading characteristics of compressible jets from nozzles of various geometries," *J. Fluid Mech.* **383**, 197 (March 1999).
- [7] K. B. M. Q. Zaman and D. Papamoschou, "Study of mixing enhancement observed with a co-annular nozzle configuration," *AIAA Paper* 2000-0094 (2000).
- [8] C. W. Kerechanin II, M. Samimy and J.-H. Kim, "Effects of nozzle trailing edge modifications on noise radiation in a supersonic rectangular jet," *AIAA Paper* 2000-0086 (2000).
- [9] C. K. W. Tam and K. B. M. Q. Zaman, "Subsonic jet noise from non-axisymmetric and tabbed nozzles," *AIAA Paper* 99-0077 (1999).
- [10] C. K. W. Tam, "Influence of nozzle geometry on the noise of high-speed jets," *AIAA J.* **36**, 1396 (1998).
- [11] M. M. Rogers and R. D. Moser, "Direct simulation of a self-similar turbulent mixing layer," *Phys. Fluids* **6**, 903 (1994).
- [12] "Separate flow low noise nozzle project," *Nasa Aerospace Technology News*, Volume 1, Issue 2 (September 2000).
- [13] D. E. Parekh, V. Kibens, A. Glezer, J. M. Wiltse and D. M. Smith, "Innovative jet flow control: mixing enhancement experiments," *AIAA Paper* 96-0308 (1996).
- [14] B. L. Smith and A. Glezer, "The formation and evolution of synthetic jets," *Phys. Fluids* **230**, 2281 (1998).
- [15] S. M. Kusek and T. C. Corke, "Seeding of helical modes in the initial region of an axisymmetric jet," *Experiments in Fluids* **10**, 116 (1990).
- [16] J. R. Roth, D. M. Sherman and S. P. Wilkinson, "Boundary layer flow control with one atmosphere uniform flow discharge surface plasma," *AIAA Paper* 98-0328 (1998).
- [17] G. McKinney, Air Force Office of Scientific Research Publication: Research Highlights, Sept./Oct 1998 (also <http://ecs.rams.com/afosr/afr/afo/any/text/any/afrrhoct.htm>).
- [18] J. B. Freund and P. Moin, "Jet mixing enhancement by high amplitude fluidic actuation," *AIAA J.* **38**, 1863 (2000).
- [19] P. Koumoutsakos, J. B. Freund and D. Parekh, "Evolution strategies for automatic optimization of jet mixing," *AIAA J.* **39**, 967 (2001).
- [20] A. Hilgers, *Center for Turbulence Research Annual Research Brief*, chapter Control and optimization of turbulent jet mixing, pages 45-54 (CTR) (2000).
- [21] A. Jameson, N. A. Pierce and L. Martinelli, "Optimum aerodynamic design using the Navier-Stokes equations," *AIAA paper* 97-0101 (1997).
- [22] A. Jameson, "Re-engineering the design process through computation," *AIAA Paper* 97-0641 (1997).

- [23] M. B. Giles and N. A. Pierce, "Improved lift and drag estimates using adjoint euler equations," AIAA paper 99-3293 (1999).
- [24] C. Sung and J. H. Kwon, "Accurate aerodynamic sensitivity analysis using adjoint equations," AIAA J. **38**, 243 (2000).
- [25] M. Nemec and D. W. Zingg, "Towards efficient aerodynamic shape optimization based on the navier-stokes equations," AIAA paper 2001-2532 (2001).
- [26] B. Mohammadi, J. I. Molho and J. A. Santiago, "Design of minimal dispersion fluidic channels in a CAD-free framework," *Center for Turbulence Research, Proceedings of the Summer Program 2000*, 49-62 (2000).
- [27] M. G. Larson and T. J. Barth, "A posteriori error estimation for discontinuous Galerkin approximations of hyperbolic systems," 1st International Symposium on Discontinuous Galerkin Methods, Newport, R.I., May 1999 (1999).
- [28] T. R. Bewley, P. Moin and R. Temam, "Dns-based predictive control of turbulence: an optimal benchmark for feedback algorithms," J. Fluid Mech. **477**, 179 (2001).
- [29] C. K. W. Tam and L. Auriault, "Mean flow refraction effects on sound radiated from localized sources in a jet," J. Fluid Mech. **370**, 149 (1998).
- [30] A. Dobrinsky and S. S. Collis, "Adjoint methods for receptivity prediction in nonparallel flows," submitted to *Phys. Fluids* (2000).
- [31] S. S. Collis, K. Ghayour, M. Heinkenschloss, M. Ulbrich and S. Ulbrich, "Optimal control of unsteady compressible viscous flows," submitted to *J. Comp. Phys.* (2001).
- [32] S. S. Collis, K. Ghayour, M. Heinkenschloss, M. Ulbrich and S. Ulbrich, "Towards adjoint-based methods for aeroacoustic control," 39th Aerospace Sciences Meeting and Exhibit, Reno, NV, AIAA Paper 2001-0821 (2001).
- [33] S. S. Collis, K. Ghayour, M. Heinkenschloss, M. Ulbrich and S. Ulbrich, "Numerical solution of optimal control problems governed by the compressible navier-stokes equations," *Proceedings of the International Conference on Optimal Control of Complex Structures*, G. Leugering, J. Sprekels, and F. Troltzsch (Eds.), Birkhauser Verlag.
- [34] M. Wei and J. B. Freund, "Optimal control of free shear flow noise," 40th Aerospace Sciences Meeting, Reno, NV, AIAA Paper 2002-0665 (January 2002).
- [35] M. Wei and J. B. Freund, "Noise control using adjoint-based optimization," 8th AIAA/CEAS Aeroacoustics Conference, Breckenridge, CO, AIAA Paper 2002-2524 (June 2002).
- [36] M. B. Giles, "Nonreflecting boundary conditions for Euler equations calculations," AIAA J. **28**, 2050 (1990).
- [37] J. B. Freund and S. K. Lele, "Computer simulation and prediction of jet noise," in G. Raman, D. K. McLaughlin and P. J. Morris, editors, *High Speed Jet Flows : Fundamentals and Applications* (Taylor & Francis) (2001).
- [38] S. K. Lele, "Compact finite difference schemes with spectral-like resolution," J. Comp. Phys. **103**, 16 (1992).

- [39] C. K. W. Tam and J. C. Webb, "Dispersion-relation-preserving finite difference schemes for computational acoustics," *J. Comp. Phys.* **107**, 262 (Aug 1993).
- [40] J. B. Freund, "A proposed inflow/outflow boundary condition for direct computation of aerodynamic sound," *AIAA J.* **35**, 740 (1997).
- [41] W. H. Press, B. P. Flannery, S. A. Teukolsky and W. T. Vetterling, *Numerical Recipes* (Cambridge) (1986).
- [42] P. A. Monkewitz and P. Huerre, "Influence of the velocity ratio on the spatial instability of mixing layers," *Phys. Fluids* **25**, 1137 (1988).
- [43] C. M. Ho and P. Huerre, "Perturbed free shear layers," *Ann. Rev. Fluid Mech.* **16**, 365 (1984).
- [44] N. Sandham and W. Reynolds, "Three-dimensional simulations of large eddies in the compressible mixing layer," *J. Fluid Mech.* **224**, 133 (1991).
- [45] M. J. Day, W. C. Reynolds and N. N. Mansour, "The structure of the compressible reacting mixing layer: Insights from linear stability analysis," *Phys. Fluids* **10**, 993 (1998).
- [46] C. S. Peskin, "Flow patterns around heart valves: a numerical method," *J. Comp. Phys.* **10**, 252 (1972).
- [47] D. Goldstein, R. Handler and L. Sirovich, "Modeling a no-slip flow boundary with an external force field," *J. Comp. Phys.* **105**, 354 (1993).
- [48] J. Mohd-Yusof, "Combined immersed-boundary/B-spline methods for simulations of flow in complex geometries," *Center for Turbulence Research, Annual Research Briefs – 1997* (1997).
- [49] A. M. Roma, C. S. Peskin and M. J. Berger, "An adaptive version of the immersed boundary method," *J. Comp. Phys.* **153**, 509 (1999).



AIAA 2002-0665

**Optimal Control of Free Shear Flow
Noise**

M. Wei and J. B. Freund

Theoretical and Applied Mechanics

University of Illinois at Urbana-Champaign

Urbana, Illinois 61801

**40th AIAA Aerospace Sciences
Meeting and Exhibit
January 14-17, 2002/Reno, NV**

Optimal Control of Free Shear Flow Noise

M. Wei* and J. B. Freund†

Theoretical and Applied Mechanics
University of Illinois at Urbana-Champaign
Urbana, Illinois 61801

Efforts to diagnose and control aerodynamic noise from turbulent flows have been hampered by a lack of the necessary computational fidelity and practical simulation procedures to use in place of expensive trial-and-error experiments. Recent direct numerical simulations of jet noise¹ provide a detailed look at the mechanisms, but have not yet shown a clear path to follow that will reduce noise. In this paper we introduce a method that uses the full flow field information of such a simulation in an automated fashion in conjunction with solutions of the adjoint of the flow equations to reduce noise. We demonstrate this method on a convective Mach number $M_c = 0.4$, Reynolds number $Re_\omega = 500$ two-dimensional mixing layer. For now, the actuation is right-hand-side forcing of the Navier-Stokes equations restricted to a small control region near the splitter plate. After 7 conjugate gradient iterations, noise is reduced by 6.3dB. The optimal forcing identified is weak, and has a nearly imperceptible effect on the structures in the mixing layer.

Nomenclature

a	Sound speed
C	Control region
e	Total energy
f_e	Bodyforce to excite instability
g	Gradient for control update
M	Mach number
M_c	Convective Mach number $= \frac{U_1 - U_2}{a_\infty}$
p	Pressure
Re_ω	Reynolds number $= \frac{\rho \delta_\omega (U_1 - U_2)}{\mu}$
St	Strouhal number $\frac{f \delta_\omega}{a_\infty}$
t	Time
u, v	Velocity in x and y
U_1	Speed of upper flow
U_2	Speed of lower flow
x, y	Cartesian coordinates
α	Line search parameter for control update
δ_ω	Vorticity thickness
μ	Viscosity coefficient
ρ	Density
ϕ	Control
Ω	Noise reduction line (target line)

Accents/Subscripts/Superscripts

$\overline{(\quad)}$	Time average
∞	Ambient
$'$	Perturbation from mean
k	Iteration #
$*$	Adjoint variables

*Research Assistant.

†Assistant Professor. AIAA member.

Copyright © 2002 by the authors. Published by the American Institute of Aeronautics and Astronautics, Inc. with permission.

Introduction

NOISE continues to be a pressing problem in the aircraft industry, with a substantial competitive advantage going to makers of planes and engines that can satisfy the ever more restrictive airport noise regulations. Even with modern high-bypass engines, jet noise remains a significant component of the overall noise from an aircraft, especially during takeoff, and must be reduced for future aircraft to meet anticipated regulations.

The development of controls is hampered by insufficient understanding of the mechanism of aerodynamic noise generation by turbulence. Most attempts to optimize the nozzle shape to reduce the jet noise are based on trial-error experimentation.² This approach is expensive. The results are confusing and do not give a clear explanation of why a particular design is preferable to others. Often procedures that reduce overall sound pressure level end up increasing net annoyance by increasing the high-frequency components of the noise.³ Procedures that work on models do not always work on full-scale engines.

The root difficulty is that noise generation, especially in subsonic free shear flows, is a subtle process with only a tiny amount of the flow's energy escaping to radiate as noise. With the availability of high-speed computers and advanced numerical methods, it has recently become possible to compute aerodynamic noise from first principles by solving the compressible flow equations without modeling approximations.¹ Two-dimensional mixing layers,⁴ axisymmetric jets,⁵ and supersonic⁶ and subsonic¹ three-dimensional turbulent jets have been computed in this way. These simulations have provided insight into the mechanism but as yet have not pointed the direction for controlling noise,⁷ which is the principal objective of this paper.

Typically, control problems approach their optimum

iteratively based on sensitivity analysis of control parameters. In this case, we are concerned with *sensitivity of the noise to changes at the nozzle*. This information is needed in order to be able to adjust controls appropriately to reduce noise. A direct method to identify sensitivities is expensive: its cost is proportional to the number of control parameters, which is excessive if there are many. Optimizing a time profile for forcing by necessity requires many parameters. This is prohibitive in experiments because most hardware lacks flexibility to fully examine the parameter space. Though in principle they offer greater flexibility, simulations with the necessary fidelity are currently far too slow to take this brute force approach. However, the adjoint method provides the full sensitivity information linearized about a particular flow by solving a single adjoint (inverse) system. Thus, its cost is independent of the number of control parameters.⁸ In fluid mechanics applications, adjoint methods have been used successfully in shape optimization⁸⁻¹⁰ and turbulence drag reduction.¹¹ Similar methods have been used to study and account for mean flow refraction effects on sound radiated by localized sources in jets.¹²

Our approach is shown schematically in figure 1. Given a numerical solution of the compressible flow equations, the adjoint of these equations with coefficients that depend on the flow solution is solved backward in time to give the sensitivity of the noise, which is defined quantitatively by an appropriate metric, to changes in the control at the nozzle. This sensitivity is used to update controls to reduce noise. At present the approach depends on the full flow field information of flow simulation, and so is impractical for direct use in most engineering applications. However, our results will be useful in several ways. The controlled case will be analyzed to develop general laws to guide future experiments and designs and to achieve a deeper understanding of what remains a poorly understood mechanism. These simulations also provide, in some sense, an upper limit for what can be accomplished reducing noise with active control.

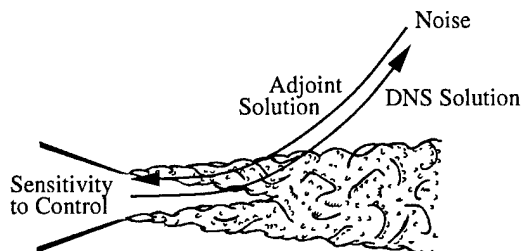


Fig. 1 Schematic of the adjoint-based procedure for determining control sensitivity.

Formulation

The present study focuses on a two-dimensional mixing layer, which is a near-nozzle model of a jet. There is no indication that any particular change is needed to use present methodology to control a more general three-dimensional turbulent flow.

Our mixing layer system is shown in figure 2. The Reynolds number is $Re_\omega = 500$, defined by vorticity thickness δ_ω , the Mach numbers of the top and bottom streams are $M = 0.8$ and $M = 0$, and the temperature is uniform.

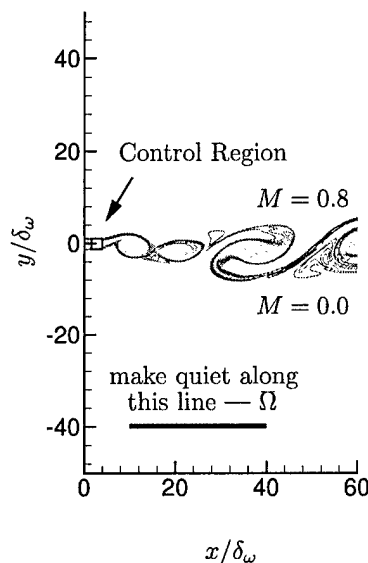


Fig. 2 Mixing layer control schematic.

Our control objective is to reduce the noise along the target line Ω at $y = -40\delta_\omega$ between $x = 10\delta_\omega$ and $x = 40\delta_\omega$. To achieve this, we apply the control ϕ , which is a generic forcing term added to the right-hand-side of the Navier-Stokes equations in a small control region \mathcal{C} , $x/\delta_\omega \in (1, 5)$ and $y/\delta_\omega \in (-2, 2)$, also shown in figure 2.

We define the cost functional to be minimized as

$$\mathcal{J}(\phi) = \int_{t_0}^{t_1} \int_{\Omega} (p - p_\infty)^2 d\Omega dt, \quad (1)$$

where p is the instantaneous pressure, p_∞ is the ambient pressure, and t_0 and t_1 are the beginning and end of the times to be made quiet. To determine the sensitivity of \mathcal{J} to small modifications of the control ϕ , we consider a small perturbation \mathcal{J}' to the cost functional \mathcal{J} resulting from an arbitrary perturbation ϕ' to the control ϕ .¹¹ \mathcal{J}' is defined as the Fréchet differential of

the cost functional \mathcal{J} as

$$\begin{aligned}\mathcal{J}'(\phi; \phi') &\equiv \frac{\mathcal{D}\mathcal{J}(\phi)}{\mathcal{D}\phi} \cdot \phi' \\ &\equiv \lim_{\varepsilon \rightarrow 0} \frac{\mathcal{J}(\phi + \varepsilon\phi') - \mathcal{J}(\phi)}{\varepsilon} \\ &= \int_{t_0}^{t_1} \int_{\Omega} 2pp' d\Omega dt.\end{aligned}\quad (2)$$

The gradient \mathbf{g} to update the control is determined directly from a solution of the adjoint system, forced by \mathcal{J} , using a well-documented procedure.¹¹ Control is updated as

$$\phi^{k+1} = \phi^k - \alpha^k \mathbf{g}^k, \quad (3)$$

where α^k is a line-search parameter determining the change along direction \mathbf{g}^k for the k^{th} iteration.

Computational Methods

For the flow and sound fields, the compressible Navier-Stokes equations are solved without modeling assumptions.

To excite the mixing layer, we apply a bodyforce with peak level $f_e \approx 0.005\rho_\infty a_\infty^2/\delta_\omega$ at the inflow. This force has 8 frequencies between $St = 0.025\pi$ and $St = 0.2\pi$, to simulate natural disturbances with a wide spectrum. Our controller, of course, has no knowledge of this excitement forcing.

A fourth-order Runge-Kutta algorithm is used for time advancement, and a sixth-order Padé scheme¹³ is used for spatial differencing. A specialized buffer zone similar to that of Freund¹⁴ and a more traditional non-reflecting boundary condition¹⁵ are used in combination to absorb disturbances as they leave the finite computational domain. The same schemes are used to solve the adjoint equations.

For the control update, the Polak-Ribiere variant of the conjugate gradient algorithm is used with Brent's line-minimization method.¹⁶

Some of the results in this paper were computed on parallel machines using MPI. In this case, the Dispersion-Relation-Preserving (DRP) scheme¹⁷ was used in y .

Results and Analysis

Noise Reduction

Figure 3 (a) shows the instantaneous flow and sound field of the uncontrolled mixing layer with contours of vorticity to show the flow structure. The corresponding controlled case after 7 iterations is shown in figure 3 (b) at the same time. The noise is clearly reduced along the target line. More quantitatively figure 4 shows a 77% reduction of cost functional, which is about 6.3dB. At present, the starting point t_0 in the cost functional is chosen to be the time for sound to travel from control region \mathcal{C} to the closest point on

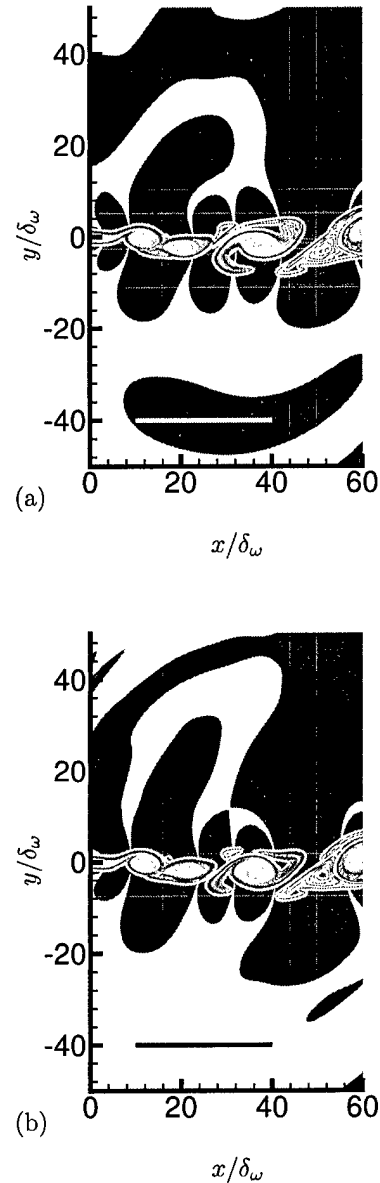


Fig. 3 Comparison of (a) without control (b) with control flow and sound field. Solid black is $|p'/p_\infty| > 0.003$. Contours show vorticity magnitude with peak $0.78a_\infty/\delta_\omega$.

Ω . Before this time, noise on the target line is not controllable. Even after t_0 , within some period the target line is not under full control by two reasons: (1) the control reaches the closest point but not the farther points; (2) the rate at which the effect of the control travels is slower than sound speed—in the mixing layer it is the structure convective Mach number, $M_c \approx 0.4$. An overlapping-time control method¹¹ will remedy this. This will make the cost \mathcal{J} , as we compute it, decrease more, though we might have already achieved the piecewise (in time) maximum reduction

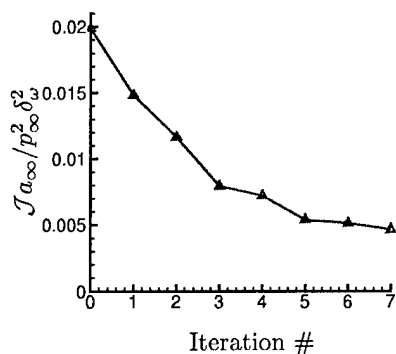


Fig. 4 The reduction of the cost.

at later times.

To measure the strength of the forcing, which for now only appears in the energy equation, we calculate the integral of the total energy (internal energy plus kinetic energy) in that region,

$$E(t) = \int_C e(\mathbf{x}, t) dC, \quad (4)$$

with and without control. The small energy input is indicated by the minor changes in figure 5. Since C is itself a small area, it is clear that very little energy is added.

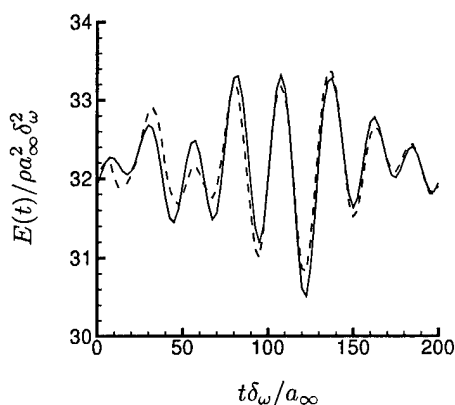


Fig. 5 Integral of the energy in the control region C : — without control; ---- with control.

To see if the radiation increases elsewhere, we compare the cost with and without control on other lines besides the target line. As shown in figure 6, other costs have not changed much and some other directions are also quieter.

Adjoint Field

To better understand the control process, the evolution of the adjoint pressure p^* is shown in figure 7. It is this quantity that gives the gradient information \mathbf{g} . Since the flow equations are self-adjoint in the acoustic limit, the adjoint pressure is initially an adjoint sound wave, excited along the target line by the difference

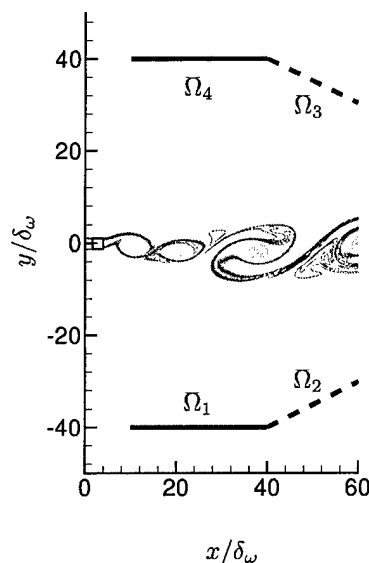


Fig. 6 Cost value $J_{a_{\infty}}/p_{\infty}^2 \delta_{\omega}^2$ without and with control on different lines: Ω_1 (target line Ω): 0.0199 (without control) \Rightarrow 0.00465 (with control); Ω_2 : 0.0746 \Rightarrow 0.0574; Ω_3 : 0.1065 \Rightarrow 0.0781; Ω_4 : 0.0394 \Rightarrow 0.0415.

between the cost and the cost expectation. As this wave encounters the mixing layer, it excites instability waves, which move upstream in the mixing layer to the control region. Finally, the gradient information is recorded inside this region. It is the instability waves in the adjoint that dominates the gradient.

Given this qualitative behavior of the adjoint, the mechanism of noise control can be expressed as follows. The control interacts with the flow. This excitation alters (slightly, we shall see) the instabilities in the flow. The modified flow field is quieter. We are working to quantify the precise mechanism.

Is It Anti-sound?

That adjoint instability waves dominate the gradient information suggests that the control mechanism is not anti-sound. This is supported more quantitatively here. Choosing the point, $x = 25\delta_{\omega}$ and $y = -40\delta_{\omega}$ on Ω , we record the pressure fluctuation history in figure 8. The vertical line indicates the moment when the first sound wave from the control box would (and does) arrive. In these initial simulations the control is started impulsively causing the jagged burst we see. If the mechanism were anti-sound, the noise reduction should appear just after this point. However, the apparent control of the noise happens after a time delay due to the slower instability wave speed. The vertical shaded belt shows the approximate time for a flow structure to convect to $x = 25\delta_{\omega}$ at $M_c \approx 0.4$, which is observed for this mixing layer (see figure 11), and then for sound to radiate from $y = 0$ to the Ω at $y = -40\delta_{\omega}$.

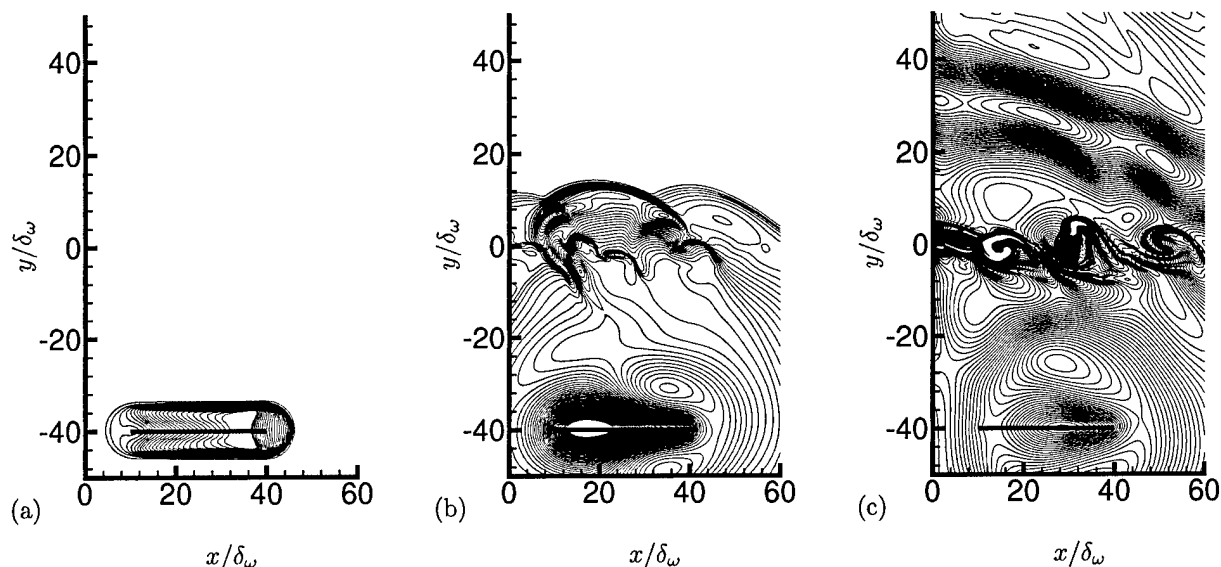


Fig. 7 Adjoint pressure: (a) $t = 195$, (b) $t = 150$, (c) $t = 75$. The time goes backward in the adjoint solution.

This is, of course, a crude estimate of the time for control to take effect. Further investigation is underway.

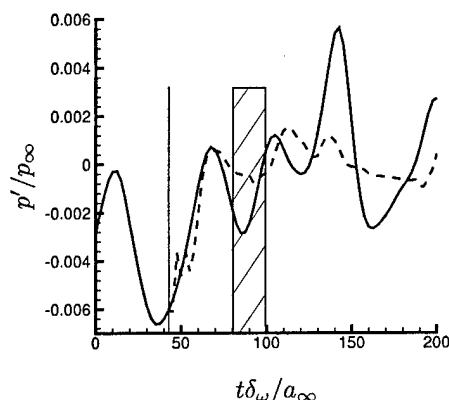


Fig. 8 Pressure fluctuation changes at $x = 25\delta_\omega$, $y = -40\delta_\omega$: — without control; --- with control.

Furthermore, we designed a numerical experiment shown in figure 9. The control is moved to the region $x/\delta_\omega \in (1, 5)$ and $y/\delta_\omega \in (-20, -16)$ away from the main flow area. Now the adjoint instability wave never reaches this control region, so control is principally by acoustic cancellation—anti-sound. After 7 iterations, only 45% reduction is observed (figure 10).

As a comparison, we check the radiation increase elsewhere for this anti-sound case too. Unlike the previous case, some of the costs increase substantially. The cost value $\mathcal{J}a_\infty/p_\infty^2\delta_\omega^2$ changes on different lines (refer to figure 6) as: Ω_1 : $0.0199 \Rightarrow 0.0109$; Ω_2 : $0.0746 \Rightarrow 0.0899$; Ω_3 : $0.1065 \Rightarrow 0.1010$; Ω_4 :

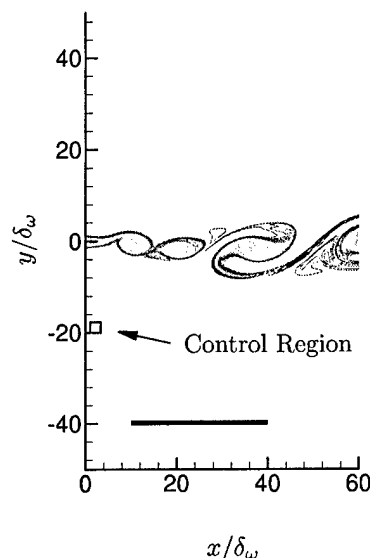


Fig. 9 Anti-sound control test schematic.

$0.0394 \Rightarrow 0.0539$.

Flow Field Changes

A remarkable result is that the large-scale structural evolution has changed little between noisy and quieted cases. Figure 11 shows the time evolutions of large structures, as demarked by pressure, at $y/\delta_\omega = 0$ with and without control. Small changes in the structural evolution are apparent, but the gross features are indistinguishable. For example, the pairing structures, which we see as the joining of the dark regions, in both pictures keep almost the same size and angle.

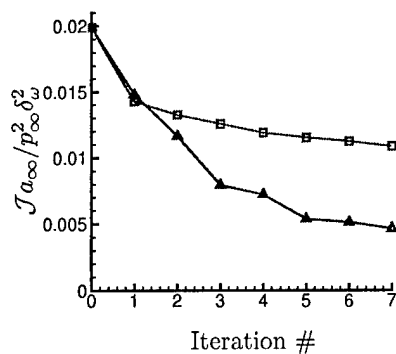


Fig. 10 The cost reduction comparison: Δ “near-nozzle” control; \square anti-sound control.

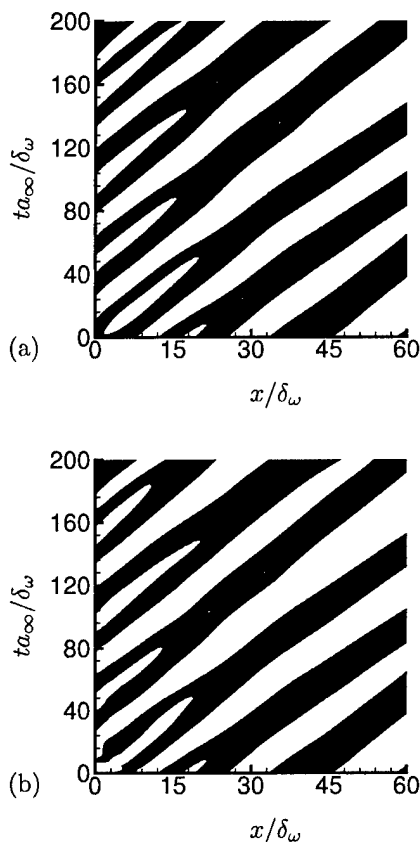


Fig. 11 Pressure at $y = 0$ shows little change in large-scale structural evolution without (a) and with (b) control. Black is $p' < 0$; white is $p' > 0$.

The turbulence kinetic “energy,” defined as

$$k = \frac{1}{2}[(u')^2 + (v')^2], \quad (5)$$

where u' and v' are fluctuation of velocities, is also nearly unchanged. Figure 12 shows

$$K_x(x) = \int_{-50\delta_\omega}^{50\delta_\omega} \bar{k} dy \quad (6)$$

and

$$K_y(y) = \int_0^{60\delta_\omega} \bar{k} dx \quad (7)$$

with and without control. The noise reduction is not obtained through turbulence suppression.

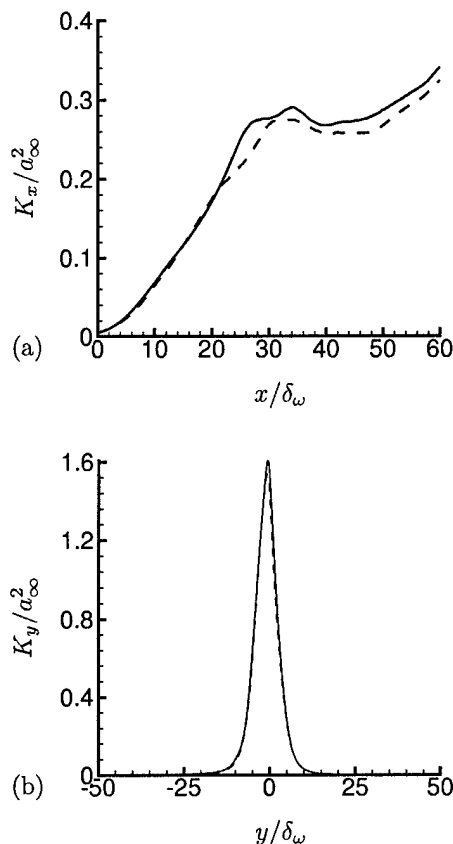


Fig. 12 Comparison of integrated turbulence kinetic energy as defined in (a) equation (6) and (b) equation (7). The lines indicate the case without control — and the case with control ----.

Conclusions

Using an adjoint-based control techniques, we reduced two-dimensional mixing layer noise by 6.3dB with little change to the apparent structural dynamics. This is possible because only a small fraction of the flow’s energy, that with a supersonic phase velocity, radiates. Our simulations indicate that, at least in a two-dimensional mixing layer, this part can be altered with minimal control authority to dramatically reduce the noise.

Work continues identifying practical control laws and understanding the details of how the present control works.

Acknowledgment

We gratefully acknowledge financial support from AFOSR and computer time from NPACI and NCSA.

References

- ¹Freund, J. B., "Noise sources in a low-Reynolds-number turbulent jet at Mach 0.9," *J. Fluid Mech.*, Vol. 438, 2001, pp. 277-305.
- ²Saiyed, N. H., "Acoustics and thrust of separate flow exhaust nozzles with mixing devices investigated for high bypass ratio engines," NASA Glenn Research Center Report RT1999, 1999.
- ³Narayanan, S., Barber, T., and Polak, D., "High subsonic jet experiments. Part II: Turbulence and noise generation studies," AIAA/CEAS Aeroacoustics Conference and Exhibit, 6th, Maui, AIAA paper 2000-2023, 2000.
- ⁴Colonius, T., Lele, S. K., and Moin, P., "Sound generation in a mixing layer," *J. Fluid Mech.*, Vol. 330, 1997, pp. 375-409.
- ⁵Mitchell, B. E., Lele, S. K., and Moin, P., "Direct computation of the sound generated by vortex pairing in an axisymmetric jet," *J. Fluid Mech.*, Vol. 383, 1999, pp. 113-142.
- ⁶Freund, J. B., Lele, S. K., and Moin, P., "Direct numerical simulation of a Mach 1.92 turbulent jet and its sound field," *AIAA J.*, Vol. 38, No. 11, 2000, pp. 2023-2031.
- ⁷Ffowcs Williams, J. E., "DAVID CRIGHTON 1942-2000: A commentary on his career and his influence on aeroacoustic theory," *J. Fluid Mech.*, Vol. 437, 2001, pp. 1-11.
- ⁸Jameson, A., Pierce, N. A., and Martinelli, L., "Optimum aerodynamic design using the Navier-Stokes equations," AIAA paper 97-0101, 1997.
- ⁹Giles, M. B. and Pierce, N. A., "Improved lift and drag estimates using adjoint Euler equations," AIAA paper 99-3293, 1999.
- ¹⁰Sung, C. and Kwon, J. H., "Accurate aerodynamic sensitivity analysis using adjoint equations," *AIAA J.*, Vol. 38, No. 2, 2000, pp. 243-250.
- ¹¹Bewley, T. R., Moin, P., and Temam, R., "DNS-based predictive control of turbulence: an optimal benchmark for feedback algorithms," *J. Fluid Mech.*, Vol. 477, 2001, pp. 179-225.
- ¹²Tam, C. K. W. and Auriault, L., "Mean flow refraction effects on sound radiated from localized sources in a jet," *J. Fluid Mech.*, Vol. 370, 1998, pp. 149-174.
- ¹³Lele, S. K., "Compact finite difference schemes with spectral-like resolution," *J. Comp. Phys.*, Vol. 103, 1992, pp. 16-42.
- ¹⁴Freund, J. B., "A proposed inflow/outflow boundary condition for direct computation of aerodynamic sound," *AIAA J.*, Vol. 35, No. 4, 1997, pp. 740-742.
- ¹⁵Giles, M. B., "Nonreflecting boundary conditions for Euler equations calculations," *AIAA J.*, Vol. 18, 1990, pp. 2050-2058.
- ¹⁶Press, W. H., Flannery, B. P., Teukolsky, S. A., and Vetterling, W. T., *Numerical Recipes*, Cambridge, 1986.
- ¹⁷Tam, C. K. W. and Webb, J. C., "Dispersion-relation-preserving finite difference schemes for computational acoustics," *J. Comp. Phys.*, Vol. 107, No. 2, Aug 1993, pp. 262-281.



AIAA 2002-2524

**Noise Control Using Adjoint-based
Optimization**

M. Wei and J. B. Freund

Theoretical and Applied Mechanics

University of Illinois at Urbana-Champaign

Urbana, Illinois 61801

**8th AIAA/CEAS Aeroacoustics Conference
June 17–19, 2002/Breckenridge, CO**

Noise Control Using Adjoint-based Optimization

M. Wei* and J. B. Freund†
Theoretical and Applied Mechanics
University of Illinois at Urbana-Champaign
Urbana, Illinois 61801

Attempts to control the jet noise have been hampered by an insufficient understanding of its mechanisms, resulting in a reliance on trial-and-error experimentation to reduce noise. This paper aims to explore the noise mechanism using adjoint-based noise control in conjunction with a direct numerical simulation. A control problem is formulated with the objective of reducing acoustic intensity on a line in the sound field. The cost function that quantifies this is used to force the adjoint of the compressible flow equation, which are solved numerically in the same way we solve the flow equations. The adjoint variables provide the sensitivity of the noise, as we have specifically defined it, to changes in actuation. Using this approach, the noise radiated from a two-dimensional mixing layer with convective Mach number $M_c = 0.4$ and Reynolds number based on vorticity thickness $Re_\omega = 500$ was reduced by 6.3dB. This flow is a model of the near nozzle region of a jet and generalization of the technique to a jet is straightforward. Despite the substantial reduction in the noise, the changes of the flow field are small, as seen by examination of the turbulence kinetic energy and the momentum thickness before and after control is applied. We conclude that the controller makes subtle changes to the radiating portion of the flow without drastically altering its energetics. Our preliminary investigations into the nature of the automatically identified control reveal little of how it works.

Nomenclature

a	Sound speed
C	Control region
f	Frequency
f_0	Fundamental frequency
F_e	Excitation forcing
\mathbf{g}	Gradient for control update
k	Turbulent kinetic energy (TKE)
K	Integrated quantity of TKE
M	Mach number
M_c	Convective Mach number = $\frac{U_1 + U_2}{2a_\infty}$
p	Pressure
Re_ω	Reynolds number = $\frac{\rho \delta_\omega \Delta U}{\mu}$
St	Strouhal number = $\frac{f \delta_m}{U_c}$
t	Time
Δt	Timestep
u, v	Velocity in x and y
U_1	Speed of high-speed stream (top)
U_2	Speed of low-speed stream (bottom)
U_c	Approximate convection speed = $\frac{U_1 + U_2}{2}$
ΔU	$U_1 - U_2$
x, y	Cartesian coordinates
α	Line search parameter for control update
β	Initial phases of excitation
δ_m	Momentum thickness
δ_ω	Vorticity thickness
μ	Viscosity
ρ	Density
ϕ	Control

ψ	Excitation function
Ω	Noise reduction line (target line)

Accents/Subscripts/Superscripts

$\overline{(\quad)}$	Time average
∞	Ambient
$'$	Perturbation from mean
n	Iteration #
$*$	Adjoint variable

Introduction

JET noise remains a significant component of aircraft noise, and thus, as noise regulations become more restrictive, it will affect the attractiveness of planes and engines on the market. Although theoretical noises were first formulated 50 years ago,¹ their direct use in modeling and control has been hampered by the lack of a detailed quantitative description of the flow field. Even with this information, provided recently for the first time by direct numerical simulation (DNS),²⁻⁵ effective controls are not obvious due to the complexity of the flow.

It has been known for a long time that certain nozzle geometry modifications reduce noise. Lobes⁶ can quiet the exhaust, but cause unacceptable thrust loss. So-called hush kits are retrofit to engines to mix the flow internally to reduce noise outside, but again with significant losses. Recently, chevrons (triangles cut out of the nozzle lip essentially parallel to the flow) have been found to reduce noise a couple decibels (effective perceived noise) with minimal incurred loss.^{7,8} However, since trial-and-error experimentation is a component of

*Research Assistant.

†Assistant Professor. AIAA member.

Copyright © 2002 by Mingjun Wei. Published by the American Institute of Aeronautics and Astronautics, Inc. with permission.

their design, there is no way of knowing how effective they can ultimately be. Active control can in principle offer greater control authority by its nature, but it is simply not known how to use available actuators or how to optimize actuator designs to reduce noise. Understanding of jet noise is too limited (or jet noise is too complex) to provide effective models, even at a phenomenological level, that can be used in an optimization procedure.

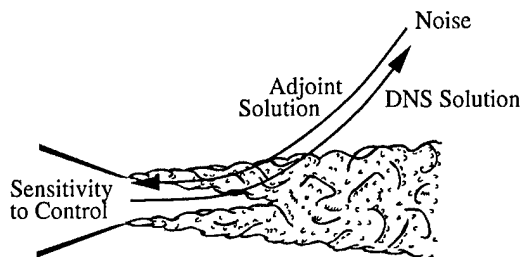


Fig. 1 Schematic of the adjoint-based procedure for determining control sensitivity.

Our approach is an automatic control optimization that employs the adjoint of the compressible flow equation, as previewed in authors' previous work.⁹ It circumvents our poor understanding of the mechanisms and provides automatic means of reducing noise despite its complexity. The approach is shown schematically in figure 1. Given a numerical solution of the compressible flow equations for a jet, which currently can only be provided by an accurate flow simulation, the adjoint of these equations is solved numerically backward in time to give the sensitivity of the noise, as defined quantitatively by an appropriate metric, to changes in the control at the nozzle. This sensitivity is used to update controls for the specific noise reduction objective that we have selected. As formulated, success depends upon the full flow field information of a DNS, so it is obviously not directly practical. Our intention is to develop general laws and guide future experiments and designs and to achieve a better understanding of what is currently a poorly understood mechanism. Several avenues of generalization are being pursued, but are not discussed in this paper.

The Two-dimensional Mixing Layer

We demonstrate the algorithm and study its results when it is applied to the two-dimensional mixing layer shown in figure 2. The Reynolds number is $Re_\omega = 500$, based on vorticity thickness,

$$\delta_\omega = \left(\frac{\Delta U}{|du/dy|_{max}} \right)_{x=0}, \quad (1)$$

the Mach numbers of the top and bottom streams are $M = 0.8$ and $M = 0.0$, respectively. The inflow temperature is uniform.

The black line Ω in figure 2 at $y = -40\delta_\omega$ and extending between $x = 10\delta_\omega$ and $x = 40\delta_\omega$ is our target

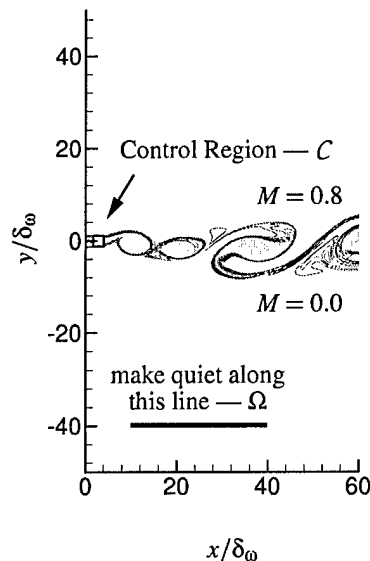


Fig. 2 Mixing layer control schematic.

line, where the noise will be reduced. The actuation is a generic forcing term $\phi(x, t)$ added to the right-hand-side of the energy equation in a small control region C , $x/\delta_\omega \in (1, 5)$ and $y/\delta_\omega \in (-2, 2)$, also shown in the figure.

Control Formulation

Our control objective is to reduce the cost functional

$$\mathcal{J}(\phi) = \int_{t_0}^{t_1} \int_{\Omega} (p - p_\infty)^2 d\Omega dt, \quad (2)$$

where p is the instantaneous pressure, p_∞ is the ambient pressure, and t_0 and t_1 are the beginning and end of the times to be made quiet. To determine the sensitivity of \mathcal{J} to small modifications of the control ϕ , we consider a \mathcal{J}' perturbation to the cost \mathcal{J} resulting from a perturbation ϕ' to the control ϕ .¹⁰ \mathcal{J}' is the Fréchet differential of the cost functional \mathcal{J} :

$$\begin{aligned} \mathcal{J}'(\phi; \phi') &\equiv \frac{\mathcal{D}\mathcal{J}(\phi)}{\mathcal{D}\phi} \cdot \phi' \\ &\equiv \lim_{\epsilon \rightarrow 0} \frac{\mathcal{J}(\phi + \epsilon\phi') - \mathcal{J}(\phi)}{\epsilon} \\ &= \int_{t_0}^{t_1} \int_{\Omega} 2pp' d\Omega dt. \end{aligned} \quad (3)$$

This form of \mathcal{J}' provides the gradient direction g , in which to adjust ϕ to reduce \mathcal{J} . Instead of being solved directly via (3) as expressed in the physical flow variables, the gradient g is more easily determined from a solution of the adjoint system,⁹ as forced by \mathcal{J} , using a well-documented procedure.¹⁰

Then, the control is updated as

$$\phi^{n+1} = \phi^n - \alpha^n g^n, \quad (4)$$

where α^n is a line-search parameter determining the change along direction g^n for the n^{th} iteration. The Polak-Ribiere variant of the conjugate gradient algorithm is used with Brent's line-minimization method¹¹ to accelerate convergence.

There are 920 mesh points in the control region C and we attempt to reduce the noise for $t_1 - t_0 = 200\delta_\omega/a_\infty$. ϕ is free to assume any value at any of the space time points. Given out timestep $\Delta t = 0.05\delta_\omega/a_\infty$, we are optimizing 3.84×10^6 free parameters. Direct exploration of this parameter space is clearly prohibitive.

Computational Methods

The flow and sound fields are governed by the compressible Navier-Stokes equations, which are solved numerically in two space dimensions without modeling assumptions using a fourth-order Runge-Kutta algorithm for time advancement. For spatial differencing, a sixth-order Padé scheme¹² is used in the x (streamwise) direction, and the Dispersion-Relation-Preserving (DRP) scheme¹³ is used in the y (cross-stream) direction. The explicit DRP scheme facilitates decomposition across different processor on a parallel machine. A specialized buffer zone similar to that of Freund¹⁴ and a more traditional non-reflecting boundary condition¹⁵ are used in combination to absorb disturbances as they leave the finite computational domain. The same schemes are used to solve the adjoint equations, also without modeling approximations.

Instability theory predicts that the most unstable mode of the incompressible mixing layer to have $St = 0.032$,^{16,17} which provides an estimation of the fundamental frequency of our compressible mixing layer, since this frequency is not very sensitive to compressibility for $M_c = 0.4$.^{18,19} So we take our fundamental frequency to be $f_0 = \frac{St U_c}{\delta_m}$. Numerical experimentation confirms that the mixing layer does respond strongly to forcing at or near this frequency. To provide a richer flow for our scheme to control, we excite the flow at a total of eight frequencies, $f_0/4$, $f_0/2$, $3f_0/4$, f_0 , $5f_0/4$, $3f_0/2$, $7f_0/4$, and $2f_0$. These were selected in an *ad hoc* fashion in this study. A more thorough investigation of the effects of this excitation on the noise and its controllability is underway.

To minimize the direct effect of the excitation on the sound field, we define a function ψ with the 8 frequencies f_i listed above, as

$$\begin{aligned} \psi = & \psi_0 e^{-\sigma_x(x-x_0)^2} e^{-\sigma_y(y-y_0)^2} \\ & \times \sum_{i=1}^8 \sin[2\pi f_i(x-x_0-M_c t) + \beta_x^i] \\ & \times \sin[2\pi f_i(y-y_0) + \beta_y^i], \end{aligned} \quad (5)$$

where ψ_0 is the amplitude, (x_0, y_0) is $(-5\delta_\omega, 0)$, both σ_x and σ_y are 0.2, $\xi_{x,y}$ are initial random phases. The excitation, which appears as a bodyforce, is then defined

as

$$F_{ex} = \frac{\partial \psi}{\partial y}, \quad F_{ey} = -\frac{\partial \psi}{\partial x}, \quad (6)$$

so that it is solenoidal and therefore relatively quiet. We observed no sound directly from this excitation. The amplitude of each mode was $\psi_0 = 0.004\rho_\infty a_\infty^2/\delta_\omega$. Our selection of x_0 and y_0 puts the excitation upstream of the physically realistic portion of the computation. Our controller, of course, has no direct knowledge of this excitation.

The flow was simulated for time $400\delta_\omega/a_\infty$ to allow it to reach a statistically stationary condition. Then the controller was turned on. We anticipate that the first $60\delta_\omega/a_\infty$ is uncontrollable based on the traveling time for the effect of the control to reach the target line Ω .

Noise Reduction

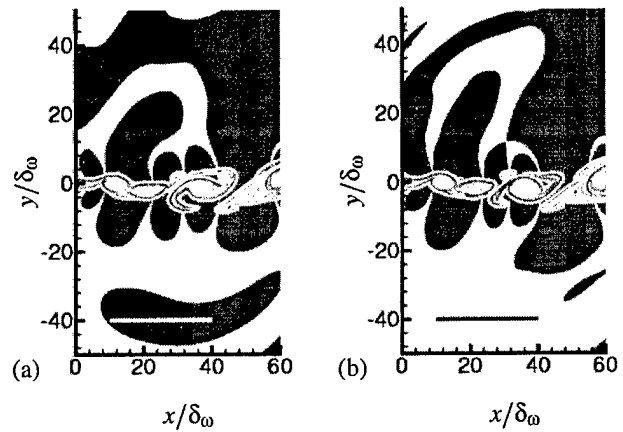


Fig. 3 Comparison of the flow and sound radiation (a) without control and (b) with control. Solid black is $|p'|/p_\infty > 0.003$. Contours show vorticity magnitude with peak $0.78a_\infty/\delta_\omega$.

Figure 3 (a) shows the instantaneous flow and sound field of the uncontrolled mixing layer with contours of vorticity to show the flow structure and regions of large $|p'|$ to mark acoustic radiation. The corresponding controlled case after 7 conjugate gradient iterations is shown in figure 3 (b) at the same time. The noise is clearly reduced along the target line.

This is confirmed quantitatively in figure 4, which shows a 77% reduction of cost functional, which is about 6.3dB. Furthermore, this sound reduction along the target line does not increase the noise elsewhere, as we showed before.⁹ It is not anti-sound.

Adjoint Field

To better understand the control process, the evolution of the adjoint pressure p^* is shown in figure 5. It is this quantity that provides the gradient information g to update control equation (4). Since the flow equations are self-adjoint in the acoustic limit, the adjoint pressure is initially an adjoint sound wave, excited along

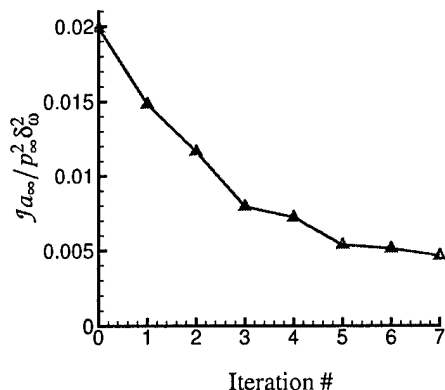


Fig. 4 The reduction of the cost.

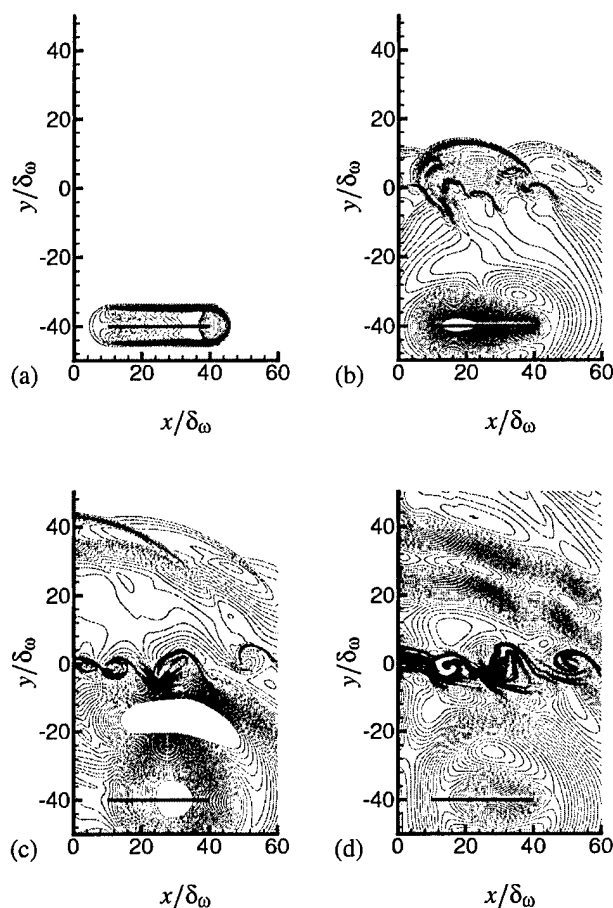


Fig. 5 Adjoint pressure: (a) $t = 195\delta_\omega/a_\infty$, (b) $t = 150\delta_\omega/a_\infty$, (c) $t = 120\delta_\omega/a_\infty$, (d) $t = 75\delta_\omega/a_\infty$. The time goes backward in the adjoint solution.

the target line by the cost. As this wave encounters the mixing layer, it excites instability waves, which move upstream in the mixing layer to the control region. Finally, the gradient information is recorded inside this region. It is the instability waves in the adjoint that dominates the gradient, which suggests that the control

mechanism is via the instabilities in the mixing layer.

Given this qualitative behavior of the adjoint, the mechanism of noise control can be expressed as follows. The control interacts with the flow. This excitation alters (slightly, we shall see) the instabilities in the flow. The modified flow field is quieter. Works are ongoing to identify the precise mechanism quantitatively.

Control Forcing

Figure 6 shows twenty snapshots of the optimal control forcing at different times. In the control box, the forcing is distributed in a non-intuitive manner. The apparent “structure” in the control $\phi(x,y)$ moves at a speed between $0.7U_c$ and $1.7U_c$, where U_c is the anticipated structure convection velocity, which is close to the expected convective speed U_c , but little else can be understood via visualizations.

In an attempt to develop a quantitative description of the action of the forcing, we define integrals over the control region to study the net influence on the flow:

$$Q(t) = \int_C q(x,t) dC. \quad (7)$$

Figure 7 shows the history of the net energy, velocity and control forcing in the control region. We see no correlation between the forcing and integrated flow variables in the control region. We anticipate that there must be some correlation, but more data will be needed to study its statistics if it is at all possible. The flat part at the end of the forcing history is caused by the time delay between the control and the target. Control in that flat piece would not alter J on the target line in $t_0 < t < t_1$.

Flow Field Change

Despite the large decrease in the radiated sound, the mixing layer flow is changed surprising little by the control. Figure 8 shows the spreading of the mixing layer in terms of its momentum thickness,

$$\delta_m = \int_{-\infty}^{+\infty} \frac{\rho(u - U_1)(U_2 - u)}{\rho_\infty \Delta U^2} dy. \quad (8)$$

We see that the control changes its downstream evolution only slightly. The waviness of the profiles is believed to be due to the limited statistical sample in the t_0 to t_1 simulation time, but might also be due to the nature of the parings which is known to cause jumps in thickness.

The turbulence kinetic energy, defined as

$$k = \frac{1}{2} \rho [(u')^2 + (v')^2], \quad (9)$$

where u' and v' are fluctuation of velocities, is also nearly unchanged. Figure 9 shows

$$K_x(x) = \int_{-50\delta_\omega}^{50\delta_\omega} k dy \quad (10)$$

and

$$K_y(y) = \int_0^{60\delta_\omega} k dx \quad (11)$$

with and without control. The noise reduction is clearly not due to turbulence suppression. Previously,⁹ we also show that there is little change in how the energy is arranged in large turbulent structures. Only a slight change in their phasing was observed.

Conclusion

An adjoint-based approach has been developed that reduces the noise radiated by a two-dimensional mixing layer by 6.3dB along a specified line in the far-field.

The changes of the flow field due to the control forcing are relatively minor, which is possible because only a small fraction of the flow's energy, that with a supersonic phase velocity, radiates. Our simulations indicate that, at least in a two-dimensional mixing layer, this part can be altered with minimal control authority to dramatically reduce the noise.

The control forcing itself is non-intuitive and the correlations between it and other flow properties are not clear yet. Work continues identifying practical control laws and understanding the details of how the present control works.

Acknowledgment

We gratefully acknowledge the financial support of AFOSR and the computer resources provided by NPACI and NCSA.

References

- ¹Lighthill, M. J., "On sound generated aerodynamically: I. General theory," *Proc. Royal Soc. Lond. A*, Vol. 211, 1952, pp. 564-587.
- ²Colonius, T., Lele, S. K., and Moin, P., "Sound generation in a mixing layer," *J. Fluid Mech.*, Vol. 330, 1997, pp. 375-409.
- ³Mitchell, B. E., Lele, S. K., and Moin, P., "Direct computation of the sound generated by vortex pairing in an axisymmetric jet," *J. Fluid Mech.*, Vol. 383, 1999, pp. 113-142.
- ⁴Freund, J. B., Lele, S. K., and Moin, P., "Direct numerical simulation of a Mach 1.92 turbulent jet and its sound field," *AIAA J.*, Vol. 38, No. 11, 2000, pp. 2023-2031.
- ⁵Freund, J. B., "Noise sources in a low-Reynolds-number turbulent jet at Mach 0.9," *J. Fluid Mech.*, Vol. 438, 2001, pp. 277-305.
- ⁶Lilley, G. M., "Jet Noise: Classical theory and experiments," In *Aeroacoustics of Flight Vehicles* edited by H. Hubbard. NASA RP 1258, 1991.
- ⁷Saiyed, N. H., Mikkelsen, K. L., and Bridges, J. E., "Acoustics and thrust of separate flow exhaust nozzles with mixing devices investigated for high bypass ratio engines," 6th AIAA/CEAS Aeroacoustics Conference, Lahaina, AIAA Paper 2000-1961, 2000.
- ⁸"Separate Flow Low Noise Nozzle Project," Nasa Aerospace Technology News, Volume 1, Issue 2, September 2000.
- ⁹Wei, M. and Freund, J. B., "Optimal control of free shear flow noise," 40th Aerospace Sciences Meeting, Reno, NV, AIAA Paper 2002-0665, January 2002.
- ¹⁰Bewley, T. R., Moin, P., and Temam, R., "DNS-based predictive control of turbulence: an optimal benchmark for feedback algorithms," *J. Fluid Mech.*, Vol. 477, 2001, pp. 179-225.
- ¹¹Press, W. H., Flannery, B. P., Teukolsky, S. A., and Vetterling, W. T., *Numerical Recipes*, Cambridge, 1986.

- ¹²Lele, S. K., "Compact finite difference schemes with spectral-like resolution," *J. Comp. Phys.*, Vol. 103, 1992, pp. 16-42.
- ¹³Tam, C. K. W. and Webb, J. C., "Dispersion-relation-preserving finite difference schemes for computational acoustics," *J. Comp. Phys.*, Vol. 107, No. 2, Aug 1993, pp. 262-281.
- ¹⁴Freund, J. B., "A proposed inflow/outflow boundary condition for direct computation of aerodynamic sound," *AIAA J.*, Vol. 35, No. 4, 1997, pp. 740-742.
- ¹⁵Giles, M. B., "Nonreflecting boundary conditions for Euler equations calculations," *AIAA J.*, Vol. 18, 1990, pp. 2050-2058.
- ¹⁶Monkewitz, P. A. and Huerre, P., "Influence of the velocity ratio on the spatial instability of mixing layers," *Phys. Fluids*, Vol. 25, 1988, pp. 1137-1143.
- ¹⁷Ho, C. M. and Huerre, P., "Perturbed free shear layers," *Ann. Rev. Fluid Mech.*, Vol. 16, 1984, pp. 365-424.
- ¹⁸Sandham, N. and Reynolds, W., "Three-dimensional simulations of large eddies in the compressible mixing layer," *J. Fluid Mech.*, Vol. 224, 1991, pp. 133-158.
- ¹⁹Day, M. J., Reynolds, W. C., and Mansour, N. N., "The structure of the compressible reacting mixing layer: Insights from linear stability analysis," *Phys. Fluids*, Vol. 10, 1998, pp. 993-1007.

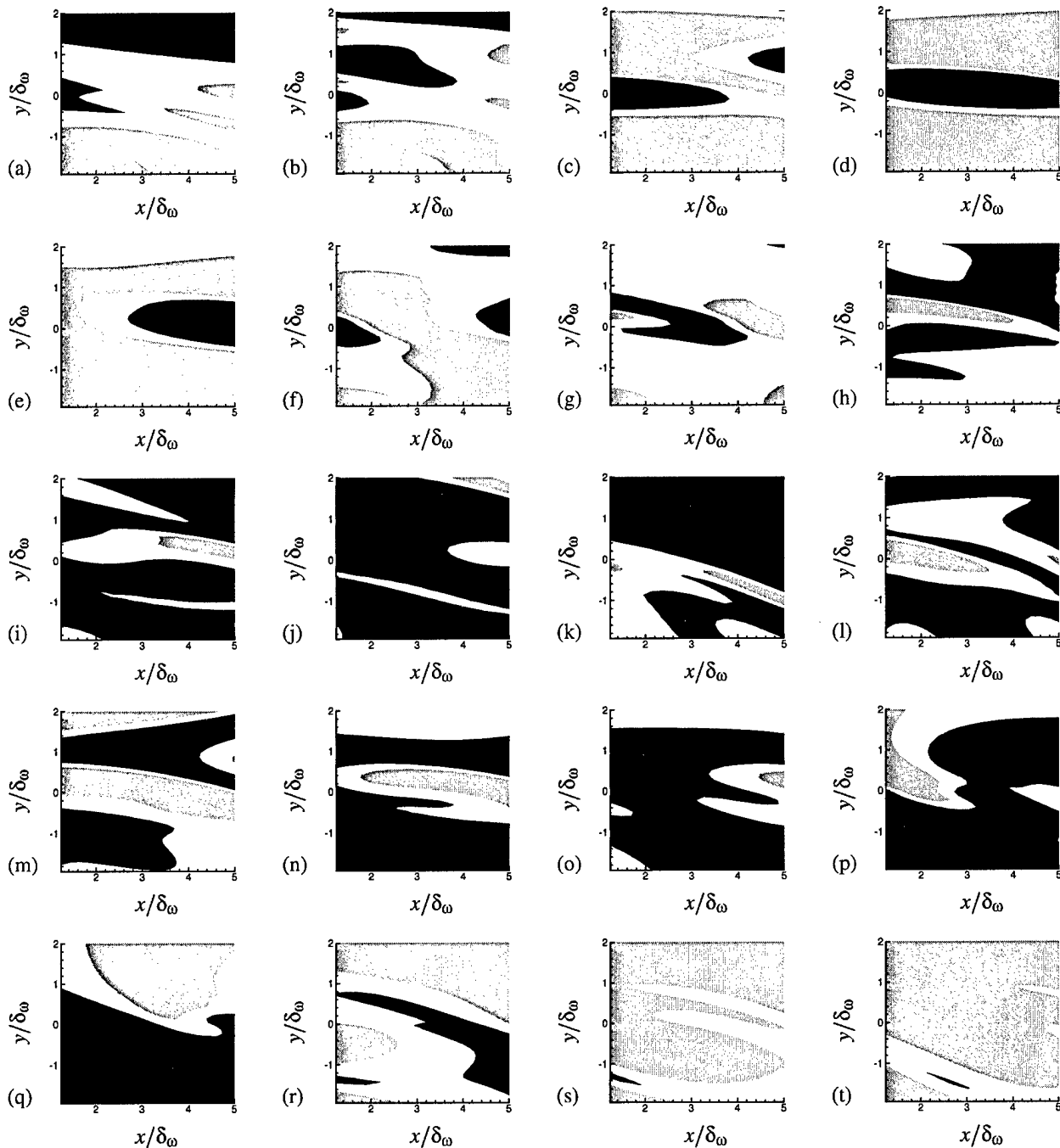


Fig. 6 Control forcing: (a) $t = 0$, (b) $t = 5\delta_\omega/a_\infty$, (c) $t = 10\delta_\omega/a_\infty$, (d) $t = 15\delta_\omega/a_\infty$, (e) $t = 20\delta_\omega/a_\infty$, (f) $t = 25\delta_\omega/a_\infty$, (g) $t = 30\delta_\omega/a_\infty$, (h) $t = 35\delta_\omega/a_\infty$, (i) $t = 40\delta_\omega/a_\infty$, (j) $t = 45\delta_\omega/a_\infty$, (k) $t = 50\delta_\omega/a_\infty$, (l) $t = 55\delta_\omega/a_\infty$, (m) $t = 60\delta_\omega/a_\infty$, (n) $t = 65\delta_\omega/a_\infty$, (o) $t = 70\delta_\omega/a_\infty$, (p) $t = 75\delta_\omega/a_\infty$, (q) $t = 80\delta_\omega/a_\infty$, (r) $t = 85\delta_\omega/a_\infty$, (s) $t = 90\delta_\omega/a_\infty$, (t) $t = 95\delta_\omega/a_\infty$. **Black indicates the positive forcing ($> 0.01\rho_\infty a_\infty^3/\delta_\omega$), and gray indicates the negative forcing ($< 0.01\rho_\infty a_\infty^3/\delta_\omega$).**

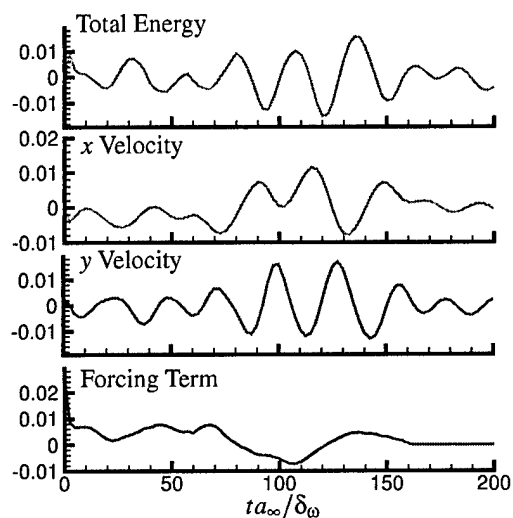


Fig. 7 History of integrals inside the control region.

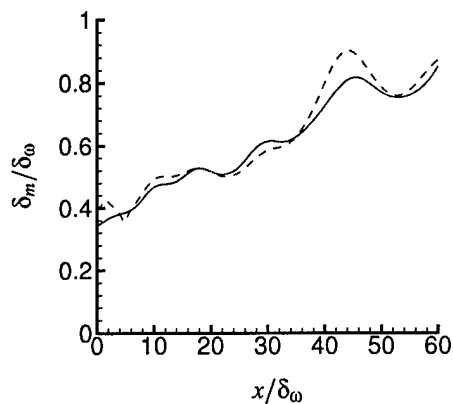


Fig. 8 Change of the momentum thickness of the mean flow:
— without control; ---- with control.

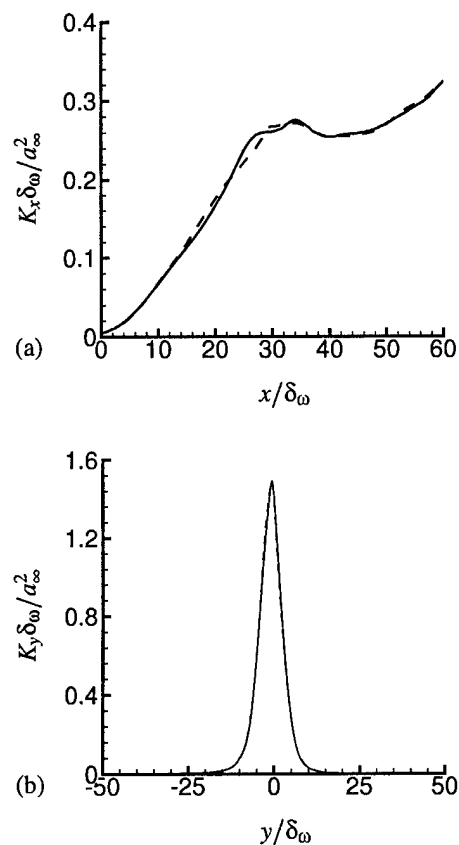


Fig. 9 Comparison of integrated turbulence kinetic energy as defined in (a) equation (10) and (b) equation (11). The lines indicate the case without control — and the case with control ----.

Aeroacoustic optimization and control

A summary of work performed at UC San Diego under AFOSR contract F49620-01-1-0048

by Thomas R. Bewley, *Flow Control Lab, Dept. of MAE, UC San Diego*

1 January 2003

During the past three years, the Flow Control Lab at UC San Diego, under the direction of Prof. Bewley, has developed and refined advanced adjoint-based tools for the analysis, optimization, and control of complex nonlinear dynamics in canonical turbulent flow systems. In particular, under the present funding, our core focus has been on the adjoint analysis of sound production in a compressible turbulent jet. This report will briefly summarize our primary accomplishments on this core effort and also review some closely related investigations which have been spawned by this effort.

1 Core focus

The focus of this work is the reduction of noise emanating from a compressible round jet. This study is motivated by the Air Force problem of the reduction of both personnel hazards and structural fatigue due to heightened sound pressure levels in the vicinity of operating jet engines. An introduction to the jet noise control problem is given in Figure 1.

In prior work, Prof. Freund developed a Direct Numerical Simulation (DNS) code which captures the production of sound in a compressible turbulent jet from first principles. Though this code has been well validated against experimental measurements, it is difficult to glean from the massive numerical databases which this code produces an adequate low-order physical explanation of the dominant jet noise production mechanisms. For this reason, the present effort has focused on the perturbation and adjoint analysis of the simulation databases produced by Prof. Freund's jet noise code. The distinction between perturbation and adjoint analyses, and the reason one is particularly interested in the latter for the optimization of high-dimensional control distributions for turbulent flow systems which exhibit complex nonlinear dynamics, is illustrated in Figures 2 and 3. The motivation for using adjoint analysis in the compressible jet noise reduction problem

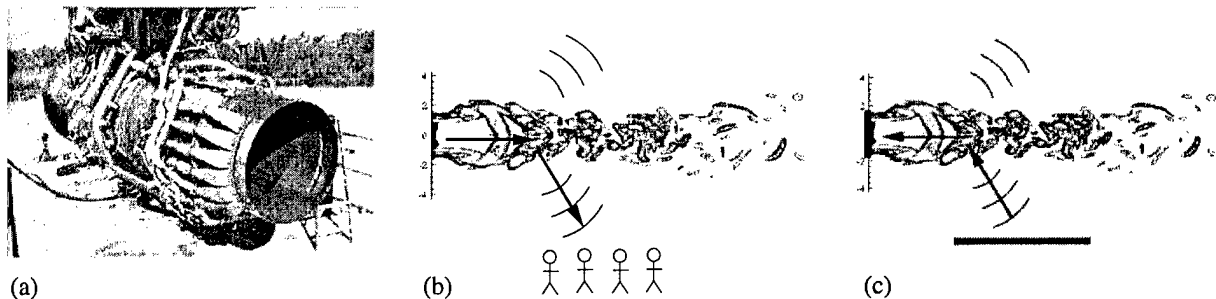


Figure 1: Introduction to the jet noise control problem. (a) A prototypical application: a Pratt & Whitney JT8D engine with high-pressure compressor air ducted to the jet nozzle to provide on-demand active control of the jet exhaust near the nozzle lip. The rig shown here is designed for mixing enhancement; it is anticipated that effective actuators for the purpose of jet noise reduction, once optimized, might be an order of magnitude smaller. (b) The control problem: the turbulent break-up of the jet core radiates a large amount of noise. Though this flow may be simulated accurately with Direct Numerical Simulation (DNS) techniques, the physics of this noise generation is still poorly understood. We wish to reduce the noise that radiates toward a particular observation region based on our accurate high-order DNS system model even in the absence of an adequate low-order physical explanation of the dominant jet noise production mechanisms. (c) The adjoint analysis: by targeting the noise in the observation region in a DNS of the jet system, an adjoint analysis provides gradient information which can be used to optimize the space/time schedule of control forcing at the jet nozzle.

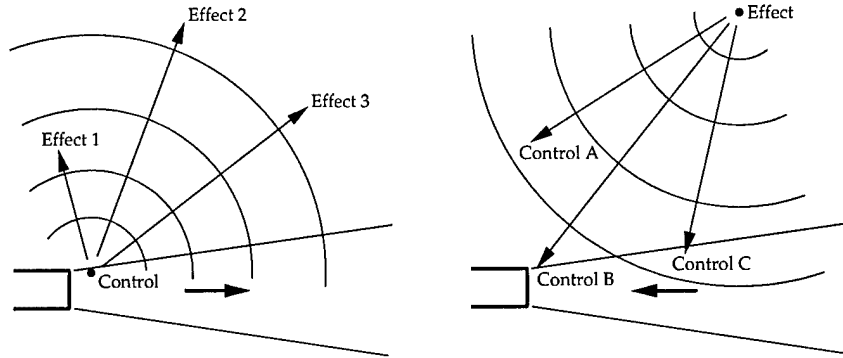


Figure 2: Perturbation analysis (left) and adjoint analysis (right) of the jet system.

Note that **perturbation analyses** characterize **control** \rightarrow **effect** relationships:

- *If I change the control here, how, when, & where will that effect the flow?*

On the other hand, **adjoint analyses** characterize **effect** \rightarrow **control** relationships:

- *If I want to achieve a desired effect here, how, when, & where should I apply control to the flow?*

The answer to the latter question is of particular interest when a high-dimensional forcing schedule for a complex system, such as that coordinating several actuators to modify the turbulent break-up of a jet exhaust (see Figure 1a), is being optimized to achieve a desired effect, such as the reduction of radiated noise in a particular direction (see Figure 1b).

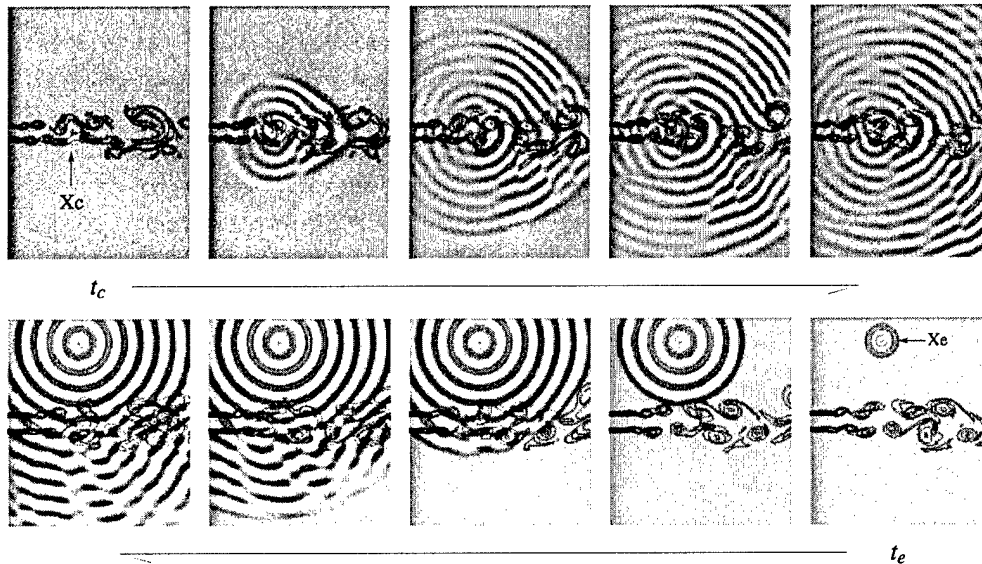


Figure 3: **Perturbation analysis** (top) characterizes the effect on the entire flow resulting from a small change to a particular control quantity, taken here to be a sinusoidally-varying mass source at point x_c . **Adjoint analysis** (bottom) characterizes the effect on a particular flow quantity, taken here to be high frequency noise at point x_e , due to small changes in the control applied anywhere in the flow. Note that a perturbation analysis involves marching the governing equation forward in time, whereas an adjoint analysis involves marching the corresponding adjoint equation backward in time.

is similar to the motivation for using adjoint analysis in the incompressible wall-bounded flows which the UCSD Flow Control Lab is studying under separate funding. However, the details involved in the compressible jet case have proven to be much more involved. In particular, the jet noise problem requires highly accurate cylindrical-coordinate compressible flow, perturbation, and adjoint solvers with appropriate treatment of the coordinate singularity at the centerline and the appropriate modeling of the “ambient” inflow and outflow boundary conditions around the entire flow domain. These numerical issues are extremely delicate, and have been examined in detail in collaboration with Profs. Jonathan Freund

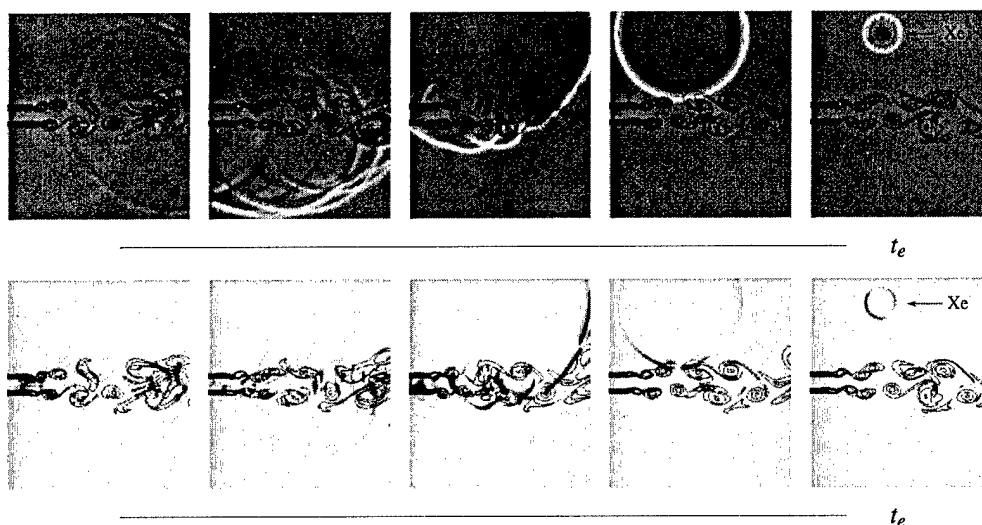


Figure 4: Adjoint analysis indicates not only when and where control may be applied to achieve the desired effect, but also to which component of the governing equation. In the simulation shown above, the **adjoint density** (top) and **adjoint pressure** (bottom) reveal the sensitivity of the radiated noise (the pressure component of the far-field perturbation) at point x_e and time t_e to additional forcing of, respectively, the energy equation (top) and the continuity equation (bottom) everywhere in space x_c and for all times $t_c < t_e$ in a 2D simulation of the jet system. Note that the disturbance in the adjoint pressure grows rapidly as it propagates within the jet towards the nozzle at the convective velocity as the adjoint field evolves (in backwards time). In contrast, the disturbance in the adjoint density essentially propagates right through the jet, experiencing significant refraction but not slowing to propagate at the convective speed of the jet within the jet shear layers. This indicates that mass sources are more efficient than energy sources in modifying the hydrodynamic field (at low temporal frequencies) in a way which changes the radiated noise (at high temporal frequencies).

and Sanjiva Lele in the present study. Details concerning our recent accomplishments in this collaborative effort may be found in Cerviño, Bewley, Freund, & Lele (2002) and Cerviño & Bewley (2002), which are attached as supplements to the present report. To summarize these supplements briefly, our 3D compressible cylindrical-coordinate perturbation and adjoint solvers have been written and thoroughly tested on 2D jet flows. A representative adjoint simulation which effectively provides an unsteady adjoint Greens function for the present problem (in 2D) is illustrated in Figure 4. We are currently testing these codes in the 3D setting.

It is important to note that, contrary to our understanding of this analysis approach at the outset of this investigation (and in our original proposal on this topic), it was found that adjoint analyses do *not* accurately identify the “source” of the radiated noise in such a system. Rather, they identify how, when, and where additional “control” forcing may be applied to the existing system to modify the radiating noise already present in a desired manner. This distinction between noise “sources” (which adjoint analyses do *not* identify) and sensitivity to additional “control” forcing (which adjoint analyses do identify) is quite important in the proper interpretation of the present work.

2 Related activities

The jet noise reduction problem which we have chosen to study in this work is itself of important engineering interest. In addition, this problem brings to light many generic issues which are to be expected when the adjoint analysis procedure is extended to other turbulent flow systems in the future. We therefore believe the present study will have a fundamental impact well beyond the analysis of the present jet noise database. We summarize below three of the more fundamental investigations recently performed by our lab which have been spawned by issues that have arisen in our investigation of

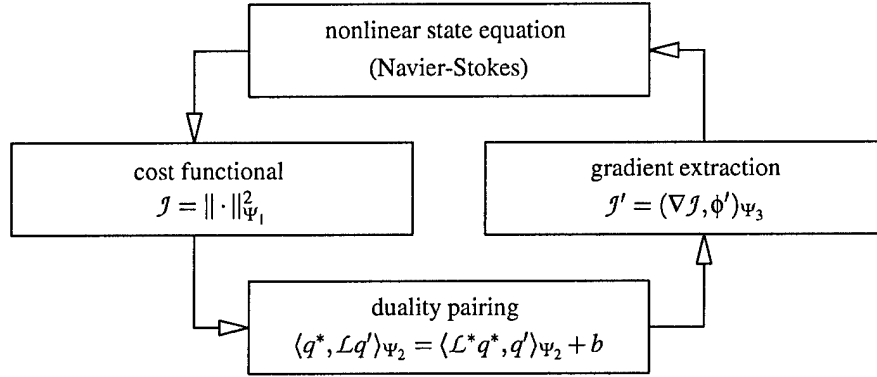


Figure 5: The four essential components of the adjoint-based optimization process of a multiscale PDE system. Each component of this process is associated with a distinct opportunity for regularization.

the jet noise control problem. We do not have any funding for any of these three efforts; they have been conducted by our lab using a small amount of the present funding together with other discretionary funding because they relate directly to our core focus problem, and will hopefully grow into funded efforts in the future so that they can be explored in greater detail.

2.1 Regularization of adjoint analysis

In the course of performing adjoint analyses of the jet noise system, we have been forced to grapple with subtle issues related to the multiscale nature of the dynamical systems under consideration. Turbulent flows are characterized by a nonlinear cascade of energetic motions over a broad range of length scales and time scales. Though much attention has been paid to the appropriate treatment of this so-called energy cascade in the turbulence simulation literature, much less is known about how to deal with it appropriately in the adjoint analysis of turbulent flow systems. Our lab has recently completed an extensive and fundamental study of this issue on a representative multiscale 1D model problem, identifying a comprehensive framework which encompasses and interrelates *all* of the regularization opportunities available, as indicated in Figure 5. Full details concerning this comprehensive framework are laid out in Protas, Bewley, & Hagen (2002), which is attached as a supplement. We are currently working to leverage and refine this new understanding of how to reframe adjoint analyses to properly treat multiscale turbulent flow systems of both fundamental and engineering interest, such as the present problem of the reduction of jet noise.

2.2 Quantifying the stabilizability of the linear modes of the system

In order to better understand the jet flow system and how it may be modified by control input, it is quite useful to quantify the degree to which the least-stable eigenmodes of the linearized system may be affected by control input at the actuators. The adjoint machinery developed in the present investigation is precisely the right tool for this purpose. In order to clarify how this may be done, we have completed an extensive study of the stabilizability of the linear complex Ginzburg-Landau (CGL) model problem. This study is reported in Lauga & Bewley (2003), which is attached as a supplement. In the CGL model system, the open-loop system eigenfunctions and adjoint eigenfunctions are available analytically. The extension of this approach to a DNS approximation of a dynamical system, in which the eigenfunctions and adjoint eigenfunctions are not available analytically, is straightforward using the implicitly-restarted Arnoldi method to determine the leading eigenvectors and adjoint eigenvectors. This analysis is currently being applied to the DNS jet code by a new post-doc in our lab.

2.3 Control of periodic orbits

A chaotic attractor is well described by its embedded periodic orbits. A strategy for the jet noise control problem which poses an attractive alternative to iterative time-evolving simulations (which are very costly computationally) is to design controls such that the embedded periodic orbits of the chaotic attractor of the turbulent flow have favorable properties (that is, low noise in the region of interest). If this (perhaps simpler) goal can be attained, the associated turbulent flow should have the same favorable properties. The difficulty with posing the jet noise control problem in this setting is that there are, in general, *many* solutions and approximate solutions to nonlinear dynamic systems in the time-periodic setting, even though the solution in the time-evolving setting (that is, from known initial conditions) is unique. Thus, one is left with a question of *which* time-periodic solution one should design the controls for, and *how* can one find this time-periodic solution? Our lab has come up with a natural and elegant solution to this problem: design for the worst case in the spirit of a noncooperative game. That is, find the best controls for the worst (of the several) time-periodic flow solutions. This may be found by an appropriate sequence of approximations, which allows both the controls and the worst solution to be identified with a gradient-based algorithm. Bewley & Trenchea (2002), which is attached as a supplement, lays the mathematical foundation for this approach, which might well provide an optimization algorithm for quasi-periodic turbulent flow systems which is significantly cheaper computationally than the standard (time-evolving) approach.

3 Publications and presentations

Prof. Bewley has given numerous conference talks and departmental seminars, to both fluids audiences and controls audiences, highlighting the present work. In the calendar year 2002, Prof. Bewley gave 17 major talks and seminars, including a full-day minicourse on Flow Control (in Madrid, Spain) sponsored by the NATO RTO Consultants & Exchange Program and two large plenary lectures, one at the Ninth European Turbulence Conference (in Southampton, U.K.), and one at the Third Symposium on Smart Control of Turbulence (in Tokyo, Japan). The papers from these two plenary lectures [Bewley (2002) and Bewley & Protas (2002)], as well as other related publications, are available at the UCSD Flow Control Lab's web page: <http://turbulence.ucsd.edu/references.html>.

References

- [1] CERVIÑO, L.I., BEWLEY, T.R., FREUND, J.B., & LELE, S.K. (2002) Perturbation and adjoint analyses of flow-acoustic interactions in an unsteady 2D jet. *Center for Turbulence Research, Proceedings of the Summer Program 2002*. (Journal version under preparation.)
- [2] CERVIÑO, L.I., & BEWLEY, T.R. On the extension of the complex-step derivative technique to pseudospectral algorithms. *Journal of Computational Physics*, submitted.
- [3] PROTAS, B., BEWLEY, T.R., & HAGEN, G. A comprehensive framework for the regularization of adjoint analysis in multiscale PDE systems. *Journal of Computational Physics*, submitted.
- [4] LAUGA, E., & BEWLEY, T.R. (2003) The decay of stabilizability with Reynolds number in a linear model of spatially developing flows. *Proc. Roy. Soc.*, to appear.
- [5] BEWLEY, T.R., & TRENCH, C. (2002) Noncooperative optimizations of controls for time-periodic Navier-Stokes systems with multiple solutions. *AIAA 2002-2754*. (Journal version under preparation.)
- [6] BEWLEY, T.R. (2002) The emerging roles of model-based control theory in fluid mechanics. *Advances in Turbulence IX, Proceedings of the Ninth European Turbulence Conference*.
- [7] BEWLEY, T.R., & PROTAS, B. (2002) Skin friction and pressure: the "footprints" of turbulence. *Proceedings of the Third Symposium on Smart Control of Turbulence, Tokyo*.

Perturbation and adjoint analyses of flow-acoustic interactions in an unsteady 2D jet

By L. I. Cerviño[†], T. R. Bewley[†], J. B. Freund[‡], AND S. K. Lele

It is well known that noise sources embedded in a jet produce sound fields which refract due to the presence of the flow. The refraction due to the mean flow has been appreciated and modeled for some time, but only occasionally is the significant refractive effect of the unsteadiness of the flow acknowledged. In the present work, perturbation and adjoint analyses of high-frequency acoustic fluctuations are performed in a numerical simulation of a cold 2D jet system at a Mach number of $M = 0.5$ and a Reynolds number based on the jet diameter of $Re_D = 5000$. The jet system is hydrodynamically excited into a sinuous mode near the jet exit at a Strouhal number of $St = 0.4$, and exhibits the classical vortex roll-up phenomenon. Acoustic perturbations to this flow system are analyzed at Strouhal numbers of $St = 0.8$, $St = 2$, and $St = 8$ (that is, $2\times$, $5\times$, and $20\times$ the vortex roll-up frequency). It is found that the unsteady effects of the flow cause a significant frequency broadening in both the perturbation and adjoint analyses.

1. Introduction

The problem of jet noise has significant engineering consequences. The far-field noise radiated by an unsteady flow system may be computed directly from a highly-accurate simulation of the compressible Navier-Stokes equation, or may be extracted from an approximate compressible flow simulation using any of several “acoustic analogies”, including the celebrated Lighthill and Lilley equations. Despite their elegance and the fact that they are exact expressions, such acoustic analogies generally fail to isolate the true “sources” of far-field noise from significantly stronger noise “sources” which almost completely destructively interfere and radiate relatively little energy to the far field, as with the so-called quadrupole noise sources in a turbulent jet.

In order to better understand the physics of far-field noise and how it may be controlled, the present investigation represents one in a series of efforts to interrogate numerical databases, which capture the production of far-field sound directly, by accurate simulations of the compressible Navier-Stokes equation. The present paper focuses on the significance of acoustic scattering due to unsteady vortex roll-up in the perturbation and adjoint analyses central to this investigation.

There have been several previous investigations aimed at analyzing the effects of refraction in perturbation and adjoint analyses due to the presence of the flow. Many of them, however, consider the governing equations only after they have been linearized about the mean flow. For example, Durbin (1983a, 1983b) derived a high-frequency Green’s function from an idealized steady jet profile. Tam & Auriault (1998) obtained an adjoint Green’s function, using a steady jet profile obtained from a RANS calculation, and related it to the corresponding Green’s function of the acoustic field at a particular point in the flow field due to additional localized sources embedded within the jet.

[†] Univ. of California, San Diego

[‡] Univ. of Illinois, Urbana-Champaign

In a turbulent flow, however, acoustic phenomena are closely related to system unsteadiness. This was characterized in Freund & Fleischman (2001), where a refraction analysis was performed by means of ray tracing. It was observed that, when a noise source was located within the laminar jet core, the difference in the directivity calculated by the mean flow analysis and the unsteady flow analysis was rather small. However, when the source was placed farther downstream on the jet axis, the rays in the mean flow were significantly refracted by the unsteady jet shear layers, and the time average of the unsteady analysis was completely different than the corresponding analysis of the mean flow. Suzuki & Lele (1999) and Suzuki (2001) performed Green's function analyses in unsteady 2D mixing layers and boundary layers and analyzed the effects of acoustic scattering. The interaction between incoming plane waves at various angles of incidence with the unsteady vortices in the flows were investigated in detail, and the results compared with the ray-tracing procedure. A significant broadening of the frequency content of the acoustic wave after it passed through the mixing layer was observed, indicating significant flow-acoustic interaction. The present paper extends these lines of investigation with perturbation and adjoint analyses of cold 2D jets.

1.1. Approach

As mentioned in the Abstract, the flow system considered in this work is a Mach 0.5 cold 2D jet at a Reynolds number $Re_D = \rho D U_j / \mu = 5000$ with sinusoidal excitation near the jet exit at $S_t = f_0 D / U_j = 0.4$. Refraction effects are expected to be significantly weaker in a cold jet than in a hot jet, as the speed of sound is identical in the ambient fluid and the jet core. In fact, in sharp contrast with the perturbation and adjoint analyses of the mean of a heated jet as considered by Tam & Auriault (1998), the corresponding analyses of the refraction due to the mean of the cold jet flow studied here exhibit very little refraction. Nevertheless, as shown in this paper, the acoustic scattering due to the unsteady vortex roll-up in the present flow is quite pronounced even in this cold jet system, illustrating significant opportunities to force the hydrodynamic field (at low frequencies) in order to modify the high-frequency radiated noise.

The simulation code used in the present work implements the full compressible Navier-Stokes equation using a numerical method based closely on that developed by Freund, Moin, & Lele (1997). The present simulations do not resolve any solid boundaries. Instead, artificial "buffer zones" have been used around the domain of physical interest, coupled with characteristic-based boundary conditions on the computational boundaries. This type of *ad hoc* but effective numerical boundary conditions simulates the effect of quiescent far-field boundary conditions on the physical system, and has now become standard for this type of problem. It is discussed further in, e.g., Freund (1997) and Colonius, Lele, & Moin (1993).

As summarized in Figure 1, two types of analyses are considered in the present work. In sec. 2, perturbation analyses of the flow field are performed in order to obtain a characterization of the propagation of disturbances in the system as it evolves forward in time. In these analyses, artificial RHS forcing (to be referred to in this paper as the "control") is introduced into the jet system, and the resulting perturbation to the flow which is introduced by this forcing is computed. As depicted in Figure 1, such analyses characterize **control**→**effect** relationships. A representative perturbation analysis of the present system is shown in the top row of Figure 2.

In sec. 3, adjoint analyses of the flow field are performed in order to characterize the sensitivity of a particular metric measuring the flow system to additional forcing of the governing equations. In these analyses, an "adjoint system" is defined and computed in

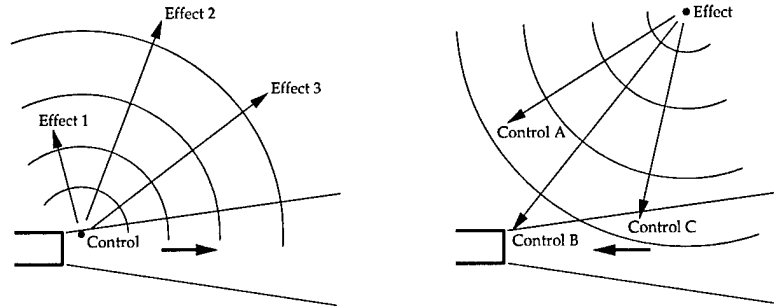


FIGURE 1. Perturbation analysis (left) and adjoint analysis (right) of the jet system.

Note that **perturbation analyses** characterize **control** \rightarrow **effect** relationships:

- If I change the “control” here, how and where will that affect the flow?

On the other hand, **adjoint analyses** characterize **effect** \rightarrow **control** relationships:

- If I want to achieve a desired effect here, how and where should I apply “control” to the flow?

The answer to the latter question is of particular interest when a high-dimensional forcing schedule for a complex system, such as a turbulent jet exhaust, is being optimized to achieve a desired effect, such as the reduction of radiated noise in a particular direction. Note that adjoint analyses do NOT identify the “source” of the radiated noise in such a system. Rather, they identify how and where additional forcing may be applied to the existing system to modify the radiating noise already present in a desired manner.

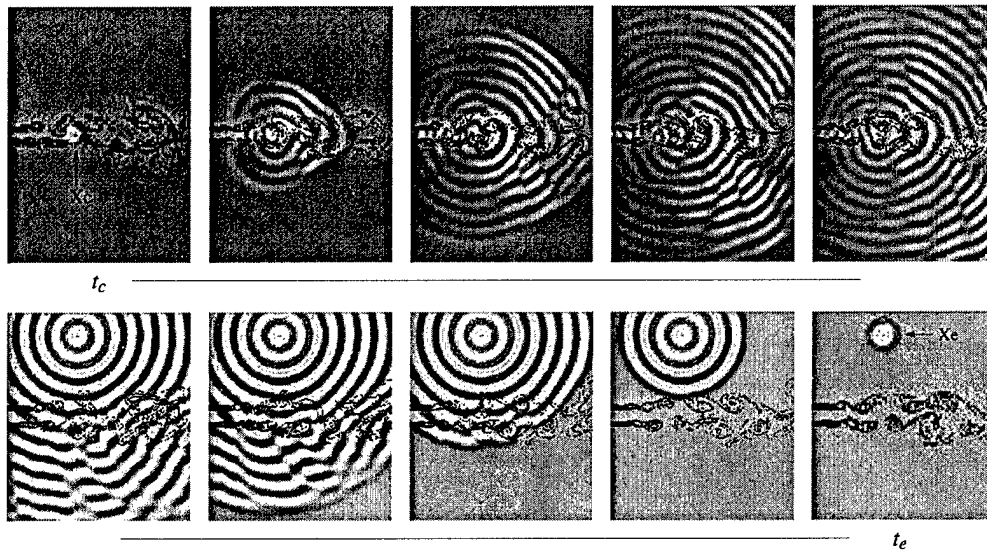


FIGURE 2. **Perturbation analysis** (top) characterizes the effect on the entire flow resulting from a small change to a particular “control” quantity, taken here to be a sinusoidally-varying mass source at point x_c . **Adjoint analysis** (bottom) characterizes the effect on a particular flow quantity, taken here to be high frequency noise at point x_e , due to small changes in the “control” applied anywhere in the flow. Note that a perturbation analysis involves marching the governing equation forward in time, whereas an adjoint analysis involves marching the corresponding adjoint equation backward in time.

order to identify the gradient of a “cost function” (which mathematically quantifies the metric of interest) to additional forcing of the jet system. As depicted in Figure 1, such analyses characterize **effect** \rightarrow **control** relationships. A representative adjoint analysis of the present system is depicted in the bottom row of Figure 2.

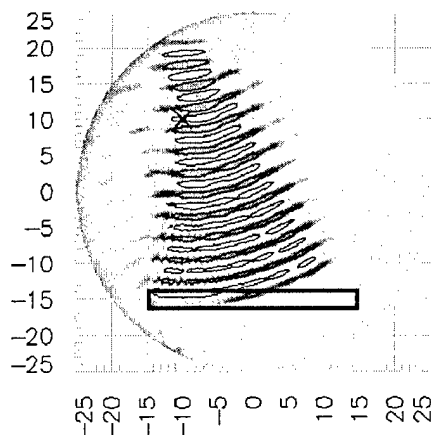


FIGURE 3. Adjoint analysis of sound waves, produced by a monopole sound source at the point marked by the X, in a stationary fluid. In the problem depicted here, the desired effect is to reduce the intensity of the sound field in the “interrogation region” outlined by the rectangular box. The corresponding adjoint field is driven by the sound waves in the box and propagates away from it, as visualized above, illustrating possible locations for “antinoise” sources where additional forcing could be applied to achieve the desired effect (namely, to reduce the sound pressure level within the box). Even though the governing system represented here is a linear, constant-coefficient PDE and the cost function is quadratic in the state variables, the adjoint field identifies a range of effective “antinoise” forcing locations, and does not accurately identify the isolated sound source. Note that the focusing of the adjoint field on the isolated sound source is found to improve when the size of the box is increased as compared with the wavelength of the sound.

It is important to note that adjoint analyses do *not* identify the “origin” or “source” of the radiated sound in such a system. This point is readily evident by considering a simpler model system (without the jet present), as depicted in Figure 3. Thus, identification of sound “sources” is not to be expected from adjoint analyses when applied to more complex systems, such as the unsteady jet considered in the present work.

Note that, in the remainder of the present work, the cost functions considered are essentially pointwise measures of the sound field, and the adjoint field computations are therefore referred to as “adjoint Green’s functions”.

2. Perturbation analyses

A logical starting place for this investigation is to assess the effects of hydrodynamic unsteadiness (that is, vortex roll-up) on small perturbations to the flow system. In particular, we will investigate the scattering of low-amplitude acoustic waves as they pass through the unsteady jet system. In order to perform a perturbation analysis of this sort, one approach is to calculate numerically the linearized (“perturbation”) equations. The code used to solve such a problem is often referred to as a “tangent linear” code. With this approach, the perturbation field is obtained directly.

An alternative “finite-difference” approach allows us to calculate the perturbation field using the nonlinear flow solver itself, without writing a separate tangent linear code. This is achieved by computing a “nominal” flow, computing a second “perturbed” flow (with the appropriate small perturbation applied to the initial conditions, the boundary conditions, or the right-hand-side forcing), and taking their difference, dividing by the

perturbation amplitude ϵ . In fact, in the $\epsilon \rightarrow 0$ limit, this is how we define the so-called “perturbation field”. However, as a computational strategy, this approach presents certain difficulties. If ϵ is made too small, the finite-precision arithmetic of the computer leads to differencing errors, as the two fields being compared are almost identical. On the other hand, if ϵ is made too large, the “small” perturbation assumption breaks down, and ϵ^2 terms in the Taylor series expansion begin to become significant. In practice, selecting an appropriate value of ϵ to minimize the sum of these spurious effects is difficult. Though higher-order finite-difference approximations of the perturbation field can be proposed, they are also plagued by the competition of these two spurious effects.

In order to circumvent the difficulties cited above associated with selecting ϵ in a finite-difference approximation of the perturbation field, an alternative approach, referred to as the Complex Step Derivative (CSD) method, has been developed (Lyness & Moler (1967); Squire & Trapp (1998)). This method has already been applied broadly in the optimization literature (see, e.g., Martins, Sturdza, & Alonso (2001)). The basis of this method is to redefine all of the real variables in the system as complex, and to perform the nominal (real) simulation as before while introducing the small perturbation into the imaginary part of the system. It can be shown by a straightforward Taylor-series expansion of the complex fields which result that, to order ϵ^2 , the real part of the resulting field contains the nominal flow and the imaginary part (divided by ϵ) contains the perturbation field sought. Further, this calculation is not plagued by the “difference of large numbers” problem, so ϵ may be made very small without inducing differencing errors in the calculation of the perturbation field. This provides an extremely accurate technique for computing a perturbation analysis when the simulation code nominally involves only real arithmetic (as is the case with the present 2D simulations), and is the approach selected in the present computations[†].

The result of a representative perturbation analysis is shown in the top row of Figure 2. A localized mass source which oscillates sinusoidally in time (at five times the vortex roll-up frequency of the jet) has been introduced in the jet at point x_c . This has been accomplished by adding a forcing term to the right-hand side of the continuity equation. The addition of this forcing excites an acoustic wave, which is significantly refracted by the unsteady vortex roll-up. Mean-flow analyses, of course, fail to capture such scattering, which is due to the unsteadiness of the flow.

It is also straightforward to characterize acoustic waves coming from the far field. Computationally, the approach is slightly different: unsteady forcing is used along a line within the non-physical “buffer zone”, and particular care must be exercised to avoid spurious effects in the corner regions of the computational domain. Physically, however, the result is qualitatively similar, and significant scattering is encountered when the acoustic field passes through the unsteady jet, as shown in Figure 4.

[†] In fact, it is interesting to note that it is straightforward to extend the CSD method to pseudospectral codes which nominally employ complex arithmetic. This approach was investigated briefly during the CTR summer program, and is reported in Cerviño & Bewley (2002). Unfortunately, the FFT's used in such pseudospectral extensions of the CSD approach combine the nominal (real) and perturbation (imaginary) parts of the analysis, and thus the accuracy of this approach for computing the perturbation field is found to be not significantly better than the second-order finite-difference approach.

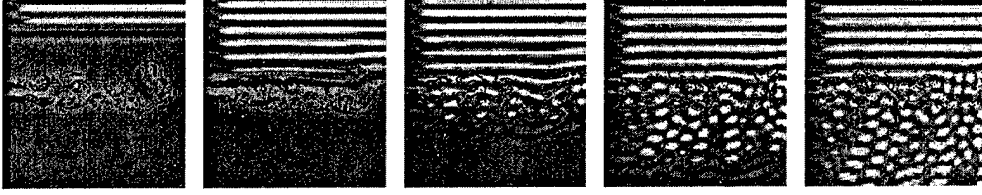


FIGURE 4. Perturbation analysis: refraction of pressure waves coming from the far-field by the unsteady 2D jet system

3. Adjoint analyses

The ultimate goal of the present research effort is to identify effective control strategies to reduce appropriate metrics of jet noise, extending the previous work reported by Wei & Freund (2002) of reducing the noise in a 2D mixing layer using a similar adjoint-based approach. Thus, though the perturbation analyses are qualitatively interesting, adjoint analyses contain significantly more relevant quantitative information related to our ultimate goal, and form the focus of the remainder of this study.

3.1. The adjoint operator

We now summarize briefly the adjoint formulation used in the present work. The continuous (PDE) description of the governing equation is first linearized and integrated by parts to obtain both an adjoint PDE operator useful in defining the adjoint field, and an identity that (once boundary conditions, initial conditions, and the right-hand-side forcing of the adjoint system are defined appropriately) may be used to express the required flow sensitivities in the continuous setting. As a final step before implementation in the numerical code, the state and adjoint equations are discretized in space and time in a consistent fashion.

We first define a state vector \mathbf{q} , a perturbation vector \mathbf{q}' , and adjoint vector \mathbf{q}^* as

$$\mathbf{q} = \begin{pmatrix} p \\ \rho \mathbf{u} \end{pmatrix} = \begin{pmatrix} p \\ \mathbf{m} \\ \rho \end{pmatrix}, \quad \mathbf{q}' = \begin{pmatrix} p' \\ \mathbf{m}' \\ \rho' \end{pmatrix}, \quad \mathbf{q}^* = \begin{pmatrix} p^* \\ \mathbf{m}^* \\ \rho^* \end{pmatrix}. \quad (3.1)$$

We may then denote the nondimensionalized full compressible Navier-Stokes equation for an ideal gas with constant specific heats c_p and c_v and constant Prandtl number Pr as

$$\mathcal{N}(\mathbf{q}) = 0, \quad (3.2)$$

where

$$\mathcal{N}(\mathbf{q}) = \begin{pmatrix} \frac{\partial \rho}{\partial t} + \nabla \cdot \mathbf{m} \\ \frac{\partial \mathbf{m}}{\partial t} + \nabla \cdot \frac{\mathbf{m} \otimes \mathbf{m}}{\rho} + \nabla p - \frac{1}{Re} \nabla \cdot \left(\mu \nabla \frac{\mathbf{m}}{\rho} \right) - \frac{1}{Re} \nabla \cdot \left[\mu \left(\frac{\mu_B}{\mu} + \frac{1}{3} \right) \nabla \cdot \frac{\mathbf{m}}{\rho} \right] \\ \frac{\partial p}{\partial t} + \nabla \cdot \frac{p \mathbf{m}}{\rho} + (\gamma - 1) p \left(\nabla \cdot \frac{\mathbf{m}}{\rho} \right) - \frac{\gamma}{Re Pr} \nabla \cdot \left(\mu \nabla \frac{p}{\rho} \right) - \Phi \end{pmatrix},$$

and Φ denotes the irreversible viscous dissipation term. Assuming appropriate expressions for μ and μ_B , the simulation code used in the present work implements the full compressible Navier-Stokes equation outlined above. In order to develop an adjoint solver, certain

additional approximations have been made, namely that $\mu = \text{constant}$, $\mu_B = \text{constant}$, and $\Phi = 0$. These convenient simplifications are thought to be acceptable in the approximate adjoint analysis, as the spatial and temporal variations of viscosity in the system and the irreversible viscous dissipation in the heat equation both affect the dynamics of the system only at the small length scales, and are thus thought to be relatively unimportant in terms of the mechanics of sound generation. Subject to these additional assumptions, and following the established procedure for performing an adjoint analysis [see, e.g., appendix B of Bewley, Moin, & Temam (2001) for the case of an unsteady compressible Euler system], we may take the Fréchet derivative of this governing equation to obtain a linearized equation of the form

$$\mathcal{N}'(\mathbf{q})\mathbf{q}' = 0. \quad (3.3)$$

Selecting an L_2 duality pairing[†] of the form $\langle \mathbf{q}^*, \mathbf{q}' \rangle \triangleq \int_0^T \int_\Omega \mathbf{q}^* \cdot \mathbf{q}' d\mathbf{x} dt$, this linearized operator is then transformed according to the identity

$$\langle \mathbf{q}^*, \mathcal{N}'(\mathbf{q})\mathbf{q}' \rangle = \langle \mathcal{N}'(\mathbf{q})^* \mathbf{q}^*, \mathbf{q}' \rangle + b. \quad (3.4)$$

After some algebra involving several integrations by parts, it is straightforward to show that the adjoint operator corresponding to the approximate linearized form of the compressible Navier-Stokes equation in this framework is:

$$\mathcal{N}'(\mathbf{q})^* \mathbf{q}^* = \begin{pmatrix} -\frac{\partial \rho^*}{\partial t} - \frac{\mathbf{m}}{\rho} \cdot \nabla \rho^* + (\gamma - 1) \rho^* \nabla \cdot \frac{\mathbf{m}}{\rho} - \nabla \cdot \mathbf{m}^* - \frac{\gamma \mu}{\rho Pr Re} \nabla^2 \rho^* \\ -\frac{\partial \mathbf{m}^*}{\partial t} - \frac{\gamma p}{\rho} \nabla \rho^* - \frac{(\gamma - 1) \rho^*}{\rho} \nabla p - \frac{\mathbf{m}}{\rho} \cdot (\nabla \otimes \mathbf{m}^* + (\nabla \otimes \mathbf{m}^*)^T) - \nabla p^* - \\ - \frac{\mu}{Re \rho} \left[\nabla^2 \mathbf{m}^* + \left(\frac{\mu_B}{\mu} + \frac{1}{3} \right) \nabla (\nabla \cdot \mathbf{m}^*) \right] \\ -\frac{\partial p^*}{\partial t} + \frac{p \mathbf{m}}{\rho^2} \cdot \nabla \rho^* + \frac{(\gamma - 1) \mathbf{m}}{\rho^2} \cdot \nabla (\rho^* p) + \frac{\mathbf{m}}{\rho} \cdot \left(\frac{\mathbf{m}}{\rho} \cdot \nabla \right) \mathbf{m}^* + \\ + \frac{\mu}{Re \rho^2} \left[\mathbf{m} \cdot \nabla^2 \mathbf{m}^* + \left(\frac{\mu_B}{\mu} + \frac{1}{3} \right) (\mathbf{m} \cdot \nabla) (\nabla \cdot \mathbf{m}^*) \right] + \frac{\gamma \mu}{\rho Pr Re} \frac{p}{\rho} \nabla^2 \rho^* \end{pmatrix}.$$

It is important to note that, in the present derivation, we have associated the “adjoint pressure” with additional forcing of the continuity equation, and the “adjoint density” with additional forcing of the selected form of the energy equation. [This is in contrast with, e.g., the nomenclature selected by Tam & Auriault (1998).] The nomenclature has been defined in this manner in order to have a logical zero-Mach-number limit. In this limit, ρ and ρ^* are constant, the forward and adjoint energy equations may be dropped, and the state, perturbation, and adjoint vectors reduce to

$$\mathbf{q} = \begin{pmatrix} p \\ \rho \mathbf{u} \end{pmatrix} = \begin{pmatrix} p \\ \mathbf{m} \end{pmatrix}, \quad \mathbf{q}' = \begin{pmatrix} p' \\ \mathbf{m}' \end{pmatrix}, \quad \mathbf{q}^* = \begin{pmatrix} p^* \\ \mathbf{m}^* \end{pmatrix}.$$

In a domain enclosed by solid boundaries, by selecting the appropriate adjoint boundary and initial conditions, we can make the boundary term b in (3.4), which results from the several integrations by parts, equal to zero. Alternatively, as in the present analysis,

[†] In multiscale PDE systems such as the present, the L_2 duality pairing is not necessarily the best choice for defining the adjoint operator, and incorporating spatial or temporal derivatives into this pairing is recognized to have an important regularizing effect on the spectra of the resulting adjoint field that must be calculated. For further discussion of this important topic, see Protas, Bewley, & Hagen (2002).

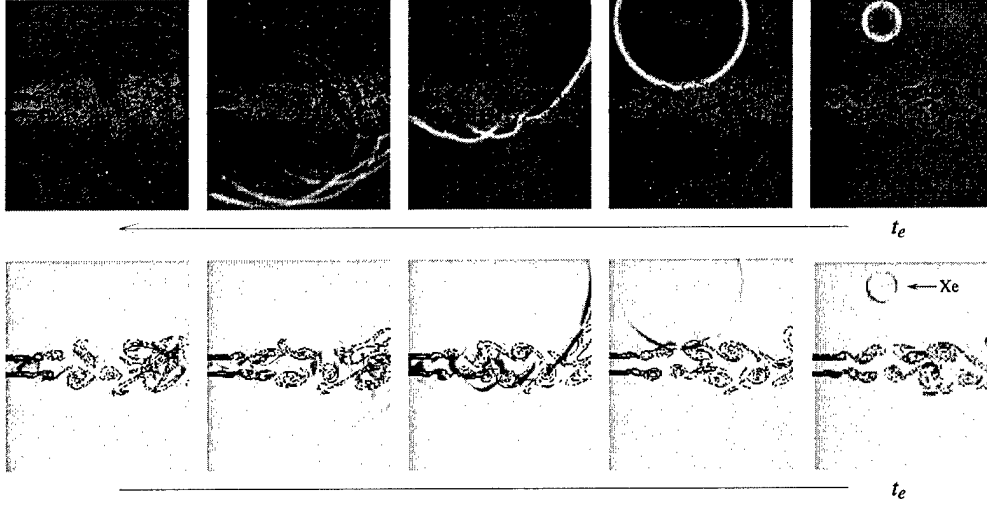


FIGURE 5. Adjoint density (top) and adjoint pressure (bottom) reveals sensitivity of the pressure component of the perturbation field at point x_e at time t_e to additional forcing of, respectively, the energy equation (top) and the continuity equation (bottom) everywhere in space x_c and for all times $t_c < t_e$. Note that, by causality, the adjoint field is zero for $t_c > t_e$; that is, the adjoint field marches backward in time from $t = t_e$.

we may surround the physical part of the domain of interest in both the flow and adjoint problems with the numerical equivalent of quiescent far-field boundary conditions which propagate no information towards the physical domain of interest; this again effectively allows us to neglect the influence of b . By so doing, the adjoint identity (3.4) then reveals that the following two analyses are equivalent:

#1) analyzing the effect on $q'_i(x_e, t_e)$ (that is, the effect on the i 'th component of the perturbation field at point $x = x_e$ and time $t = t_e$) created by applying a localized force $g'_j = \delta(x - x_c)\delta(t - t_c)$ to the j 'th component of the perturbation equation, and

#2) analyzing the effect on $q^*_j(x_c, t_c)$ created by applying a localized force $g^*_i = \delta(x - x_e)\delta(t - t_e)$ to the i 'th component of the adjoint equation.

By the identity (3.4), we may relate the perturbation and adjoint fields in these two analyses by

$$q'_i(x_e, t_e) = q^*_j(x_c, t_c). \quad (3.5)$$

Note that the point x_c and time t_c do not appear in the formulation of the adjoint system in problem #2, but arise only in the subsequent analysis of the resulting adjoint field. Thus, a *single* adjoint calculation allows us to quantify the effect of forcing *anywhere* in the flow system (for any x_c , t_c , and j) on the particular flow quantity $q'_i(x_e, t_e)$. This relation between the perturbation and adjoint Green's functions provides an alternative but equivalent explanation of the significance of adjoint analyses to the more general "controls-oriented" explanation provided in Figure 1.

3.2. Calculation of an adjoint Green's function

Figure 5 illustrates a computation of the adjoint Green's function, as formulated at the end of the previous section, obtained by forcing the adjoint system $\mathcal{N}'(\mathbf{q})^* \mathbf{q}^* = \mathbf{g}^*$ with

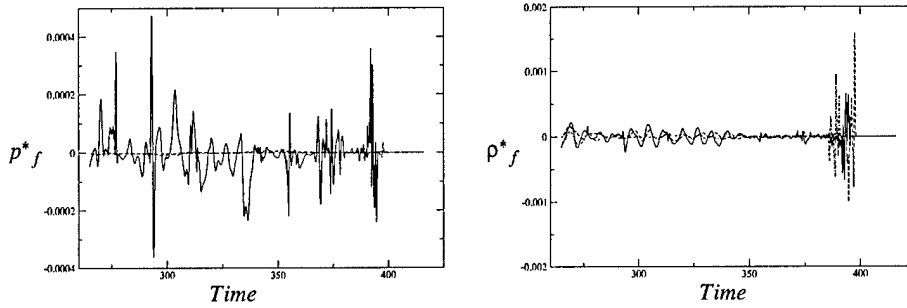


FIGURE 6. Evolution of adjoint pressure (left) and adjoint density (right) in time at the points $\{x, y\}$ of (solid) $\{5D, 0\}$, (dashed) $\{5D, 2.5D\}$, (dot-dashed) $\{5D, -2.5D\}$.

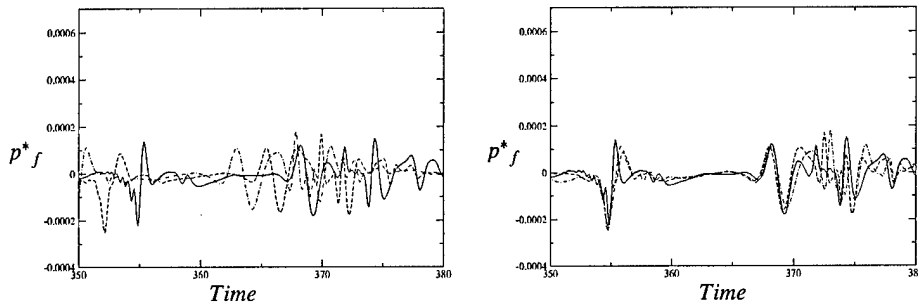


FIGURE 7. Adjoint pressure at three different locations at the centerline: at (dot-dashed) $x = 8$, (dashed) $x = 9$, and (solid) $x = 10$. When the actual evolutions of the variable (left) are shifted by the time corresponding to the convection velocity (right), there is an approximate superposition of the three lines, which indicates that these perturbations convect toward the nozzle at the convective speed.

an isolated force at a particular point in space and time, that is, $g_i^* = \delta(\mathbf{x} - \mathbf{x}_e)\delta(t - t_e)$. As discussed above, each component j of the resulting adjoint Green's function, at each point in space \mathbf{x}_c and each instant in time t_c , may be interpreted as the i 'th component of the perturbation to the flow at point \mathbf{x}_e and time t_e that would arise due to localized forcing of the corresponding component j of the flow system at the corresponding point in space \mathbf{x}_c and time t_c . The calculation reported in Figure 5 takes $i = 1$, that is, the adjoint field shown characterizes the effect on the perturbation pressure $p'(x_e, t_e)$.

It is interesting to note (see Figure 5) that the disturbance in the adjoint pressure grows rapidly as it propagates within the jet towards the nozzle at the convective velocity as the adjoint field evolves (in backwards time). In contrast, the disturbance in the adjoint density essentially propagates right through the jet, experiencing significant refraction. This behavior is quantified further in Figures 6 and 7. The component of the adjoint density that propagates at the convective speed of the jet within the jet shear layers is found to be quite small. This indicates, as one might expect, that mass sources are more efficient than energy sources in modifying the hydrodynamic field in a way which changes the radiated noise.

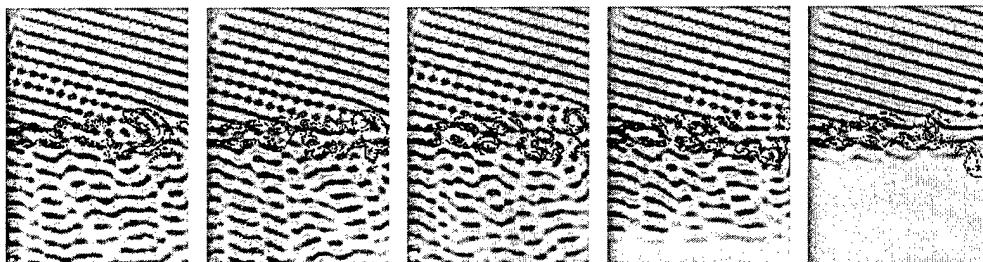


FIGURE 8. Adjoint density field due to incoming waves from the far field.

3.3. An adjoint Green's function at temporal frequency f

An alternative to forcing the adjoint problem at an isolated time t_e is to force it at a specific temporal frequency f . This corresponds roughly to looking at the sensitivity of the sound field at point x_e (at the frequency and phase selected) to additional forcing of the governing equations. This correspondence is only approximate, however, as the system under consideration has time-varying coefficients, and therefore frequency-based characterizations of the system's response are of limited usefulness. Note that, in systems with constant coefficients, a Bode plot completely characterizes the frequency response of the system. Such a frequency-domain analysis may only be applied to the mean flow. Nonetheless, an approximate characterization of this sort may still be developed for the present system (in the time domain) simply by forcing the adjoint system sinusoidally at the frequency of interest during the backwards march for the adjoint field. The result of such a calculation is illustrated in the bottom row of Figure 2. The scattering of the adjoint field due to the vortex roll-up is a necessary consequence of the scattering in the corresponding perturbation fields.

3.4. An adjoint Green's function corresponding to far-field noise

An alternative to forcing the adjoint problem at an isolated point in the computational domain x_e is to force it along a line near the boundary of the computational domain (that is, in the "buffer zone" used to approximate the far-field boundary conditions). By so doing, one may set up a propagating wave in the adjoint field which is the same as if the computational domain extended deep into the far field and the adjoint problem was forced a very long distance away. By varying the forcing along this line sinusoidally, one may simulate the arrival of a wave in the adjoint field corresponding to the effect on the far-field noise in any direction of interest. A representative example is given in Figure 8. Note that both reflection and refraction of the adjoint field are observed in this computation.

3.5. Quantification of scattering of adjoint Green's functions

In an attempt to quantify the scattering of a wave in the adjoint field due to the unsteady vortex roll-up, the values of the adjoint density and adjoint pressure have been measured at three different points in the representative adjoint Green's function analysis illustrated in Figure 9. The points where the adjoint density and adjoint pressure were measured are above the jet (where the scattering will be referred to as reflection), at the centerline, and below the jet (where the scattering will be referred to as refraction). The time series of these measurements were Fourier-transformed in time, and the results are plotted in Figure 10. The analysis was performed for adjoint forcing at three different Strouhal

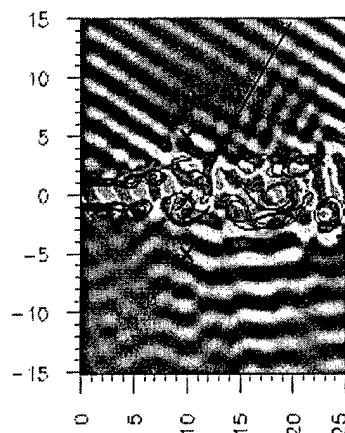


FIGURE 9. Adjoint pressure wave corresponding to far-field noise at an angle of 60° off the jet axis and at a frequency of $St = 2.0$. The Fourier transform of this field evaluated at the three points indicated is shown in Figure 10.

numbers: $St = 0.8$ ($2\times$ the vortex roll-up frequency), $St = 2.0$ ($5\times$ the vortex roll-up frequency), and $St = 8.0$ ($20\times$ the vortex roll-up frequency).

Perhaps the most important observation to make in Figure 10 is that there is very significant frequency broadening in all of the adjoint spectra measured. The adjoint systems are excited by forcing at the single frequency indicated ($St = 0.8, 2.0$, or 8.0) but, due to the time-varying coefficients (from the unsteady flow field \mathbf{q}) in the adjoint operator, the measurements of the adjoint field at the points indicated exhibit energy over a broad range of temporal frequencies. For comparison, the spectra of the hydrodynamic fluctuations of the base flow is shown in Figure 11. Note that the frequency broadening of the adjoint field cannot be captured by a steady-flow analysis.

The frequency broadening present when the adjoint field is forced at a high frequency is much larger than when it is forced at a low frequency. This fact was noticed by Suzuki (2001) for the direct problem, and was interpreted as “multiple scattering”. In the present adjoint analysis, this suggests that high-frequency noise may be modified by a broad range of possible forcing frequencies.

Note in particular that the frequency spectrum is generally narrower at the point above the jet (dashed lines) than below the jet (dot-dashed lines), apparently because the refraction of the traveling wave in the adjoint field is stronger than the reflection of this wave for the incidence angle tested. Within the jet (solid line), it is observed that the frequency broadening is strongest.

The low-wavenumber components of the spectra of the adjoint pressure at the centerline are especially strong for all three forcing frequencies tested. This indicates that low-frequency modulation of the hydrodynamic field via mass sources within the jet can have a significant impact on the high-frequency noise in the far field, and provides impetus for further studies in jet-noise control based on such characterizations to exploit this sensitivity.

Note also that all of the spectra are somewhat jagged, and the distance between of each small peak in this jaggedness is $\Delta f = 0.2D/U$, which is exactly half of the vortex roll-up frequency. This appears to indicate (as one might expect) that the scattering of the wave in the adjoint field is closely related to its interactions with the large-scale vortex roll-up.

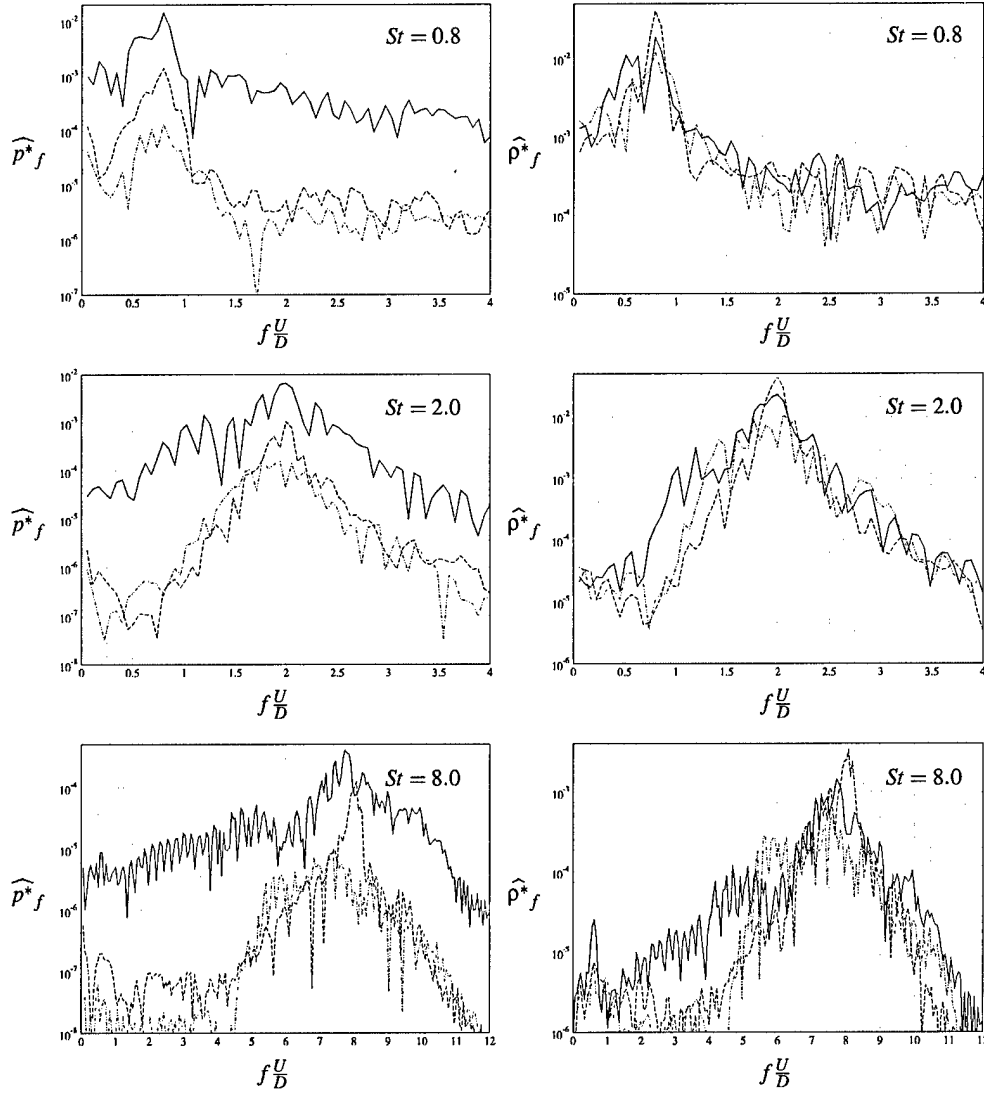


FIGURE 10. Temporal spectra of (left) the adjoint pressure \widehat{p}_f^* and (right) the adjoint density $\widehat{\rho}_f^*$ for an incident wave in the adjoint field coming from above (at an angle of 60° off the jet axis), at a frequency of (top) $St = 0.8$, (middle) $St = 2.0$, and (bottom) $St = 8.0$ and measured at the points $\{x, y\}$ of (solid) $\{5D, 0\}$, (dashed) $\{5D, 2.5D\}$, (dot-dashed) $\{5D, -2.5D\}$. See Figure 9 for flow configuration.

A second set of cases was also run in which the wave in the adjoint field approaches the jet at a 90° angle off the jet axis (cf. Figure 9). The results showed very similar trends, and are thus not included here.

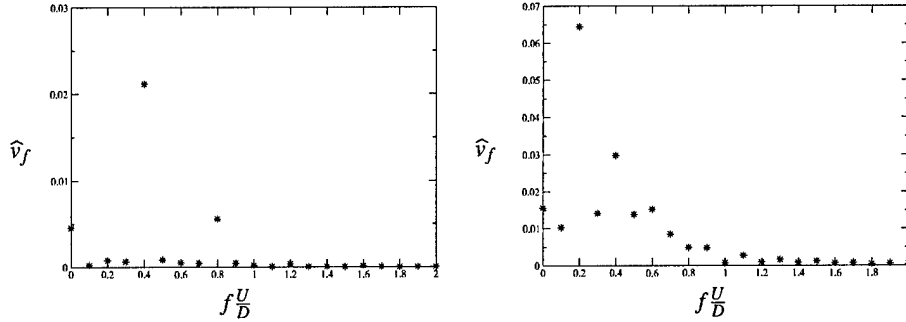


FIGURE 11. Spectra of the vertical velocity of the flow at $\{x,y\} = \{1.5D, 0.5D\}$ (left) and $\{x,y\} = \{3D, 0.5D\}$ (right). The appearance of the peak at $S_l = 0.2$ at the downstream station (right) is a result of vortex pairing (recall that the jet is forced at $S_l = 0.4$).

4. Concluding remarks

Perturbation and adjoint analyses of flow-acoustic interactions in an unsteady 2D jet have been performed. Attention has been focused on the scattering of adjoint Green's functions corresponding to far-field high-frequency noise. Significant scattering of the adjoint field is detected both above and below the jet, as quantified by a spectral analysis of the adjoint field. This scattering is a direct result of system unsteadiness (vortex roll-up), and cannot be captured by mean flow analyses.

The degree to which frequency broadening extends into the low frequencies within the jet in the adjoint analyses indicates the degree to which low-frequency alteration of the hydrodynamic field can be used to affect the high-frequency radiated acoustic field. This distinguishes promising low-frequency "hydrodynamic" control strategies from simple (but perhaps impractical) "antinoise" control strategies, which must be applied at the frequency of the radiated noise.

REFERENCES

- BEWLEY, T.R., MOIN, P., & TEMAM, R. 2001 DNS-based predictive control of turbulence: an optimal benchmark for feedback algorithms. *J. Fluid Mech.* **447**, 179-225.
- CERVINO, L.I. & BEWLEY, T.R. 2002 On the extension of the complex-step derivative technique to pseudospectral algorithms. Submitted for publication.
- COLONIUS, T., LELE, S.K., & MOIN, P. 1993 Boundary conditions for direct computation of aerodynamic sound generation. *AIAA J.* **31**, 1574-1582.
- DURBIN, P.A. 1983a High frequency Green function for aerodynamic noise in moving media, Part I: general theory. *J. Sound Vib.* **91**, 519-525.
- DURBIN, P.A. 1983b High frequency Green function for aerodynamic noise in moving media, Part II: Noise from a spreading jet. *J. Sound Vib.* **91**, 527-538.
- FREUND, J.B., MOIN, P., & LELE, S.K. 1997 Compressibility effects in a turbulent annular mixing layer. Mech. Engg. Dept., Stanford University, Tech. Rept. TF-72.
- FREUND, J.B. 1997 Proposed inflow/outflow boundary condition for direct computation of aerodynamic sound. *AIAA J.* **35**, 740-742.
- FREUND, J.B., & FLEISCHMAN, T.G. 2001 A numerical study of jet noise mechanisms: sound scattering by turbulence. *AIAA Paper* 2001-0375.

- LYNESS, J.N. & MOLER, C.B. 1967 Numerical differentiation of analytic functions. *SIAM J. Numer. Anal.* **4**, 202-210.
- MARTINS, J.R.R.A., STURDZA, P., & ALONSO, J.J. 2001 The connection between the complex-step derivative approximation and algorithmic differentiation. *AIAA Paper* 2001-0921.
- PROTAS, B., BEWLEY, T.R., & HAGEN, G. 2002 A comprehensive framework for the regularization of adjoint analysis in multiscale PDE systems. Submitted.
- SQUIRE, W. & TRAPP, G. 1998 Using complex variables to estimate derivatives of real functions. *SIAM Rev.* **40**, 110-112.
- SUZUKI, T., & LELE, S.K. 1999 Acoustic scattering from a mixing layer: role of instability waves. *AIAA Paper* 99-0228.
- SUZUKI, T. 2001 Acoustic wave propagation in transversely sheared flows. PhD Thesis, Stanford University, Department of Aeronautics and Astronautics. Also available as SUDAAR 739.
- TAM, C.K.W. & AURIAULT, L. 1998 Mean flow refraction effects on sound radiated from localized sources in a jet. *J. Fluid Mech.* **370**, 149-174.
- WEI, M. & FREUND, J.B. 2002 Optimal control of free shear flow. *AIAA Paper* 2002-0665.

On the extension of the complex-step derivative technique to pseudospectral algorithms

Laura I. Cerviño & Thomas R. Bewley

Dept. of MAE, UC San Diego, La Jolla, CA 92093-0411, USA

1 Introduction

The complex-step derivative (CSD) technique is a convenient and highly-accurate technique to perform a linearized “perturbation” analysis to determine a “directional derivative” using a nonlinear simulation code. The technique has previously been applied to numerical simulation codes (such as finite-element codes) which employ real arithmetic only. The present note examines the suitability of this technique for application to pseudospectral numerical simulation codes, which nominally use fast Fourier transforms (FFTs) to convert back and forth between real and complex representations of a system. It is found that, though this extension does indeed work, complex-to-complex FFTs combine the real and imaginary parts of the system, and thus the CSD approximation technique to compute the directional derivative presents no substantial numerical advantages over standard second-order finite-difference techniques when pseudospectral simulation codes and finite-precision arithmetic are employed.

2 Background

The idea of using complex variables in order to differentiate a function was (apparently) first mentioned in [1] and [2]. The applicability of this old technique to differentiate a complicated function, such as that computed by an involved finite-element code, was recognized by [3]. Recently, the CSD technique has become popular in aerodynamic optimization [4–7]. This approach has proven to be very accurate and easy to apply to finite-element and finite-difference simulation codes but, to the best of our knowledge, has not yet been extended to pseudospectral simulation codes. The present note explores the suitability of this extension

2.1 The Finite-Difference (FD) approximation

The directional derivative of a continuous function $J(\phi)$ in the direction ϕ_1 is simply the amount $J(\phi)$ changes when ϕ is updated in the direction ϕ_1 , scaled by the size of the update, in the limit that the size of the update approaches zero. It is denoted $d \triangleq \mathcal{D}J(\phi)/\mathcal{D}\phi \cdot \phi_1$. There are a variety of ways to calculate numerically this seemingly simple quantity. The most straightforward method to compute d is to consider a Taylor series expansion of the function $J(\phi + \epsilon \phi_1)$ near ϕ ,

$$J(\phi + \epsilon \phi_1) = J(\phi) + \epsilon \frac{\mathcal{D}J(\phi)}{\mathcal{D}\phi} \cdot \phi_1 + \mathcal{O}(\epsilon^2), \quad (1)$$

from which a first-order finite-difference formula the directional derivative is easily obtained:

$$d = \frac{J(\phi + \epsilon \phi_1) - J(\phi)}{\epsilon} + \mathcal{O}(\epsilon). \quad (2a)$$

Likewise, the second-order central finite-difference formula for the directional derivative is

$$d = \frac{\mathcal{J}(\phi + \epsilon \phi_1) - \mathcal{J}(\phi - \epsilon \phi_1)}{2\epsilon} + \mathcal{O}(\epsilon^2), \quad (2b)$$

and the fourth-order central finite-difference formula for the directional derivative is

$$d = \frac{\mathcal{J}(\phi - 2\epsilon \phi_1) - 8\mathcal{J}(\phi - \epsilon \phi_1) + 8\mathcal{J}(\phi + \epsilon \phi_1) - \mathcal{J}(\phi + 2\epsilon \phi_1)}{12\epsilon} + \mathcal{O}(\epsilon^4). \quad (2c)$$

The drawback with these methods when calculating d using a finite-precision arithmetic computer is the difficulty in finding the most suitable value for the step size ϵ . The accuracy of the numerical approximation of d is very sensitive to this value. When ϵ is large, the Taylor-series truncation is not valid, and when it is small, subtractive cancellation errors become dominant (the so-called “difference-of-large-numbers” problem).

To illustrate, the derivative of a scalar nonlinear function $f(x) = \frac{e^{-x}}{\sqrt{\tan x}}$ at $x = 1$ has been computed using the FD difference approximations given by truncation of the higher-order terms of (2a), (2b), and (2c) using both single-precision and double-precision arithmetic. Figure 1 shows that, for large ϵ , the error of these FD approximations scales with ϵ^n , where n is the order of truncation of the higher-order terms of the corresponding FD formulae.

For small ϵ , the error of all three FD formula in Figure 1 is $\mathcal{O}(1/\epsilon)$ due to the “difference-of-large-numbers” problem mentioned previously. In other words, when comparing two numbers which are almost the same using finite-precision arithmetic, the relative round-off error is proportional to the inverse of the difference between the two numbers. That this must be the case is easily seen by example. Denoting with a question mark the first digit past the decimal

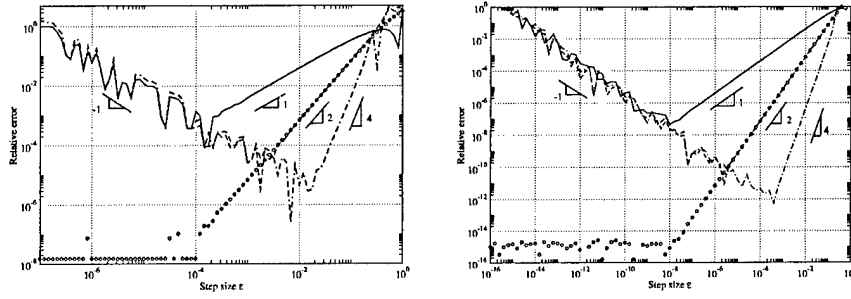


Fig. 1. Relative error of the derivative of $f(x) = \frac{e^{-x}}{\sqrt{\tan x}}$ at $x = 1$ given by (solid) first-order, (dashed) second-order, and (dot-dashed) fourth-order finite-difference approximations and (circles+dots) the complex-step approximation using single-precision arithmetic (left) and double-precision arithmetic (right). Note that both plots have essentially the same shape.

point that is unknown in a double-precision representation, we may write:

$$\begin{aligned} 1.0001111? - 1.0000000? &= 0.0001111? & \text{and} \\ 1.0000111? - 1.0000000? &= 0.0000111? \end{aligned}$$

As seen in this example, if the difference between the two numbers is decreased by an order of magnitude, the relative accuracy with which this difference may be calculated is also decreased by an order of magnitude.

2.2 The Complex-Step Derivative (CSD) approximation

The CSD approximation makes use of complex variables in order to compute the directional derivative. If the complex extension $\mathcal{J}(z)$ of a real-valued function $\mathcal{J}(\phi)$ is analytic, it can be expanded with a complex Taylor series. In particular, the expansion of $\mathcal{J}(\phi + i\epsilon\phi_1)$, where $i = \sqrt{-1}$, may be written:

$$\mathcal{J}(\phi + i\epsilon\phi_1) = \mathcal{J}(\phi) + i\epsilon \frac{\mathcal{D}\mathcal{J}(\phi)}{\mathcal{D}\phi} \cdot \phi_1 - \epsilon^2 E_1 - i\epsilon^3 E_2 + \mathcal{O}(\epsilon^4), \quad (3)$$

where E_1 and E_2 are real and are related to the higher-order derivatives of \mathcal{J} . Taking the imaginary part and dividing by ϵ gives a formula for the directional derivative:

$$d = \Im\left\{\frac{\mathcal{J}(\phi + i\epsilon\phi_1)}{\epsilon}\right\} + \mathcal{O}(\epsilon^2); \quad (4)$$

note that the error in this formula is $\mathcal{O}(\epsilon^2)$ because the leading-order error of (3) is real. This method has the advantage that it does not face the problem of the subtractive cancellation error; that is, d is computed simply by taking the imaginary part of the complex number $\mathcal{J}(\phi + i\epsilon\phi_1)$.

To illustrate, Figure 1 also shows the error in the calculation of the derivative of the function $f(x) = \frac{e^{-x}}{\sqrt{\tan x}}$ using the CSD approximation (4). It is observed that, for large ϵ , the error is $\mathcal{O}(\epsilon^2)$. This error is introduced by the truncation of the higher-order terms of the Taylor series in (4).

For small ϵ , on the other hand, the relative error of the CSD approximation reaches an asymptotic value given by the machine precision. Thus, when the CSD method is applied to this test problem, *any* choice of the step-size (providing it is sufficiently small) gives a very accurate result. Similar results are also seen when the CSD approach is applied to much more complicated functions, such as the calculation of the drag of a wing using an involved finite-element code [6,7]. As the CSD technique is both highly accurate and quite easy to apply to an existing numerical code (simply convert all real variables in the code to complex and perturb the imaginary component of the control variable), it has become a popular technique for computing the directional derivative.

3 Extension of complex-step derivative to pseudospectral codes

Many codes in both fundamental turbulence research and numerical weather prediction are pseudospectral. In such codes, products are computed in physical space, spatial derivatives are computed in Fourier space, and the conversion between these two representations is made efficiently with the fast Fourier transform (FFT). Pseudospectral techniques are essential for the accurate computation of spatial derivatives in multiscale fluid systems when marginal resolution is employed. Unfortunately, as pseudospectral codes already employ complex arithmetic, direct application of the standard complex-step derivative method, as discussed above, is not possible. However, as the FFT is simply a linear manipulation of an otherwise real problem, the idea behind the CSD method is still valid. To implement the CSD method in a pseudospectral code, it is necessary to:

- (1) Convert all formerly real arrays into complex arrays.
- (2) Replace real-to-complex FFTs with complex-to-complex FFTs.
- (3) Double the size of all formerly complex arrays. When computing the FFT of a real function f (in one-dimensional, two-dimensional and three-dimensional problems), it is only necessary to store half of the Fourier coefficients, since the other half may be recovered by the identity $\hat{f}(\mathbf{k}) = \hat{f}^*(-\mathbf{k})$. This identity no longer holds if f is complex.

To illustrate the difference in accuracy between the FD and CSD methods when applied to a pseudospectral numerical code, both methods have been implemented on an artificial optimization problem in which the dynamical

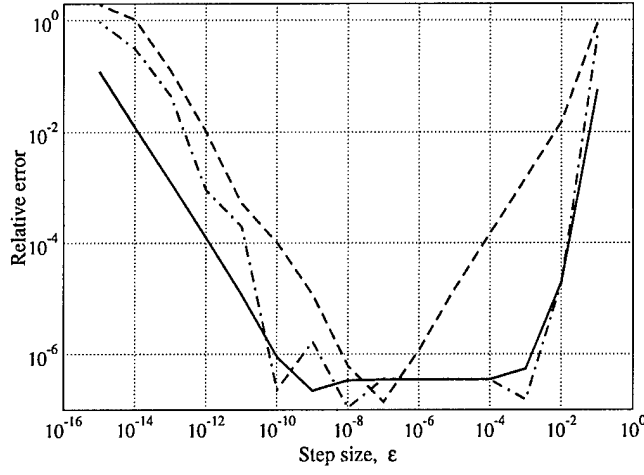


Fig. 2. Relative error of (dashed) first-order and (dot-dashed) second-order FD approximations and (solid) the CSD approximation of the directional derivative. Note that there is little substantial difference between the overall performance of the CSD and second-order FD methods.

system is governed by the nonlinear viscous Burgers equation

$$\frac{\partial u}{\partial t} + u \frac{\partial u}{\partial x} = \nu \frac{\partial^2 u}{\partial x^2}$$

in the periodic domain $x \in [0, 2\pi]$. A pseudospectral technique is used to advance the system in time from 0 to T , and the values $\nu = 0.2$ and $T = 6$ were used in the numerical simulation. The initial condition is given by $u(0) = 1 + 0.2 \sin(x) + 0.02 \sin^2(x - 1) + \phi \sin(x - 1)$, where ϕ is the “control parameter”. The function of interest is defined as $\mathcal{J}(\phi) = \int_0^T \int_{4.5}^{5.0} |u(x, t)|^2 dx dt$. The relative error of both the FD and CSD approximation of $d\mathcal{J}/d\phi$ at $\phi = 0$ is shown in Figure (2). The exact value is obtained with a “direct” method, formed by writing a separate numerical simulation code (sometimes called a “tangent linear” code) which explicitly calculates the perturbation equation (for further discussion, see, e.g., [8]). As seen in Figure 2, for large ϵ , the errors of both the FD and CSD approximations are seen to scale with ϵ in a manner which is similar to the case evaluated in Figure 1.

Unfortunately, for small ϵ , the error of the CSD approximation in the present problem does not approach an asymptotic value, as it did in the problem considered in §1. Instead, the error of the CSD approximation scales like $\mathcal{O}(1/\epsilon)$. This is due to the fact that complex-to-complex Fourier transforms combine real and imaginary parts of the data. Thus, the large (real) and small (imaginary) numbers in this analysis are combined by the FFTs, leading to numerical inaccuracies which are comparable to the second-order FD approach. A similar behavior is expected (and has been obtained) when the CSD method is applied to other pseudospectral codes.

4 Conclusions

The present work has investigated the possible extension of the CSD technique to compute directional derivatives from pseudospectral numerical codes. It has been shown that, due to the fact that Fourier transforms combine large (real) and small (imaginary) numbers in such an analysis, the error of the CSD approximation of the directional derivative does not approach asymptotic value as the step size ϵ is made small. The performance of the second-order FD approximation and the CSD approximation are found to be roughly equivalent for the model problem tested. As both techniques have approximately the same computational cost [that is, twice the cost of computing $J(\phi)$], the extension of the CSD method to pseudospectral algorithms is found to present little or no inherent advantages over the more standard second-order FD approach for such problems.

References

- [1] J. N. Lyness and C. B. Moler, "Numerical differentiation of analytic functions", *SIAM J. Numer. Anal.* **4**, 202–210, (1967).
- [2] J. N. Lyness, "Numerical algorithms based on the theory of complex variable", in *Proc. ACM 22nd Nat. Conf.*, Thomas Book Co., Washington DC, 124–134, (1967).
- [3] W. Squire and G. Trapp, "Using complex variables to estimate derivatives of real functions", *SIAM Rev.* **40** (1), 110–112, (1998).
- [4] J. C. Newman, W. K. Anderson and D. L. Whitfield, "Multidisciplinary Sensitivity Derivatives Using Complex Variables", Tech. rep., Engineering Research Center Report, Mississippi State University, mSSU-COE-ERC-98-08, (July 1998).
- [5] W. K. Anderson, J. C. Newman, D. L. Whitfield and E. J. Nielsen, "Sensitivity Analysis for the Navier-Stokes Equations on Unstructured Meshes Using Complex Variables", *AIAA Paper* 99-3294.
- [6] J. R. R. A. Martins, I. M. Kroo and J. J. Alonso, "An automated method for sensitivity analysis using complex variables", *AIAA Paper* 00-0689.
- [7] J. R. R. A. Martins, P. Sturdza and J. J. Alonso, "The connection between the complex-step derivative approximation and algorithmic differentiation", *AIAA Paper* 01-0921.
- [8] H. M. Adelman and R. T. Haftka, "Sensitivity analysis of discrete structural systems", *AIAA Journal* **24** (5), 823–832, (1986).

A comprehensive framework for the regularization of adjoint analysis in multiscale PDE systems

B. Protas, T. Bewley, & G. Hagen

Dept. of MAE, UC San Diego, La Jolla, CA 92093-0411, USA

Abstract

This paper examines the regularization opportunities available in the adjoint analysis and optimization of multiscale PDE systems. Regularization may be introduced into such optimization problems by modifying the form of the evolution equation and the forms of the norms, duality pairings, and inner products used to frame the adjoint analysis. Typically, L_2 brackets are used in the definition of the cost functional, the adjoint operator, and the cost functional gradient. If instead we adopt the more general Sobolev brackets, the various fields involved in the adjoint analysis may be made smoother and therefore easier to resolve numerically. The present paper identifies several relationships which illustrate how the different regularization options fit together to form a general framework. Many commonly-used strategies for regularization, including implicit Tikhonov regularization and *ad hoc* smoothing of the gradient with the inverse Laplacian, are shown to fit into the present framework as special cases. The regularization strategies proposed are exemplified using a 1D Kuramoto–Sivashinsky forecasting problem, and computational examples are provided which exhibit their utility. A multiscale preconditioning algorithm is also proposed that noticeably accelerates convergence of the optimization procedure. Application of the proposed regularization strategies to more complex optimization problems of physical and engineering relevance is also discussed.

Key words: Adjoint analysis, optimization, regularization, flow control, 4DVAR

Contents

1	Introduction	2
2	The four fundamental classes of regularization opportunities	5
3	Forecasting a Kuramoto–Sivashinsky system: the standard framework	7
4	Regularizing the Kuramoto–Sivashinsky forecasting problem	13
4.1	The adjoints of alternative forms of the evolution equation	15
4.2	Targeting the cost functional	18
4.3	Modifying the duality pairing	19
4.4	Preconditioning the gradient	21

Email address: bprotas@ucsd.edu, bewley@ucsd.edu, greggh@turbulence.ucsd.edu (B. Protas, T. Bewley, & G. Hagen).

4.5	Relations between different regularization strategies	23
5	Computational examples	31
5.1	Spectra of the adjoint fields obtained with alternative formulations	33
5.2	Optimization	34
6	Extensions	38
6.1	Controlling a 3D Navier–Stokes System	39
6.2	Controlling a Kuramoto–Sivashinsky System in a Bounded Domain	42
7	Discussion & Conclusions	45
A	Adjoint derivation with the “ H^1 –in–time” duality pairing	47
	References	49

1 Introduction

Adjoint analysis forms a significant foundation for many applications of model-based control and estimation theory to nonlinear fluid systems, including:

- A) transonic airfoil shape optimization [1],
- B) optimization of open-loop control distributions for transitional and turbulent flow systems [2], [3], [4], [5], and
- C) state reconstruction and parameter estimation in numerical weather prediction (known operationally as “4D-VAR”).

For recent general reviews we refer the reader to, e.g., Gunzburger [7] and Sritharan [8]. In order to apply adjoint analysis, an appropriately-defined *cost functional* is first expressed which represents mathematically the physical objective in performing the computational optimization. In problem A, the objective is typically to maximize the lift/drag ratio of the airfoil for a range of different cruise configurations while respecting a variety of practical “feasibility” constraints related to the construction of the airfoil. In problem B, the objective is typically to reduce drag, surface pressure fluctuations, or flow-induced noise or to reduce the kinetic energy of the flow perturbations in order to inhibit transition to turbulence, though in combustion applications the objective is typically the opposite—that is, to excite the flow with minimal control input in order to enhance turbulent mixing. In problem C, the objective is typically to reconcile the numerical weather model with recent weather measurements in order to obtain accurate weather forecasts. All of the above problems in fact represent *inverse problems*, in which one seeks to determine inputs to the system such that the outputs will have desired properties. Once the control objective is expressed mathematically as a cost functional, an appropriately-defined *adjoint field* may be used as a tool to determine an appropriately-defined *gradient* of the cost functional with respect to the control variables. The adjoint field calculation is thus a central component of high-dimensional gradient-based control optimization strategies. Refs. [9] and [5] contain brief reviews of our perspective on a few of the relevant issues related to such problems.

Even though the mathematical framework for adjoint-based optimization is fairly mature and has already been used successfully in a broad range of applications in

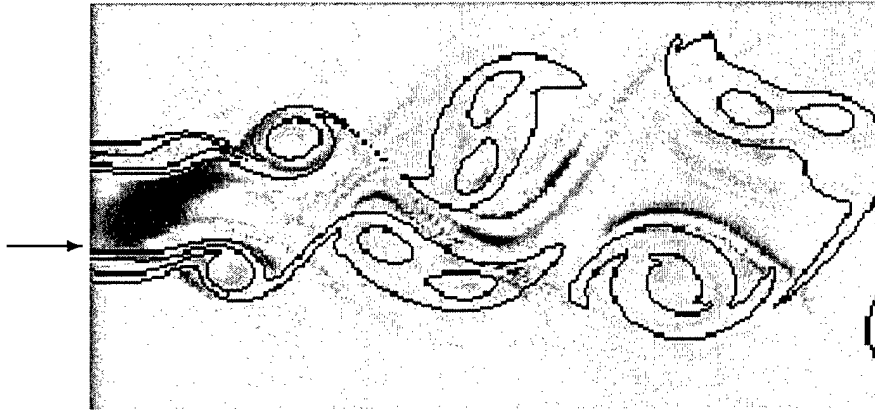


Fig. 1. The field of adjoint density (grayscale) obtained at the end of the backward march in a 2D jet-noise optimization problem. The contour lines represent vorticity of the primal flow. The arrow indicates the areas where the adjoint field reveals particularly rapid exponential growth at small length scales. (Simulation by Laura Cerviño [private communication].)

fluid mechanics, many flow systems still present fundamental challenges to this approach. Due to their nonlinear nature, fluid-mechanical systems are often characterized by energetic motions over a broad range of length scales and time scales. Such multiscale systems present significant difficulties for numerical characterization. Adjoint analyses of such flows must be crafted with care in order to be well behaved over this full range of scales. Inverse problems are often ill-posed in the sense that multiple solutions which locally minimize the relevant cost functional exist, and the solution found by the optimization algorithm does not necessarily have a continuous dependence on the data provided. For instance, in numerical weather prediction, the problem of finding the future state of the nonlinear model based on past measurements is often ill-posed in this regard. In such problems, errors magnify exponentially in time in the linearized (“perturbation”) analysis. In the iterative numerical solution of such an inverse problem in the nonlinear setting, a small change in the data provided (the measurements) can sometimes lead to a large change in the forecast. Even in the control of laminar flows, adjoint fields typically grow exponentially when they are calculated (in reverse time), and can thus be exceedingly difficult to resolve in regions where flow perturbations amplify quickly, such as in thin shear layers. The rapid growth of an adjoint field calculation in such regions is illustrated in Figure 1, which shows the adjoint density obtained near the end of the backward march in a jet-noise optimization problem.

The presence of a broad range of interacting length- and time-scales thus complicates an adjoint-based analysis of a nonlinear multiscale system by causing difficulties of twofold nature: on the one hand, the dependence of the solution on the data in such cases is irregular, resulting in the presence of many local minima of the cost functional; on the other hand, the various fields involved in an adjoint analysis are not smooth and therefore difficult to resolve numerically. These two issues are related, and may be addressed, at least partially, by considering the regularity

of the various fields involved in the analysis of such systems. We therefore define the term *regularization* rather broadly in the present work as a reformulation of an adjoint-based algorithm in such a manner that at least some of the fields involved in this analysis are more “smooth”, in the sense that the energy in these fields decays more rapidly with wavenumber at the length scales of concern from the perspective of a numerical implementation. Such regularization will thus render a given optimization problem more amenable to numerical treatment, and may sometimes turn an initially ill-posed problem into a well-posed problem. A more narrow definition of the term regularization is often adopted in the precise mathematical study of ill-posed inverse problems (see [10], [11], and [12]); however our broader usage of the term is adequate for the present investigation.

Though great attention has been paid to the appropriate treatment of subgrid-scale effects in the numerical simulation literature, much less is known about how to address the multiscale nature of fluid-mechanical systems in adjoint analysis. The central issue is that norms, duality pairings, and inner products, collectively to be referred to in this paper as “brackets”, are implied, if not explicitly stated, at three distinct steps of the derivation of an adjoint analysis. Each of these brackets implies a relative weighting between the various length scales and time scales in the relationship expressed. “Traditional” approaches have typically selected L_2 brackets at most, if not all, of these steps in the adjoint formulation. However, this choice is by no means unique. Other choices are sometimes more appropriate when the system must be solved on a computer with finite-precision arithmetic using a discrete numerical grid in both space and time. Modifying the definitions of the three brackets used to frame the adjoint analysis facilitates a range of distinct but related regularization opportunities. Capitalizing on these regularization opportunities can result in significantly smoother space-time systems requiring numerical approximation in the adjoint analysis, thus leading to faster convergence, greater numerical stability, and improved accuracy in marginally-resolved numerical approximations of multiscale fluid systems. The purpose of the present paper is to clarify these important regularization opportunities and to illustrate how they may be used in concert to increase the speed, stability, and accuracy of adjoint-based numerical optimization algorithms.

The possibility of achieving a regularizing effect through modification of some of the brackets used in the derivation of an adjoint algorithm was already recognized by Collis et al. [13]. A similar set of ideas, but in the finite-dimensional setting, was earlier suggested by Heinkenschloss & Vicente [14]. Other approaches explicitly addressing data assimilation in multiscale environments include the works of Liu [15], Brandt & Zaslavsky [16], Grimstad & Mannseth [17], and Brusdal & Mannseth [18]. In particular, [15] and [18] invoke the concept of “basis norm rescaling,” which is further elaborated here. Multigrid approaches to optimization problems were studied by Lewis & Nash [19]. Similar ideas also appear in the Numerical Weather Prediction (NWP) literature: e.g., Lorenc [20] discussed performing optimization with respect to a rescaled variable, whereas Thepaut & Moll

[21] recognized the possibility of using various inner products to precondition the adjoint algorithm. An adaptive method to enforce smoothness constraints in data assimilation was recently presented by Lin et al. [22]. In the present study, we attempt to synthesize these various regularization opportunities into a comprehensive framework and characterize the interplay between the various definitions of the brackets upon which adjoint analyses are based. We believe that the present work represents the first time that a “comprehensive” framework for the reformulation of adjoint analysis has been obtained, as the present paper characterizes flexibility in the definition of the duality pairing which, apparently, has not previously been exploited in numerical simulations.

To make this study concrete, the bulk of the paper illustrates how these regularization techniques may be applied to a Kuramoto-Sivashinsky model system. This 1D model problem illustrates self-sustained chaotic behavior of a multiscale nature, and thus provides an appropriate testbed for the present study. The Kuramoto-Sivashinsky equation was used successfully as a low-dimensional prototype for complicated fluid systems by Holmes, Lumley & Berkooz [23]. In fact, many advanced flow control strategies were initially investigated using similar 1D models; see, e.g., Choi et al. [24], Kunisch & Volkwein [25], and Atwell, Borggaard, & King [26].

In §2 we identify and discuss in general terms the four fundamental classes of regularization opportunities available in the framing of an adjoint analysis. As a point of reference, the standard optimization framework for the Kuramoto-Sivashinsky model is formulated in §3. The different regularization possibilities available in framing the adjoint analysis, and interrelationships between these different formulations, are discussed in §4, and some numerical examples are presented in §5. Several extensions of this study are also underway, and are briefly introduced in §6. Concluding remarks are presented in §7.

2 The four fundamental classes of regularization opportunities

The objective of the present research effort is to develop a comprehensive framework for understanding regularization issues in the adjoint analysis of unsteady PDE systems. In the adjoint-based optimization of PDE systems in general, there are three spatial domains of interest: the domain on which cost functional is defined, which we denote Ω_1 , the domain over which the state of the system modeled, which we denote Ω_2 , and the domain on which the control is applied, which we denote Ω_3 . In an unsteady problem, the system model is defined on Ω_2 over some time interval $[0, T]$. The cost functional which measures this model on Ω_1 may average over the interval $[0, T]$, as in “regulation” problems, or may focus the attention on the state at time T , which is called a “terminal control” problem. The control on Ω_3 can also be defined over $[0, T]$, when an unsteady control distribution is sought, or may be

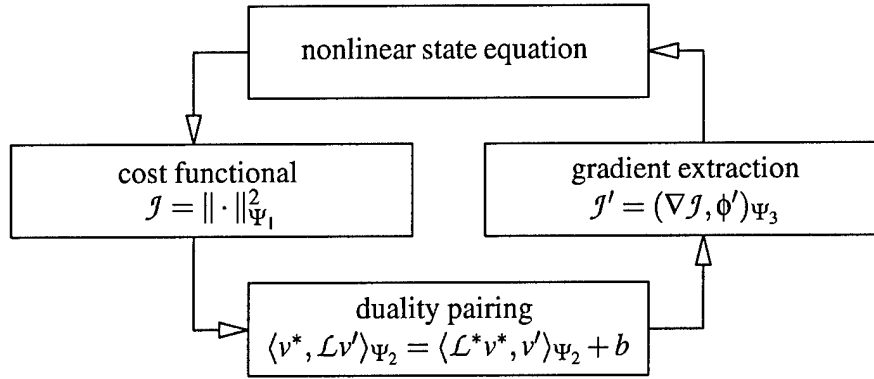


Fig. 2. The four essential components of the adjoint-based optimization process. As outlined in the text, each component of this process is associated with a distinct opportunity for regularization.

defined at time $t = 0$, as done in the forecasting problem (where the “control” is actually the initial condition). In the process of adjoint-based optimization, brackets are used (or implied, if not explicitly stated) on all three of these space–time domains.

In the continuous setting, the form of each of these three brackets may incorporate either derivatives or “anti-derivatives” in both space and time. Mathematically, these brackets are related to the natural measures for functions defined in the Sobolev space $H^p(0, T; H^q(\Omega_i))$, where q is the differentiability order in space, p is the differentiability order in time, and Ω_i denotes the spatial domain. Note that Sobolev brackets with negative differentiability indices can also be considered in this framework by taking p and/or q negative. Such brackets are natural alternatives to the L_2 bracket when considering functions of different degrees of regularity in both space and time. How each of these brackets is defined, in addition to any smoothing that might be applied to the state equation itself, has important consequences on the smoothness of the several variables in the optimization problem, as summarized in Figure 1. As a shorthand, we use Ψ_1 , Ψ_2 , and Ψ_3 to identify the brackets selected for the three space–time domains of interest in this problem.

The first regularization opportunity is given by adding an artificial (but well-motivated) term to the discretized state equation itself. Two common examples are dynamic subgrid-scale models (in turbulence research) and hyperviscosity (in numerical weather prediction). Addition of such a term to the numerical model is useful for tuning the behavior of the numerical model at the unresolvable scales, and can be used to make a system well-posed if it is not otherwise. In addition to modifying the actual governing equation, we can also consider its different derived forms (e.g., the vorticity form instead of the velocity-pressure form of the Navier-Stokes equation). These different yet equivalent forms may serve to focus on different aspects of the dynamics in numerical simulations and adjoint analyses thereof.

The second regularization opportunity is given by the definition of the cost func-

tional. As mentioned previously, the cost functional can take any of a wide variety of forms depending on the problem under consideration. However, in most such formulations, the cost functional involves the norm of a flow quantity taken over some subdomain of the space–time domain under consideration. Selecting for this purpose a norm Ψ_1 which incorporates either derivatives or anti-derivatives, instead of using the standard L_2 norm, effectively builds in a “filter” into the definition of the cost functional, thereby allowing extra emphasis to be placed on certain scales of interest in the multiscale problem. Note that the cost functional may also incorporate a term penalizing the magnitude of the control on Ω_3 , using an appropriate norm, in order to limit the magnitude of the control that results from the optimization¹. Such an approach is known as Tikhonov regularization [27]. Analysis of the effect of this additional term on the regularity of the optimization algorithm is deferred to §4.5.5.

The third regularization opportunity is given by the form of the duality pairing, which is used to define the adjoint operator and, ultimately, the adjoint field itself. Incorporating derivatives or anti-derivatives into the definition of the duality pairing Ψ_2 , instead of using the standard L_2 duality pairing, can be useful to obtain well-behaved (that is, numerically tractable) adjoint operators.

Finally, the fourth regularization opportunity is the definition of the inner product used to extract the cost functional gradient. Incorporating derivatives into the inner product Ψ_3 , instead of using the standard L_2 inner product, has the effect of scale-dependent filtering, and allows one to extract smoother gradients, thereby preconditioning the optimization process.

In this paper we present a comprehensive framework for regularizing various aspects of the adjoint-based optimization process. Though adjoint-based optimization has already seen a broad range of applications in fluid mechanics, understanding the interplay between these various regularization opportunities appears to be very important when applying such techniques to difficult multiscale problems of both physical and engineering interest, such as high Reynolds-number turbulence.

3 Forecasting a Kuramoto–Sivashinsky system: the standard framework

In this section, we first describe three different yet equivalent forms of a dynamically-rich 1D model system governed by the Kuramoto–Sivashinsky equation, then outline a relatively standard adjoint-based algorithm for the forecasting of this system based on limited noisy measurements. In the section that follows, we illustrate, in turn, the application of the four regularization opportunities summarized above.

¹ Note that inclusion of such a term is sometimes, but not always, necessary to insure that the optimization problem has a bounded solution. See [5] for further discussion.

The Kuramoto–Sivashinsky equation ([28], [29]) has been widely studied due to its chaotic, pattern-forming behavior. Out of the several different normalizations of the parameters of this system which are available in the literature, we have selected the one proposed by Hyman and Nicolaenko [30], in which the system is written

$$\begin{cases} \partial_t u + 4\partial_x^4 u + \kappa \left[\partial_x^2 u + \frac{1}{2} (\partial_x u)^2 \right] = 0, & x \in \Omega, \ t \in [0, T], \\ \partial_x^i u(0, t) = \partial_x^i u(2\pi, t), & t \in [0, T], \ i = 0, \dots, 3, \\ u(x, 0) = \psi, & x \in \Omega, \end{cases} \quad (1)$$

where we define $\partial_x^i \triangleq \frac{\partial^i}{\partial x^i}$. Integrating this system over the domain $\Omega \triangleq [0, 2\pi]$, the evolution of the mean of u is given by $\partial_t \int_0^{2\pi} u dx = -(\kappa/2) \int_0^{2\pi} (\partial_x u)^2 dx \neq 0$. For this reason, it is common to transform the system (1) into a different form, which is achieved by first differentiating it with respect to x and then re-expressing it in terms of a new variable $v \triangleq \partial_x u$ such that

$$\begin{cases} \partial_t v + 4\partial_x^4 v + \kappa (\partial_x^2 v + v \partial_x v) = 0, & x \in \Omega, \ t \in [0, T], \\ \partial_x^i v(0, t) = \partial_x^i v(2\pi, t), & t \in [0, T], \ i = 0, \dots, 3, \\ v(x, 0) = \partial_x \psi \triangleq \phi, & x \in \Omega. \end{cases} \quad (2)$$

This is the form of the Kuramoto–Sivashinsky system that is studied most often. As $v = \partial_x u$ and u is periodic in x , it follows immediately that $\int_0^{2\pi} v dx = 0$ for all t . The variable u can be recovered from v by inverting the differential operator ∂_x and accounting for the mean of u properly. For this purpose we define the “anti-derivative” operator ∂_x^{-1} such that

$$\partial_x^{-1} z(x) \triangleq \int_0^x z(x') dx' - \frac{1}{2\pi} \int_0^{2\pi} \int_0^s z(x') dx' ds.$$

Note that the constant is selected such that $\int_0^{2\pi} \partial_x^{-1} z(x) dx = 0$. Using this operator, we may recover u from v with

$$u(x, t) = \partial_x^{-1} v(x, t) + \frac{1}{2\pi} \int_0^{2\pi} \psi(x') dx' - \frac{\kappa}{4\pi} \int_0^t \int_0^{2\pi} [v(x', t')]^2 dx' dt'.$$

Yet another form of the Kuramoto–Sivashinsky system can be obtained by further differentiating the system (2) and defining $w \triangleq \partial_x v$

$$\begin{cases} \partial_t w + 4\partial_x^4 w + \kappa [\partial_x^2 w + \partial_x(vw)] = 0, & x \in \Omega, \ t \in [0, T], \\ w = \partial_x v, & x \in \Omega, \ t \in [0, T], \\ \partial_x^i w(0, t) = \partial_x^i w(2\pi, t), & t \in [0, T], \ i = 0, \dots, 3, \\ w(x, 0) = \partial_x \phi \triangleq \phi, & x \in \Omega. \end{cases} \quad (3)$$

We observe that this formulation contains both v and w , with the relation between these variables serving as a *constraint* on the system. Note that we may recover v

from w with the simple expression

$$v(x, t) = \partial_x^{-1} w(x, t). \quad (4)$$

We may thus simplify the expression of the system (3) by substitution of (4) to eliminate the variable v . In the derivations to come, we will primarily focus on system (2), which we will dub the *primitive formulation*. By analogy with the equations of fluid dynamics, we will refer to the integral form (1) as the *stream-function formulation* and the derivative form (3) as the *vorticity formulation* of the Kuramoto-Sivashinsky system; the same qualifiers will be used with regard to the corresponding variables.

In the above equations, κ is the order parameter, and its meaning is similar to the Reynolds number in fluid systems, as it may roughly be considered as the ratio of the convective and dissipative effects at the characteristic length scales of the system. All three forms (1), (2), and (3) are forced by destabilizing second-order anti-diffusion terms, and the nonlinear terms redistribute energy to the higher wavenumbers, where it is eventually dissipated by stabilizing fourth-order diffusion terms. Looking at the system dynamics over a range of different values of κ , it is seen for low values of κ that intervals of κ corresponding to chaotic solutions are interwoven with intervals of κ in which the solution approaches a fixed point; as κ is increased, the latter intervals become vanishingly small. For values of κ selected in the former intervals, the unsteady dynamics of the Kuramoto-Sivashinsky system is *self-sustained*, that is, the system does not require external stochastic forcing to excite an interesting multiscale behavior. The self-sustained chaotic solutions of this system are characterized in physical space by what might be described as a jittering array of oscillatory bumps which are created and annihilated in a deterministic fashion that is highly sensitive to small disturbances. Links of this equation with dynamical systems theory are discussed by Hyman & Nicolaenko [30]. The weak formulation of the Kuramoto-Sivashinsky equation, its associated functional setting, and a characterization of its chaotic attractor is discussed by Temam [31].

We now review the relatively standard framework for adjoint-based data assimilation in PDE systems. As mentioned previously, adjoint-based data assimilation is commonly used for state estimation and forecasting based on limited noisy measurements in multiscale PDE systems, such as in the forecasting the Earth's weather. In the present work, we will discuss the regularization of the adjoint analysis at the heart of such an optimization problem by focusing on an admittedly contrived, yet dynamically rich, 1D model forecasting problem based on the Kuramoto-Sivashinsky system discussed above. Extensions of these approaches for the regularization of adjoint analyses in more realistic forecasting and control problems in fluid mechanics are discussed in §6.

In the model problem to be considered, the three spatial domains Ω_i , $i = 1, 2, 3$, mentioned in the previous section happen to coincide. Note that this will not necessarily be the case in general (cf. §6.2). More precisely, the “control”, which is taken

to be the initial condition ϕ in this problem, is defined on $\Omega = [0, 2\pi]$ at time $t = 0$, whereas both the system evolution and the cost functional are defined on $\Omega \times [0, T]$. We begin by first defining the norm

$$\|z\|_{L_2(0,T;L_2(\Omega))}^2 \triangleq \int_0^T \int_0^{2\pi} z^2 dx dt, \quad (5)$$

and then attempting to minimize the cost functional

$$\mathcal{J}(\phi) = \frac{1}{2} \|\mathcal{H}v - y\|_{L_2(0,T;L_2(\Omega))}^2, \quad \text{where} \quad y = \mathcal{H}v^{act} + \eta, \quad (6)$$

v^{act} is the “actual” state (which is unknown to the forecasting algorithm), and v is the “reconstructed” state, which is assumed to be related to the initial state ϕ (the quantity to be determined in the reconstruction problem) via the primitive form (2) of the Kuramoto-Sivashinsky system. Note that \mathcal{H} denotes the “observation” operator, y denotes the corresponding noisy measurements taken of the system, and η denotes the measurement noise. The problem to be solved is to find the initial state ϕ in the reconstruction problem which will minimize \mathcal{J} , thereby minimizing the deviation of the measurements from the corresponding quantities in the reconstructed system.

The observation operator \mathcal{H} which we have selected for this model problem is based on the cosine decomposition of the flow system. To define \mathcal{H} , we will make use of a linear projection operator \mathcal{P}_r defined such that

$$\mathcal{P}_r z \triangleq \left[\frac{1}{\pi} \int_0^{2\pi} \cos(rx') z(x') dx' \right] \cos(rx). \quad (7)$$

Note that the projection operator so defined satisfies $\mathcal{P}_r^2 = \mathcal{P}_r$. We now define the observation operator as

$$\mathcal{H} \triangleq \sum_{r \in \Lambda_r} \mathcal{P}_r, \quad (8)$$

where Λ_r is the set of modes which we choose to observe.

For $\mathcal{J}(\phi)$ to be minimized by ϕ , it is necessary that, in the immediate neighborhood of ϕ , the perturbation \mathcal{J}' of the cost functional \mathcal{J} that arises from perturbations $\varepsilon\phi'$ to the control distribution ϕ vanish for all feasible directions ϕ' as ε is made small. To be precise, the quantity $\mathcal{J}'(\phi; \phi')$ is defined by a limiting process as the differential² of the cost functional \mathcal{J} with respect to ϕ such that

$$\mathcal{J}'(\phi; \phi') \triangleq \lim_{\varepsilon \rightarrow 0} \frac{\mathcal{J}(\phi + \varepsilon\phi') - \mathcal{J}(\phi)}{\varepsilon}. \quad (9)$$

² In the present work we assume that $\mathcal{J}(\phi)$ is sufficiently smooth that it is Fréchet differentiable.

To summarize, if $\mathcal{J}(\phi)$ is minimized by ϕ , then $\mathcal{J}'(\phi; \phi') = 0$ for all feasible ϕ' ; this is referred to as the *first-order necessary optimality condition* for the present problem. Higher-order differentials may also be considered (namely, the second-order sufficient optimality condition), however, we will not make use of such higher-order expressions in this paper.

The differential of the cost functional defined in (6) can now be calculated in the neighborhood of some state $v(\phi)$, which yields

$$\mathcal{J}'(\phi; \phi') = \int_0^T \int_0^{2\pi} (\mathcal{H}v - y) \mathcal{H}v' dx dt, \quad (10)$$

where, by linearization of (2), it follows that $v'(\phi; \phi')$ is the solution of the system

$$\begin{cases} \mathcal{L}v' = 0, & x \in \Omega, t \in [0, T], \\ \partial_x^i v'(0, t) = \partial_x^i v'(2\pi, t), & t \in [0, T], i = 0, \dots, 3, \\ v'(x, 0) = \phi', & x \in \Omega, \end{cases} \quad (11)$$

where the linear operator \mathcal{L} is

$$\mathcal{L}v' \triangleq \partial_t v' + 4\partial_x^4 v' + \kappa [\partial_x^2 v' + v \partial_x v' + (\partial_x v) v'] \quad (12)$$

and $v(\phi)$ is the solution of (2). Note that, as was the case with v , it follows immediately that $\int_0^{2\pi} v' dx = 0$ for all t .

Numerically, the optimal initial state ϕ and the corresponding evolution of the system v cannot be determined solely from the mathematical statement of the first-order necessary optimality condition, that is, the vanishing of the differential of the cost functional at the optimum distribution of ϕ for all feasible ϕ' . A stable numerical procedure to find such a minimum of $\mathcal{J}(\phi)$ even when no good initial guess of the optimum controls is available (which is quite often the case) is to use an iterative gradient-based optimization procedure: given some initial guess ϕ_0 for the initial conditions ϕ , consecutive refinements $\phi^{(n)}$ are computed using a gradient-based optimization algorithm³ until convergence to a (local) minimum of \mathcal{J} is obtained. In order to apply such a gradient-based optimization procedure, we need somehow to define a gradient in the space of the control distributions. This is accomplished by identifying the differential (10) as an appropriately-defined *inner product*⁴ of a quantity, which we will denote $\nabla \mathcal{J}$, with the control perturbation ϕ' . The quantity

³ In such high-dimensional optimization problems, quasi-Newton methods are becoming increasingly popular. Such approaches approximate some of the information contained in the Hessian or inverse Hessian by intelligent use of the recently-computed gradient vectors, thereby accelerating convergence (see, e.g., Nocedal and Wright [32]). The concepts discussed in this paper appear to extend to such optimization algorithms; such extensions will be considered in future work.

⁴ A representation of the bounded linear functional \mathcal{J}' in the form of an inner product, as given in (13), is guaranteed by the Riesz Representation Theorem [33].

$\nabla \mathcal{J}$ so defined represents the rate of change in \mathcal{J} when ϕ is updated an infinitesimal amount in the direction ϕ' . We thus identify $\nabla \mathcal{J}$ as a *gradient* in the space where the metric, which effectively defines angles and distances, is given by the inner product selected. Significantly, note that different choices of this inner product will result in different gradients of \mathcal{J} for a particular value of the control distribution ϕ . However, for convex \mathcal{J} , all such definitions of the gradient eventually lead to the same minimizer (that is, the optimal value of ϕ), at which $\nabla \mathcal{J} = 0$ regardless of the inner product used to define the gradient.

The most common choice for the inner product used to extract the gradient $\nabla \mathcal{J}$ from the expression for \mathcal{J}' is the L_2 inner product and, for the time being, our derivation is performed using this inner product, that is

$$\mathcal{J}' \triangleq (\nabla \mathcal{J}, \phi')_{L_2(\Omega)} \triangleq \int_0^{2\pi} (\nabla \mathcal{J}) \phi' dx. \quad (13)$$

In order to identify $\nabla \mathcal{J}$, we first need to transform the expression (10) into a form in which the control perturbation ϕ' is factored out in a convenient manner, as shown above. Note that v' is related to ϕ' through the involved yet linear relationship (11). To accomplish this factorization, we introduce a new bracket, which we will refer to by the special name of a *duality pairing*

$$\langle z_1, z_2 \rangle_{L_2(0,T;L_2(\Omega))} \triangleq \int_0^T \int_0^{2\pi} z_1 z_2 dx dt. \quad (14)$$

Based on this duality pairing, we may derive an adjoint operator \mathcal{L}^* and a corresponding boundary term $b_{\mathcal{L}}$ from the following identity

$$\langle v^*, \mathcal{L}v' \rangle_{L_2(0,T;L_2(\Omega))} = \langle \mathcal{L}^*v^*, v' \rangle_{L_2(0,T;L_2(\Omega))} + b_{\mathcal{L}}. \quad (15)$$

Using integration by parts and the definition of \mathcal{L} given in (12), it follows that

$$\begin{aligned} \mathcal{L}^*v^* &= -\partial_t v^* + 4\partial_x^4 v^* + \kappa(\partial_x^2 v^* - v\partial_x v^*), \quad \text{and} \\ b_{\mathcal{L}} &= \left[\int_0^{2\pi} v^* v' dx \right]_{t=0}^{t=T} + \left\{ \int_0^T 4 \left[v^* \partial_x^3 v' - (\partial_x v^*) \partial_x^2 v' + (\partial_x^2 v^*) \partial_x v' - (\partial_x^3 v^*) v' \right] \right. \\ &\quad \left. + \kappa \left[v^* \partial_x v' - (\partial_x v^*) v' + v^* v v' \right] dt \right\}_{x=0}^{x=2\pi}. \end{aligned} \quad (16)$$

Making use of the adjoint operator derived above, we may now *define* an adjoint system in the following (as yet, arbitrary) manner

$$\begin{cases} \mathcal{L}^*v^* = \mathcal{H}^*(\mathcal{H}v - y) \triangleq f, & x \in \Omega, \quad t \in [0, T], \\ \partial_x^i v^*(0, t) = \partial_x^i v^*(2\pi, t), & t \in [0, T], \quad i = 0, \dots, 3, \\ v^*(x, T) = 0, & x \in \Omega, \end{cases} \quad (17)$$

where \mathcal{H}^* is defined in a manner analogous to \mathcal{L}^* in (15), and thus it is easy to show that \mathcal{H} is self-adjoint (that is, that $\mathcal{H}^* = \mathcal{H}$). We will refer to (17) as the *primitive* adjoint system and to v^* as the *primitive* adjoint variable. To see why the adjoint state so defined is in fact useful, we now combine the state, perturbation, and adjoint systems [(2), (11), and (17)] into the identity given in (15). Note that all the boundary terms in $b_{\mathcal{L}}$ resulting from integrations by parts in space vanish due to periodicity⁵. Due to the clever choice of the RHS forcing term in the adjoint system (17), we may use (15) to re-express the differential given in (10) in the desired factored form

$$\mathcal{J}'(\phi; \phi') = \int_0^{2\pi} v^*|_{t=0} \phi' dx = (v^*|_{t=0}, \phi')_{L_2(\Omega)}, \quad (18)$$

where v^* denotes the solution of the adjoint problem defined in (17). Finally, note that the mean of the adjoint field defined by (17) is not zero, yet all feasible ϕ' under consideration have zero mean mode. Because of this restriction on the class of ϕ' under consideration, (18) is in fact equivalent to

$$\mathcal{J}'(\phi; \phi') = (\bar{v}^*|_{t=0}, \phi')_{L_2(\Omega)}, \quad (19)$$

where the overbar implies that the given variable has the mean mode removed, that is,

$$\bar{z} \triangleq z - \frac{1}{2\pi} \int_0^{2\pi} z dx. \quad (20)$$

Note that \bar{v}^* denotes an “orthogonal projection” with respect to the inner product (13) of the adjoint variable v^* onto the space of feasible ϕ' . Thus, the gradient which we seek in the space of feasible ϕ' , as indicated in (13), may now be identified as

$$\nabla \mathcal{J} = \bar{v}^*|_{t=0}. \quad (21)$$

The gradient so defined can now be used to find the optimal feasible initial condition using any of a number of standard gradient-based optimization algorithms.

4 Regularizing the Kuramoto–Sivashinsky forecasting problem

In the subsections that follow, we discuss how the regularization opportunities introduced in §2 can be applied to fine-tune the adjoint algorithm outlined in §3 to better treat multiscale phenomena. In this discussion, we will first investigate

⁵ Without further mention, we will make use of this fact in many of the transformations to follow.

adjoint analyses based on the different yet equivalent forms (1) and (3) of the governing equation (2). We will then consider a variety of alternative definitions of the three distinct brackets at the heart of the adjoint formulation, as outlined in §2 and listed in the above “standard” formulation as

- the norm $\|\cdot\|_{\Psi_1}$ in (5), which is used to define the cost functional,
- the duality pairing $\langle \cdot, \cdot \rangle_{\Psi_2}$ in (14), which is used to define the adjoint operator, and
- the inner product $(\cdot, \cdot)_{\Psi_3}$ in (13), which is used to define the gradient.

Note that, in the standard formulation given in §3, L_2 brackets over the appropriate space–time domains were used in all three cases. In the subsections to come, we will discuss at length the effects of various different choices for Ψ_1 , Ψ_2 , and Ψ_3 . In particular, we will make extensive use of H^q brackets of the form

$$\|z\|_{L_2(0,T;H^q(\Omega))}^2 \triangleq \int_0^T \int_0^{2\pi} (\partial_x^q z)^2 dx dt, \quad (22a)$$

$$\langle z_1, z_2 \rangle_{L_2(0,T;H^q(\Omega))} \triangleq \int_0^T \int_0^{2\pi} (\partial_x^q z_1) (\partial_x^q z_2) dx dt, \quad (22b)$$

$$(z_1, z_2)_{H^q(\Omega)} \triangleq \int_0^{2\pi} (\partial_x^q z_1) (\partial_x^q z_2) dx, \quad (22c)$$

where H^q denotes the Sobolev spaces where these brackets are commonly used (though we will not make use of any of the sophisticated mathematical machinery of functional analysis in Sobolev spaces). For simplicity, we will restrict our attention to the cases with $q = 0$ and ± 1 , though higher-order derivatives may also be considered. Note that the special case of $q = 0$ reduces the H^q brackets defined above to the L_2 cases considered previously, as defined in (5), (14), and (13). Also, the present paper will focus on brackets incorporating spatial derivatives only. Formulation generalizing the bracket definitions to include time derivatives as well as space derivatives is also possible, and is discussed briefly in Appendix A. Finally, note that it is straightforward to extend these bracket definitions by taking linear combinations of the H^q brackets for various values of q . This fact was recognized previously in [5] for the purpose of extending the definition of the norm used in the cost functional, thereby focusing the cost functional on the particular range of length scales of interest in the system under consideration. In the present work (in §4.4), we will develop this extension further by demonstrating how it may be applied to the definition of the inner product used to extract the gradient, thereby preconditioning the optimization process in a tunable manner. In this discussion, the following inner product, defined as a weighted linear combination of the L_2 ,

H^1 , and H^{-1} inner products, will be used heavily

$$\begin{aligned} (z_1, z_2)_{W^{l_1, l_{-1}}} \triangleq & \frac{l_{-1}^2}{(1+l_1^2)(1+l_{-1}^2)} \int_0^{2\pi} \left[z_1 z_2 + \right. \\ & \left. \frac{l_1^2 l_{-1}^2}{l_1^2 + l_{-1}^2} (\partial_x z_1) (\partial_x z_2) + \frac{1}{l_1^2 + l_{-1}^2} (\partial_x^{-1} z_1) (\partial_x^{-1} z_2) \right] dx. \end{aligned} \quad (23)$$

The justification for the specific choice used above for the coefficients weighing the three terms will become apparent in §4.4. Taking the appropriate limits as l_1 and l_{-1} approach zero and infinity, it follows that

$$(z_1, z_2)_{W^{0, \infty}} = (z_1, z_2)_{L_2(\Omega)}, \quad (z_1, z_2)_{W^{\infty, \infty}} = (z_1, z_2)_{H^1(\Omega)}, \quad (z_1, z_2)_{W^{0, 0}} = (z_1, z_2)_{H^{-1}(\Omega)}.$$

The form $(z_1, z_2)_{W^{l_1, \infty}}$ is thus a linear combination of the L_2 and H^1 inner products, whereas $(z_1, z_2)_{W^{0, l_{-1}}}$ is a linear combination of the H^{-1} and L_2 inner products. We will use the symbols $W^{l_1, l_{-1}}$, $W^{l_1, \infty}$ and $W^{0, l_{-1}}$ to refer to these different inner products. Symbols representing the spatial components of the different brackets will be used as superscripts to identify the way in which the different objects (that is, the cost functionals, the adjoint operators with the associated adjoint variables, and the cost functional gradients) are constructed. When such symbols are omitted, L_2 brackets are implied (see §3).

4.1 The adjoints of alternative forms of the evolution equation

As indicated in (1) and (3), by applying integral or differential operators to the governing equation in the primitive form (2) and suitably redefining the state variable, we obtain a family of systems representing the same conservation law, but emphasizing different aspects (length scales) of the system dynamics. Needless to say, all of these systems are formally equivalent. However, they are characterized by different energy spectra, and thus some of these systems are easier to compute accurately than others when marginal resolution is employed. We can further expect that the adjoint operators derived from these equations might be different as well, with some forms possibly being easier to compute than others. In this subsection, we present two alternative forms of the adjoint operator using the standard L_2 brackets in all three steps of the adjoint derivation, essentially reproducing the “standard” derivation of §3, but applying it to the streamfunction and vorticity forms of the governing equation presented in (1) and (3). The subsequent three subsections discuss the effects of choosing alternative forms for the three brackets used in the adjoint derivation. A detailed summary of the inter-relationships between these options is presented in §4.5.

4.1.1 The standard adjoint derivation based on the vorticity formulation

We now proceed to minimize the original cost functional (6) by modeling the system evolution with the vorticity form (3) of the Kuramoto–Sivashinsky system. Specifically, we consider a cost functional written in the form

$$\mathcal{J}_\varphi(\varphi) = \frac{1}{2} \left\| \mathcal{H} \partial_x^{-1} w - y \right\|_{L_2(0,T;L_2(\Omega))}^2. \quad (24)$$

Note that, as $\partial_x^{-1} w = v$, \mathcal{J}_φ is equivalent to \mathcal{J} , but depends on the control variable $\varphi = \partial_x \phi$, that is, $\mathcal{J}_\varphi(\partial_x \phi) = \mathcal{J}(\phi)$. The differential of this cost functional can now be expressed as

$$\mathcal{J}'_\varphi(\varphi; \varphi') = - \int_0^T \int_0^{2\pi} \left[\partial_x^{-1} \mathcal{H}^* (\mathcal{H} \partial_x^{-1} w - y) \right] w' dx dt, \quad (25)$$

where integration by parts was used to reveal explicit dependence of \mathcal{J}'_φ on the vorticity perturbation $w'(\varphi; \varphi')$. The boundary terms obtained as a result of this transformation vanish due to periodicity of all the variables involved. The field w' satisfies the system obtained by linearizing (3)

$$\begin{cases} \mathcal{M} w' = 0, & x \in \Omega, t \in [0, T], \\ \partial_x^i w'(0, t) = \partial_x^i w'(2\pi, t), & t \in [0, T], i = 0, \dots, 3, \\ w'(x, 0) = \varphi', & x \in \Omega, \end{cases} \quad (26)$$

where the linear operator \mathcal{M} is

$$\mathcal{M} w' \triangleq \partial_t w' + 4 \partial_x^4 w' + \kappa (\partial_x^2 w' + 2 w w' + \partial_x^{-1} w' \partial_x w + \partial_x^{-1} w \partial_x w'), \quad (27)$$

and $w(\varphi)$ is the solution of (3). By an identity of the same form as (15), that is,

$$\left\langle w^*, \mathcal{M} w' \right\rangle_{L_2(0,T;L_2(\Omega))} = \left\langle \mathcal{M}^* w^*, w' \right\rangle_{L_2(0,T;L_2(\Omega))} + b_{\mathcal{M}}, \quad (28)$$

it follows [cf. (16)] that

$$\begin{aligned} \mathcal{M}^* w^* &= -\partial_t w^* + 4 \partial_x^4 w^* + \kappa [\partial_x^2 w^* + \partial_x^{-1} (w \partial_x w^*) - \partial_x^{-1} w \partial_x w^*], \\ b_{\mathcal{M}} &= \left[\int_0^{2\pi} w^* w' dx \right]_{t=0}^{t=T} + \left[\dots \right]_{x=0}^{x=2\pi} \end{aligned}$$

Making use of this adjoint operator, we define the *vorticity* adjoint system [cf. (17)] with

$$\begin{cases} \mathcal{M}^* w^* = -\partial_x^{-1} \mathcal{H}^* (\mathcal{H} \partial_x^{-1} w - y), & x \in \Omega, t \in [0, T], \\ \partial_x^i w^*(0, t) = \partial_x^i w^*(2\pi, t), & t \in [0, T], i = 0, \dots, 3, \\ w^*(x, T) = 0, & x \in \Omega. \end{cases} \quad (29)$$

Defining the gradient $\nabla \mathcal{J}_\phi$ such that

$$\mathcal{J}'_\phi \triangleq \left(\nabla \mathcal{J}_\phi, \phi' \right)_{L_2(\Omega)}, \quad (30)$$

it follows by an analogous derivation that

$$\nabla \mathcal{J}_\phi = \bar{w}^* \Big|_{t=0}, \quad (31)$$

where the projection operator implied by the overbar is defined as in (20).

4.1.2 The standard adjoint derivation based on the streamfunction formulation

We may also minimize the cost functional (6) by modeling the system evolution with the streamfunction form (1) of the Kuramoto–Sivashinsky system. Specifically, we consider a cost functional written in the form

$$\mathcal{J}_\psi(\psi) = \frac{1}{2} \left\| \mathcal{H} \partial_x u - y \right\|_{L_2(0,T;L_2(\Omega))}^2. \quad (32)$$

If we restrict ψ to have zero mean mode, then it follows that $\psi = \partial_x^{-1} \phi$. Noting that $\partial_x u = v$, it is seen that \mathcal{J}_ψ is equivalent to \mathcal{J} , that is, $\mathcal{J}_\psi(\partial_x^{-1} \phi) = \mathcal{J}(\phi)$. The differential of \mathcal{J}_ψ is

$$\mathcal{J}'_\psi(\psi; \psi') = - \int_0^T \int_0^{2\pi} [\partial_x \mathcal{H}^* (\mathcal{H} \partial_x u - y)] u' dx dt, \quad (33)$$

where, by linearization of (1), it follows that $u'(\psi; \psi')$ is the solution of the system

$$\begin{cases} \mathcal{K} u' = 0, & x \in \Omega, t \in [0, T], \\ \partial_x^i u'(0, t) = \partial_x^i u'(2\pi, t), & t \in [0, T], i = 0, \dots, 3, \\ u'(x, 0) = \psi', & x \in \Omega, \end{cases} \quad (34)$$

where the linear operator \mathcal{K} is

$$\mathcal{K} u' \triangleq \partial_t u' + 4 \partial_x^4 u' + \kappa [\partial_x^2 u' + (\partial_x u)(\partial_x u')] \quad (35)$$

and $u(\psi)$ is the solution of (1). By the identity

$$\left\langle u^*, \mathcal{K} u' \right\rangle_{L_2(0,T;L_2(\Omega))} = \left\langle \mathcal{K}^* u^*, u' \right\rangle_{L_2(0,T;L_2(\Omega))} + b_{\mathcal{K}}, \quad (36)$$

it follows that

$$\mathcal{K}^* u^* = -\partial_t u^* + 4 \partial_x^4 u^* + \kappa [\partial_x^2 u^* - \partial_x (u^* \partial_x u)].$$

Making use of this adjoint operator, we define the *streamfunction* adjoint system with

$$\begin{cases} \mathcal{K}^* u^* = -\partial_x \mathcal{H}^* (\mathcal{H} \partial_x u - y), & x \in \Omega, \ t \in [0, T], \\ \partial_x^i u^*(0, t) = \partial_x^i u^*(2\pi, t), & t \in [0, T], \ i = 0, \dots, 3, \\ u^*(x, T) = 0, & x \in \Omega. \end{cases} \quad (37)$$

Defining the gradient $\nabla \mathcal{J}_\Psi$ such that

$$\mathcal{J}'_\Psi \triangleq \left(\nabla \mathcal{J}_\Psi, \Psi' \right)_{L_2(\Omega)}, \quad (38)$$

it follows that

$$\nabla \mathcal{J}_\Psi = u^* \Big|_{t=0}. \quad (39)$$

4.2 Targeting the cost functional

As indicated in (22a), the definition of the cost functional may be generalized by taking the H^q norm (rather than the L_2 norm) of the quantity of interest (in the present case, the measurement misfit). By so doing, we can focus the cost functional on a particular range of length scales of interest. For example, taking the H^1 norm [see (22a)] of the misfit of the measurement y , we define [cf. (6)]

$$\mathcal{J}^{H^1}(\phi) = \left\| \mathcal{H}v - y \right\|_{L_2(0, T; H^1(\Omega))}^2. \quad (40)$$

It is straightforward to show that the only modification to the standard formulation of the adjoint analysis which results from this change in the cost functional is the right-hand-side forcing of the evolution equation for the associated adjoint field, which now takes the form [cf. (17)]

$$\mathcal{L}^* v^* = -\partial_x^2 \mathcal{H}^* (\mathcal{H}v - y) = -\partial_x^2 f.$$

Similarly, taking the H^{-1} norm of the misfit of the measurement y , we define

$$\mathcal{J}^{H^{-1}}(\phi) = \left\| \mathcal{H}v - y \right\|_{L_2(0, T; H^{-1}(\Omega))}^2. \quad (41)$$

The modification of the right-hand-side forcing of the adjoint field in the standard formulation which results from this change in the cost functional is

$$\mathcal{L}^* v^* = -\partial_x^{-2} \mathcal{H}^* (\mathcal{H}v - y) = -\partial_x^{-2} f.$$

4.3 Modifying the duality pairing

As indicated in (22b), the definition of the adjoint operator may be generalized by using an H^q duality pairing rather than the standard L_2 duality pairing. By so doing, we may determine the same gradient of the same cost functional as found by the standard adjoint framework, but do so via an adjoint system with a substantially different energy spectra which makes it more or (preferably) less difficult to compute accurately on a marginally-resolved space-time grid.

4.3.1 An adjoint derivation with the H^1 duality pairing

We again proceed to minimize the original cost functional (6) by modeling the system evolution with the primitive form (2) of the Kuramoto–Sivashinsky system, but now derive the adjoint operator with an H^1 duality pairing via the identity

$$\langle v^{*,H^1}, \mathcal{L}v' \rangle_{L_2(0,T;H^1(\Omega))} = \langle \mathcal{L}^{*,H^1} v^{*,H^1}, v' \rangle_{L_2(0,T;H^1(\Omega))} + b_1, \quad (42)$$

from which it follows that

$$\begin{aligned} \mathcal{L}^{*,H^1} v^{*,H^1} &= -\partial_t v^{*,H^1} + 4\partial_x^4 v^{*,H^1} + \kappa[\partial_x^2 v^{*,H^1} - \partial_x^{-2}(v \partial_x^3 v^{*,H^1})], \\ b_1 &= \left[\int_0^{2\pi} (\partial_x v^{*,H^1}) (\partial_x v') dx \right]_{t=0}^{t=T} + \left[\dots \right]_{x=0}^{x=2\pi}. \end{aligned} \quad (43)$$

Making use of this adjoint operator, we define an adjoint system with

$$\begin{cases} \mathcal{L}^{*,H^1} v^{*,H^1} = -\partial_x^{-2} \mathcal{H}^*(\mathcal{H}v - y) = -\partial_x^{-2} f, & x \in \Omega, \quad t \in [0, T], \\ \partial_x^i v^{*,H^1}(0, t) = \partial_x^i v^{*,H^1}(2\pi, t), & t \in [0, T], \quad i = 0, \dots, 3, \\ v^{*,H^1}(x, T) = 0, & x \in \Omega. \end{cases} \quad (44)$$

Note that the differential of the cost functional (10) may be written in a form consistent with the new duality pairing

$$\begin{aligned} \mathcal{J}'(\phi; \phi') &= - \int_0^T \int_0^{2\pi} \partial_x [\partial_x^{-2} \mathcal{H}^*(\mathcal{H}v - y)] \partial_x v' dx dt \\ &= \langle -\partial_x^{-2} \mathcal{H}^*(\mathcal{H}v - y), v' \rangle_{L_2(0,T;H^1(\Omega))}. \end{aligned}$$

Combining (11) and (44) with (42) and substituting the above expression, we obtain

$$\mathcal{J}'(\phi; \phi') = - \int_0^{2\pi} \partial_x^2 v^{*,H^1} \Big|_{t=0} \phi' dx = \left(-\partial_x^2 v^{*,H^1} \Big|_{t=0}, \phi' \right)_{L_2(\Omega)}. \quad (45)$$

Using an L_2 inner product to extract the gradient as in (13), we may identify the gradient as

$$\nabla \mathcal{J} = -\partial_x^2 v^{*,H^1} \Big|_{t=0}. \quad (46)$$

Note that the gradient so defined has zero mean mode and thus lies in the space of feasible ϕ' . An analogous derivation using a duality pairing which incorporates derivatives with respect to the time variable (that is “ H^1 -in-time”) is presented in Appendix A.

4.3.2 An adjoint derivation with the H^{-1} duality pairing

We again minimize the original cost functional (6) by modeling the system evolution with the primitive form (2) of the Kuramoto–Sivashinsky system, but now derive the adjoint operator with an H^{-1} duality pairing via the identity

$$\left\langle v^{*,H^{-1}}, \mathcal{L} v' \right\rangle_{L_2(0,T;H^{-1}(\Omega))} = \left\langle \mathcal{L}^{*,H^{-1}} v^{*,H^{-1}}, v' \right\rangle_{L_2(0,T;H^{-1}(\Omega))} + b_{-1}, \quad (47)$$

from which it follows that

$$\begin{aligned} \mathcal{L}^{*,H^{-1}} v^{*,H^{-1}} &= -\partial_t v^{*,H^{-1}} + 4\partial_x^4 v^{*,H^{-1}} + \kappa[\partial_x^2 v^{*,H^{-1}} - \partial_x^2(v\partial_x^{-1} v^{*,H^{-1}})], \\ b_{-1} &= \left[\int_0^{2\pi} \left(\partial_x^{-1} v^{*,H^{-1}} \right) \left(\partial_x^{-1} v' \right) dx \right]_{t=0}^{t=T} + \left[\dots \right]_{x=0}^{x=2\pi}. \end{aligned} \quad (48)$$

Making use of this adjoint operator, we define an adjoint system with

$$\begin{cases} \mathcal{L}^{*,H^{-1}} v^{*,H^{-1}} = -\partial_x^2 \mathcal{H}^*(\mathcal{H}v - y) = -\partial_x^2 f, & x \in \Omega, \quad t \in [0, T], \\ \partial_x^i v^{*,H^{-1}}(0, t) = \partial_x^i v^{*,H^{-1}}(2\pi, t), & t \in [0, T], \quad i = 0, \dots, 3, \\ v^{*,H^{-1}}(x, T) = 0, & x \in \Omega. \end{cases} \quad (49)$$

Note that the differential of the cost functional (10) may be written in a form consistent with the new duality pairing

$$\begin{aligned} \mathcal{J}'(\phi; \phi') &= -\int_0^T \int_0^{2\pi} \partial_x^{-1} \left[\partial_x^2 \mathcal{H}^*(\mathcal{H}v - y) \right] \partial_x^{-1} v' dx dt \\ &= \left\langle -\partial_x^2 \mathcal{H}^*(\mathcal{H}v - y), v' \right\rangle_{L_2(0,T;H^{-1}(\Omega))}. \end{aligned}$$

Combining (11) and (49) with (47) and substituting the above expression, we obtain

$$\mathcal{J}'(\phi; \phi') = -\int_0^{2\pi} \partial_x^{-2} v^{*,H^{-1}} \Big|_{t=0} \phi' dx = \left(-\partial_x^{-2} v^{*,H^{-1}} \Big|_{t=0}, \phi' \right)_{L_2(\Omega)}. \quad (50)$$

Using the L_2 inner product (13) to extract the gradient, we may identify the gradient as

$$\nabla j = -\partial_x^{-2} v^{*, H^{-1}} \Big|_{t=0}. \quad (51)$$

4.4 Preconditioning the gradient

As indicated in (22c), the definition of the gradient may be generalized by taking the H^q inner product (rather than the L_2 inner product) when extracting the gradient from the expression of the cost functional differential. By so doing, we may emphasize the importance of some length scales over others during the iterative gradient-based optimization procedure, a strategy commonly referred to as preconditioning. Note again that (in a convex problem) the minimizer is not changed by such a procedure, though the gradients are significantly altered. For example, the cost functional differential (13) in the primitive formulation of the adjoint analysis may be rewritten to incorporate either an H^1 inner product or an H^{-1} inner product

$$j'(\phi; \phi') \triangleq \left(\nabla^{H^1} j, \phi' \right)_{H^1(\Omega)}, \quad j'(\phi; \phi') \triangleq \left(\nabla^{H^{-1}} j, \phi' \right)_{H^{-1}(\Omega)}. \quad (52)$$

By the definition of these inner products and the relation given in (18), it follows that the H^1 gradient, $\nabla^{H^1} j$, and the H^{-1} gradient, $\nabla^{H^{-1}} j$, may be identified as

$$\nabla^{H^1} j = -\partial_x^{-2} \bar{v}^* \Big|_{t=0}, \quad \nabla^{H^{-1}} j = -\partial_x^2 v^* \Big|_{t=0}. \quad (53)$$

We may thus extract different gradients from a given adjoint field calculation. Note that the H^1 gradient emphasizes the large length scales and the H^{-1} gradient emphasizes the small length scales. Conversely, as shown in (21), (46), and (51), we may also extract a given gradient from different adjoint field calculations.

We now explore the utility of the weighted linear combination of L_2 , H^1 , and H^{-1} inner products defined in (23) for preconditioning the gradient. For clarity, we first consider for this purpose the inner product $(z_1, z_2)_{W^{l_1, \infty}}$ which, as discussed previously, represents a linear combination of the L_2 and H^1 inner products. Returning to the standard formulation of the adjoint analysis, but extracting the gradient via this inner product, we obtain

$$\begin{aligned} j' &\triangleq \left(\nabla^{W^{l_1, \infty}} j, \phi' \right)_{W^{l_1, \infty}} = \frac{1}{1 + l_1^2} \int_0^{2\pi} \left[\left(\nabla^{W^{l_1, \infty}} j \right) \phi' + l_1^2 \left(\partial_x \nabla^{W^{l_1, \infty}} j \right) \left(\partial_x \phi' \right) \right] dx \\ &= \left(\frac{1}{1 + l_1^2} [1 - l_1^2 \partial_x^2] \nabla^{W^{l_1, \infty}} j, \phi' \right)_{L_2(\Omega)} = \left(\bar{v}^* \Big|_{t=0}, \phi' \right)_{L_2(\Omega)}. \end{aligned} \quad (54)$$

We may thus identify the desired gradient $\nabla^{W^{l_1, \infty}} j$ by solving the 1D Helmholtz

equation

$$\begin{cases} \frac{1}{1+l_1^2} [1-l_1^2 \partial_x^2] \nabla^{W^{l_1, \infty}} j = \bar{v}^*|_{t=0}, \\ \nabla^{W^{l_1, \infty}} j(0) = \nabla^{W^{l_1, \infty}} j(2\pi). \end{cases} \quad (55)$$

The interpretation of the significance of this expression is clear in Fourier space. Using $[\cdot]_k$ to denote the corresponding spatial Fourier coefficient at wavenumber k , it follows that

$$\left[\widehat{\nabla^{W^{l_1, \infty}} j} \right]_k = \frac{k_1^2 + 1}{k_1^2} \mathcal{F}_{lp}(k) \left[\widehat{\bar{v}^*}|_{t=0} \right]_k, \quad (56)$$

where $\mathcal{F}_{lp}(k) \triangleq k_1^2 / (k_1^2 + k^2)$ is a low-pass filter (see Figure 3a) with a cut-off wavenumber of $k_1 = 1/l_1$. A gradient defined with such a scale-dependent filter de-emphasizes the spatial wavenumbers greater than k_1 in the gradient-based optimization process. Note that taking $k_1 \rightarrow \infty$ recovers the standard L_2 gradient (which weights all wavenumbers equally), whereas taking $k_1 \rightarrow 0$ recovers the H^1 gradient. Note also that the inverse Laplacian is commonly used as a “smoother” in this type of problems. The inverse Helmholtz operator used to obtain the solution to (55) is a generalization of the inverse Laplacian, which is used to solve this system in the $l_1 \rightarrow \infty$ (that is, $k_1 \rightarrow 0$) limit. Both such operations may be used to obtain a “smooth” gradient even when the system is defined on a complicated domain in which Fourier analysis is not possible. Thus, this form of preconditioning has the effect of enforcing smoothness of the control and in this sense is similar to Tikhonov regularization. Formal connection between these two approaches is established in §4.5.5.

We now consider reintroducing the H^{-1} component into the weighted linear combination of inner products used to extract the gradient

$$\begin{aligned} j' &\triangleq \left(\nabla^{W^{l_1, l_{-1}}} j, \phi' \right)_{W^{l_1, l_{-1}}} = \dots \\ &= \left(\frac{l_{-1}^2}{(1+l_1^2)(1+l_{-1}^2)} \left[1 - \frac{l_1^2 l_{-1}^2}{l_1^2 + l_{-1}^2} \partial_x^2 - \frac{1}{l_1^2 + l_{-1}^2} \partial_x^{-2} \right] \nabla^{W^{l_1, l_{-1}}} j, \phi' \right)_{L_2(\Omega)} \\ &= \left(\bar{v}^*|_{t=0}, \phi' \right)_{L_2(\Omega)}. \end{aligned}$$

We may thus identify the desired gradient $\nabla^{W^{l_1, l_{-1}}} j$ by solving the system

$$\begin{cases} \frac{l_{-1}^2}{(1+l_1^2)(1+l_{-1}^2)} \left[1 - \frac{l_1^2 l_{-1}^2}{l_1^2 + l_{-1}^2} \partial_x^2 - \frac{1}{l_1^2 + l_{-1}^2} \partial_x^{-2} \right] \nabla^{W^{l_1, l_{-1}}} j = \bar{v}^*|_{t=0}, \\ \nabla^{W^{l_1, l_{-1}}} j(0) = \nabla^{W^{l_1, l_{-1}}} j(2\pi). \end{cases} \quad (57)$$

Again, the interpretation of this expression is clear in Fourier space. Taking $k_1 =$

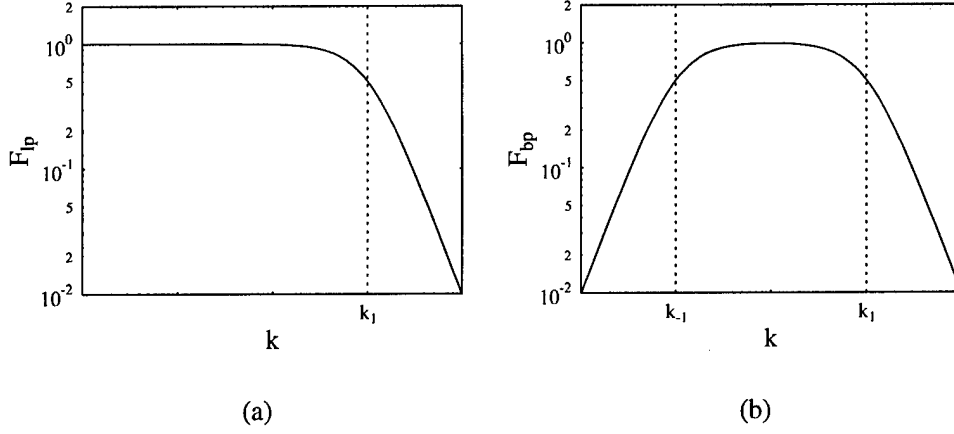


Fig. 3. Interpretation of the systems (55) and (57) in Fourier space as (a) low-pass and (b) band-pass filters which de-emphasize certain ranges of wavenumbers in the extraction of the gradient.

$1/l_1$ and $k_{-1} = 1/l_{-1}$, it follows that

$$\left[\widehat{\nabla^{l_1, l_{-1}} g} \right]_k = \frac{(k_1^2 + k_{-1}^2)(k_1^2 + 1)(k_{-1}^2 + 1)}{k_1^4} \mathcal{F}_{bp}(k) \left[\widehat{v}^*|_{t=0} \right]_k, \quad (58)$$

where $\mathcal{F}_{bp}(k) \triangleq \mathcal{F}_{lp}(k) \cdot k^2 / (k^2 + k_{-1}^2)$ is a band-pass filter (see Figure 3b) formed by the product of the low-pass filter found previously (with a cut-off wavenumber of $k_1 = 1/l_1$) and a high-pass filter with a cut-off wavenumber of $k_{-1} = 1/l_{-1}$. A band-pass filter of this sort is useful to employ when the optimization process in the multiscale system is designed to target “intermediate-scale” phenomena.

4.5 Relations between different regularization strategies

We now summarize the relations between the various alternatives in the framing of an adjoint analysis, as discussed in detail in the example considered above. We will first (in §4.5.1) show how adjoint operators corresponding to alternative forms of the evolution equation (§4.1) and alternative duality pairings (§4.3) are related to the primitive adjoint operator \mathcal{L}^* determined in §3. We will then (in §4.5.2) discuss how the associated adjoint fields are related, and tabulate how any of three cost functional gradients sought may be determined from any of five alternative forms of the adjoint system. After brief discussions of an interesting special case (in §4.5.3), an alternative method of deriving an adjoint analysis (in §4.5.4), and the relation of Tikhonov regularization to gradient preconditioning (in §4.5.5), we conclude the section (in §4.5.6) with a discussion of the important numerical consequences of these alternative formulations of an adjoint analysis.

4.5.1 Relations between the various adjoint operators

Recall first that $w = \partial_x v$, $w' = \partial_x v'$, and thus, by (12) and (27), that $\partial_x \mathcal{L}z = \mathcal{M}\partial_x z$. By the identity (15), which defines \mathcal{L}^* , it thus follows (assuming all variables are periodic in x) that

$$\begin{aligned} \langle w^*, \mathcal{M}w' \rangle_{L_2(0,T;L_2(\Omega))} &= \langle w^*, \partial_x \mathcal{L}v' \rangle_{L_2(0,T;L_2(\Omega))} = \langle -\partial_x w^*, \mathcal{L}v' \rangle_{L_2(0,T;L_2(\Omega))} \\ &= \langle \mathcal{L}^*(-\partial_x w^*), v' \rangle_{L_2(0,T;L_2(\Omega))} - \left[\int_0^{2\pi} (\partial_x w^*) v' dx \right]_{t=0}^{t=T} \\ &= \langle \partial_x^{-1} \mathcal{L}^*(\partial_x w^*), \partial_x v' \rangle_{L_2(0,T;L_2(\Omega))} - \left[\int_0^{2\pi} (\partial_x w^*) v' dx \right]_{t=0}^{t=T}. \end{aligned}$$

Note that the above derivation computes the adjoint of a composition of operators, $\partial_x \mathcal{L}$, and the result is consistent with a general property of adjoint calculus, namely that $(\mathcal{T}_1 \mathcal{T}_2)^* = \mathcal{T}_2^* \mathcal{T}_1^*$, where \mathcal{T}_1 and \mathcal{T}_2 are two linear operators. Note also that, in general, $\mathcal{T}_2^* \mathcal{T}_1^* \neq \mathcal{T}_1^* \mathcal{T}_2^*$. Noting (28), it follows that

$$\mathcal{M}^* z = \partial_x^{-1} \mathcal{L}^*(\partial_x z). \quad (59)$$

Using a similar approach, it is also straightforward to show that

$$\mathcal{K}^* z = \partial_x \mathcal{L}^*(\partial_x^{-1} z). \quad (60)$$

Similar relationships may be found for the adjoint operators derived from the H^1 and H^{-1} duality pairings. For example, it is easily seen (again assuming all variables are periodic in x) that

$$\begin{aligned} \langle v^{*,H^1}, \mathcal{L}v' \rangle_{L_2(0,T;H^1(\Omega))} &= \langle \partial_x v^{*,H^1}, \partial_x \mathcal{L}v' \rangle_{L_2(0,T;L_2(\Omega))} = \langle -\partial_x^2 v^{*,H^1}, \mathcal{L}v' \rangle_{L_2(0,T;L_2(\Omega))} \\ &= \langle -\mathcal{L}^*(\partial_x^2 v^{*,H^1}), v' \rangle_{L_2(0,T;L_2(\Omega))} - \left[\int_0^{2\pi} (\partial_x^2 v^{*,H^1}) v' dx \right]_{t=0}^{t=T} \\ &= \langle \partial_x^{-2} \mathcal{L}^*(\partial_x^2 v^{*,H^1}), v' \rangle_{L_2(0,T;H^1(\Omega))} - \left[\int_0^{2\pi} (\partial_x^2 v^{*,H^1}) v' dx \right]_{t=0}^{t=T}. \end{aligned}$$

Noting (42), it follows that

$$\mathcal{L}^{*,H^1} z = \partial_x^{-2} \mathcal{L}^*(\partial_x^2 z). \quad (61)$$

Using a similar approach, it is also straightforward to show that

$$\mathcal{L}^{*,H^{-1}} z = \partial_x^2 \mathcal{L}^*(\partial_x^{-2} z). \quad (62)$$

4.5.2 Relations between the various adjoint fields

Substituting (59) into (29), it is seen that $-\partial_x w^*$ satisfies an equivalent set of equations as that defining v^* in (17). We may thus conclude that the primitive adjoint variable v^* and the vorticity adjoint variable w^* are related such that $v^* = -\partial_x w^*$. By (31), it thus follows that

$$\nabla \mathcal{J}_\varphi = -\partial_x^{-1} v^* \Big|_{t=0}. \quad (63)$$

The quantity $\nabla \mathcal{J}_\varphi$ is simply the gradient of the cost functional $\mathcal{J}_\varphi(\varphi)$ in the space of φ , where the metric is defined by the L_2 inner product.

We now consider two gradient descent algorithms: one conducted in the space of φ and proceeding at each step in the direction $\nabla \mathcal{J}_\varphi$, and the other conducted in the space of ϕ and proceeding at each step in some direction s_ϕ . We then constrain s_ϕ such that the two descent algorithms are equivalent in the sense that $\varphi^{(n)} = \partial_x \phi^{(n)}$ for all iterations i . It follows that

$$\left. \begin{aligned} \varphi^{(n)} &= \varphi^{(n-1)} - \alpha \nabla \mathcal{J}_\varphi \\ \phi^{(n)} &= \phi^{(n-1)} - \alpha s_\phi \end{aligned} \right\} \implies s_\phi = \partial_x^{-1} (\nabla \mathcal{J}_\varphi),$$

that is, the corresponding descent direction in the space of ϕ is given by $s_\phi \triangleq \partial_x^{-1} (\nabla \mathcal{J}_\varphi)$. Combining this with (63) and (53), we obtain

$$s_\phi = -\partial_x^{-2} v^* \Big|_{t=0} = \nabla^{H^1} \mathcal{J},$$

that is, gradient extraction via the L_2 inner product in the space of $\varphi = \partial_x \phi$ and gradient extraction via the H^1 inner product in the space of ϕ are equivalent. Using a similar approach, it is straightforward to show that gradient extraction via the L_2 inner product in the space of $\psi = \partial_x^{-1} \phi$ (where ψ is again restricted to have zero mean) and gradient extraction via the H^{-1} inner product in the space of ϕ are equivalent. Similar observations regarding gradient computations before and after a transformation of the independent variables in a system (in the finite-dimensional setting) were made by Dennis & Schnabel [34].

Noting the convenient form of the terms b_1 and b_{-1} in (42) and (47), it is seen that the derivation of the H^1 gradient [see (52)] follows naturally from the adjoint field defined with the H^1 duality pairing, and that the H^{-1} gradient follows naturally from the adjoint field defined with the H^{-1} duality pairing

$$\nabla^{H^1} \mathcal{J} = v^{*,H^1} \Big|_{t=0}, \quad \text{and} \quad \nabla^{H^{-1}} \mathcal{J} = v^{*,H^{-1}} \Big|_{t=0}.$$

In order to summarize the pattern that emerges from the application of the various regularization strategies to the formulation of adjoint-based analyses, we collect

some of the significant relations between the various adjoint operators, the corresponding adjoint fields, and the different gradients in Table 1.

4.5.3 Special case: spatially-uniform linearized systems

The relationships between the various alternative forms of adjoint analyses summarized above simplify greatly when the linearization of the governing evolution equation is spatially uniform (that is, it does not have spatially-varying coefficients). This is the case, for instance, when the system (2) is linearized about the state $v = \text{constant}$. The perturbation operator for such a case will be denoted \mathcal{L}_0 and its adjoint \mathcal{L}_0^* ; both may be obtained from (12) and (17) by setting $v = \text{constant}$. The reason for the simplification in this special case is that both \mathcal{L}_0 and \mathcal{L}_0^* commute with ∂_x , and thus, by (59)-(61), $\mathcal{L}_0^* = \mathcal{K}_0^* = \mathcal{M}_0^* = \mathcal{L}_0^{*,H^1} = \mathcal{L}_0^{*,H^{-1}}$.

We now consider the system (17), with the operator \mathcal{L}^* replaced by \mathcal{L}_0^* . Defining $v_1^* \triangleq -\partial_x^{-2} v^*$ and noting (53), the gradient of the cost functional \mathcal{J} extracted using the H^1 inner product may be written $\nabla^{H^1} \mathcal{J}^{L_2} = v_1^*|_{t=0}$. Thus,

$$\mathcal{L}_0^* v^* = \mathcal{L}_0^* (-\partial_x^2 v_1^*) = -\partial_x^2 \mathcal{L}_0^* v_1^* = \mathcal{H}^* (\mathcal{H}v - y) \implies \mathcal{L}_0^* v_1^* = -\partial_x^{-2} \mathcal{H}^* (\mathcal{H}v - y).$$

By the discussion in §4.2, it is seen that v_1^* is exactly the adjoint variable used when the cost functional $\mathcal{J}^{H^{-1}}$ is minimized. It follows (in this special case only) that $\nabla^{H^1} \mathcal{J}^{L_2} = \nabla^{L_2} \mathcal{J}^{H^{-1}}$ and, similarly, that $\nabla^{H^{-1}} \mathcal{J}^{L_2} = \nabla^{L_2} \mathcal{J}^{H^1}$.

4.5.4 Optimization derivations based on Lagrange multipliers

It is important to note that the four distinct regularization opportunities considered in this paper are also available when the evolution equation of the system is incorporated into the optimization problem with a Lagrange multiplier approach. In such derivations, the cost functional selected is first augmented with a selected form of the duality pairing (cf. §4.3) of a Lagrange multiplier with a selected form of the governing equation (cf. §4.1). This augmented cost functional is then minimized with respect to both the chosen control variable and the Lagrange multiplier, often using a gradient-based strategy using a selected form of an inner product to define the gradient. This setting effectively renders the optimization problem as “unconstrained”, and the Lagrange multiplier itself turns out to be equivalent to the adjoint field used in the present derivation. In derivations based on such Lagrange multiplier techniques, all four of the regularization opportunities outlined in this paper are still available and may be selected to achieve the desired regularizing effect.

Section introduced	Perturbation system	Duality pairing	Adjoint system	$\nabla^{L_2} \mathcal{J}$	$\nabla^{H^1} \mathcal{J}$	$\nabla^{H^{-1}} \mathcal{J}$
§3	$\mathcal{L}v' = 0$ $v'(0) = \phi$	$\langle \cdot, \cdot \rangle_{L_2(0,T;L_2(\Omega))}$	$\mathcal{L}^*v^* = f = \mathcal{H}^*(\mathcal{H}v - y),$ $v^*(T) = 0$	$v^* _{t=0}$	$-\partial_x^{-2}v^* _{t=0}$	$-\partial_x^2v^* _{t=0}$
§4.1.1	$\mathcal{M}w' = \partial_x \mathcal{L}v' = 0,$ $w'(0) = \varphi = \partial_x \phi$	$\langle \cdot, \cdot \rangle_{L_2(0,T;L_2(\Omega))}$	$\mathcal{M}^*w^* = \partial_x^{-1} \mathcal{L}^*(\partial_x w^*) = -\partial_x^{-1} f,$ $w^*(T) = 0$	$-\partial_x w^* _{t=0}$	$\partial_x^{-1}w^* _{t=0}$	$\partial_x^3w^* _{t=0}$
§4.1.2	$\mathcal{K}u' = \partial_x^{-1} \mathcal{L}v' = 0,$ $u'(0) = \psi = \partial_x^{-1} \phi$	$\langle \cdot, \cdot \rangle_{L_2(0,T;L_2(\Omega))}$	$\mathcal{K}^*u^* = \partial_x \mathcal{L}^*(\partial_x^{-1}u^*) = -\partial_x f,$ $u^*(T) = 0$	$-\partial_x^{-1}u^* _{t=0}$	$\partial_x^{-3}u^* _{t=0}$	$\partial_x u^* _{t=0}$
§4.3.1	$\mathcal{L}v' = 0,$ $v'(0) = \phi$	$\langle \cdot, \cdot \rangle_{L_2(0,T;H^1(\Omega))}$	$\mathcal{L}^{*,H^1}v^{*,H^1} = \partial_x^{-2} \mathcal{L}^*(\partial_x^2 v^{*,H^1}) = \partial_x^{-2} f,$ $v^{*,H^1}(T) = 0$	$-\partial_x^2 v^{*,H^1} _{t=0}$	$v^{*,H^1} _{t=0}$	$\partial_x^4 v^{*,H^1} _{t=0}$
§4.3.2	$\mathcal{L}v' = 0,$ $v'(0) = \phi$	$\langle \cdot, \cdot \rangle_{L_2(0,T;H^{-1}(\Omega))}$	$\mathcal{L}^{*,H^{-1}}v^{*,H^{-1}} = \partial_x^2 \mathcal{L}^*(\partial_x^{-2} v^{*,H^{-1}}) = \partial_x^2 f,$ $v^{*,H^{-1}}(T) = 0$	$-\partial_x^{-2} v^{*,H^{-1}} _{t=0}$	$\partial_x^{-4} v^{*,H^{-1}} _{t=0}$	$v^{*,H^{-1}} _{t=0}$

Table 1. Summary of the principal relations resulting from application of various regularization strategies to the formulation of an adjoint-based optimization algorithm.

4.5.5 Tikhonov regularization in the gradient optimization setting

One common technique to regularize an optimization problem is to modify the cost functional (see §4.2) by adding a term which explicitly penalizes the irregularity of the control ϕ . This approach is commonly referred to as Tikhonov regularization (see, e.g., [27], [10], [11], and [12]). When applied to the data assimilation problem formulated in §3, this results in a new cost functional

$$\mathcal{J}_r(\phi) = \mathcal{J}(\phi) + \ell_r^2 \|\phi\|_{H^r(\Omega)}^2, \quad (64)$$

where ℓ_r and $r > 0$ are constants characterizing the degree and form of the regularization. The differential of this functional is given by

$$\mathcal{J}'_r(\phi; \phi') = \mathcal{J}'(\phi; \phi') + \ell_r^2 \int_0^{2\pi} (\partial_x^r \phi) (\partial_x^r \phi') dx,$$

from which we may extract the L_2 gradient of the functional as

$$\widehat{\nabla \mathcal{J}}_r = \widehat{\nabla \mathcal{J}} + \ell_r^2 k^{2r} \hat{\phi}, \quad (65)$$

where $\nabla \mathcal{J}$ may be determined as in §3 and for convenience we adopt the Fourier-space representation.

The optimization problem which we are attempting to solve may be written as $\widehat{\nabla \mathcal{J}}_r(\phi) = 0$. Further, the gradient-based optimization strategy which we have employed to solve this problem may be interpreted as a method to find the stationary solution of the following system, which evolves in the artificial “pseudo-time” coordinate τ

$$\begin{cases} \frac{d\hat{\phi}}{d\tau} = -\widehat{\nabla \mathcal{J}}_r = -\widehat{\nabla \mathcal{J}} - \ell_r^2 k^{2r} \hat{\phi} & \text{on } \tau \in (0, \infty), \\ \hat{\phi} = \hat{\phi}_0 & \text{at } \tau = 0. \end{cases} \quad (66)$$

Effectively, we are attempting to march this artificial system as rapidly as possible to steady state characterized by $\frac{d\hat{\phi}}{d\tau} \approx 0$. Time accuracy during this artificial march is not required. This interpretation facilitates solution of the optimization problem at hand by adopting a variety of different time-discretization strategies applied to (66). Due to complexity involved in its evaluation (employing both forward and adjoint simulations), the term $\widehat{\nabla \mathcal{J}}$ must be calculated explicitly. However, the term $\ell_r^2 k^{2r} \hat{\phi}$ is easily handled with a variety of either implicit or explicit treatments. This leads to many possible forms of the optimization algorithm, including:

1. explicit (Euler) treatment of the penalty term

$$\hat{\phi}^{(n+1)} = \hat{\phi}^{(n)} - \Delta\tau (\widehat{\nabla \mathcal{J}}_r)^{(n)} = -\Delta\tau (\widehat{\nabla \mathcal{J}})^{(n)} + [1 - \Delta\tau \ell_r^2 k^{2r}] \hat{\phi}^{(n)},$$

2. implicit (Cranck–Nicholson) treatment of the penalty term

$$\begin{aligned}
\hat{\phi}^{(n+1)} &= \hat{\phi}^{(n)} - \Delta\tau \left[(\widehat{\nabla \mathcal{J}})^{(n)} + \ell_r^2 k^{2r} \left(\hat{\phi}^{(n)} + \hat{\phi}^{(n+1)} \right) / 2 \right] \\
&= -\frac{\Delta\tau}{1 + \frac{1}{2}\Delta\tau \ell_r^2 k^{2r}} (\widehat{\nabla \mathcal{J}})^{(n)} + \left[\frac{1 - \frac{1}{2}\Delta\tau \ell_r^2 k^{2r}}{1 + \frac{1}{2}\Delta\tau \ell_r^2 k^{2r}} \right] \hat{\phi}^{(n)} \\
&= \hat{\phi}^{(n)} - \Delta\tau \frac{(\widehat{\nabla \mathcal{J}})^{(n)}}{1 + \frac{1}{2}\Delta\tau \ell_r^2 k^{2r}},
\end{aligned}$$

where $\Delta\tau$ is some discrete stepsize in the pseudo-time coordinate τ . Taking $\Delta\tau = \text{constant}$ results in what is sometimes referred to as Landweber iteration (see, e.g., [10]), and is often the approach most amenable to numerical analysis. In practice, however, it is usually more efficient to adjust the stepsize $\Delta\tau$ at every iteration in order to minimize \mathcal{J}_r . Note that the explicit method #1 suffers from a stability constraint $\Delta\tau \leq 2\ell_r^{-2}k_{\max}^{-2r}$ which is reminiscent of a CFL condition and, if violated, will result in an unstable explicit march and amplification of the small scales of the field $\hat{\phi}$. In practice, method #1 is therefore generally not preferred. On the other hand, no such restriction applies to method #2. Furthermore, we observe that the semi-implicit method #2 may in fact be regarded as an explicit approach utilizing the cost functional $\mathcal{J}_r(\phi)$ and a smoothed gradient extracted with the inner product $(z_1, z_2)_{L_2(\Omega)} + \frac{\ell_r^2 \Delta\tau}{2} (z_1, z_2)_{H^r(\Omega)}$ (see §4.4). We thus see that the semi-implicit variant of Tikhonov regularization is in fact a special case of the regularization framework proposed in the present study, incorporating appropriate forms of the cost function and the inner product used to extract the gradient.

4.5.6 Numerical implications

As summarized in Table 1, the alternative adjoint systems considered in this paper are related, and any of the cost functional gradients sought may be found from any of several alternative definitions of the adjoint system. Thus, these alternative definitions of the adjoint system might not be of much interest from a purely mathematical standpoint, as (in the continuous setting) they all contain essentially the same information. From the standpoint of a discrete numerical implementation, however, the distinction between these various derivations can be quite significant. To illustrate this, the present subsection analyzes the adjoint systems considered in §3, §4.3.1, and §4.3.2 (that is, the adjoint systems formulated in the standard approach and the approaches incorporating H^1 and H^{-1} duality pairings). In §5.1, this analysis is further supported with numerical simulations.

There are two essential features of the alternative definitions of the adjoint systems which are noteworthy. The first is that, as compared with the standard adjoint system (17), which is forced by a term $f = \mathcal{H}^*(\mathcal{H}v - y)$ related to the measurement misfit, the adjoint system considered in (44) (that is, when the H^1 duality pairing is used) is forced by a significantly smoother term, $-\partial_x^{-2}f$, whereas the adjoint

system considered in (49) (that is, when the H^{-1} duality pairing is used) is forced by a significantly less smooth term, $-\partial_x^2 f$. We may thus expect the energy as a function of spatial wavenumber of the field v^{*,H^1} to have a significantly faster roll-off with wavenumber, and the energy as a function of spatial wavenumber of the field $v^{*,H^{-1}}$ to have a significantly slower roll-off with wavenumber, as compared with the primitive adjoint system v^* . The field v^{*,H^1} is thus significantly easier to compute accurately than both v^* and $v^{*,H^{-1}}$.

The second noteworthy feature is that the alternative adjoint systems differ in their “advection terms”, which [by (16), (43), and (48)] we identify as

$$\mathcal{B}^* z = v \partial_x z, \quad \left[\widehat{\mathcal{B}^* z} \right]_k = \sum_{k'=-k_{\max}}^{k_{\max}} [\hat{v}]_{k-k'} i k' [\hat{z}]_{k'}, \quad (67a)$$

$$\mathcal{B}^{*,H^1} z = \partial_x^{-2} (v \partial_x^3 z), \quad \left[\widehat{\mathcal{B}^{*,H^1} z} \right]_k = \sum_{k'=-k_{\max}}^{k_{\max}} \frac{k'^2}{k^2} [\hat{v}]_{k-k'} i k' [\hat{z}]_{k'}, \quad (67b)$$

$$\mathcal{B}^{*,H^{-1}} z = \partial_x^2 (v \partial_x^{-1} z), \quad \left[\widehat{\mathcal{B}^{*,H^{-1}} z} \right]_k = \sum_{\substack{k'=-k_{\max} \\ k' \neq 0}}^{k_{\max}} \frac{k^2}{k'^2} [\hat{v}]_{k-k'} i k' [\hat{z}]_{k'}. \quad (67c)$$

Note again that we have used the convention $[\hat{z}]_k$ for the k -th component of the discrete Fourier transform of z , and that $[\widehat{z_1 z_2}]_k = \sum_{k'} [\hat{z}_1]_{k'} [\hat{z}_2]_{k-k'}$. Due to presence of the spatially-varying coefficient (that is, the field v), these advection terms act to redistribute energy among different Fourier modes, much in the same way as does the nonlinear term in the original Kuramoto–Sivashinsky equation. The presence of the extra factors of k'^2/k^2 and k^2/k'^2 in the Fourier transforms of these advection terms distinguishes the alternative adjoint operators \mathcal{L}^{*,H^1} and $\mathcal{L}^{*,H^{-1}}$ from the standard adjoint operator \mathcal{L}^* . To appreciate the impact of these extra factors in a marginally-resolved system, it is of interest to consider their influence on the largest resolved wavenumber (that is, the smallest resolved length scale) in the numerical representation of the system. Thus, taking $k = k_{\max}$ in the above expressions, it is seen that, as compared with the primitive adjoint advection term in (67a), the sum in (67b) representing the the corresponding term in the H^1 adjoint equation has a coefficient which varies from 0 to 1. The contribution to this sum with the largest coefficient is due to the adjoint modes with large wavenumber k' (which do not contain much energy anyway, due to the reasons discussed in the previous paragraph), and the primal modes with small wavenumber $k_{\max} - k'$ (which are well resolved in the numerical simulation). On the other hand, the sum in (67c) representing the corresponding term in the H^{-1} adjoint equation has a coefficient which varies from 1 to k_{\max}^2/k_{\min}^2 (which might be quite large). The contribution to this sum with the largest coefficient is due to the adjoint modes with small wavenumber k' (which do contain significant energy), and the primal modes with large wavenumber $k_{\max} - k'$ (which might not be well resolved in the numerical simulation, and may thus be corrupted by noise). We thus again conclude that the field v^{*,H^1} should be significantly easier

to compute accurately on a marginally-resolved numerical grid.

5 Computational examples

In this section, we provide a few computational examples to illustrate how the different brackets used in the framing of an adjoint analysis may be used to affect the computational accuracy and the rate of convergence of a numerical optimization algorithm. Based on this analysis, we then propose a promising multiscale preconditioning approach that improves the convergence of the state reconstruction problem highlighted in the previous two sections. Note that the present computational study is by no means meant to be exhaustive, but simply to indicate the utility of pursuing the various regularization opportunities outlined previously. Many interesting related questions are left to be characterized numerically in future work.

In the PDE setting, the descent direction determined via an adjoint analysis depends solely on the choice of the norm in the cost function (see §4.2) and the inner product used to extract the gradient (see §4.4). The choice of the form of the evolution equation (see §4.1) and the duality pairing (see §4.3) affect only *how* the desired gradient of the cost functional selected is determined.

In the discrete numerical implementation, however, selecting appropriate forms for the evolution equation and the duality pairing can have a very significant effect on the computational complexity of the resulting finite-dimensional approximations of the flow and adjoint systems. The choice of the form of the evolution equation (primitive, vorticity, or streamfunction) and its effect on the complexity of the state simulation has already been studied extensively in the numerical simulation literature. This choice together with the choice of the duality pairing (L_2 , H^1 , or H^{-1}) and their combined effect on the complexity of the associated adjoint simulation, though equally important, have barely even been mentioned in the numerical optimization literature. The present paper attempts to draw attention to these important issues.

The specific problem considered in the data assimilation results reported here is obtained by setting $\kappa = 4 \cdot 10^3$ in (2). This rather high value for κ insures the system under consideration exhibits chaotic multiscale dynamics. The peak of the energy spectrum of the system is generally between $k = 20$ and $k = 25$ and, for higher wavenumbers, the spectrum rolls off rapidly after that. Around 22 to 23 peaks may usually be counted in the domain Ω at any given time. A typical numerical simulation of this system is shown in Figure 4.

The initial condition (selected on the chaotic attractor of the system) which we will seek to reconstruct, based solely on measurements of the system on $[0, T]$, is that shown in Figure 4a. The length of the optimization horizon T used, which corre-

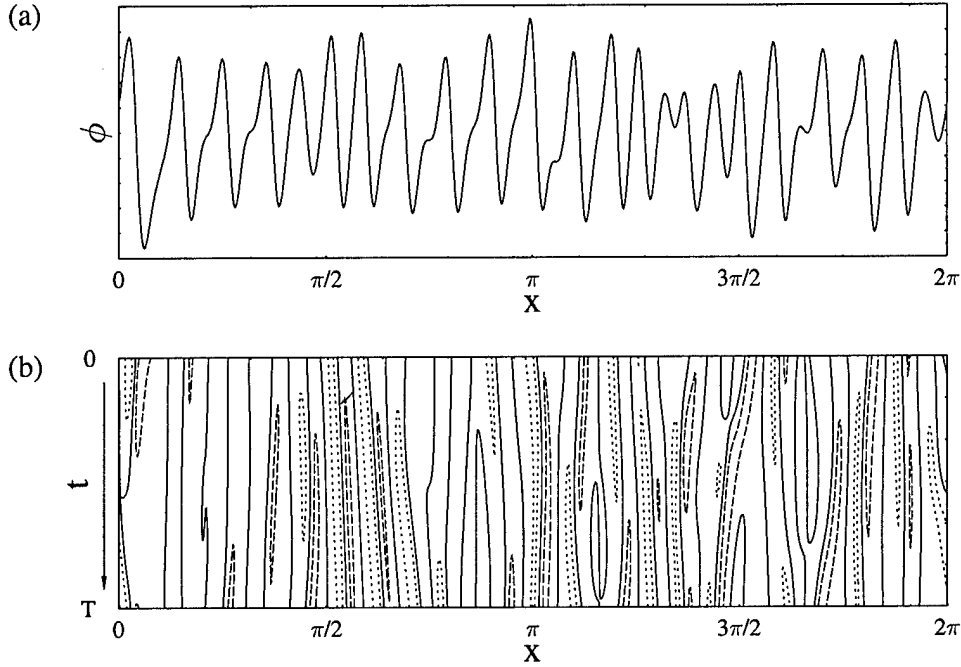


Fig. 4. Dynamics of the Kuramoto-Sivashinsky system for $\kappa = 4 \cdot 10^3$: (a) initial condition $v(0) = \phi$ (chosen on the chaotic attractor of the system), and (b) spatio-temporal evolution of the system (visualized are the zero (solid), several positive (dotted) and negative (dashed) isocontours of v in the space-time plane).

sponds to about 300 time steps, is sufficient to demonstrate significant dynamics of the chaotic system, as illustrated in Figure 4b. The observation operator \mathcal{H} selected represents observation of the real part of the first 50 Fourier coefficients (*i.e.*, the first 50 coefficients of the cosine decomposition) of the primitive variable v [that is, $\Lambda_r = \{1, \dots, 50\}$ in (8)]. We will assume for the purpose of this discussion that our measurements are not corrupted by noise [that is, $\eta = 0$ in (6)]. The initial guess for the initial conditions, $\phi^{(0)}$, will be taken to be zero in all optimizations attempted. These several choices make the (admittedly contrived) state reconstruction problem studied here difficult, yet still solvable in a reasonable number of iterations. This problem thus provides a tractable 1D multiscale chaotic testbed which is useful in quantifying the effectiveness of the various regularization strategies proposed. Extension of these strategies from the present 1D model problem to 2D and 3D systems of engineering relevance are straightforward—a few such extensions of particular interest are discussed briefly in §6.

In the present work, the state and adjoint systems are both solved in the well-resolved setting (on 512 grid points) using a dealiased pseudospectral method. Time advancement is performed using an RK3 scheme on the nonlinear term and a generalized trapezoidal method with $\theta = 5/8$ (see [35]) on the linear terms. Gradient iterations are carried out using the Polak-Ribiere version of the Conjugate Gradient (CG) method (see, *e.g.*, Nocedal and Wright [32]). The “momentum” term in the CG method is calculated using a standard L_2 inner product, and is reset to

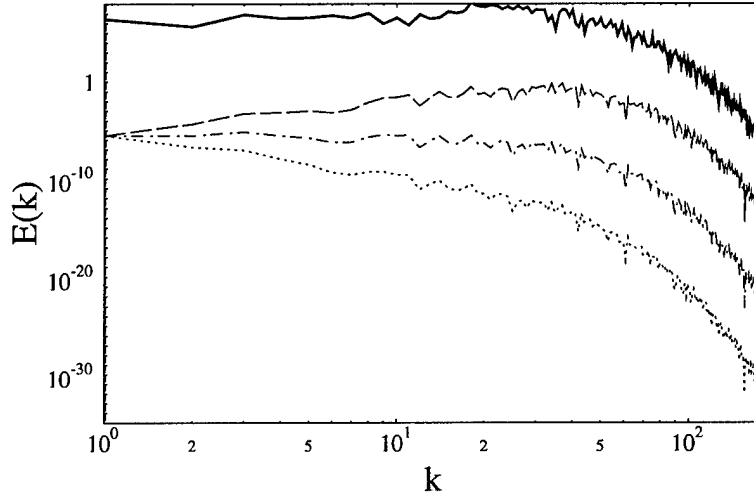


Fig. 5. Energy spectra of (solid) a typical solution of the Kuramoto-Sivashinsky equation (2) and of three different definitions of the corresponding adjoint system: (dashed) $v^{*,H^{-1}}$, as defined in (49), (dot-dashed) v^* , as defined in (17), and (dotted) v^{*,H^1} , as defined in (44).

zero every 20 iterations. Minimization in the descent direction is performed using Brent's method [36] at each iteration. A gradient method has been selected for the optimization rather than a quasi-Newton method (which is an attractive alternative) in order to provide a simple environment for comparison of the different adjoint formulations.

5.1 Spectra of the adjoint fields obtained with alternative formulations

Noting the discussion in §4.5.5, it is expected that the adjoint variables v^* , v^{*,H^1} , and $v^{*,H^{-1}}$ will have very different spectra, implying that some of these adjoint fields will require significantly higher spatial resolution to determine accurately than others. This behavior is clearly evident in Figure 5, where we compare the energy spectra of the adjoint variable at $t = 0$ (after the backward-time adjoint march) for three different definitions of the duality pairing after the 100th iteration of the optimization process. For comparison, we also show the energy spectrum of a typical solution $v(t)$ of the Kuramoto-Sivashinsky system (2) on the chaotic attractor. Note that the decay rates of the spectra are consistent with the relations shown in columns 5–7 of Table 1. Specifically, the energy spectrum of v^{*,H^1} rolls off k^4 faster than the energy spectrum of v^* , which rolls off k^4 faster than the energy spectrum of $v^{*,H^{-1}}$. The key issue is that, even though the adjoint equations are linear, the nonconstant coefficients in these equations relate the different Fourier modes of the adjoint field during its evolution in time. Thus, the differences between the energy spectra for the various possible definitions of the adjoint field are significant when

considering what resolution (or cut-off wavenumber) is required to compute accurately even the low-frequency components of the adjoint field. In particular, the accelerated roll-off with wavenumber of the Fourier transform of v^{*,H^1} may render this definition preferable in systems for which only marginal resolution can be afforded.

5.2 Optimization

As defined in (41), (6), (40), the three cost functionals $J^{H^{-1}}$, J , and J^{H^1} effectively measure the misfit of the model with the observed measurements with particular focus, respectively, on the large length scales, on all length scale, and on the small length scales. In this section, we will consider optimizations based on the minimization of all three of these cost functionals. To perform the optimizations, we will consider gradients extracted using the $W^{l_1,\infty}$ inner product, as defined in (54), for various values of l_1 . Recall that the $W^{l_1,\infty}$ inner product reduces to the L_2 inner product in the $l_1 \rightarrow 0$ limit, and to the H^1 inner product in the $l_1 \rightarrow \infty$ limit. To simplify the notation, the different cases considered in this section will be referred to using a shorthand notation $\{z_1, z_2\}$ to characterize the spatial component of the brackets Ψ_1 and Ψ_3 . For example, $\{L_2, L_2\}$ will be used to denote the standard (L_2 -based) formulation discussed in §3, whereas $\{H^1, W^{l_1,\infty}\}$ will be used to denote the formulation derived from the H^1 cost functional (40) together with the $W^{l_1,\infty}$ inner product used to define the gradient.

For the simulations presented in this section, to bypass further consideration of the numerical resolution issues discussed in the previous section, we will continue to use fine resolution, discretizing the system on 512 grid points. This resolution is sufficient to resolve the adjoint system obtained using any of the duality pairing definitions considered in the previous section. Thus, as summarized in Table 1, we may determine the gradient sought via appropriate use of any of these definitions of the adjoint operator. For simplicity, all calculations discussed in the present section are performed using just the primitive adjoint equation (16), which is based on the primitive form of the Kuramoto-Sivashinsky system and the standard L_2 duality pairing. This allows us to focus our attention in this section on the effects of modifying the brackets Ψ_1 and Ψ_3 .

5.2.1 Analysis after one iteration

We first analyze the effect of the choice of Ψ_1 and Ψ_3 after just one iteration. The progress made towards the minimum on the large length scales, over all length scales, and on the small length scales will be assessed based on the reduction of $J^{H^{-1}}$, J , and J^{H^1} respectively, regardless of which cost functional is actually minimized in the case considered.

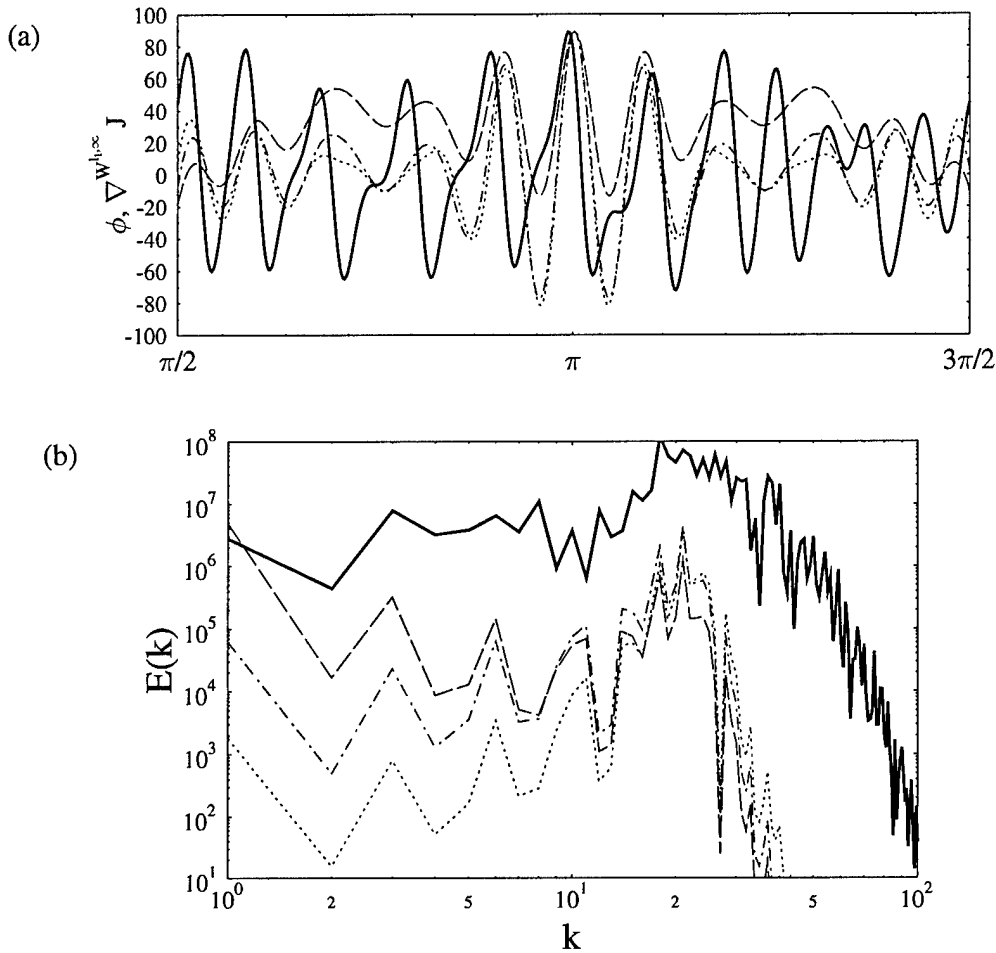
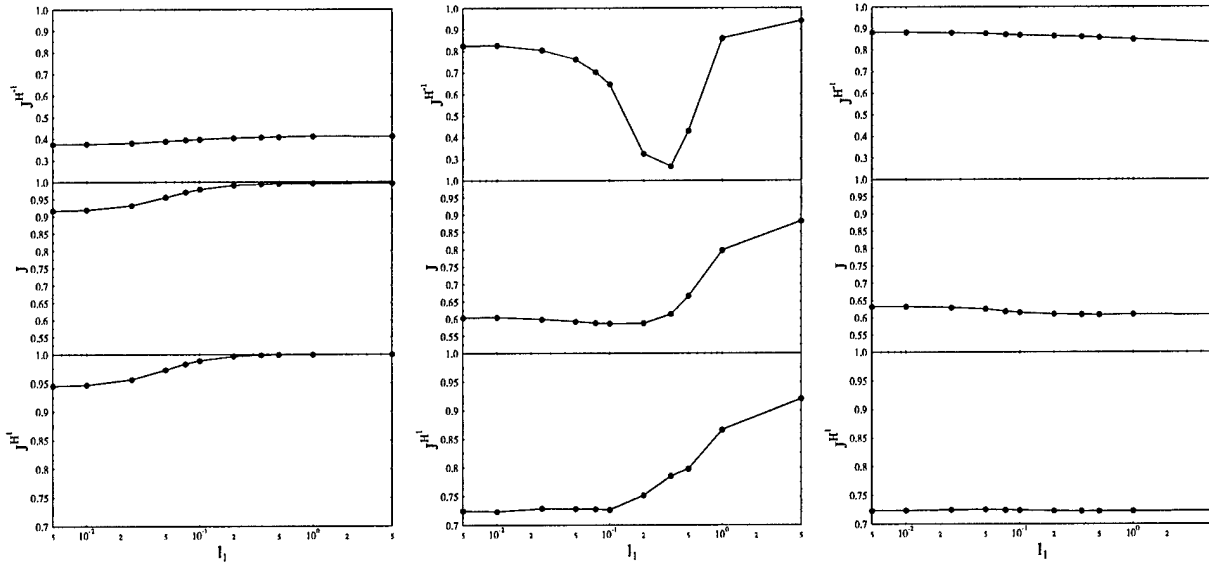


Fig. 6. (a) The shape of the gradients $\nabla^{W^{l_1, \infty}} j$ in physical space, normalized by their peak value on the subinterval shown. (b) The energy contained in the gradient field as a function of spatial wavenumber. The cases considered are: (dashed) $l_1 = 0.5$, (dot-dashed) $l_1 = 0.1$, and (dotted) $l_1 = 0$. For comparison, the solid lines depict the actual initial condition sought.

We begin by comparing the shapes of the gradients themselves in the case $\{L_2, W^{l_1, \infty}\}$ for different values of l_1 (Figure 6). Note that the various choices for l_1 which have been used result in substantially different gradients, and that, as l_1 increases, the gradients $\nabla^{W^{l_1, \infty}} j$ become significantly smoother (that is, as l_1 increases, the energy in the gradient field rolls off more rapidly with wavenumber). However, it is difficult to determine visually which of the gradients best captures the actual initial condition.

In Figure 7, we present values of the functionals $j^{H^{-1}}$, j , and j^{H^1} obtained after the first iteration in all the cases considered as a function of the length l_1 which parameterizes the inner product used in gradient extraction. Note in all the cases that the three functionals vary smoothly with l_1 and reveal similar trends. The upper-left subfigure illustrates the effect on $j^{H^{-1}}$ when a control strategy is used which



(a) minimizing $J^{H^{-1}}$

(b) minimizing J

(c) minimizing J^{H^1}

Fig. 7. Dependence of the functionals $J^{H^{-1}}$, J , and J^{H^1} on the length l_1 parameterizing the inner products $W^{l_1, \infty}$ used to extract the gradients during the first iteration. In all figures, the vertical axis is normalized by the value of the corresponding cost functional for the initial guess $\phi^{(0)}$ (that is, before the first iteration). Thus, a cost functional value of 0.6 in the above figures implies a 40% reduction of the corresponding cost functional after one iteration.

targets $J^{H^{-1}}$. Similarly, the lower-right subfigure illustrates the effect on J^{H^1} when a control strategy is used which targets J^{H^1} . Note in both cases that, after a single iteration, the functional targeted by the control algorithm is reduced substantially. However, as one might expect, control strategies that target large length scales do not work well at small length scales (see lower-left subfigure) and control strategies that target small length scales do not work well at large length scales (see upper-right subfigure). Also note that, in the case when J is minimized (center column), the functional $J^{H^{-1}}$ (which measures the quality of the fit at the large length scales) exhibits a particularly well-defined minimum for intermediate values of l_1 in the range $[0.1 - 0.35]$. For the case in which J is minimized with l_1 selected in this range, the performance on the large length scales is as good as when the functional $J^{H^{-1}}$ was targeted, and the performance on the intermediate and small scales is not significantly sacrificed. Further, the overall performance (in terms of all three metrics) is significantly better using the $W^{l_1, \infty}$ inner product for intermediate values of l_1 than when using either the L_2 or the H^1 inner products. We thus see that, when posing an optimization problem of this sort, it is useful to select appropriate definitions of both the cost functional (by appropriate selection of Ψ_1) and its gradient (by appropriate selection of Ψ_3) in order to tune the performance on the length scales of interest.

5.2.2 Analysis after many iterations

We now analyze the effect of the choice of Ψ_1 and Ψ_3 after 100 iterations are performed. Several cases were run; for brevity, the following cases of particular interest are reported here:

- 1) $\{H^{-1}, L_2\}$,
- 2) $\{L_2, L_2\}$
- 3) $\{L_2, W^{l_1, \infty}\}$ with $l_1 = 0.1$, and
- 4) $\{L_2, W^{l_1, \infty}\}$ with $l_1^{(n)} = l_1^{(0)} \zeta^n$, where $l_1^{(0)} = 0.1$ and $\zeta = 2/3$.

The fourth case will be referred to as a *multiscale preconditioning* approach. The motivation for this new approach is based on the observation that in multiscale nonlinear systems (such as hydrodynamic turbulence) the large-scale modes are usually more energetic than the small-scale modes. In such systems it appears logical to attempt first to determine the large length scales of the control ϕ (in the present problem, the estimate of the initial conditions) at the early iterations (for n small), before eventually attempting to tune ϕ at the small scales at later iterations (for n large). To facilitate this, the gradient is extracted using an $W^{l_1, \infty}$ inner product, where l_1 is relatively large at the early iterations and is subsequently reduced towards zero; $l_1^{(n)}$ thus provides a convenient “knob” controlling the cut-off length scale as a function of the iteration number n . This approach may be regarded as a *multiscale* version of the *variable preconditioning* method discussed in the context of finite-dimensional linear systems by Axelsson [37]. Appropriate values of $l_1^{(0)}$ and ζ for the present system were found by trial and error.

Note that, when computing the descent direction at every iteration of the present conjugate gradient descent algorithm, we need to evaluate a “momentum” term formed by a ratio of inner products of the recently-calculated gradients. Though there is some discussion of this issue in the literature, there appears to be no commonly-accepted strategy for selecting the inner product to use to calculate the momentum term when a variable preconditioning strategy is employed. We have used simple L_2 inner products to evaluate the momentum term in the present work. Other strategies were also tried, including the use of inner products in this calculation that varied from one iteration to the next. Unfortunately, none of these strategies were found to significantly accelerate convergence.

In Figure 8 we show the reduction of the three metrics $J^{H^{-1}}$, J , and J^{H^1} in the four cases mentioned above. The best convergence in terms of all three of these metrics is obtained using the multiscale preconditioning approach outlined above. Note also that the value of ζ selected in the multiscale preconditioning approach effectively resulted in “smoothing” of the gradient only during the first 10 – 20 iterations. After that, l_1 was so small that the gradients extracted using the $W^{l_1, \infty}$ inner product were virtually indistinguishable from the gradients extracted using the L_2 inner product. Even so, the multiscale preconditioning strategy had an appreciable beneficial effect on the overall optimization.

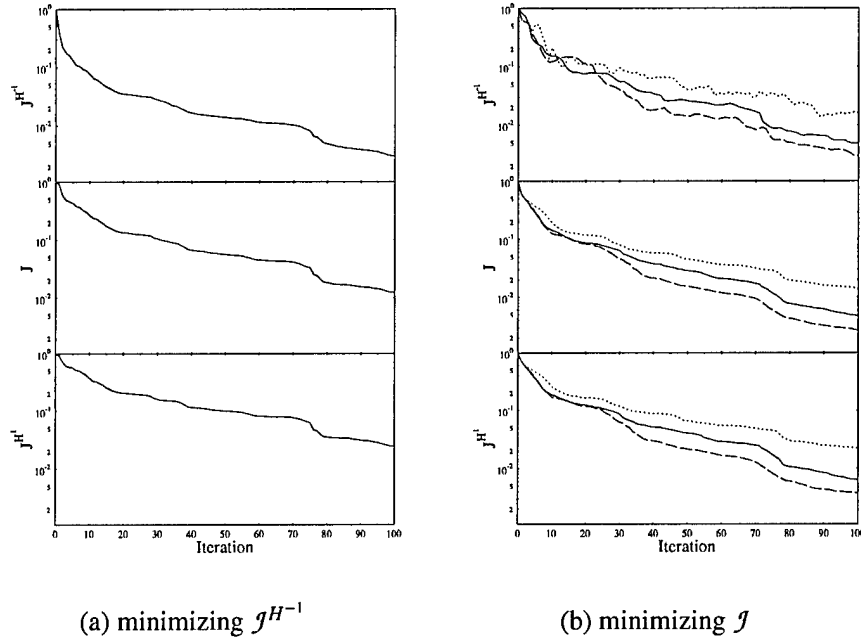


Fig. 8. Variation of the functionals $J^{H^{-1}}$, J , and J^{H^1} as a function of the iteration count for reconstructions based on the following inner products: (solid) L_2 , (dotted) $W^{l_1, \infty}$ with l_1 fixed, and (dashed) $W^{l_1, \infty}$ with l_1 progressively decreased towards zero.

6 Extensions

In §4 we presented a comprehensive picture of different regularization strategies applied to a simple model system. Since the ultimate goal is to apply these methods to real systems of physical and engineering interest, such as the Navier–Stokes equation in a bounded domain, below we show that such generalization is in fact straightforward. One significant difference is the more complicated structure of the governing equation and its adjoint when working in higher spatial dimensions. Another significant difference is related to the fact that various terms obtained from the integration by parts do not vanish on the solid boundaries. In order to highlight some of the issues, below we will study the effect of applying selected regularization options to the adjoint–based optimization of the Navier–Stokes system in a periodic domain (§6.1) and the Kuramoto–Sivashinsky equation in a bounded domain (§6.2). Due to space limitations, the case of the Navier–Stokes system in a bounded domain is deferred to a forthcoming paper.

6.1 Controlling a 3D Navier–Stokes System

We consider here a Navier–Stokes system

$$\begin{cases} \frac{\partial \mathbf{v}}{\partial t} + (\mathbf{v} \cdot \nabla) \mathbf{v} + \nabla p - \mu \Delta \mathbf{v} = \boldsymbol{\phi}, & \text{in } \Omega \times (0, T) \\ \nabla \cdot \mathbf{v} = 0, & \text{in } \Omega \times (0, T) \\ \mathbf{v} = \mathbf{v}_0 & \text{at } t = 0 \\ \mathbf{v} \text{ periodic in } x_1, x_2, x_3, \end{cases} \quad (68)$$

where \mathbf{v} is the velocity field, p is the pressure, μ is the viscosity, and $\boldsymbol{\phi}$ is an externally applied body force representing the control. The system is supplemented with the initial condition \mathbf{v}_0 and its evolution takes place in a domain $\Omega = [0, 2\pi]^3$ periodic in all three spatial dimensions. The domains Ω_1 , Ω_2 and Ω_3 (see §2) all coincide with Ω , while the system evolution, the control, and the cost function are all defined on $\Omega \times [0, T]$. Since we now deal with vector quantities depending on three spatial variables, and the control now also depends on time, the brackets (22a)–(22c) used to frame the adjoint analysis need to be suitably redefined

$$\|\mathbf{z}\|_{L_2(0,T;H^q(\Omega))}^2 \triangleq \int_0^T \int_{\Omega} \frac{\partial^q z_i}{\partial x_j^q} \frac{\partial^q z_i}{\partial x_j^q} d\Omega dt, \quad (69a)$$

$$\langle \mathbf{y}, \mathbf{z} \rangle_{L_2(0,T;H^q(\Omega))} \triangleq \int_0^T \int_{\Omega} \frac{\partial^q y_i}{\partial x_j^q} \frac{\partial^q z_i}{\partial x_j^q} d\Omega dt, \quad (69b)$$

$$(\mathbf{y}, \mathbf{z})_{L_2(0,T;H^q(\Omega))} \triangleq \int_0^T \int_{\Omega} \frac{\partial^q y_i}{\partial x_j^q} \frac{\partial^q z_i}{\partial x_j^q} d\Omega dt, \quad (69c)$$

where repeated indices imply summation and we will restrict our attention to the cases with $q \geq 0$. By analogy with (23), we can define inner products as a weighted linear combination of terms of the form (69c) with different values of q , e.g.,

$$(\mathbf{y}, \mathbf{z})_{L_2(0,T;W^{l_1,\infty})} \triangleq \frac{1}{1+l_1^2} \left[(\mathbf{y}, \mathbf{z})_{L_2(0,T;L_2(\Omega))} + l_1^2 (\mathbf{y}, \mathbf{z})_{L_2(0,T;H^1(\Omega))} \right]. \quad (70)$$

In order to emphasize the differences with respect to the standard approach, we analyze here the problem studied initially in the seminal paper of Abergel & Temam [38], i.e., enstrophy minimization with control in the form of the body force applied to the 3D Navier–Stokes system in a periodic domain. Consequently, we attempt to minimize the functional⁶

$$\mathcal{J}_{ns}(\boldsymbol{\phi}) \triangleq \frac{1}{2} \left\| \nabla \times \mathbf{v} \right\|_{L_2(0,T;L_2(\Omega))}^2. \quad (71)$$

⁶ For the sake of simplicity we skip here the penalty on the control $\boldsymbol{\phi}$. As noted in the numerical experiments of [5], the removal of this control penalty in nonlinear Navier–Stokes control problems apparently leads to bounded control feedback at least in a subset of well-defined problems.

The classical formulation is obtained by following the methodology of §3 (see also [38]). The differential of the cost functional is

$$\mathcal{J}'_{ns}(\phi, \phi') = \int_0^T \int_{\Omega} (\nabla \times \mathbf{v}) \cdot (\nabla \times \mathbf{v}') d\Omega dt = - \int_0^T \int_{\Omega} \Delta \mathbf{v} \cdot \mathbf{v}' d\Omega dt, \quad (72)$$

where ϕ' is a perturbation of the control and $\mathbf{v}'(\phi, \phi')$ solves the system

$$\begin{cases} \mathcal{N} \begin{bmatrix} \mathbf{v}' \\ p' \end{bmatrix} = \begin{bmatrix} \phi' \\ 0 \end{bmatrix} & \text{in } \Omega \times (0, T), \\ \mathbf{v}' = 0 & \text{at } t = 0, \\ \mathbf{v}' \text{ periodic in } x_1, x_2, x_3, \end{cases} \quad (73)$$

with the linear operator

$$\mathcal{N} \begin{bmatrix} \mathbf{v}' \\ p' \end{bmatrix} = \begin{bmatrix} \frac{\partial \mathbf{v}'}{\partial t} + (\mathbf{v} \cdot \nabla) \mathbf{v}' + (\mathbf{v}' \cdot \nabla) \mathbf{v} - \mu \Delta \mathbf{v}' + \nabla p' \\ -\nabla \cdot \mathbf{v}' \end{bmatrix}. \quad (74)$$

We now define an adjoint operator with the identity

$$\left\langle \mathcal{N} \begin{bmatrix} \mathbf{v}' \\ p' \end{bmatrix}, \begin{bmatrix} \mathbf{v}^* \\ p^* \end{bmatrix} \right\rangle_{L_2(0, T; L_2(\Omega))} = \left\langle \begin{bmatrix} \mathbf{v}' \\ p' \end{bmatrix}, \mathcal{N}^* \begin{bmatrix} \mathbf{v}^* \\ p^* \end{bmatrix} \right\rangle_{L_2(0, T; L_2(\Omega))} + b_{ns}, \quad (75)$$

where the duality pairing of vectors is defined in (69b). Consequently, the adjoint operator has the form

$$\mathcal{N}^* \begin{bmatrix} \mathbf{v}^* \\ p^* \end{bmatrix} = \begin{bmatrix} -\frac{\partial \mathbf{v}^*}{\partial t} - \mathbf{v} \cdot [\nabla \mathbf{v}^* + (\nabla \mathbf{v}^*)^T] - \mu \Delta \mathbf{v}^* + \nabla p^* \\ -\nabla \cdot \mathbf{v}^* \end{bmatrix}, \quad (76)$$

and the adjoint system may be defined as

$$\begin{cases} \mathcal{N}^* \begin{bmatrix} \mathbf{v}^* \\ p^* \end{bmatrix} = \begin{bmatrix} -\Delta \mathbf{v} \\ 0 \end{bmatrix} & \text{in } \Omega \times (0, T), \\ \mathbf{v}^* = 0 & \text{at } t = T, \\ \mathbf{v}^* \text{ periodic in } x_1, x_2, x_3. \end{cases} \quad (77)$$

In such a case we obtain $b_{ns} = 0$ and the relations (75), (73) and (77) can be used to re-express $\mathcal{J}'_{ns}(\phi, \phi')$ as

$$\mathcal{J}'_{ns}(\phi, \phi') = \int_0^T \int_{\Omega} \phi' \cdot \mathbf{v}^* d\Omega dt = \left(\nabla^{L_2(0, T; L_2(\Omega))} \mathcal{J}_{ns}, \phi' \right)_{L_2(0, T; L_2(\Omega))},$$

which yields the L_2 functional gradient

$$\nabla^{L_2(0,T;L_2(\Omega))} j_{ns} = \mathbf{v}^*. \quad (78)$$

In the vein of §4.3 and §4.4, below we examine how this derivation is modified when a different form of the duality pairing or a different inner product for the gradient extraction is selected.

6.1.1 Adjoint derivation with the H^1 duality pairing

We now derive the adjoint operator using the identity

$$\left\langle \mathcal{N} \begin{bmatrix} \mathbf{v}' \\ p' \end{bmatrix}, \begin{bmatrix} \mathbf{v}^{*,H^1} \\ p^{*,H^1} \end{bmatrix} \right\rangle_{L_2(0,T;H^1(\Omega))} = \left\langle \begin{bmatrix} \mathbf{v}' \\ p' \end{bmatrix}, \mathcal{N}^{*,H^1} \begin{bmatrix} \mathbf{v}^{*,H^1} \\ p^{*,H^1} \end{bmatrix} \right\rangle_{L_2(0,T;H^1(\Omega))} + b_{ns,1}, \quad (79)$$

which yields the new adjoint operator

$$\mathcal{N}^{*,H^1} \begin{bmatrix} \mathbf{v}^{*,H^1} \\ p^{*,H^1} \end{bmatrix} = \begin{bmatrix} -\frac{\partial \mathbf{v}^{*,H^1}}{\partial t} - \Delta_0^{-1} \left\{ \mathbf{v} \cdot \Delta \left[\nabla \mathbf{v}^{*,H^1} + (\nabla \mathbf{v}^{*,H^1})^T \right] \right\} - \mu \Delta \mathbf{v}^{*,H^1} + \nabla p^{*,H^1} \\ -\nabla \cdot \mathbf{v}^{*,H^1} \end{bmatrix}, \quad (80)$$

where Δ_0^{-1} is the inverse Laplace operator associated with homogeneous Dirichlet boundary conditions. We define the new adjoint system as

$$\begin{cases} \mathcal{N}^{*,H^1} \begin{bmatrix} \mathbf{v}^{*,H^1} \\ p^{*,H^1} \end{bmatrix} = \begin{bmatrix} \Delta_0^{-1} \Delta \mathbf{v} \\ 0 \end{bmatrix} & \text{in } \Omega \times (0, T), \\ \mathbf{v}^{*,H^1} = 0 & \text{at } t = T, \\ \mathbf{v}^{*,H^1} \text{ periodic in } x_1, x_2, x_3, \end{cases} \quad (81)$$

from which we obtain $b_{ns,1} = 0$ and

$$j'_{ns}(\Phi, \Phi') = \int_0^T \int_{\Omega} \frac{\partial v_i^{*,H^1}}{\partial x_j} \frac{\partial \phi'_i}{\partial x_j} d\Omega dt.$$

Identifying this expression with either $\left(\nabla^{L_2(0,T;L_2(\Omega))} j_{ns}, \Phi' \right)_{L_2(0,T;L_2(\Omega))}$ or $\left(\nabla^{L_2(0,T;H^1(\Omega))} j_{ns}, \Phi' \right)_{L_2(0,T;H^1(\Omega))}$ allows us to extract the corresponding gradients as

$$\begin{aligned} \nabla^{L_2(0,T;L_2(\Omega))} j &= -\Delta \mathbf{v}^{*,H^1}, \\ \nabla^{L_2(0,T;H^1(\Omega))} j &= \mathbf{v}^{*,H^1}. \end{aligned}$$

6.1.2 Preconditioning the gradient

We can extract preconditioned gradients by identifying the differential of the cost functional $J_{ns}^l(\phi, \phi')$ with an alternative form of the inner product, such as that defined in (70). As in §4.4, the new gradient can be obtained for all $t \in [0, T]$ as a solution of the Helmholtz equation

$$\begin{cases} \frac{1}{1+l_1^2} [1 - \Delta] \nabla^{L_2(0,T;W^{l_1,\infty})} J_{ns} = \mathbf{v}^* \\ \nabla^{L_2(0,T;W^{l_1,\infty})} J_{ns}, \frac{\partial}{\partial n} \nabla^{L_2(0,T;W^{l_1,\infty})} J_{ns} \text{ periodic in } x_1, x_2, x_3. \end{cases} \quad (82)$$

We remark that we obtain by this approach the same properties with respect to scale-dependent filtering as discussed in §4.4. Since in the present case the control ϕ is also a function of time, the definition of the inner product used to extract the gradient can also be generalized by incorporating derivatives with respect to time. Using such an inner product will result in smoothing the gradient in the time domain. This approach is discussed further in §6.2.3.

6.2 Controlling a Kuramoto–Sivashinsky System in a Bounded Domain

We now proceed to investigate how the presence of solid boundaries affects the regularization strategies developed in §4. We first briefly review the standard formulation and then see how it is modified when alternative forms of the duality pairing and the inner product for the gradient extraction are selected. For this purpose we consider the system (2) in a bounded domain $\Omega = [0, 2\pi]$ (see, e.g., [39])

$$\begin{cases} \partial_t v + 4\partial_x^4 v + \kappa (\partial_x^2 v + v \partial_x v) = 0, & x \in \Omega, \ t \in [0, T], \\ v(0, t) = v(2\pi, t) = 0, & t \in [0, T], \\ \partial_x v(0, t) = \phi, \ \partial_x v(2\pi, t) = 0, & t \in [0, T], \\ v(x, 0) = v_0, & x \in \Omega, \end{cases} \quad (83)$$

where a time-dependent control ϕ is applied on one boundary to regulate a quantity defined on the opposite boundary (note that for consistency with the initial data we must have $\partial_x v_0|_{x=0} = \phi|_{t=0}$). Consequently, the norm and the inner product needed to formulate the adjoint analysis are redefined as follows

$$\|z\|_{H^p(0,T)}^2 \triangleq \int_0^T (\partial_t^p z)^2 dt, \quad (84a)$$

$$(z_1, z_2)_{H^p(0,T)} \triangleq \int_0^T (\partial_t^p z_1) (\partial_t^p z_2) dx. \quad (84b)$$

(Note that discussion of incorporating time derivatives into the duality pairing is deferred to Appendix A.) We now select the cost functional as

$$J_b(\phi) = \frac{1}{2} \left\| \partial_x^2 v \Big|_{x=2\pi} \right\|_{L_2(0,T)}^2. \quad (85)$$

In the present problem we have therefore the following relations between the spatial domains of interest: $\Omega_1 = \{2\pi\}$, $\Omega_2 = \Omega$ and $\Omega_3 = \{0\}$. Both the cost functional and the control are defined on $[0, T]$, whereas the system evolution again takes place over $\Omega \times [0, T]$. The differential of the cost functional is

$$J'(\phi; \phi') = \int_0^T [(\partial_x^2 v)(\partial_x^2 v')]_{x=2\pi} dt, \quad (86)$$

where v' is the solution of the system

$$\begin{cases} \mathcal{L}v' = 0, & x \in \Omega, t \in [0, T], \\ v'(0, t) = v'(2\pi, t) = 0, & t \in [0, T], \\ \partial_x v'(0, t) = \phi', \partial_x v'(2\pi, t) = 0, & t \in [0, T], \\ v'(x, 0) = 0, & x \in \Omega, \end{cases} \quad (87)$$

with the operator \mathcal{L} defined as in (12). Note that consistency between the initial and boundary conditions requires that $\phi'(0) = 0$. The adjoint operator \mathcal{L}^* is introduced using duality pairing (15) and is given by (16). Defining the adjoint state v^* such that

$$\begin{cases} \mathcal{L}^*v^* = 0, & x \in \Omega, t \in [0, T], \\ v^*(0, t) = v^*(2\pi, t) = 0, & t \in [0, T], \\ \partial_x v^*(0, t) = 0, \partial_x v^*(2\pi, t) = \partial_x^2 v(2\pi, t), & t \in [0, T], \\ v^*(x, 0) = T, & x \in \Omega, \end{cases} \quad (88)$$

we can use (15), (87), and (88) to re-express the differential of the cost functional as

$$J'_b(\phi; \phi') = - \int_0^T (\partial_x^2 v^* \Big|_{x=0}) \phi' dt = \left(\nabla^{L_2(0,T)} J_b, \phi' \right)_{L_2(0,T)}, \quad (89)$$

from which we obtain the L_2 gradient

$$\nabla^{L_2(0,T)} J_b = -\partial_x^2 v^*(0, t). \quad (90)$$

6.2.1 Targeting the cost functional

Since the regulated quantity is now a function of time only, an alternative, targeted, cost functional may be selected as, for instance,

$$J_b^{H^1}(\phi) = \frac{1}{2} \left\| \partial_x^2 v \Big|_{x=2\pi} \right\|_{H^1(0,T)}^2, \quad (91)$$

in which case the differential becomes

$$\begin{aligned} j_b'^{H^1}(\phi; \phi') &= \int_0^T [(\partial_t \partial_x^2 v)(\partial_t \partial_x^2 v')]_{x=2\pi} dt, \\ &= - \int_0^T [(\partial_t^2 \partial_x^2 v)(\partial_x^2 v')]_{x=2\pi} dt + \{ [(\partial_t \partial_x^2 v)(\partial_x^2 v')]_{x=2\pi} \}_{t=0}^{t=T}, \end{aligned} \quad (92)$$

so that the corresponding adjoint system is now

$$\begin{cases} \mathcal{L}^* v^* = 0, & x \in \Omega, \quad t \in [0, T], \\ v^*(0, t) = v^*(2\pi, t) = 0, & t \in [0, T], \\ \partial_x v^*(0, t) = 0, \quad \partial_x v^*(2\pi, t) = -\partial_t^2 \partial_x^2 v(2\pi, t) + \delta(t - T) (\partial_t \partial_x^2 v) \Big|_{x=2\pi}, & t \in [0, T], \\ v^*(x, 0) = 0, & x \in \Omega. \end{cases}$$

This system must be interpreted in the sense of a distribution, as one of the boundary conditions involves a “delta function” in time, effectively forcing the adjoint system from the “corner” of the space–time domain. The fact that here, unlike in all the previous cases, we are strictly able to identify only a weak form of the adjoint system is not considered an insurmountable problem, as there are well–established methods for the numerical approximation of such systems.

6.2.2 Adjoint derivation with the H^1 duality pairing

We now derive the adjoint using the H^1 duality pairing (42), and write out the complete form of the term b_1 appearing in this relation as

$$\begin{aligned} b_1 &= \int_0^{2\pi} [(\partial_x v')(\partial_x v^{*,H^1})]_{t=0}^{t=T} dx + \int_0^T \left\{ \kappa [(\partial_x v^{*,H^1})(\partial_x^2 v') - (\partial_x^2 v^{*,H^1})(\partial_x v')] \right. \\ &\quad + \kappa [(\partial_x v^{*,H^1})\partial_x(vv') - (\partial_x^2 v^{*,H^1})vv' + \partial_x^{-1}(v\partial_x^3 v^{*,H^1})v'] + \\ &\quad \left. 4 [(\partial_x v^{*,H^1})(\partial_x^4 v') - (\partial_x^2 v^{*,H^1})(\partial_x^3 v') + (\partial_x^3 v^{*,H^1})(\partial_x^2 v') - (\partial_x^4 v^{*,H^1})(\partial_x v')] \right\}_{x=0}^{x=2\pi} dt. \end{aligned}$$

Making use of the expression for \mathcal{L}^{*,H^1} in (43), we now define the new adjoint system as

$$\begin{cases} \mathcal{L}^{*,H^1} v^{*,H^1} = 0, & x \in \Omega, \quad t \in [0, T], \\ \partial_x^2 v^{*,H^1}(0, t) = \partial_x^2 v^{*,H^1}(2\pi, t) = 0, & t \in [0, T], \\ \partial_x^3 v^{*,H^1}(0, t) = 0, \quad \partial_x^3 v^{*,H^1}(2\pi, t) = \partial_x^2 v(2\pi, t), & t \in [0, T], \\ v^{*,H^1}(x, T) = 0, & x \in \Omega, \end{cases} \quad (93)$$

which allows us to re–express the differential of the cost functional as

$$j_b'(\phi; \phi') = - \int_0^T (\partial_x^4 v^{*,H^1} \Big|_{x=0}) \phi' dt = \left(\nabla^{L_2(0,T)} j_b, \phi' \right)_{L_2(0,T)}. \quad (94)$$

As a result, the L_2 gradient can be extracted as

$$\nabla^{L_2(0,T)} j_b = -\partial_x^4 v^{*,H^1}(0,t).$$

By comparing this to the standard formulation culminating with (90), we note that the same L_2 gradient of the cost functional is now obtained by applying a higher-order differential to the adjoint field obtained in the new formulation, which is consistent with the relationship between the corresponding expressions for the L_2 gradient in the periodic case as tabulated in Table 1.

6.2.3 Preconditioning the gradient

The control ϕ in the present problem is a function of time only, and new gradients of the cost function (85) can be obtained by identifying its differential with an inner product (84b) incorporating either derivatives ($p = 1$), or anti-derivatives ($p = -1$) with respect to the time variable. In the former case we obtain

$$j'_b(\phi; \phi') = - \int_0^T (\partial_x^2 v^*|_{x=0}) \phi' dt = \left(\nabla^{H^1(0,T)} j_b, \phi' \right)_{H^1(0,T)}, \quad (95)$$

so that the following holds

$$\begin{cases} \partial_t^2 \nabla^{H^1(0,T)} j_b = \partial_x^2 v^*|_{x=0}, \\ \partial_t \nabla^{H^1(0,T)} j_b(0,0) = \partial_t \nabla^{H^1(0,T)} j_b(0,T) = 0. \end{cases} \quad (96)$$

We see that the new gradient is obtained by solving this elliptic-in-time boundary-value problem, and therefore will be smoother in the time domain. In the spirit of §4.4, this approach can be generalized by considering an inner product which is a combination of the L_2 and H^1 terms, as this would allow us to focus the optimization on a specific range of time scales that are of interest in a given optimization problem.

7 Discussion & Conclusions

In this paper we have identified and related the four opportunities for generalizing the formulation of an adjoint-based gradient optimization algorithm. The first opportunity concerns the choice of the specific form of the equation assumed to govern the system evolution. The remaining three opportunities are related to the choice of the norm, the duality pairing, and the inner product (collectively referred to in the paper as “brackets”) on the three space-time domains that are of interest in a generic optimization problem applied to an unsteady PDE system. Most studies to date have used L_2 brackets on all three of these space-time domains. In the present

study we have explored formulations based on the more general Sobolev brackets, which include the L_2 brackets as special cases. Choosing an alternative form of the evolution equation together with the adoption of different Sobolev brackets has the effect of emphasizing or de-emphasizing different length- and time-scales in the definition of the cost functional, the adjoint operator and the associated adjoint field, and the gradient of the cost functional. These opportunities allow one to fine-tune the optimization algorithm to specific the length- and time-scales of interest. By so doing, one may make the original PDE optimization problem more “regular”, and thereby easier to discretize and solve numerically.

The four regularization opportunities discussed in §4 fall into two categories: those that affect the descent direction (i.e., targeting the cost functional in §4.2 and preconditioning the gradient in §4.4), and those that affect the manner in which a given descent direction is computed (i.e., changing the form of the evolution equation in §4.1 and the duality pairing in §4.3). In a discrete setting, all four of these opportunities are significant, and the different opportunities may be used to amend the different elements of the algorithm. For example, gradient extraction performed using an inner product which combines the H^{-1} , L_2 , and H^1 brackets was shown to be equivalent to applying a suitable scale-dependent filter to the adjoint field. A low-pass filter of this sort is useful to employ when the high-frequency components of the system are somehow considered “less significant” during the optimization process in the multiscale system. In a data assimilation problem this could be the case, for instance, when one is attempting to obtain a long-term forecast, in which the smallest-scale variations of the initial conditions are thought to play a relatively unimportant role. On the other hand, a band-pass filter could be useful to employ when one is attempting to obtain a short-term “meso-scale” forecast, in which the small-scale variations of the initial conditions are again thought to play a relatively unimportant role and the large-scale variations of the initial conditions are determined by a separate (global-scale) optimization code. Alternative forms of the duality pairing may serve to define new adjoint operators and new adjoint fields which are better behaved from the point of view of the numerical implementation. In this way, one may obtain adjoint fields which are smoother and can therefore be satisfactorily resolved on coarser numerical grids. This opportunity can be very useful in applications to complex multiscale systems where only marginal numerical resolution can be afforded. It should be remarked that, even though the new adjoint systems so defined may yield smoother adjoint fields, the equations governing such adjoint systems may themselves be more complicated and therefore more difficult to implement. As indicated in the literature survey in §1, approaches related to some of the regularization options presented here had already been mentioned in earlier studies. The present paper examines in detail all of the different opportunities and attempts to unify them into a coherent framework by highlighting the relations between the different possibilities. It is also shown how the more traditional approaches based on Tikhonov regularization and inverse-Laplacian-based gradient smoothing fit into the present framework as special cases.

The presented framework opens up the possibility for adoption of a wide range of regularization strategies. In order to illustrate these opportunities in a clear and exhaustive fashion, we chose to analyze them in this work based on a simple Kuramoto–Sivashinsky model forecasting problem. Moreover, studying a spatially–periodic system allowed us to recast parts of the analysis in Fourier space, which facilitated drawing conclusions regarding spatial regularity of the various fields involved. We also addressed some of the issues arising when the framework presented is extended to systems governed by more complicated evolutions equations (e.g., the 3D Navier–Stokes system), and systems evolving in bounded domains. In such systems, analysis is more difficult, but the fundamental concepts remain the same. A forthcoming paper will discuss the application of some of the regularization opportunities presented here to complex optimization problems involving the Navier–Stokes system in 3D bounded domains.

The computational examples presented in this paper, while far short of exhaustively examining all of the various regularization opportunities, highlighted a few of the computational advantages inherent in the proposed framework. Based on a modified inner–product definition used to extract the gradient, a physically–motivated multiscale preconditioning strategy was proposed which noticeably accelerates convergence of an optimization procedure applied to a nonlinear multiscale system. Adoption of similar approaches to the optimization of more complex systems of physical and engineering interest is currently underway.

A Adjoint derivation with the “ H^1 –in–time” duality pairing

We present here yet another way of deriving the adjoint operator, namely using the duality pairing of the form [cf. (22b)]

$$\langle z_1, z_2 \rangle_{H^p(0,T;L_2(\Omega))} \triangleq \int_0^T \int_0^{2\pi} (\partial_t^p z_1) (\partial_t^p z_2) dx dt. \quad (\text{A.1})$$

We will focus here on the case with $p = 1$, and define the “anti-derivative” operator ∂_t^{-1} as

$$\partial_t^{-1} z(t) \triangleq \int_0^t z(t') dt' - \int_0^T z(t') dt' = \int_T^t z(t') dt', \quad (\text{A.2})$$

so that $\partial_t^{-1} z(T) = 0$ for any $z(t)$. In order not to further complicate the notation, we will use the symbols \mathcal{L}^* and v^* to also denote the new adjoint operator and the new adjoint variable. The adjoint identity has now the following form

$$\langle v^*, \mathcal{L} v' \rangle_{H^1(0,T;L_2(\Omega))} = \langle \mathcal{L}^* v^*, v' \rangle_{H^1(0,T;L_2(\Omega))} + b_{1t}, \quad (\text{A.3})$$

where

$$\begin{aligned} \mathcal{L}^* v^* &= -\partial_t v^* + 4\partial_x^4 v^* + \kappa [\partial_x^2 v^* - \partial_t^{-2} (v \partial_x \partial_t^2 v^*)], \quad \text{and} \\ b_{1t} &= \left\{ \int_0^{2\pi} [(\partial_t v^*) (\partial_t v') + (\partial_t v^*) \partial_x (v v') + v' \partial_t^{-1} (v \partial_x \partial_t^2 v^*)] dx \right\}_{t=0}^{t=T} + \left[\dots \right]_{x=0}^{x=2\pi}. \end{aligned} \quad (\text{A.4})$$

We now define the new adjoint system as

$$\begin{cases} \mathcal{L}^* v^* = -\partial_t^{-2} \mathcal{H}^* (\mathcal{H} v - y) = -\partial_t^{-2} f, & x \in \Omega, \quad t \in [0, T], \\ \partial_x^i v^*(0, t) = \partial_x^i v^*(2\pi, t), & t \in [0, T], \quad i = 0, \dots, 3, \\ v^*(x, T) = 0, & x \in \Omega, \end{cases} \quad (\text{A.5})$$

which, when considering the spatially-periodic problem defined in §3 and combining with (11), (A.3), and (A.2), allows us to re-express the differential (10) as

$$j'(\phi; \phi') = \int_0^{2\pi} \partial_t^2 v^* \Big|_{t=0} \phi' dx = \left(\nabla^{L_2} j, \phi' \right)_{L_2(\Omega)}.$$

From this we identify the L_2 gradient in terms of the new adjoint variable as

$$\nabla^{L_2} j = \partial_t^2 v^* \Big|_{t=0}.$$

We note that the new adjoint operator (A.4) and the RHS forcing term used in (A.5) have terms involving ∂_t^{-1} and are therefore non-local in time. However, as is evident from (A.2), at a given time instant t the operator ∂_t^{-1} depends on its argument in the interval $[t, T]$ only. Consequently, the system (A.5) can be marched backward in time (i.e. from T to 0) using conventional numerical time-marching methods. We also observe that, as compared to the primitive adjoint operator (16), the new adjoint operator (A.4) has a different “advection” term in which additional time derivatives and anti-derivatives are present. In this sense (A.4) is similar to (43), where the “advection” term includes additional space derivatives and anti-derivatives. Consequently, we can expect system (A.5) to produce adjoint fields which are more regular in the time domain (cf. §4.5.6).

Acknowledgements

The authors thank Prof. Scott Collis for his inspiring and thoughtful feedback, and gratefully acknowledge the generous funding of the AFOSR programs directed by Dr. John Schmisser and Prof. Belinda King.

References

- [1] J. Reuther, A. Jameson, J. Farmer, L. Martinelli, D. Saunders, "Aerodynamic Shape Optimization of Complex Aircraft Configurations Via an Adjoint Formulation" *AIAA Paper* 96-0094, (1996).
- [2] J. O. Pralits, C. Airiau, A. Hanifi and D. S. Henningson, "Sensitivity analysis using adjoint parabolized stability equations for compressible flows", *Flow Turbul. Combust.* **65**, 321-346, (2000).
- [3] P. Cathalifaud, and P. Luchini, "Algebraic growth in boundary layers: optimal control by blowing and suction at the wall", *Eur. J. Mech. B* **19**, 469-490, (2000).
- [4] S. Walter, C. Airiau, A. Bottaro, "Optimal Control of Tollmien-Schlichting waves in a developing boundary layer", *Phys. Fluids* **13**, 2087-2096, (2001).
- [5] T. R. Bewley, P. Moin and R. Temam, "DNS-based predictive control of turbulence: an optimal benchmark for feedback algorithms", *J. Fluid Mech.* **447**, 179-225, 2001.
- [6] F. -X. Le Dimet and O. Talagrand, "Variational algorithms for analysis and assimilation of meteorological observations: theoretical aspects", *Tellus* **38A**, 97-100, (1986).
- [7] M. D. Gunzburger, "Flow Control", The Institute for Mathematics and its Applications **68**, Springer-Verlag, (1995).
- [8] S. S. Sritharan, "Optimal Control of Viscous Flows", SIAM, (1998).
- [9] T. R. Bewley, "Flow control: new challenges for a new Renaissance", *Progress in Aerospace Sciences* **37**, 21-58, (2001).
- [10] H. Engl, M. Hanke and A. Neubauer, "Regularization of Inverse Problems", Kluwer, Dordrecht, (1996).
- [11] P. Ch. Hansen, "Rank-Deficient and Discrete Ill-Posed Problems", SIAM, Philadelphia, (1998).
- [12] C. R. Vogel, "Computational Methods for Inverse Problems", SIAM, Philadelphia, (2002).
- [13] S. S. Collis, K. Ghayour, M. Heinkenschloss, M. Ulbrich and S. Ulbrich, "Optimal Control of Unsteady Compressible Viscous Flows", (preprint), 2002.
- [14] M. Heinkenschloss and L. N. Vicente, "An Interface between Optimization and Application for the Numerical Simulation of Optimal Control Problems", *ACM Trans. Math. Soft.* **25** (2), 157-190, (1999).
- [15] J. Liu, "A Multiresolution Method for Distributed Parameter Estimation", *SIAM J. Sci. Comp.*, **14** (2), 389-405, (1993).
- [16] A. Brandt and L. Y. Zaslavsky, "Multiscale Algorithm for Atmospheric Data Assimilation", *SIAM J. Sci. Comp.*, **18** (3), 949-956, (1997).

- [17] A. -A. Grimstad and T. Mannseth, "Nonlinearity, scale and sensitivity for parameter estimation problems", *SIAM J. Sci. Comp.* **21** (6), 2096-2113, (2000).
- [18] K. Brusdal and T. Mannseth, "Basis norm rescaling for nonlinear parameter estimation", *SIAM J. Sci. Comp.* **21** (6), 2114-2125, (2000).
- [19] R. M. Lewis and S. G. Nash, "Model Problems for the Multigrid Optimization of Systems Governed by Differential Equations", (preprint), (2002).
- [20] A. C. Lorenc, "Optimal Nonlinear Objective Analysis", *Q. J. R. Meteorol. Soc.* **114**, 205-240 (1988).
- [21] J. -N. Thepaut and P. Moll, "Variational Inversion of Simulated TOVS Radiances Using the Adjoint Technique", *Q. J. R. Meteorol. Soc.* **116**, 1425-1448 (1990).
- [22] C. L. Lin, T. Chai and J. Sun, "On the Smoothness Constraints for Four-Dimensional Data Assimilation", *J. Comp. Phys.* **181**, 430-453, (2002).
- [23] P. Holmes, J. L. Lumley and G. Berkooz, "Turbulence, Coherent Structures, Dynamical Systems and Symmetry", Cambridge University Press, (1996).
- [24] H. Choi, R. Temam, P. Moin and J. Kim, "Feedback control for unsteady flow and its application to the stochastic Burgers equation", *J. Fluid Mech.* **253**, 509-543, (1993).
- [25] K. Kunisch and S. Volkwein, "Control of the Burgers equation by a reduced-order approach using proper orthogonal decomposition", *J. Optimiz. Theory App.* **102** (2), 345-371, (1999).
- [26] J. A. Atwell, J. T. Borggaard, and B. B. King, "Reduced Order Controllers for Burgers' Equation with a Nonlinear Observer", *Applied Mathematics and Computational Science* in press, (2002).
- [27] A. N. Tikhonov and V. Y. Arsenin, "Solution of Ill-Posed Problems", John Wiley, NY, (1977).
- [28] Y. Kuramoto, "Diffusion induced chaos in reaction systems", *Prog. Theoret. Phys. Suppl.* **64**, 346-367, (1978).
- [29] G. Sivashinsky, "Nonlinear analysis of hydrodynamic instability in laminar flames", *Acta Astronaut.* **4**, 1177-1206, (1977).
- [30] J. M. Hyman and B. Nicolaenko, "The Kuramoto-Sivashinsky equation: a bridge between PDE's and dynamical systems", *Physica D* **18**, 113-126, (1986).
- [31] R. Temam, "Infinite-Dimensional Dynamical Systems in Mechanics and Physics", *Applied Mathematical Sciences* **68** (2nd edition), Springer, (1997).
- [32] J. Nocedal and S. J. Wright, "Numerical Optimization", Springer Verlag, Berlin, Heidelberg, New York, (1999).
- [33] A. E. Taylor, "Introduction to functional analysis", Wiley, New York, (1958).
- [34] J. E. Dennis and R. B. Schnabel, "Numerical Methods for Unconstrained Optimization and Nonlinear Equations", Prentice-Hall, (1983).

- [35] Ch. Hirsch, "Numerical Computation of Internal and External Flows", John Wiley & Sons, 1989.
- [36] W. H. Press, B. P. Flanner, S. A. Teukolsky and W. T. Vetterling, "Numerical Recipes: the Art of Scientific Computations", Cambridge University Press, Cambridge, (1986).
- [37] O. Axelsson, "Iterative Solution Methods", Cambridge University Press, (1994).
- [38] F. Abergel and R. Temam, "On Some Control Problems in Fluid Mechanics", *Theoret. Comput Fluid Dyn.* **1**, 303-325, (1990).
- [39] V. M. Eguíluz *et al.*, "Average patterns of spatiotemporal chaos: a boundary effect", *Phys. Rev. E* **59** (3), 2822-2825, (1999).

The decay of stabilizability with Reynolds number in a linear model of spatially developing flows

BY ERIC LAUGA^{1,2} † & THOMAS R. BEWLEY¹

¹*Flow Control Lab, Dept. of MAE, UC San Diego, La Jolla CA 92093, USA,*

²*LadHyX, École Polytechnique-CNRS, 91128 Palaiseau Cedex, FRANCE*

This article characterizes the gradual decay of stabilizability with Reynolds number in the linear complex Ginzburg-Landau model of spatially developing flow systems when a single, spatially-localized actuator is used for applying the control forcing. It is shown that, technically, the system considered is linearly stabilizable for all actuator locations at any Reynolds number. However, as the Reynolds number is increased and an increasing number of modes of the open-loop system become unstable, the control authority on some of these open-loop unstable modes is found to be exponentially small. Using finite-precision arithmetic and any given numerical method for computing the feedback gains, an effective upper bound on the Reynolds number is reached, above which it is not possible to compute a linearly stabilizing control algorithm. This “effective upper bound”, however, is not a fundamental characteristic of the system; rather, it is a persistent artifact of the numerical precision used in the controller calculation. The most suitable location for the actuator as the Reynolds number is increased is well predicted by analysis of the domain of support of the open-loop adjoint eigenfunctions. Further understanding is provided by analysis of the closed-loop system eigenfunctions, which are shown to become increasingly nonnormal as the Reynolds number is increased.

Keywords: Flow control (47.62.+q), Instability of shear flows (47.20.Ft)

1. Introduction

Spatially developing open shear-flow instabilities have been extensively studied in the last fifteen years using the concepts of local and global instability (Huerre & Monkewitz 1990). In the laboratory reference frame (chosen without ambiguity because of inlet conditions or the presence of a body in the flow), the existence of a mean advection velocity allows the local flow instabilities to be either of *convective* type, when the advection is strong enough to wash downstream all growing perturbations, or of *absolute* type, when the local flow instabilities grow in both the upstream and downstream directions.

Flows displaying a sufficiently large region of local absolute instability will typically display self-sustained unsteadiness, as is the case with mixing layers (Huerre & Monkewitz 1985), jets (Monkewitz & Sohn 1988), and wakes (Monkewitz 1988). In such systems, when a physical bifurcation parameter (such as the Reynolds number) exceeds a critical value, an eigenfunction of the linearized governing equations, sometimes termed a *linear global mode*, is linearly unstable and thus small system disturbances inevitably trigger unsteady flow behaviour. Due to stabilizing nonlinear effects, this unsteadiness typically “saturates” into a “self-sustained” finite-amplitude limit cycle, sometimes termed a *nonlinear global mode*. In the well-known case of the cylinder wake, self-sustained oscillations appear downstream of the body when the Reynolds number based on the cylinder diameter exceeds 47. In this system, the nonlinear global mode is referred to as the von Karman vortex street.

† present address: Division of Engineering and Applied Sciences, Harvard University, Cambridge MA 02138, USA

The important engineering consequences of delaying the appearance of self-sustained unsteady flow phenomena, and the recent successful control implementations in both experimental (Roussopoulos 1993) and numerical (Park *et al.* 1994, Min & Choi 1999) investigations of such systems, has lead to the following fundamental questions: Is there an effective upper bound on the bifurcation parameter, above which the system can not be linearly stabilized with *any* control strategy for a given actuator configuration? If so, why? The present article is devoted to these two questions.

2. The Ginzburg-Landau model of weakly nonparallel flows

As a model of inhomogeneous, weakly nonparallel flows, the complex Ginzburg-Landau (CGL) equation has proven to be particularly well suited in several previous studies (see, e.g., Monkewitz *et al.* 1993 and Pier & Huerre 2001). In particular, the CGL model has proven to be accurate in determining global frequency criteria in both the linear (Chomaz *et al.* 1991) and nonlinear (Pier *et al.* 1998) regimes. Moreover, because the CGL model roughly captures the streamwise structure of the system eigenfunctions and the variation of the complex frequency of these eigenmodes with Reynolds number, the CGL model has also allowed quantitative predictions of the effects of proportional feedback control on the actual flow system in several previous studies (Monkewitz 1989, 1993; Monkewitz *et al.* 1991; Roussopoulos & Monkewitz 1996). In the present paper, we thus consider the CGL model of the flow exclusively. By so doing, we may focus our attention directly on the fundamental issues responsible for the decay of stabilizability with Re in such systems.

The linear CGL equation considered in this work models the time evolution of a perturbation quantity ψ in the presence of streamwise advection, amplification, diffusion, and control input:

$$\frac{\partial \psi}{\partial t} + U \frac{\partial \psi}{\partial x} = \mu \psi + \nu \frac{\partial^2 \psi}{\partial x^2} + \delta(x - x_f)u \quad \Leftrightarrow \quad \frac{\partial \psi}{\partial t} = \mathcal{L}\psi + \delta(x - x_f)u. \quad (2.1)$$

In order to model a wide range of spatially-developing flow systems, the coefficients $\mu = \mu(\epsilon x)$ and ν in this equation are allowed to be complex. Note that the scalar control input $u = u(t)$ is modeled as a pointwise forcing term at $x = x_f$. The amplification term in this model equation depends on an inhomogeneous local parameter $\mu(\epsilon x)$ analogous to the local Reynolds number based on, for example, the local diameter and velocity defect of a 3D bluff-body wake. In the present work, the spatial variation of this coefficient is assigned the form $\mu(\epsilon x) = \mu_0 - [\epsilon(x - x_t)]^2$, where the real parameter μ_0 is a global bifurcation parameter analogous to the global Reynolds number based on, for example, the bluff-body dimension and free-stream velocity, and the small parameter ϵ accounts for the slowly diverging characteristics of the basic flow. The spatial position x_t , which is generally taken to be complex, is found by analytic continuation of local dispersion relations (Hammond & Redekopp 1997), and characterizes the hydrodynamic resonance phenomenon (Chomaz *et al.* 1991). The parabolic form used here is motivated by many previous studies which focused on the modelling of spatially developing flows (Chomaz *et al.* 1987, 1990; Huerre & Monkewitz 1990; Roussopoulos & Monkewitz 1996). Using this parabolic form, it was shown by Chomaz *et al.* (1987) that local instability appears in a finite region in the system when $\mu_0 > 0$, this local instability being everywhere convective if $\mu_0 < \mu_a \triangleq U^2 \Re(\nu)/4|\nu|^2$, and absolute in a portion of the unstable region if $\mu_0 > \mu_a$. Significantly, the localized control forcing term applied to (2.1) does not change these local instability properties of the system, though it can substantially alter its global dynamics.

The analytic solution (Chomaz *et al.* 1987) for the eigenmodes $\psi(x, t) = \xi(x)e^{\lambda t}$ of the unforced CGL equation is given by the countable set of eigenvalues λ_k and corresponding eigenfunctions $\xi_k(x)$

$$\left. \begin{aligned} \lambda_k &= \mu_0 - U^2/4\nu - \epsilon\nu^{1/2}(2k+1) \\ \xi_k(x) &= \exp\left[\frac{Ux}{2\nu} - \frac{\epsilon(x-x_t)^2}{2\nu^{1/2}}\right] \text{He}_k\left[\left(\frac{4\epsilon^2}{\nu}\right)^{1/4}(x-x_t)\right] \end{aligned} \right\} \quad k = 0, 1, 2, \dots \quad (2.2)$$

where He_k designs the k 'th Hermite polynomial. The first mode is linearly unstable [*i.e.*, $\Re(\lambda_0) > 0$] when the supercriticality $\delta \triangleq (\mu_0 - \mu_c)/\mu_c$ is positive, with $\mu_c \triangleq \mu_a + \epsilon \Re(\nu^{1/2})$. The fact that $\mu_c > \mu_a$ confirms the need for a sufficiently large region of local absolute instability to give rise to global instability (Chomaz *et al.* 1991). Note that the shapes of these modes do not depend on the global bifurcation parameter μ_0 .

The numerical values used in this paper are $U = 6$, $\nu = 1 - 10i$, and $x_t = 0.1i$ to be consistent with previous studies (Chomaz *et al.* 1987, 1990). The value $\epsilon = 0.01$ was chosen to represent a weakly inhomogeneous media, corresponding to a ratio of a typical local instability wavelength λ to a global length scale L of $\lambda/L \approx 0.1$. This choice is physically realistic; for example, inside the wake behind a rectangular body, this ratio typically varies between 0.05 and 0.2 (Hammond & Redekopp 1997).

Designating by \mathbf{x} , A , and B the spatial discretizations of the state variable ψ , the Ginzburg-Landau operator \mathcal{L} , and the Dirac delta function $\delta(x - x_f)$ respectively, it is straightforward to represent a discretization of the CGL equation (2.1) in the standard state-space form

$$\dot{\mathbf{x}} = A\mathbf{x} + B\mathbf{u}. \quad (2.3)$$

In the present work, an efficient spatial discretization of the CGL equation was achieved using a Fourier collocation method on a stretched grid clustered near the forcing location. Other numerical schemes were also implemented for comparison, and achieved the same results upon grid refinement.

3. Stabilizability

The CGL system (2.1) is termed “stabilizable” iff a control strategy coordinating u with ψ can be found such that the controlled linear system eventually decays exponentially in time everywhere in space regardless of initial conditions. In the discrete setting, the system operator pair (A, B) in (2.3) is termed stabilizable iff a feedback rule $\mathbf{u} = K\mathbf{x}$ may be found such that all of the eigenvalues of $A + BK$ have negative real part. In the present section, we discuss three equivalent tests for determining whether or not the CGL system (2.1), or its discretization (2.3), is stabilizable:

a) checking (analytically) whether or not the “controllability matrix” corresponding to the dynamic equation for the unstable modes of the system (2.1) has full rank,

b) checking (numerically) whether or not the discretized optimal control problem given by minimization of $\mathcal{J} = \int_0^\infty (\mathbf{x}^* Q \mathbf{x} + \mathbf{u}^* R \mathbf{u}) dt$ with feedback of the form $\mathbf{u} = K\mathbf{x}$ has a stabilizing solution, where $Q > 0$ and $R > 0$ and \mathbf{x} and \mathbf{u} are related by (2.3), and

c) checking (numerically) whether or not a minimal-energy stabilizing control feedback rule may be found by pole placement, resulting in a closed-loop system matrix which reflects the unstable eigenvalues of A to the left-half plane and leaves the stable eigenvalues of A unchanged.

(a) Analytic determination of the controllability of the unstable modes

At any time t , the solution $\psi(x, t)$ of the CGL equation is spanned by the eigenfunctions $\xi_\kappa(x)$, also known as “linear global modes” in much of the CGL literature. Recall that the ξ_κ are available analytically, and the eigenvalues λ_κ are distinct. We now define the “adjoint eigenfunctions” $\eta_\kappa(x)$ (also known as “adjoint global modes” in much of the CGL literature) by changing $\{U, \mu, \nu\} \rightarrow \{-U, \mu^*, \nu^*\}$ in the unforced CGL equation, resulting in

$$\frac{\partial \tilde{\psi}}{\partial t} - U \frac{\partial \tilde{\psi}}{\partial x} = \mu^* \tilde{\psi} + \nu^* \frac{\partial^2 \tilde{\psi}}{\partial x^2} \quad \Leftrightarrow \quad \frac{\partial \tilde{\psi}}{\partial t} = \mathcal{L}^* \tilde{\psi}, \quad (3.1)$$

and solving for the eigenmodes analytically, resulting in the complex conjugate of the eigenvalues found previously, λ_κ^* , and the adjoint eigenfunctions

$$\eta_\kappa(x) = \exp \left[-\frac{Ux}{2\nu^*} - \frac{\epsilon(x-x_t^*)^2}{2(\nu^*)^{1/2}} \right] \text{He}_\kappa \left[\left(\frac{4\epsilon^2}{\nu^*} \right)^{1/4} (x-x_t^*) \right], \quad \kappa = 0, 1, 2, \dots \quad (3.2)$$

Defining the inner product $\langle \eta_\iota, \xi_\kappa \rangle = \int_{-\infty}^{\infty} \eta_\iota^*(x) \xi_\kappa(x) dx$, note that

$$\left. \begin{aligned} \langle \eta_\iota, \mathcal{L}\xi_\kappa \rangle &= \langle \eta_\iota, \lambda_\kappa \xi_\kappa \rangle = \lambda_\kappa \langle \eta_\iota, \xi_\kappa \rangle \\ \langle \eta_\iota, \mathcal{L}^* \xi_\kappa \rangle &= \langle \mathcal{L}^* \eta_\iota, \xi_\kappa \rangle = \lambda_\iota^* \langle \eta_\iota, \xi_\kappa \rangle = \lambda_\iota \langle \eta_\iota, \xi_\kappa \rangle \end{aligned} \right\} \quad (\lambda_\kappa - \lambda_\iota) \langle \eta_\iota, \xi_\kappa \rangle = 0,$$

and thus $\langle \eta_\iota, \xi_\kappa \rangle = 0$ for $\iota \neq \kappa$. Scaling the eigenfunctions appropriately, it follows that $\langle \eta_\iota, \xi_\kappa \rangle = \delta_{\iota\kappa}$.

In order to establish a correspondence between the analytically-determined eigenfunctions and adjoint eigenfunctions discussed above and the appropriately-defined discrete right and left eigenvectors, it is necessary to define a discrete scalar product $\tilde{\mathbf{x}}^* \mathbf{Q} \mathbf{x}$ which is equivalent to its continuous analog, the inner product $\langle \eta_\iota, \xi_\kappa \rangle = \int_{-\infty}^{\infty} \eta_\iota^*(x) \xi_\kappa(x) dx$. Using the definition of the (stretched) numerical grid and a trapezoidal integration rule, it is straightforward to compute the diagonal matrix $\mathbf{Q} > 0$ which accomplishes this task. The discrete analog of the eigenfunction $\xi_\kappa(x)$ is then found to be the κ 'th right eigenvector of A , which we will denote $\mathbf{r}^{(\kappa)}$, and the discrete analog of the adjoint eigenfunction $\eta_\kappa(x)$ is the κ 'th left eigenvector of $\mathbf{Q}A\mathbf{Q}^{-1}$, which we will denote $\mathbf{s}^{(\kappa)}$.[†] Using this definition, it follows that

$$\left. \begin{aligned} (\mathbf{s}^{(\iota)})^* \mathbf{Q} A \mathbf{r}^{(\kappa)} &= (\mathbf{s}^{(\iota)})^* \mathbf{Q} \lambda_\kappa \mathbf{r}^{(\kappa)} = \lambda_\kappa (\mathbf{s}^{(\iota)})^* \mathbf{Q} \mathbf{r}^{(\kappa)} \\ (\mathbf{s}^{(\iota)})^* \mathbf{Q} A \mathbf{r}^{(\kappa)} &= [(\mathbf{s}^{(\iota)})^* \mathbf{Q} A \mathbf{Q}^{-1}] \mathbf{Q} \mathbf{r}^{(\kappa)} = \lambda_\iota (\mathbf{s}^{(\iota)})^* \mathbf{Q} \mathbf{r}^{(\kappa)} \end{aligned} \right\} \quad (\lambda_\kappa - \lambda_\iota) (\mathbf{s}^{(\iota)})^* \mathbf{Q} \mathbf{r}^{(\kappa)} = 0,$$

and thus the discrete analog of the orthogonality property $\langle \eta_\iota, \xi_\kappa \rangle = \delta_{\iota\kappa}$ is the discrete relationship $(\mathbf{s}^{(\iota)})^* \mathbf{Q} \mathbf{r}^{(\kappa)} = \delta_{\iota\kappa}$.

Consider now a particular value of μ_0 and x_f for which the CGL system has n unstable eigenmodes. Decompose ψ such that

$$\psi(x, t) = \sum_{k=1}^n \xi_k(x) \chi_k(t) + \phi(x, t) \quad \text{with} \quad \phi \in N(\text{span}\{\xi_1, \xi_2, \dots, \xi_n\}),$$

i.e., ϕ lies in the nullspace of the space spanned by $\{\xi_1, \xi_2, \dots, \xi_n\}$. Taking the inner product of the adjoint eigenfunction $\eta_\kappa(x)$ with the CGL equation and applying this decomposition and the orthogonality property derived above, we obtain

$$\left\langle \eta_\kappa(x), \left[\frac{\partial \psi}{\partial t} = \mathcal{L}\psi + \delta(x-x_f)u \right] \right\rangle \Rightarrow \frac{d\chi_\kappa}{dt} = \lambda_\kappa \chi_\kappa + \langle \eta_\kappa(x), \delta(x-x_f)u \rangle = \lambda_\kappa \chi_\kappa + \eta_\kappa(x_f)u.$$

Assembling these dynamic equations for all of the unstable modal coefficients χ_κ in vector form, we obtain the diagonal system

$$\frac{d\chi}{dt} = \Lambda \chi + \bar{B}u, \quad \Lambda = \begin{pmatrix} \lambda_1 & & 0 \\ & \ddots & \\ 0 & & \lambda_n \end{pmatrix}, \quad \bar{B} = \begin{pmatrix} \eta_1(x_f) \\ \vdots \\ \eta_n(x_f) \end{pmatrix}. \quad (3.3)$$

[†] Note that the eigenvalues of the resolved modes of both A and $\mathbf{Q}A\mathbf{Q}^{-1}$ are accurate approximations of the analytically-determined eigenvalues in the continuous case in (2.2). Note also that, as is also true in the continuous case, all discrete left and right eigenvectors are enumerated by the real part of their corresponding eigenvalues in the open-loop setting, with the least-stable eigenmodes listed first.

This is an analytic expression of the dynamic equation for the unstable modes of the system.

We now review the following facts:

- 1) A system is state stabilizable iff all unstable modes are state controllable.
- 2) (Λ, \bar{B}) is state controllable iff the matrix $C = (\bar{B} \quad \Lambda \bar{B} \quad \Lambda^2 \bar{B} \quad \dots \quad \Lambda^{n-1} \bar{B})$ has full row rank.

In the present case, as Λ is diagonal and $\lambda_i \neq 0 \forall i$, it follows that C has full row rank iff the vector \bar{B} has all nonzero entries. The adjoint eigenfunctions of the CGL equation, with the coefficients selected as described in §2, are nonzero everywhere on the real axis (their zeros lie in the complex plane). Thus, technically, the CGL system considered in this paper is stabilizable for any value of μ_0 and all choices of x_f .

(b) Computation of optimal state-feedback control

In the previous section, we showed analytically that the system under consideration is stabilizable for any value of μ_0 and all choices of x_f . One might think that the issue of characterizing stabilizability for the present system would be closed at this point. However the present control problem is found to be increasingly delicate to solve numerically as the Reynolds number is increased, to the point that incorrect conclusions about stabilizability can be drawn from numerical calculations unless such calculations are interpreted properly. In the two sections that follow, we thus interpret the results from two different numerical characterizations of the stabilizability property.

We first attempt to compute stabilizing feedback for the discretized CGL equation using optimal control theory. This approach involves the choice of a quadratic cost function \mathcal{J} weighing together a generalized state “energy” and a measure of the control effort:

$$\mathcal{J} = \int_0^\infty [\mathbf{x}^* Q \mathbf{x} + \mathbf{u}^* R \mathbf{u}] dt.$$

In the present work, we chose $R = \ell^2 I$ and $Q = Q$ (determined in the previous section) so that $\mathbf{x}^* Q \mathbf{x}$ is simply a numerical approximation of $\int_{-\infty}^\infty |\psi|^2 dx$. The design parameter ℓ allows us to adjust the resulting control magnitude; in the limit that $\ell \rightarrow \infty$, the minimal-energy stabilizing control feedback is obtained. Optimal control theory allows us to compute the control forcing \mathbf{u} that minimizes the cost function \mathcal{J} . This solution is conveniently represented in the state-feedback form $\mathbf{u} = K \mathbf{x}$, where the gain matrix K is computed using the unique positive-definite solution X to the algebraic Riccati equation (ARE)

$$A^* X + X A - X B R^{-1} B^* X + Q = 0 \quad \Rightarrow \quad K = -B^* R^{-1} X. \quad (3.4)$$

Optimal control theory provides an alternative method of determining the stabilizability of the matrix pair (A, B) , since, at least in theory (*i.e.*, using infinite-precision arithmetic), a stabilizing positive-definite solution X to the matrix equation given above exists if and only if A is stabilizable by control input through B , independent of the choice of the positive definite weighting matrices R and Q . Thus, in theory, by determining whether or not a stabilizing positive-definite solution X to (3.4) exists, one may determine the stabilizability of the Ginzburg-Landau operator by pointwise forcing and thus, by iteration, the maximum Reynolds number at which stabilization can be achieved.

The algebraic Riccati equation (3.4) is typically solved using the Schur decomposition technique (Laub 1991). In the present case, this equation was found to become increasingly difficult to solve as the supercriticality is increased. Thus, three alternative methods for solving (3.4) were also implemented (see, *e.g.*, Jamshidi 1980). As a first alternative, an eigenvalue decomposition technique was used instead of the Schur decomposition. As a second alternative we chose to transform the continuous-time Riccati equation (3.4) into the corresponding discrete-time Riccati equation, and to solve the latter using a doubling algorithm (Jamshidi 1980). Finally, we implemented a Newton-iterative algorithm to solve (3.4). In all cases, the results obtained agreed within $\pm 6\%$.

Using double-precision arithmetic, an effective upper bound on the supercriticality was determined, above which a stabilizing solution $X > 0$ to the ARE could not be found. This upper bound, which we denote $\tilde{\delta}(x_f)$, is a function of the forcing position x_f , and is displayed as the solid curve in Figure 1. This figure also indicates the boundaries (dotted) between the local instability regions and, for each δ , the position of the optimal actuator location (dashed) which results in the minimum value of the cost function \mathcal{J} over all actuator locations tested.

Somewhat surprising (and, perhaps, somewhat misleading) is the observation that the upper bound $\tilde{\delta}(x_f)$ indicated in Figure 1, above which a stabilizing solution to the ARE (3.4) could not be found using double precision arithmetic, appears to be quite independent of several choices in the formulation of the discrete optimal control problem, including:

- (1) the positive-definite weighting matrices Q and R ,
- (2) the number of grid points N used (as long as N is sufficiently large),
- (3) the numerical technique used to perform the spatial discretization, and
- (4) the numerical technique used to solve the ARE.

For each actuator location x_f tested, all calculations of $\tilde{\delta}(x_f)$ agreed to within $\pm 6\%$, even as the items listed above were varied. For the parameter values tested, the curve $\tilde{\delta}(x_f)$ reaches a peak value of $\delta_m \triangleq \max_{x_f} \tilde{\delta}(x_f) = 5.3 \pm 0.3$ with the actuator location $x_f = -47 \pm 1$. For $0 < \delta < 5.3$, there exists a window of possible actuator locations (indicated by the solid line in Figure 1) inside of which stabilizing solutions of the ARE may be found using double-precision arithmetic.

Significantly, the location of the upper bound above which a stabilizing solution to the ARE can not be found turns out to be a strong function of the level of numerical precision used in the solution of the ARE; a single-precision calculation of this curve is shown as the dashed line in Figure 1. In this case, the curve $\tilde{\delta}(x_f)$ reaches a peak value of $\delta_m = 1.9 \pm 0.1$ with the actuator location $x_f = -23 \pm 1$. Thus, the “effective upper bound” for stabilizability so determined is *not* a fundamental stabilization limitation, but rather a persistent artifact of the numerical precision used in the solution of the optimal control problem.

(c) Computation of a minimal-energy stabilizing control feedback rule

It is a classical result in control theory that, if a minimal-energy stabilizing control feedback rule is used, the eigenvalues of the stabilized closed-loop system $A + BK$ are given by the union of the stable eigenvalues of A and the reflection of the unstable eigenvalues of A into the left-half plane across the imaginary axis. Since we know where the closed-loop eigenvalues of the system are in this case, the feedback gain matrix K may be computed by the process of *pole assignment*. As shown below, this leads to a simple closed-form expression for the minimal-energy stabilizing control feedback rule.

(i) Review of the solution of the pole assignment problem

In order to formulate the pole assignment problem, we first write down the Hamiltonian which eventually leads to the Riccati equation in the standard derivation of the LQR problem:

$$\begin{pmatrix} A & -BR^{-1}B^* \\ -Q & -A^* \end{pmatrix} V = V\Lambda_{cl} \quad \text{with} \quad V = \begin{pmatrix} V_1 \\ V_2 \end{pmatrix}, \quad (3.5)$$

where the desired eigenvalues of the closed-loop system, λ_{cl} , are listed on the diagonal elements of the diagonal matrix Λ_{cl} , and the corresponding eigenvectors of the Hamiltonian are given by the columns of V , which is partitioned as indicated. In the pole assignment problem, we prescribe the closed-loop eigenvalues λ_{cl} in advance, then compute the corresponding eigenvector matrix V . As with the formulation of the LQR problem, once this eigenvalue/eigenvector problem is solved, the desired feedback

rule is given by $\mathbf{u} = K\mathbf{x}$ with $K = -B^*R^{-1}X$, where $X = -V_2V_1^{-1}$. Multiplying out (3.5), it is easy to show that

$$AV_1 - BR^{-1}B^*V_2 = V_1\Lambda_{cl}, \quad (3.6a)$$

$$-QV_1 - A^*V_2 = V_2\Lambda_{cl}, \quad (3.6b)$$

and thus

$$AQ^{-1}(A^*V_2 + V_2\Lambda_{cl}) + BR^{-1}B^*V_2 = Q^{-1}(A^*V_2 + V_2\Lambda_{cl})\Lambda_{cl}, \quad (3.7a)$$

$$V_1 = -Q^{-1}(A^*V_2 + V_2\Lambda_{cl}). \quad (3.7b)$$

As equation (3.7a) is linear in the unknown matrix V_2 , finding a nonsingular solution V_2 to this equation amounts to a straightforward linear algebra problem. Once V_2 is obtained, calculation of V_1 is trivial using (3.7b) or, equivalently, (3.6a). Standard techniques to solve this problem in the general setting discussed here include those by Ackerman (1972) and Kautsky, Nichols, & Van Dooren (1985), and are well developed.

(ii) *Simplification of the linear algebra problem in modal form*

In the case in which we are simply trying to compute the minimal-energy stabilizing control feedback for the CGL system, the pole placement problem reviewed above can be simplified greatly. First note that, if

$$\Lambda = \begin{pmatrix} \lambda_1 & & & 0 \\ & \lambda_2 & & \\ & & \ddots & \\ 0 & & & \lambda_n \end{pmatrix} \quad \text{and} \quad V = \begin{pmatrix} v_{11} & v_{12} & \dots & v_{1n} \\ v_{21} & v_{22} & \dots & v_{2n} \\ \vdots & \vdots & \ddots & \vdots \\ v_{n1} & v_{n2} & \dots & v_{nn} \end{pmatrix},$$

then the products ΛV and $V\Lambda$ have special structure:

$$\Lambda V = \begin{pmatrix} \lambda_1 v_{11} & \lambda_1 v_{12} & \dots & \lambda_1 v_{1n} \\ \lambda_2 v_{21} & \lambda_2 v_{22} & \dots & \lambda_2 v_{2n} \\ \vdots & \vdots & \ddots & \vdots \\ \lambda_n v_{n1} & \lambda_n v_{n2} & \dots & \lambda_n v_{nn} \end{pmatrix} \quad \text{and} \quad V\Lambda = \begin{pmatrix} \lambda_1 v_{11} & \lambda_2 v_{12} & \dots & \lambda_n v_{1n} \\ \lambda_1 v_{21} & \lambda_2 v_{22} & \dots & \lambda_n v_{2n} \\ \vdots & \vdots & \ddots & \vdots \\ \lambda_1 v_{n1} & \lambda_2 v_{n2} & \dots & \lambda_n v_{nn} \end{pmatrix}.$$

We now consider the pole placement algorithm applied to the equation for the unstable dynamics of the CGL system in modal form, determined analytically in (3.3). Partitioning V_2 into its respective columns, $V_2 = (\xi^{(1)} \ \xi^{(2)} \ \dots \ \xi^{(n)})$, taking $A = \Lambda$, $B = \bar{B}$, $Q = I$, $R = \ell^2 I$, and $\Lambda_{cl} = -\Lambda^*$, and applying the above relationships, it follows that (3.7a) may be written as

$$[-BB^*/\ell^2 + \text{diag}(d_1^{(k)}, d_2^{(k)}, \dots, d_n^{(k)})]\xi^{(k)} \triangleq M^{(k)}\xi^{(k)} = 0,$$

where

$$d_i^{(k)} = \begin{cases} -\lambda_i \lambda_i^* + \lambda_i \lambda_k^* + \lambda_k^* \lambda_k^* - \lambda_i^* \lambda_k^* \neq 0 & \text{for } i \neq k \\ 0 & \text{for } i = k. \end{cases}$$

Thus, the vectors $\xi^{(k)}$ lie in the nullspace of $M^{(k)}$, and may be found by the process of Gaussian elimination, manipulating $M^{(k)}$ to reduced row-echelon form. In the limit $\ell \rightarrow 0$, $M^{(k)}$ approaches a diagonal matrix with a zero in the k 'th diagonal element, and thus $V_2 \rightarrow I$. In order to avoid taking

the difference of two quantities which are almost equal in the computation of V_1 , we return to (3.6a), which we may now write in the form

$$\Lambda V_1 + V_1 \Lambda^* = BB^*/\ell^2 \triangleq C/\ell^2.$$

Defining now the $\{i, j\}$ -component of V_1 as v_{ij} , it follows immediately that $v_{ij} = c_{ij}/[(\lambda_i + \lambda_j^*)\ell^2] \triangleq f_{ij}/\ell^2$. With $V_1 = F/\ell^2$ and $V_2 = I$, it follows that $X = -\ell^2 IF^{-1}$ and thus $\bar{K} = -BX/\ell^2 = -B^*F^{-1}A$.

The resulting closed-form solution for the minimal-energy stabilizing control feedback is now summarized.

Theorem 3.1. *Consider a stabilizable system with no pure imaginary open-loop eigenvalues, for which the dynamics of the unstable modes of the open-loop system may be written in the form $\dot{\chi} = \Lambda\chi + \bar{B}u$, where the diagonal matrix Λ contains the unstable eigenvalues of the open-loop system, which are assumed to be distinct. Define $C = \bar{B}\bar{B}^*$, and compute a matrix F with components $f_{ij} = c_{ij}/(\lambda_i + \lambda_j^*)$. The minimal-energy stabilizing feedback controller is then given by $u = \bar{K}\chi$, where $\bar{K} = \bar{B}^*F^{-1}$.*

Proof. Follows immediately from the derivation presented above. \square

In the continuous setting, by the modal decomposition and orthogonality property developed in §3a, $\chi_k = \langle \eta_k, \psi \rangle$, and thus the control feedback in the continuous setting is

$$u = \bar{K} \begin{pmatrix} \langle \eta_1, \psi \rangle \\ \langle \eta_2, \psi \rangle \\ \vdots \\ \langle \eta_n, \psi \rangle \end{pmatrix}.$$

In the discrete setting, the corresponding modal decomposition and orthogonality property leads to $\chi_k = (s^{(k)})^* Q x$, and thus the corresponding control feedback rule in the discrete setting is

$$u = Kx \quad \text{where} \quad K = \bar{K}S^*Q \quad \text{and} \quad S = (s^{(1)} \quad s^{(2)} \quad \dots \quad s^{(n)}).$$

(iii) Numerical results

The closed-form solution for K described above was applied to the modal form of the CGL equation, which may be determined analytically [see equation (3.3)], for a variety of values of supercriticality δ and forcing locations x_f . Remarkably, numerical calculations of the minimal-energy stabilizing control feedback were found to break down (failing to provide a stable closed-loop system matrix $A + BK$) for values of δ and x_f which accurately coincide with the effective upper bounds for stabilizability obtained by solving the Riccati equation (3.4), as displayed on Figure 1, using both single- and double-precision arithmetic. We reach the same conclusion as in the previous section: the stabilizability limit so determined is *not* a fundamental stabilization limitation, but a persistent artifact of the finite precision arithmetic used in the numerical computations.

4. Actuator placement

It is well known that adjoint eigenfunctions, when properly defined, have a direct relation with the sensitivity of the corresponding system eigenfunctions to applied forcing. Chomaz *et al.* (1990) quantified this property in the case of the CGL equation, showing that the amplitude of the n 'th adjoint eigenfunction at a given position represents, in a quantifiable manner, the magnitude of the response of the n 'th system eigenfunction to small amounts of actuator forcing at this location. Recall that the

adjoint eigenfunctions are the system eigenfunctions for the adjoint CGL equation, which may be obtained simply by changing $\{U, \mu, \nu\}$ to $\{-U, \mu^*, \nu^*\}$ in equation (2.1). Because of the change of sign in the advection term, the support of the adjoint eigenfunctions [which is straightforward to calculate using equation (2.2)] typically lies upstream of the peak of local instability in the CGL system.

We now extend this analysis to the closed-loop setting and to the case in which many system eigenfunctions need to be stabilized. As mentioned previously, the amplitude of each adjoint eigenfunction along the x axis may be interpreted as the *sensitivity* of the corresponding unforced system eigenfunction to small amounts of control forcing as a function of the forcing location. Thus, in order to stabilize several unstable system eigenfunctions, it is necessary that the actuator lie within the domain of support of each of the corresponding adjoint eigenfunctions. As several of these domains of support overlap (Figure 2), it is possible to stabilize several unstable system eigenfunctions simultaneously with a single, appropriately-situated, localized actuator.

Note that, to stabilize a particular mildly unstable system eigenfunction, it is not necessary that the actuator be located near the maximum amplitude of the corresponding adjoint eigenfunction; this only denotes where the influence of a small amount of forcing on the system eigenfunction is maximum. Thus, as indicated in Figure 1, in the slightly supercritical case ($0 < \delta \ll 1$), the window of actuator locations which can be used to stabilize the system extends well into the locally stable regions of the system, far upstream and downstream of the maximum of the first adjoint eigenfunction located at $x = -12.8$. In this case, the optimum location for the actuator for minimizing \mathcal{J} (illustrated by the dashed line in Figure 1) is $x_f = -11.6 \pm 0.7$, which is slightly downstream of the maximum of the first adjoint eigenfunction; a similar result was observed by Chomaz *et al.* (1990).

Theoretically (*i.e.*, using infinite-precision arithmetic), the adjoint eigenfunctions are never exactly zero on the real axis in the present system. Thus, the present system should be stabilizable for any values of μ_0 and x_f , as discussed in §3a. However, as illustrated in (3.2), each adjoint eigenfunction decreases to zero exponentially away from its maximum. Thus, the control authority of localized forcing on the unstable eigenfunctions becomes exponentially small far from the maximum of the corresponding adjoint eigenfunctions. As a consequence, using finite precision arithmetic, effective controls may be computed for only a limited range of values of both μ_0 and x_f .

Figure 2 indicates the “principle support” of the first 14 adjoint eigenfunctions, where the “principle support” Ω is defined as that region, centered at the maximum value of the adjoint eigenfunction, which contains 99% of the energy of that adjoint eigenfunction (that is, $\int_{\Omega} |\eta_{\kappa}|^2 dx = 0.99 \int_{-\infty}^{\infty} |\eta_{\kappa}|^2 dx$). It is seen that the first system eigenfunction for which the principle support of the corresponding adjoint eigenfunction does not have an intersection with the principle support of the previous adjoint eigenfunctions is the fourteenth, and that this eigenmode goes unstable in the uncontrolled CGL system when $\delta = 5.42$. This value compares fairly well with the effective stabilizability limit obtained with double precision arithmetic, $\delta_m = 5.3$. The intersection of the supports of the first thirteen adjoint modes extends from $x = -50.4$ to $x = -47.8$, which also compares favorably with the optimum forcing location $x_f = -47 \pm 1$.

Figure 3 indicates the principle support of the first 22 adjoint eigenfunctions when the definition of “principle support” is modified to be that region which contains 99.9% of the energy of each adjoint eigenfunction. It is seen that, in this case, the first system eigenfunction for which the principle support of the corresponding adjoint eigenfunction does not have an intersection with the principle support of the previous adjoint eigenfunctions is the twenty-second, and that this eigenmode goes unstable in the uncontrolled CGL system when $\delta = 9.17$.

We thus see that studying the degree of overlap of the “principle support” of the adjoint eigenfunctions corresponding to the open-loop unstable system eigenmodes provides valuable insight into the reason for the “effective stabilizability limit” of the system when controls are computed using finite-

precision arithmetic. However, such a characterization in itself does not provide a quantitative prediction of this bound, as it depends on the definition of the “principle support” of the adjoint eigenfunctions.

5. Nonnormality of the closed-loop system

The previous section discussed an *open-loop* characterization of an effective stabilization limitation based on the overlap of the “principle support” of the adjoint eigenfunctions corresponding to the unstable modes of the system. This is an *a priori* analysis technique in the sense that it can be performed before any control algorithm is actually computed. An *a posteriori* observation of the *closed-loop* (controlled) CGL system can also be used to improve our understanding of this limitation.

As mentioned previously, when an unstable system matrix A is stabilizable by control input through B , the minimal-energy stabilizing control feedback (*i.e.*, the optimal control feedback computed in the limit of large ℓ) will leave the stable eigenmodes of the system unchanged, and will reflect the unstable eigenvalues of A across the imaginary axis. Recall from §2 that the eigenvalues of the open-loop CGL equation may be computed analytically. The symmetric reflection property of the minimal-energy optimal control solution is illustrated in Figure 4, taking $\ell = 10^4$ and $\delta = 3$, for the first twenty eigenvalues of the CGL equation. In this minimal-energy optimal control setting, it is quite easy to track numerically the effect of the control on each individual system eigenfunction.

Figure 5 displays the amplitude of the two most unstable open-loop eigenfunctions before and after control is applied for several values of δ , again taking $\ell = 10^4$, with double precision arithmetic. The discontinuity in slope of the closed-loop eigenmodes is due to the Dirac delta function introduced in the CGL equation as the forcing. The main point of Figure 4 is that, though the amplitudes of the two modes are of quite different shape before application of the control, in the closed-loop setting (after application of the control) they tend toward the same shape as δ increases; this property is also observed for the phase of the two modes. Since the corresponding eigenvalues remain well separated even in closed loop (see Figure 4), the closed-loop system becomes what has become known in the fluid mechanics community as a “highly nonnormal” operator. In this situation, a particular (destructive) linear combination of these two stable eigenmodes as an initial condition can have almost zero initial energy, but can lead to very large transient energy growth, possibly triggering nonlinear instability. Characterizations of both open-loop and closed-loop system nonnormality have recently received a tremendous amount of attention in the fluid mechanics community (see, *e.g.*, Butler & Farrell 1992, Trefethen *et al.* 1993; Bewley & Liu 1998; Bamieh & Dahleh 2001; Schmid & Henningson 2001). In the present problem, such a characterization allows interpretation of the stabilization limitation as an approach toward a defective closed-loop system matrix $A + BK$.

Table 1 displays the scalar products of the first system eigenfunction with the following four system eigenfunctions (ordered by the real part of their open-loop eigenvalues), before and after control is applied, for various values of the supercriticality δ . These five eigenfunctions become numerically indiscernible with double precision arithmetic when $\delta = 5.20 \pm 0.2$. (The uncertainty accounts for the difficulty of precisely resolving the eigenvectors close to the stabilization limitation.) This result coincides closely with the stabilization limitation, $\delta_m = 5.30 \pm 0.3$.

6. Discussion

A potentially important role for control theory in fluid mechanics is the prediction and characterization of fundamental performance and stabilization limitations inherent in fluid-mechanical systems. Such limitations are independent of the particular control approach chosen, and thus provide *a priori* estimates as to the possible engineering benefits that might be realized in the search for effective control strategies. The present paper represents one of the first attempts to quantify such a fundamental lim-

itation in a spatially-distributed model of a fluid-mechanical system. The Complex Ginzburg-Landau equation was chosen as a model of inhomogeneous weakly non-parallel flows, and the focus of the article was placed on the fundamental issues pertaining to the decay of stabilizability with Reynolds number. The main results of the present paper are:

1) The chosen system is (theoretically) linearly stabilizable for all values of the bifurcation parameter and the forcing location. However, finite-precision numerical computations of both the optimal control feedback and the minimal-energy stabilizing control feedback display an effective stabilizability limit. The effective stabilizability limit so obtained appears to be fairly independent of the weights chosen in the formulation of the control problem and the numerical methods used for both the discretization of the system and the solution of the result control equations. This apparent limitation, though persistent, is simply an artifact of the numerical precision chosen, and changes significantly when a different numerical precision is used. As a consequence, it does not represent a fundamental feature of the system considered.

2) An open-loop analysis based on the overlap of open-loop adjoint eigenfunctions allows approximate identification of the optimal actuator placement for minimization of the cost function and a characterization of a fundamental closed-loop property, that is, the limiting Reynolds number beyond which stabilizability of the system breaks down. This characterization is a function of the definition the "principle support" of the adjoint eigenfunctions, and thus does not reveal a quantitative prediction of this effective limitation, which itself is a function of numerical precision used. Though not presented here, further numerical calculations show that the optimal actuator placement and characterization of the effective stabilization limitation in the case of two actuators follows in a similar fashion.

3) An examination of the eigenmodes of the closed-loop system reveal that loss of stabilizability in the system considered as the bifurcation parameter is increased is characterized by heightened nonnormality of the closed-loop eigenmodes and an approach toward a defective closed-loop system matrix $A + BK$. As the effective stabilization limitation is approached, the shapes of the leading closed-loop system eigenfunctions become numerically indiscernible.

The linear CGL equation studied in the present paper approximately models small perturbations of spatially-developing flow systems over only a limited range of Reynolds numbers. The conclusions about high-Reynolds number behavior drawn from the present study of the linear CGL equation are thus not directly applicable to real flow systems. However, the linear analysis approaches developed in the present paper extend naturally to the study of both stabilization and detection (that is, the stabilization of estimation error) in a range of spatially-developing flow models, including linearizations of the full 3D Navier-Stokes equation itself. In such systems, the system eigenfunctions and adjoint eigenfunctions are generally not available analytically. However, the leading eigenfunctions and adjoint eigenfunctions (that is, those corresponding to the open-loop unstable eigenvalues) may be computed numerically using the implicitly-restarted Arnoldi method applied to standard computational fluid dynamics (CFD) codes which accurately model the flow and adjoint systems of interest. Extension of the analysis approaches developed in the present paper to more physically-relevant numerical models of spatially-developing flow systems is thus straightforward; a few such extensions are currently well underway, and will be reported in a forthcoming paper. The three main results of the present study, as itemized above, are also expected when the same analysis approaches are applied to higher-fidelity models of spatially-developing flow systems which exhibit similar dynamics, such as jets and wakes. Specifically, in such systems, it is anticipated that:

i) Linear stabilizability/detectability is lost gradually as the Reynolds number is increased. That is, there is no critical Reynolds number above which such systems fundamentally become linearly unstabilizable/undetectable. However, practically speaking, linear stabilization/detection of such systems becomes impossible at sufficiently high Reynolds number.

ii) Analysis of the overlap of the open-loop adjoint eigenfunctions corresponding to the open-loop unstable eigenvalues reveals effective actuator locations for the linear stabilization of the system.

iii) The linear closed-loop system becomes increasingly non-normal as the Reynolds number is increased. The approach towards loss of stabilizability (or detectability) is accompanied by an approach towards a defective closed-loop system matrix $A + BK$ (or $A + LC$) regardless of the control design technique used.

The identification of these inherent properties in high-fidelity models of spatially-developing flow systems should provide us with important new insights in the design of effective control strategies.

The authors gratefully acknowledge many fruitful discussions with Jean-Marc Chomaz, Carlo Cossu, François Gallaire, Patrick Huerre, and Benoit Pier regarding the CGL equation, with Roberts Bitmead and Skelton regarding linear control theory, and with Patricia Catalifaud regarding the Fortran implementation. Generous funding from both AFOSR (Belinda King) and CTE, Ecole des Mines de Paris, is also gratefully acknowledged.

References

- Ackermann, J. 1972 Der Entwurf Linearer Regelungssysteme in Zustandsraum *Regelungstechnik und Prozessdatenverarbeitung* **7**, 297-300.
- Bamieh, B., & Dahleh, M. 2001 Energy amplification in channel flows with stochastic excitation *Phys. Fluids* **13**, 3258-3269.
- Bewley, T.R., & Liu, S. 1998 Optimal and robust control and estimation of linear paths to transition. *J. Fluid Mech.* **365**, 305-349.
- Butler, K.M., & Farrell, B.F. 1992 Three-dimensional optimal perturbations in viscous shear flows. *Phys. Fluids A* **4**, 1637-1650.
- Chomaz, J.M., Huerre, P., & Redekopp, L.G. 1987 Models of hydrodynamics resonances in separated shear flows *Proceedings of the 6th Symposium on Turbulent Shear Flows*, Paul Sabatier Univ., Toulouse 1987 (France), 321-326.
- Chomaz, J.M., Huerre, P., & Redekopp, L.G. 1990 The effect of nonlinearity and forcing on global modes, in *New Trends in Nonlinear Dynamics and Pattern-Forming Phenomena* (ed. P. Coullet & P. Huerre), pp 259-274, Plenum Press.
- Chomaz, J.M., Huerre, P., & Redekopp, L.G. 1991 A frequency selection criterion in spatially developing flows *Stud. App. Math.* **84**, 119-144.
- Doki, H., Hiramoto, K., & Skelton, R.E. 1998 Active control of cantilevered pipes conveying fluid with constraints on input energy *Journal of Fluids and Structures* **12**, 615-628.
- Hammond, D.A., & Redekopp, L.G. 1997 Global dynamics of symmetric and asymmetric wakes *J. Fluid Mech.* **331**, 231-260.
- Huerre, P., & Monkewitz, P.A. 1985 Absolute and convective instabilities in free shear layers *J. Fluid Mech.* **159**, 151-168.
- Huerre, P., & Monkewitz, P.A. 1990 Local and global instabilities in spatially developing flows *Annu. Rev. Fluid Mech.* **22**, 473-537.
- Jamshidi, M. 1980 An overview on the solutions of the algebraic matrix Riccati equation and related problems *Large Scale Systems* **1** 167-192.
- Kautsky, J., Nichols, N.K., & Van Dooren, P. 1985 Robust pole assignment in linear state feedback *Int. J. Control* **41**, 1129-1155.
- Laub, A.J. 1991 Invariant subspace methods for the numerical solution of Riccati equations, in *The Riccati equation* (ed. Bittaini, Laub & Willems), pp. 163-196. Springer.
- Min, C., & Choi, H. 1999 Suboptimal feedback control of vortex shedding at low Reynolds numbers *J. Fluid Mech.* **401**, 123-156.
- Monkewitz, P.A. 1988 The absolute and convective nature of instability in two-dimensional wakes at low Reynolds number *Phys. Fluids* **31** 999-1006.
- Monkewitz, P.A. 1989 Feedback control of global oscillations in fluid systems *AIAA Paper* No 89-0991.
- Monkewitz, P.A. 1993 Wake control, in *Bluff-Body Wakes, Dynamics and Instabilities* (ed. H. Eckelmann, J. M. R. Graham, P. Huerre & P. A. Monkewitz), pp 227-290, Springer.

- Monkewitz, P.A., Berger, E., & Schumm, M. 1991 The nonlinear stability of spatially inhomogeneous shear flows, including the effect of feedback *Eur. J. Mech. B/Fluids*, **10** (2), suppl. 295-300
- Monkewitz, P.A., Huerre, P., & Chomaz, J.M. 1993 Global linear stability analysis of weakly non-parallel shear flows *J. Fluid Mech.* **251**, 1-20
- Monkewitz, P.A., & Sohn, K.D. 1988 Absolute instability in hot jets *AIAA J.* **26** (8), 911-916
- Park, D.S. 1994 Theoretical analysis of feedback control of von-Karman vortex street at slightly supercritical Reynolds number *Eur. J. Mech. B/Fluids* **13**, 4, 387-399
- Park, D.S., Ladd, D.M., & Hendricks, E.W. 1994 Feedback control of von Kármán vortex shedding behind a circular cylinder at low Reynolds numbers *Phys. Fluids* **6** (7), 2390-2405
- Pier, B., & Huerre, P. 2001 Nonlinear self-sustained structures and fronts in spatially developing wake flows *J. Fluid Mech.* **435**, 145 - 174
- Pier, B., Huerre, P., Chomaz, J.M., & Couairon, A. 1998 Steep nonlinear global modes in spatially developing media *Phys. Fluids* **10** (10), 2433-2435
- Roussopoulos, K. 1993 Feedback control of vortex shedding at low Reynolds numbers *J. Fluid Mech.* **248**, 267-296
- Roussopoulos, K., & Monkewitz, P.A. 1996 Nonlinear modelling of vortex shedding control in cylinder wakes *Physica D* **97**, 264-273
- Schmid, P.J., & Henningson, D.S. 2001 Stability and transition in shear flows *Springer*
- Trefethen, L.N., Trefethen, A.E., Reddy, S., & Driscoll, T.A. 1993 Hydrodynamic stability without eigenvalues *Science*, **261**, 578-584
- Zhou, K., & Doyle, J.C. 1997 Essentials of robust control, *Prentice Hall*.

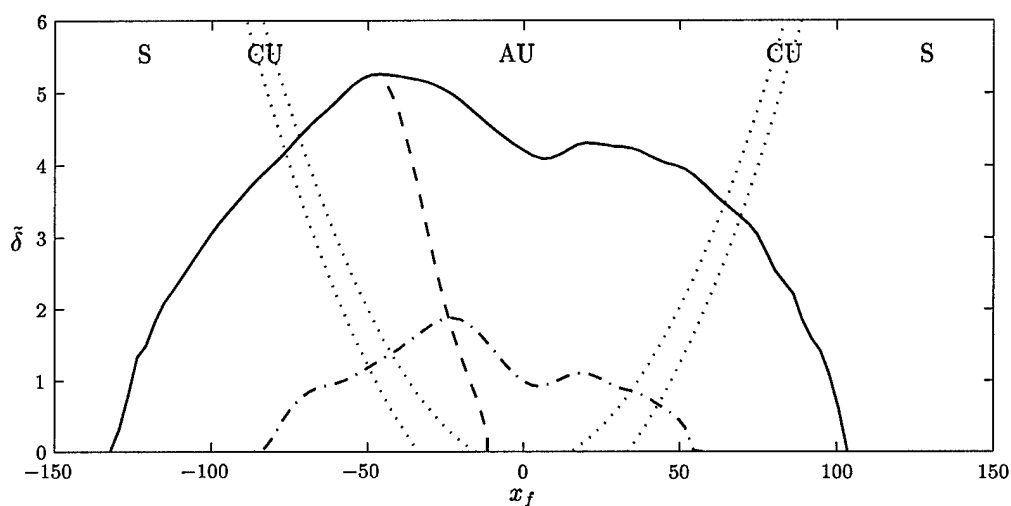


Figure 1. Effective upper bound $\tilde{\delta}(x_f)$ of supercriticality δ above which a stabilizing solution $X > 0$ to the ARE could not be found using (solid) double precision arithmetic and (dot-dashed) single precision arithmetic. Also indicated (dashed) is the optimal actuator location (as a function of δ) for minimization of \mathcal{J} , taking $Q = Q$ (defined in §3a); this curve was found to be essentially independent of both ℓ and the level of numerical precision used. The boundaries between the different local stability regions are indicated by the dotted lines (S: stable, CU: convectively unstable, AU: absolutely unstable).

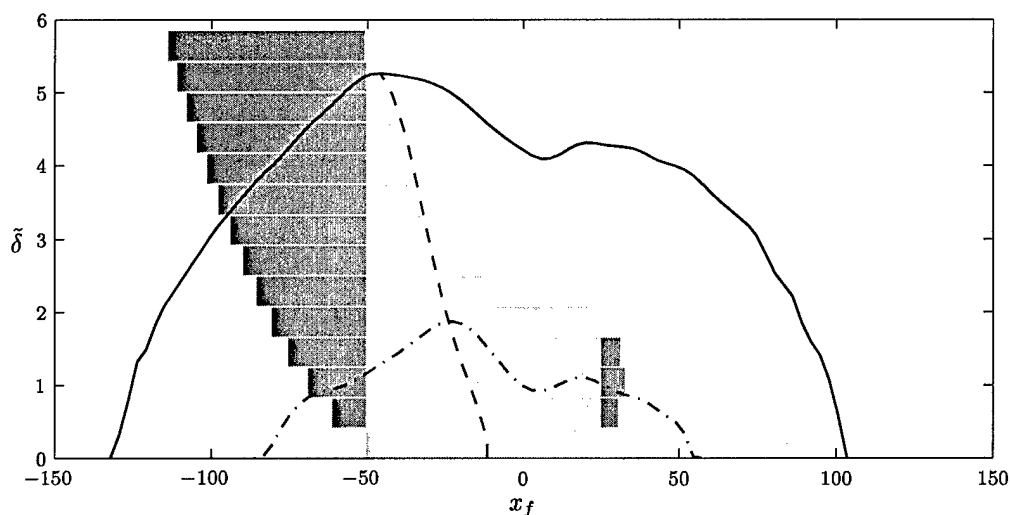


Figure 2. Principle support of the first 14 adjoint eigenfunctions η_k as a function of x . The lower edge of each bar demarks the supercriticality δ at which the corresponding system eigenfunction becomes unstable. The horizontal extent of each bar demarks the region which contains 99% of the energy of each adjoint eigenfunction centered around its maximum value; each bar includes a portion which has a non-zero intersection with the support of all the adjoint eigenfunctions below it (light grey) and a portion outside of this intersection (dark grey). The stabilization limitations using single- and double-precision arithmetic from Figure 1 have been added for interpretation, as well as the optimal actuator location.

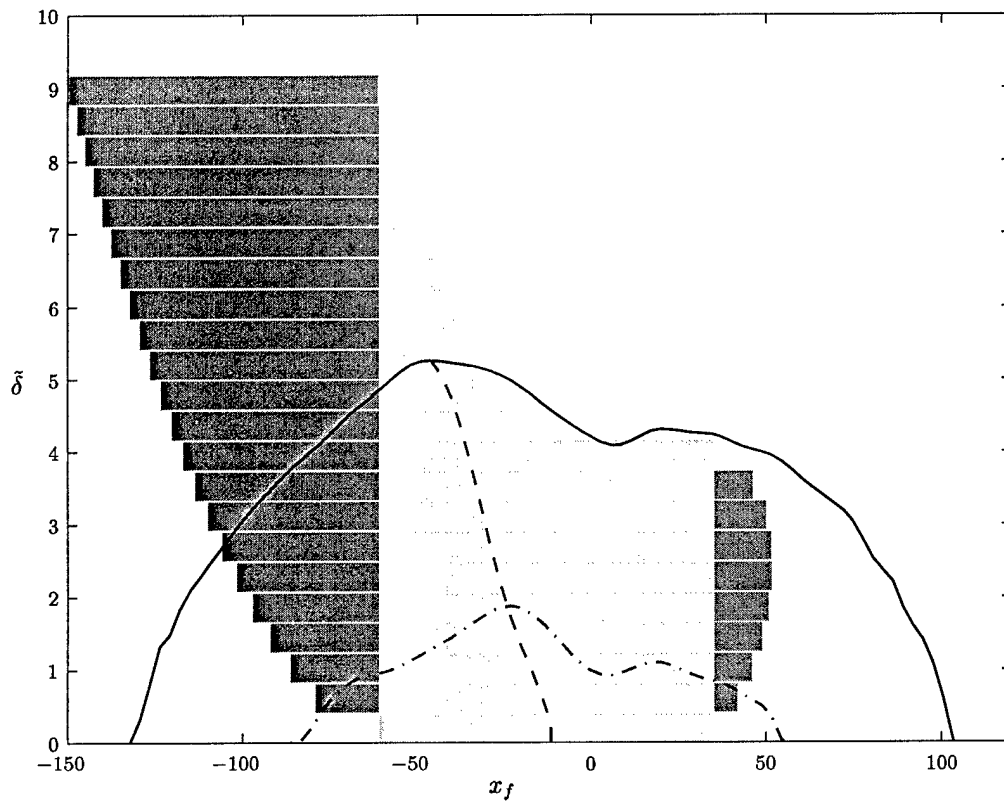


Figure 3. Same as Figure 2, with the principle support redefined as the region which contains 99.9% of the energy of each adjoint eigenfunction.

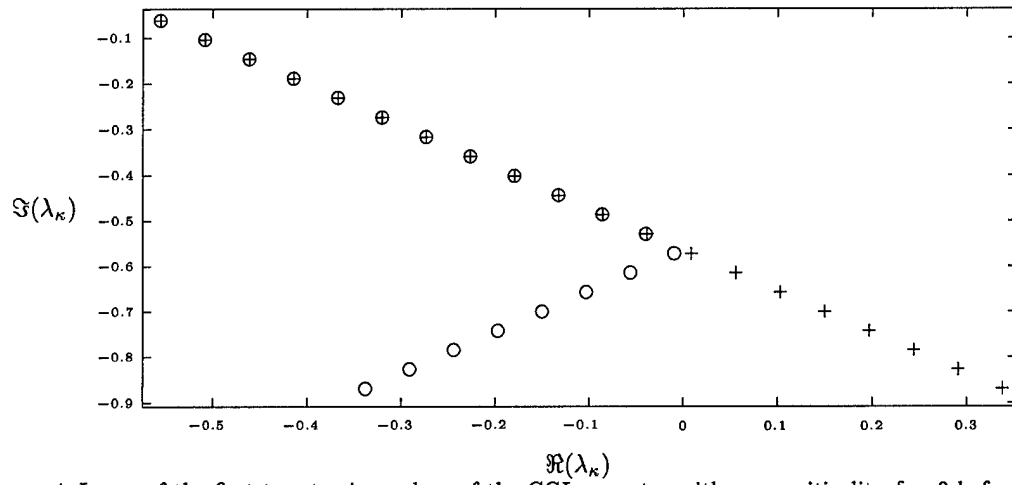


Figure 4. Locus of the first twenty eigenvalues of the CGL operator with supercriticality $\delta = 3$ before (+) and after (o) optimal control is applied (with $\ell = 10^4$ and $x_f = 47$). Note that, in this minimal-energy optimal control setting, the stable eigenmodes of the system matrix are unchanged, and the unstable eigenvalues of the system matrix are reflected across the imaginary axis.

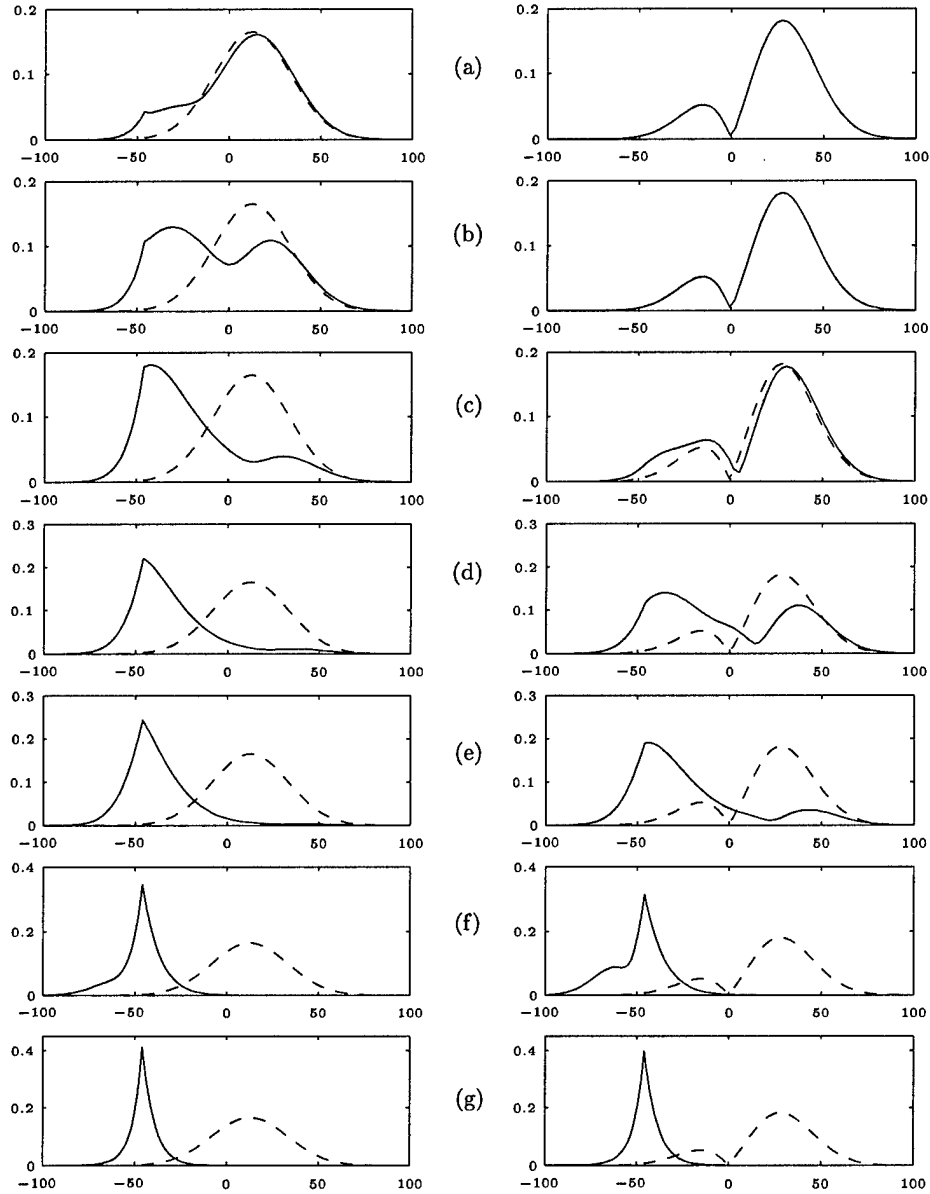


Figure 5. Amplitude of the two most unstable open-loop eigenfunctions (dashed) before and (solid) after optimal control is applied for seven values of the supercriticality δ (with $\ell = 10^4$, $x_f = -47$, and double-precision arithmetic). Left, most unstable open loop eigenfunction; right, second most unstable. The eigenmodes are scaled to be of unit norm (that is, $|\langle \tilde{\phi}_i, \tilde{\phi}_i \rangle| = 1$). $\delta =$ (a) 0.01, (b) 0.25, (c) 0.5, (d) 0.75, (e) 1, (f) 2.5, (g) 4.

δ	$ \langle \tilde{\phi}_0, \tilde{\phi}_1 \rangle $	$ \langle \tilde{\phi}_0, \tilde{\phi}_2 \rangle $	$ \langle \tilde{\phi}_0, \tilde{\phi}_3 \rangle $	$ \langle \tilde{\phi}_0, \tilde{\phi}_4 \rangle $
0	0.6567	0.5028	0.3558	0.2431
1	0.9549	0.3292	0.1037	0.0548
2	0.9291	0.4964	0.3826	0.2790
3	0.9980	0.9804	0.8411	0.4677
4	0.9999	0.9973	0.9924	0.9411
5	0.9999	0.9999	0.9979	0.9930
5.1	0.9999	0.9999	0.9992	0.9988
5.2	0.9999	0.9999	0.9999	0.9999

Table 1. Scalar product of the most unstable open-loop eigenfunction $\tilde{\phi}_0$ with the following four most unstable open-loop eigenfunctions $\tilde{\phi}_1$, $\tilde{\phi}_2$, $\tilde{\phi}_3$ and $\tilde{\phi}_4$ after optimal control is applied as a function of the supercriticality δ (with $\ell = 10^4$, $x_f = -47$, and double-precision arithmetic). The modes are scaled to be of unit norm.



AIAA 2002-2754

Noncooperative optimizations of controls for time-periodic Navier-Stokes systems with multiple solutions

Thomas R. Bewley¹ and Catalin Trenchea^{1,2}

¹*Dept. of MAE, UC San Diego, La Jolla, CA 92093-0411 USA*

²*Institute of Mathematics of the Romanian Academy, 6600 Iași,
Romania*

**1st AIAA Flow Control Conference
June 24–26, 2002, St. Louis, MO**

Noncooperative optimizations of controls for time-periodic Navier-Stokes systems with multiple solutions

Thomas R. Bewley^{1*} and Catalin Trenchea^{1,2†}

¹*Dept. of MAE, UC San Diego, La Jolla, CA 92093-0411 USA*

²*Institute of Mathematics of the Romanian Academy, 6600 Iași, Romania*

Time-periodic systems governed by differential equations are somewhat difficult to consider in the numerical setting because they may possess many solutions. The number of solutions of such systems may be finite or infinite. Further, some trajectories which are exactly time-periodic over a given period might only approximately solve the governing equation, whereas nearby trajectories which exactly solve the governing equation might only be approximately time-periodic over the given period. The difficulty of the time-periodic setting is compounded in the case of systems governed by the Navier-Stokes equation, as the solutions of such systems in the time-evolving setting may be chaotic and multiscale. When considering the optimization of controls for such systems in the time-periodic setting, the situation is thus particularly delicate, as one doesn't know a priori which time-periodic solution (or approximate solution) one should design the controls for.

In the present work, the idea of noncooperative optimization is applied in an attempt to develop a tractable framework to solve the problem of optimization of controls for time-periodic Navier-Stokes systems. The noncooperative aspect of the optimization, however, is somewhat nonstandard: the best controls are found for the worst (of the many) time-periodic solutions of the governing equation. As the number of solutions may be finite, we have employed a technique developed by Barbu (1998) of first looking at a suitable approximation of the time-periodic system of interest with an infinite number of solutions, finding the solution to this approximate system with a gradient-based algorithm leveraging an adjoint analysis, then refining the level of approximation until we have solved (with a sufficient level of accuracy) the optimization problem we are actually interested in. The present brief note motivates this work, presents the structure of our analysis, and outlines the resulting numerical algorithm. A future paper (under preparation) will describe our mathematical proofs of the associated theorems in detail and present some preliminary numerical results.

Introduction

AN essential ingredient which is fundamental to the numerical study of the very physical problem of near-wall turbulence is the very artificial assumption of spatial periodicity (see, e.g., Kim, Moin, & Moser 1987). It is well known in the numerical simulation literature that even though this assumption is highly artificial, it has little to no effect on the quantities of interest in the system (that is, the statistics of the near-wall turbulence) if the problem is formulated correctly (that is, if the computational box is chosen to be large as compared with the correlation length scales of the turbulence).

A possible generalization of this technique is to assume time periodicity in the numerical model of the physical system over a time period which is long with respect to the correlation time scales of the turbulence. Such a technique has the attractive feature that spectral methods may be used in time, affording a high degree of accuracy with a small

number of discretization points in time and obviating the need for a CFL constraint on the timestep to insure numerical stability. However, this assumption converts a smaller problem which evolves parabolically in time into a much larger problem which is elliptic in both space and time, necessitating a large, stationary, four-dimensional problem to be solved with a multigrid-type strategy. For this reason, in addition to the several disadvantages mentioned in the first paragraph of the abstract, the time-periodic framework has not found favor in the turbulence simulation literature.

Many fluid-mechanical systems of physical interest, such as jets and wakes, are dominated by the approximately time-periodic phenomenon of vortex shedding. Flow systems dominated by such behavior are typically characterized in numerical simulations by marching the governing equations in time (from random initial conditions) until the flow reaches an approximately time-periodic statistical steady state. For representative examples of such numerical simulations, see the cylinder wake flow simulation of Kravchenko & Moin (2000) and the turbulent round jet flow simulation of Freund (2001). Time-periodic simula-

*bewley@ucsd.edu

†trenchea@turbulence.ucsd.edu

tions for periods which are large with respect to the shedding period, if they could be made numerically tractable, would certainly be able to capture the quantities of interest in such systems. In fact, one might even hypothesize that time-periodic simulations which are only a few integer multiples of the shedding period might also capture these systems with adequate fidelity.

In the setting of the iterative optimization of controls for flow systems dominated by time-periodic behavior (a setting which is receiving a growing amount of interest for a variety of engineering systems), an important new consideration is introduced: that is, after each small update of the controls, a very good initial guess for the entire trajectory of the controlled flow system is known (*i.e.*, the flow solution before the control was updated). Unfortunately, the time-evolving numerical model can not easily take advantage of this information. To evaluate the effect of the control update on the system using the time-evolving model, the entire system must again be marched in time towards statistical steady state.

Fortunately, the time-periodic numerical model *can* take advantage of the knowledge of this nearby periodic orbit. A very small number of multigrid cycles (perhaps a single W cycle, depending on the scheme implemented) would be needed to update the entire flow solution (over the whole domain of space-time under consideration) when the change to the control distribution is small. This represents a distinct advantage for the time-periodic numerical model when it is to be used as the core of an iterative optimization algorithm. This advantage may indeed tip the scales in favor of such a numerical model in future numerical optimization of controls for such systems.

However, the mathematical infrastructure for the adjoint-based optimization of controls for time-periodic Navier-Stokes systems is not yet in place. In fact, in the standard setting for adjoint analysis of fluid systems (see, e.g., the seminal work of Aberger & Temam 1990), it is not obvious even how to formulate the present problem. We believe that valuable insight into this very practical problem can be gained via mathematical analysis before jumping into large numerical simulations which may or may not converge. The insight we seek includes how to approximate the present optimization problem in order to make it manageable, how to compute the relevant gradient information, how to select which flow solution to optimize for (recall that time-periodic systems in general have multiple solutions), how to refine the level of approximation, and how to insure convergence to a relevant and useful solution.

Complete mathematical analysis of this problem is beyond the scope of this note, and will appear elsewhere. What appears below is a brief skeleton of this analysis with all mathematical proofs and much of the precise mathematical characterization removed. We hope that such a brief presentation might be useful to introduce to the aeronautics and astronautics engineering community a summary of where we are going with this new class of Navier-Stokes optimization problems.

1 Mathematical setting

We are controlling the worst case that appears due to the nonuniqueness of the solutions to the time-periodic Navier-Stokes equation. More precisely, for the cost functional

$$(1.1) \quad J(u, \phi) = \frac{1}{2} \int_Q (C_1 u(x, t))^2 dx dt + \int_0^T h(\phi(t)) dt$$

we compute the

$$(1.2) \quad \inf_{\phi \in L^2(Q)} \sup_{u \in L^2(Q)} J(u, \phi)$$

subject to

$$(1.3) \quad \begin{aligned} \frac{\partial u}{\partial t} + (u \cdot \nabla) u - \nu \Delta u + \nabla p &= B_2 \phi + f_0 \text{ in } \Omega \times \mathbf{R} \\ \nabla \cdot u &= 0 \text{ in } \Omega \times \mathbf{R}; u = 0 \text{ in } \partial\Omega \times \mathbf{R} \\ u(x, t) &= u(x, t + T), \forall (x, t) \in \Omega \times \mathbf{R}. \end{aligned}$$

Here $Q = \Omega \times (0, T)$, Ω is an open bounded subset of \mathbf{R}^2 with smooth boundary $\partial\Omega$, $f_0 \in L^2(\mathbf{R}; L^2(\Omega))$ is a T -periodic source field, $u(x, t) = (u_1(x, t), u_2(x, t))$ is the velocity vector, p stands for the pressure, while $\phi \in L^2_{loc}(\mathbf{R}; L^2(\Omega))$ is a T -periodic input. We denote by U the real Hilbert space of controllers, B_2 is a linear continuous operator from U to $L^2(\Omega)^2$ and h a lower semicontinuous, convex function on U . Finally, C_1 is a unbounded operator in $L^2(\Omega)^2$ satisfying

$$(1.4) \quad \int_{\Omega} (C_1 u(x))^2 dx \leq \alpha \int_{\Omega} u(x)^2 dx + \beta \int_{\Omega} (\nabla u(x))^2 dx.$$

In particular,

$$C_1 = d_1 I \Rightarrow \text{regulation of turbulent kinetic energy, or}$$

$$C_1 = d_2 \nabla \times \Rightarrow \text{regulation of the square vorticity.}$$

We shall briefly recall the setting of (1.3) as an infinite-dimensional differential equation (see [6]-[9]). Let V be the divergence free subspace of $H_0^1(\Omega)^2$, i.e.

$$V = \{u \in H_0^1(\Omega)^2; \nabla \cdot u = 0\}$$

and

$$H = \{u \in L^2(\Omega)^2; \nabla \cdot u = 0 \text{ in } \Omega; n \cdot u = 0 \text{ in } \partial\Omega\}.$$

The space H is endowed with the usual $L^2(\Omega)^2$ -norm denoted $|\cdot|$ and V with the norm $\|\cdot\|$ defined

$$\|u\|^2 = \sum_{1 \leq i \leq 2} \int_{\Omega} |\nabla u_i|^2 dx, \quad u = (u_1, u_2).$$

If we denote V^* the dual of V and identify H with its own dual, we have $V \subset H \subset V^*$. Let $A \in L(V, V^*)$ and $b : V \times V \times V$ be defined by

$$(1.5) \quad (Au, v) = \int_0^T \nabla u_i \cdot \nabla v_i dx, \quad \forall u, v \in V$$

$$(1.6) \quad b(u, v, w) = \sum_{i,j=1}^2 \int_{\Omega} u_i \frac{\partial v_j}{\partial x_i} w_j dx, \quad \forall u, v, w \in V$$

and $B : V \times V \rightarrow V^*$ given by

$$\begin{aligned} (B(u, v), w) &= b(u, v, w) & \forall u, v, w \in V \\ B(u) &= B(u, u), & \forall u \in V. \end{aligned}$$

We set $D(A) = \{u \in V; Au \in H\}$ and denote again by A the restriction of A to H . Recall that b defined in (1.6) is a trilinear continuous functional satisfying (see [8]-[9])

$$b(u, v, w) = -b(u, w, v) \quad \forall u, v, w \in V,$$

$$|b(u, v, w)| \leq C(|u||u||w||w|)^{1/2} \|v\| \quad \forall u, v, w \in V$$

$$|b(u, v, w)| \leq C(|u||u||v||Av|)^{1/2} |w|$$

$$\forall u \in V, v \in D(A), w \in H.$$

Let $f(t) = Pf_0(t)$ and $\mathcal{B}_2 \in L(U, H)$ be given by $\mathcal{B}_2 = PB_2$, where $P : L^2(\Omega)^2 \rightarrow H$ is the projection on H . Now we can write the state equation (1.3) as

$$(1.7) \quad \frac{du}{dt}(t) + vAu(t) + Bu(t) = \mathcal{B}_2\phi(t) + f(t) \quad t \in (0, T)$$

$$u(0) = u(T).$$

Problem (P)

We shall confine to solutions u in (1.7) which satisfy the condition

$$u \in W^{1,2}([0, T]; H), \quad Au \in L^2(0, T; H), \quad Bu \in L^2(0, T; H)$$

and we may reformulate the problem (1.2) as

$$(P) \quad \inf_{\phi} \sup_u \int_0^T \left(\frac{1}{2} |C_1 u(t)|^2 + h(\phi(t)) \right) dt$$

over $(u, \phi) \in (W^{1,2}([0, T]; H) \cap L^2(0, T; D(A))) \times L^2(0, T; U)$ subject to (1.7). We have denoted by $W^{1,2}([0, T]; H)$ the space of all absolutely continuous functions $u : [0, T] \rightarrow H$ such that $u' = du/dt \in L^2(0, T; H)$. We have

$$W^{1,2}(0, T; H) \cap L^2(0, T; D(A)) \subset C(0, T; V).$$

2 Existence of optimal solutions

We consider first the inner problem

$$(2.1) \quad \text{Maximize}_u \int_0^T \frac{1}{2} |C_1 u(t)|^2 dt$$

for all $u \in W^{1,2}([0, T]; H) \cap L^2(0, T; D(A))$ satisfying (1.7), while $\phi \in L^2(0, T; U)$ is fixed.

Proposition 2.1 Problem (2.1) has at least one solution $u_* \in W^{1,2}([0, T]; H) \cap L^2(0, T; D(A))$.

Proof. ... (proof to be presented elsewhere) ... □

We shall study now the existence in problem (P). Assume that

(i) The function $h : U \rightarrow \mathbf{R}$ is convex, lower semi-continuous and satisfies the coercivity condition

$$h(\phi) \geq \omega |\phi|_U^2 + \beta, \quad \forall \phi \in U$$

for some $\omega > 0$, $\beta \in \mathbf{R}$.

Theorem 2.1 Under hypotheses (i), (1.4) problem (P) has at least one solution.

Proof. ... (proof to be presented elsewhere) ... □

3 Approximation of Problem (2.1)

Due to the genericity properties of the time-periodic Navier-Stokes equation (see [10], [11]), it is difficult to derive a gradient algorithm based on adjoint field information for problem (P). The main obstacle is this: the application $\phi \rightarrow u(\phi)$ is neither differentiable, nor continuous. In fact, the result mentioned above states that, for a dense set in $L^2(0, T; H) \ni f + \mathcal{B}_2 \phi$, equation (1.7) has a finite number of solutions, which is constant on every connected part of this set. Therefore, for a small variation of ϕ , the number of solutions to (1.7) may vary to infinity.

Thus, let consider first the approximate inner problem, which in the appropriate limit, approaches the solution of (2.1). To accomplish this, consider the maximization of

$$(3.1) \quad \int_0^T \left(\frac{1}{2} |C_1 u|^2 - \frac{1}{2\epsilon} |\xi|^2 \right) dt$$

over $u \in W^{1,2}([0, T]; H) \cap L^2(0, T; D(A))$, $\xi \in L^2(0, T; H)$ subject to

$$(3.2) \quad \begin{aligned} \frac{du}{dt}(t) + \nu A u(t) + B u(t) &= \mathcal{B}_2 \phi(t) + f(t) + \xi(t) & t \in (0, T) \\ u(0) &= u(T). \end{aligned}$$

Lemma 3.1 For each $\epsilon > 0$ sufficiently small problem (3.1) has at least one solution $(u_\epsilon, \xi_\epsilon)$.

Proof. ... (proof to be presented elsewhere) ... □

Proposition 3.1 For $\epsilon \rightarrow 0$, we have

$$\begin{aligned} u_\epsilon &\rightarrow u_* \text{ strongly in } L^2(0, T; V) \cap C([0, T]; H) \\ \epsilon^{-1/2} \xi_\epsilon &\rightarrow 0 \text{ weakly in } L^2(0, T; H) \\ \lim_{\epsilon \rightarrow 0} \sup_{u, \xi} (3.1) &= \sup_u (2.1). \end{aligned}$$

Proof. ... (proof to be presented elsewhere) ... □

Proposition 3.2 If $(u_\epsilon, \xi_\epsilon)$ is an optimal pair in problem (3.1), then there is $q_\epsilon \in W^{1,2}([0, T]; H) \cap L^2(0, T; D(A))$ such that

$$(3.10) \quad -q'_\epsilon(t) + \nu A q_\epsilon(t) + B'(u_\epsilon(t))^* q_\epsilon(t) = C_1^* C_1 u_\epsilon(t), \text{ a.e. } t \in (0, T)$$

$$q_\epsilon(0) = q_\epsilon(T)$$

$$(3.11) \quad \xi_\epsilon(t) = \epsilon q_\epsilon(t), \text{ a.e. } t \in (0, T).$$

Here $B'(u_\varepsilon(t)), B'(u_\varepsilon(t))^* \in L(V, V^*) \cap L(D(A), H)$ are defined by

$$(3.12) \quad \begin{aligned} (B'(u_\varepsilon)z, w) &= b(z, u_\varepsilon, w) + b(u_\varepsilon, z, w), \quad \forall z \in D(A), w \in H \\ (B'(u_\varepsilon)^*q, w) &= b(w, u_\varepsilon, q) + b(u_\varepsilon(t), w, q), \quad \forall q \in D(A), w \in H. \end{aligned}$$

Proof. ... (proof to be presented elsewhere) ... □

Remark. From Propositions 3.1, 3.2 we have

$$\text{Sup}_u(2.1) = \lim_{\varepsilon \rightarrow 0} \text{Sup}_{u, \xi}(3.1) = \lim_{\varepsilon \rightarrow 0} \int_0^T \left(\frac{1}{2} |C_1 u_\varepsilon|^2 - \frac{\varepsilon}{2} |q_\varepsilon|^2 \right) dt$$

where $(u_\varepsilon, q_\varepsilon)$ satisfies

$$\begin{cases} u'_\varepsilon + \nu A u_\varepsilon + B(u_\varepsilon) = \mathcal{B}_2 \phi + f + \varepsilon q_\varepsilon, & u_\varepsilon(0) = u_\varepsilon(T) \\ -q'_\varepsilon + \nu A q_\varepsilon + B'(u_\varepsilon)^* q_\varepsilon = C_1^* C_1 u_\varepsilon, & q_\varepsilon(0) = q_\varepsilon(T). \end{cases}$$

Therefore we can develop an algorithm that computes, for a fixed ϕ , a solution of maximum energy in the sense of (2.1) to the time periodic Navier-Stokes equation (1.7).

4 Approximation of Problem (P)

For each $\varepsilon > 0$ consider the following optimization problem: minimize

$$(P_\varepsilon) \quad J_\varepsilon(u_\varepsilon, q_\varepsilon, \phi) = \int_0^T \left(\frac{1}{2} |C_1 u_\varepsilon|^2 + h(\phi) - \frac{\varepsilon}{2} |q_\varepsilon|^2 \right) dt$$

over $(u_\varepsilon, q_\varepsilon) \in W^{1,2}([0, T]; H) \cap L^2(0, T; D(A)), \phi \in L^2(0, T; U)$ subject to

$$(4.1) \quad \begin{cases} u'_\varepsilon(t) + \nu A u_\varepsilon(t) + B(u_\varepsilon(t)) = \mathcal{B}_2 \phi(t) + f(t) + \varepsilon q_\varepsilon(t), & u_\varepsilon(0) = u_\varepsilon(T) \\ -q'_\varepsilon(t) + \nu A q_\varepsilon(t) + B'(u_\varepsilon(t))^* q_\varepsilon(t) = C_1^* C_1 u_\varepsilon(t), & q_\varepsilon(0) = q_\varepsilon(T). \end{cases}, t \in (0, T),$$

By Lemma 4.1 and Proposition 3.2 we know that the system (4.1) has at least one solution $(u_\varepsilon, q_\varepsilon)$, which also solves the Problem (3.1)-(3.2).

Instead of (i) we shall use the following hypothesis.

(i)' The function $h : U \rightarrow \mathbf{R}$ is convex, lower semi-continuous and satisfies

$$\omega |\phi|_U^2 + \beta \leq h(\phi) \leq \omega_1 |\phi|_U^2 + \beta_1, \quad \forall \phi \in U$$

for some $\omega, \omega_1 > 0, \beta, \beta_1 \in \mathbf{R}$.

Proposition 4.1 Under hypotheses (i)', (1.4) problem (P_ε) has at least one solution $(u_\varepsilon, q_\varepsilon, \phi_\varepsilon)$. □

Proof. ... (proof to be presented elsewhere) ...

Proposition 4.2 For $\varepsilon \rightarrow 0$ we have

$$(4.13) \quad \lim_{\varepsilon \rightarrow 0} \inf_{\phi, u_\varepsilon, q_\varepsilon} (P_\varepsilon) = \inf_{\phi, u} \sup_{u^*} (P).$$

Proof. ... (proof to be presented elsewhere) ... □

Recall that if K is a closed convex subset of H , we may define the indicator function $I_K : V \rightarrow \overline{\mathbf{R}}$

$$I_K(q) = \begin{cases} 0 & \text{if } q \in K, \\ +\infty & \text{if } q \notin K \end{cases}$$

and the normal cone

$$N_K(q) = \partial I_K(q) = \{q^* \in V^*; (q - w, q^*) \geq 0 \quad \forall q \in K\} \quad \forall q \in K.$$

We denote by $K = \{q \in L^2(0, T; H); \varepsilon \|q\|_{L^2(0, T; H)}^2 \leq 1\}$. Note that this indicator function is used for convenience in the derivation, by incorporating the restriction of q to K in the cost function.

In order to get necessary optimality conditions for the approximate problem $(P_{\epsilon\lambda})$ we encounter again the obstacle of nonuniqueness for the solution to system (4.1). Let consider instead the following optimization problem: minimize

$$(P_{\epsilon\lambda}) \quad J_{\epsilon\lambda}(u_\epsilon, q_\epsilon, \phi, \psi_1, \psi_2) = \int_0^T \left(\frac{1}{2} |C_1 u_\epsilon|^2 - \frac{\epsilon}{2} |q_\epsilon|^2 + I_K(q_\epsilon) + h(\phi) + \frac{1}{2\lambda} |\psi_1|^2 + \frac{1}{2\lambda} |\psi_2|^2 \right) dt$$

over $(u_\epsilon, q_\epsilon) \in W^{1,2}([0, T]; H) \cap L^2(0, T; D(A))$, $\phi \in L^2(0, T; U)$, $\psi_1, \psi_2 \in L^2(0, T; H)$ subject to

$$(4.14) \quad \begin{cases} u'_\epsilon(t) + vAu_\epsilon(t) + B(u_\epsilon(t)) = \mathcal{B}_2\phi(t) + f(t) + \epsilon q_\epsilon(t) + \psi_1(t), & t \in (0, T), & u_\epsilon(0) = u_\epsilon(0) \\ -q'_\epsilon(t) + vAq_\epsilon(t) + B'(u_\epsilon(t))^* q_\epsilon(t) = C_1^* C_1 u_\epsilon(t) + \psi_2(t) & & q_\epsilon(0) = q_\epsilon(T). \end{cases}$$

We note that (u_ϵ, q_ϵ) is again a solution to problem (3.1).

Using an argument similar to Proposition 4.1 we get that $(P_{\epsilon\lambda})$ has at least one solution $(\phi_\lambda, u_{\epsilon\lambda}, q_{\epsilon\lambda}, \psi_{1\lambda}, \psi_{2\lambda})$.

Proposition 4.3 For $\epsilon > 0$ sufficiently small we have

$$(4.15) \quad \lim_{\lambda \rightarrow 0} \inf_{\phi, u_\epsilon, q_\epsilon, \psi_1, \psi_2} (P_{\epsilon\lambda}) = \inf_{\phi, u_\epsilon, q_\epsilon} (P_\epsilon).$$

Proof. ... (proof to be presented elsewhere) ... □

We note that Propositions 4.2 and 4.3 prove that

$$(4.17) \quad \lim_{\epsilon \rightarrow 0} \lim_{\lambda \rightarrow 0} \inf_{\phi, u_\epsilon, q_\epsilon, \psi_1, \psi_2} (P_{\epsilon\lambda}) = \inf_{\phi, u_*} \sup_u (P).$$

5 Necessary Conditions for Optimality

Here we shall establish a maximum principle type result for problem $(P_{\epsilon\lambda})$.

Theorem 5.1 Under hypotheses (1.4), (i)' if $(\phi_\lambda, u_{\epsilon\lambda}, q_{\epsilon\lambda}, \psi_{1\lambda}, \psi_{2\lambda})$ is optimal in problem $(P_{\epsilon\lambda})$ then there is $U_{\epsilon\lambda}, Q_{\epsilon\lambda} \in W^{1,2}([0, T]; H) \cap L^2(0, T; D(A))$ such that

$$(5.1) \quad \begin{aligned} -U'_\lambda + vAU_\lambda + (B'(u_{\epsilon\lambda}))^* U_\lambda &= C_1^* C_1 Q_\lambda - B'(Q_\lambda)^* q_{\epsilon\lambda} - C_1^* C_1 u_{\epsilon\lambda}, & a.e. t \in (0, T) \\ Q'_\lambda + vAQ_\lambda + (B'(u_{\epsilon\lambda})) Q_\lambda &= \epsilon U_\lambda - \epsilon q_{\epsilon\lambda}, & a.e. t \in (0, T) \end{aligned}$$

$$(5.2) \quad \begin{aligned} U_\lambda(0) &= U_\lambda(T), & Q_\lambda(0) &= Q_\lambda(T). \\ \psi_{1\lambda} &= \lambda U_\lambda, & \psi_{2\lambda} &= \lambda Q_\lambda, & \mathcal{B}_2^* \phi_\lambda &\in \partial h(Q_\lambda), & a.e. in (0, T). \end{aligned}$$

Here $\partial h : U \rightarrow U$ is the subdifferential of h .

Proof. ... (proof to be presented elsewhere) ... □

Due to the lack of differentiability in application $\phi \rightarrow u(\phi)$, we have replaced problem (P) by a sequence of approximating problems $(P_{\epsilon\lambda})$, for which we can compute necessary conditions for optimality. An algorithm of gradient type is now proposed in order to compute a optimal solution to problem $(P_{\epsilon\lambda})$. We use iterative processes to solve the inner loop $(P_{\epsilon\lambda})$ and the outer loop (P_ϵ) .

6 Numerical algorithm

Let us assume that $C_1 \equiv I$ and rewrite the optimality system in the following form

$$(4.14)' \quad \begin{cases} u_\epsilon'(t) + \nu A u_\epsilon(t) + B(u_\epsilon(t)) = \mathcal{B}_2 \phi(t) + f(t) + \epsilon q_\epsilon(t) + \psi_1(t), t \in (0, T), u_\epsilon(0) = u_\epsilon(T) \\ \mathcal{A}_\epsilon^* q = P_{R(\mathcal{A}_\epsilon)}(u_\epsilon + \psi_2) \end{cases}$$

$$(5.1)' \quad \begin{cases} \mathcal{A}_\epsilon^* U = P_{R(\mathcal{A}_\epsilon^*)}(\mathcal{Q}_\lambda - u_{\epsilon\lambda} - B'(Q_\lambda)^* q_{\epsilon\lambda}) \\ \mathcal{A}_\epsilon Q = P_{R(\mathcal{A}_\epsilon)}(\epsilon U - \epsilon q). \end{cases}$$

1. Initialize $\epsilon, \lambda > 0$ and ϕ_λ^0 on $t \in [0, T]$.
2. Initialize $i = 0$ and $(\psi_{1\lambda}^0, \psi_{2\lambda}^0)$ on $[0, T]$, where i is the iteration index and $(\phi_\lambda^i, \psi_{1\lambda}^i, \psi_{2\lambda}^i)$ represent the approximation of the control and forcing that we use in $J_{\epsilon\lambda}$.
3. Determine the state $(u_{\epsilon\lambda}^i, q_{\epsilon\lambda}^i)$ on $[0, T]$ from the state equation (4.14)'.
4. Determine the adjoint state $(U_\lambda^i, Q_\lambda^i)$ from the adjoint equation (5.1)'.
5. Determine local expressions for the gradients

$$\frac{DJ_{\epsilon,\lambda}}{D\phi}(\phi_\lambda^i, \psi_{1\lambda}^i, \psi_{2\lambda}^i) = \nabla h(\phi_\lambda^i) - \mathcal{B}_2(\psi_{1\lambda}^i), \frac{DJ_{\epsilon,\lambda}}{D\psi_1} = \frac{1}{\lambda} \psi_{1\lambda}^i - U_\lambda^i, \frac{DJ_{\epsilon,\lambda}}{D\psi_2} = \frac{1}{\lambda} \psi_{2\lambda}^i - Q_\lambda^i.$$

6. Determine the updated control ϕ_λ^{i+1} and forcing $\psi_{1\lambda}^{i+1}, \psi_{2\lambda}^{i+1}$ with

$$\phi_\lambda^{i+1} = \phi_\lambda^i - \alpha^i \frac{DJ_{\epsilon,\lambda}}{D\phi}(\phi_\lambda^i, \psi_{2\lambda}^i), \quad \psi_{1\lambda}^{i+1} = \psi_{1\lambda}^i - \alpha^i \frac{DJ_{\epsilon,\lambda}}{D\psi_1}(\phi_\lambda^i, \psi_{2\lambda}^i), \quad \psi_{2\lambda}^{i+1} = \psi_{2\lambda}^i - \alpha^i \frac{DJ_{\epsilon,\lambda}}{D\psi_2}(\phi_\lambda^i, \psi_{2\lambda}^i),$$

where $0 < \alpha^i < 1$.

7. Increment index $i = i + 1$. Repeat from step 3 until converged.
 8. Reset $\phi_\lambda^0 = \phi_\lambda^i, \psi_{1\lambda}^0 = \psi_{1\lambda}^i, \psi_{2\lambda}^0 = \psi_{2\lambda}^i$.
 9. $\lambda = \lambda/2$. Repeat from step 3 until stop criterion in λ is satisfied (eg., $\|\psi_{1\lambda}\| + \|\psi_{2\lambda}\| < \text{Tolerance}$).
- At this point we have solved problem (P_ϵ) .
10. Reset $\phi_\lambda^0 = \phi_\lambda^i$.
 11. $\epsilon = \epsilon/2$. Repeat from step 2 until stop criterion in ϵ is satisfied.

References

1. BARBU, V. 1998 Optimal control of Navier-Stokes equations with periodic inputs. *Nonlinear Analysis, Theory, Methods & Applications*, **31**, 15-31.
2. KIM, J., MOIN, P., & MOSER, R. 1987 Turbulence statistics in fully developed channel flow at low Reynolds number. *J. Fluid Mech.* **177**, 133-166.
3. KRAVCHENKO, A.G., & MOIN, P. 2000 Numerical studies of flow over a circular cylinder at $Re_D = 3900$. *Phys. Fluids* **12**, 403-417.
4. FREUND, J.B. 2001 Noise sources in a low Reynolds number turbulent jet at Mach 0.9. *J. Fluid Mech.* **438**, 277-305.
5. ABERGEL, F., & TEMAM, R. 1990 On some control problems in fluid mechanics. *Theor. and Comp. Fluid Dyn.* **1**, 303-325.
6. CONSTANTIN, P., & FOIAS, C., 1988 *Navier-Stokes Equations*, The University of Chicago Press.
7. FURSIKOV, A.V., 2000 *Optimal control of distributed systems. Theory and Applications*, Translations of Mathematical Monographs, 187. AMS, Providence, RI.
8. LIONS, J.L., 1969 *Quelques methods de resolution des problemes aux limites nonlineaires*, Dunod, Gauthier-Villars, Paris.
9. TEMAM, R., 1979 *Navier-Stokes Equations*, North-Holland, Amsterdam.
10. SAUT, J.C., & TEMAM, R. 1980 Generic properties of Navier-Stokes Equations: genericity with respect to the boundary values, *Indiana University Mathematics Journal*, **29**, 427-446.
11. TEMAM, R. *Une propriété générique des solutions stationnaires ou périodiques des équations de Navier-Stokes*, Symposium Franco-Japonais, Septembre 1976 in H. Fujita, ed., *Functional Analysis and Numerical Analysis*, Japan Society for the Promotion of Science, 1978.